



Thèse

présentée pour obtenir le grade de docteur

de Télécom ParisTech

Spécialité : Signal et Images

Xin SU

Exploitation of Multi-Temporal SAR Series

Soutenue le 16 mars 2015 devant le jury composé de

M. FERRO-FAMIL Laurent
M. COLLET Christophe
M. LOPEZ-MARTINEZ Carlos
M. PIECZYNSKI Wojciech
Mme TUPIN Florence
Mme SUN Hong
M. DELEDALLE Charles

Rapporteur
Rapporteur
Examineur
Examineur
Directeurs de thèse
Directeurs de thèse
Invité

Contents

1	Introduction	9
1.1	Context of the PhD	9
1.1.1	Development of SAR systems	9
1.1.2	Challenges when dealing with multi-temporal SAR images	10
1.2	Purposes and contributions of this thesis	11
1.3	Organization of this thesis	13
2	SAR Fundamentals	15
2.1	SAR imagery	15
2.1.1	Single look SAR imagery	15
2.1.2	Interferometric SAR imagery	17
2.1.3	Polarimetric SAR and polarimetric interferometric SAR imagery	19
2.2	Statistics of SAR data	20
2.2.1	Single SAR data	20
2.2.2	Scattering vector \mathbf{z} of SAR imagery	21
2.2.3	Empirical matrix \mathbf{C} of SAR imagery	21
2.3	Summary of SAR image	22
I	Information Enhancement: Multi-Temporal Denoising (2S-PPB)	23
3	State of the Art of Denoising	25
3.1	Noise models	25
3.1.1	Independent additive Gaussian noise	25
3.1.2	Multiplicative (signal-dependent) speckle noise	26
3.1.3	Other noise models	26
3.2	Main approaches of denoising	27
3.2.1	Spatial domain approaches	27
3.2.2	Transform domain approaches	30
3.3	Non local means methods	32
3.3.1	The choice of similarity	32
3.3.2	Kernel functions $f(\cdot)$	39
3.3.3	Weight of the center pixel	41
3.3.4	Selection of searching window and patch size	41
3.3.5	NLMs with iteration strategy	42
3.3.6	NLMs in non-spatial domains	42
3.4	Multi-temporal images denoising	43
3.4.1	Extension of denoising range	44

3.4.2	Extension of denoising model	45
3.5	Evaluation of denoising	46
3.6	Summary of image denoising	47
4	Two Steps Non-Local Means for Multi-temporal SAR images	51
4.1	Direct Extension of PPB	51
4.1.1	Comparison of PPB method	51
4.1.2	Analysis and motivation	52
4.2	Two-steps non-local means (2S-PPB)	53
4.2.1	Criteria of change	55
4.2.2	Two Steps Denoising	59
4.3	Experiments of denoising	60
4.3.1	Synthetic Images	61
4.3.2	Realistic SAR Synthetic Images	61
4.3.3	Real Multi-Temporal SAR Images	62
4.4	Extension of 2S-PPB for miss-registered images	64
4.4.1	Estimation of miss-registration	64
4.4.2	Two-steps non-local means on miss-registered images	67
4.4.3	Experiments of denoising on miss-registered images	68
4.5	Conclusion	69
 II Information Change Analysis: Change Detection and Change Classification (NORCAMA)		73
5	State of the Art of Change Analysis	75
5.1	General methods of change detection	75
5.1.1	Change criteria for optical images	76
5.1.2	Change criteria for SAR images	78
5.1.3	General criteria for change detection	82
5.1.4	Thresholds for change detection	83
5.1.5	Change detection Evaluations	85
5.2	Change pattern classification	86
5.3	Long-term Change analysis	87
5.4	Summary of change analysis	87
6	Likelihood Ratio Test based Change Detection	89
6.1	Approximate likelihood ratio test	89
6.2	Generalized likelihood ratio test	90
6.3	Thresholds for change detection	91
6.4	Experiments of change detection	92
6.4.1	Data Set	92
6.4.2	Change detection methods	93
6.4.3	Results	93
6.5	Conclusion	94

7	Change Classification: NORCAMA	101
7.1	Change criterion matrix	101
7.2	Normalized cut on change criterion matrix	102
7.2.1	Normalized cut	102
7.2.2	Clustering using CCM	104
7.3	Recognition of change patterns	105
7.4	Experiments of Change Classification	105
7.4.1	Test on realistic SAR synthetic images	105
7.4.2	Test on real SAR images	107
7.5	Conclusion	107
III	Information Updating and Compression	111
8	Information Updating of SAR Time Series	113
8.1	Concept and method of compression	114
8.1.1	Pixel-level compression	114
8.1.2	Patch-level compression	118
8.1.3	The relation with usual data compression schemes	120
8.2	Updating method	121
8.2.1	2S-PPB filtering for stable information updating	121
8.2.2	Change detection for updating	122
8.2.3	Change classification for updating	122
8.2.4	Database updating	122
8.3	Experiments of compression and updating	123
8.3.1	Time and space consumptions	123
8.3.2	Updating results	124
8.4	Experiments of Sentinel-1 images	128
8.5	Conclusion	134
9	Conclusion	135
9.1	Summary	135
9.2	Perspectives	136
	Bibliographie	157

Notations

SAR Fundamentals:

$z = z e^{j\theta}$	Complex value of SAR image;
z^\dagger	Complex conjugate of z ;
j	Imaginary number such that $j^2 = -1$;
θ	Phase of z ;
ϕ	Difference of phase between θ_1 and θ_2 (corresponding to the argument of $z_1 z_2^\dagger$);
$y = z ^2$	Intensity of SAR image;
\sqrt{y} or $ z $	Amplitude of SAR image;
$y^{\text{M-L}}$	Multi-looking result of y (averaging of intensity samples);
\mathbf{z}	$\{z_1, z_2, \dots\}$
Σ	Covariance matrix;
$\hat{\Sigma}$	Estimator of covariance matrix;
\mathbf{C}	Empirical covariance matrix of \mathbf{z}
D	Coherence ($D_{i,j} = \frac{z_i z_j^\dagger}{\mathbf{E}(z_i)\mathbf{E}(z_j)}$);
$\mathbf{G}(0, \sigma^2)$	Gaussian (normal) distribution with mean 0 and variance σ^2

Images:

y_t	Noisy intensity image acquired at time t ;
$\{y_{t_1}, y_{t_2}, \dots, y_{t_N}\}$	Noisy multi-temporal intensity images;
u_t	Noise-free image of y_t (estimation of u_t);
\hat{u}_t	Denosed image of y_t ;
\hat{u}_t^{PPB}	Denosed image of y_t by PPB filter (estimation of u_t by PPB filter);
y_t^{1st}	Output of the first (temporal) step in the proposed filter;

Pixels:

$y_t(i)$	Intensity of pixel at position i in image y_t ;
$y_t(i+k)$	Intensity of pixel at position $i+k$, the k -th neighbor of pixel $y_t(i)$ in patch $\mathbf{y}_t(i)$ (in image y_t) with $k = \{1, 2, \dots, K\}$;
$u_t(i)$	Noise-free pixel at position i in image u_t ;
$\hat{u}_t(i)$	Denosed pixel at position i in image \hat{u}_t ;

$\hat{u}_t(i+k)$ Denoised pixel at position $i+k$, the k -th neighbor of pixel $\hat{u}_t(i)$ in patch $\hat{\mathbf{u}}_t(i+k)$ (in image \hat{u}_t) with $k = \{1, 2, \dots, K\}$;

y_m, y_n Abbreviations of $y_{t_m}(i)$ and $y_{t_n}(i)$;

Patches:

$\mathbf{y}_t(i)$ Patch of size $\sqrt{K} \times \sqrt{K}$ of intensities with pixel i as center in image y_t ;

$\mathbf{u}_t(i)$ Noise-free patch of size $\sqrt{K} \times \sqrt{K}$ with pixel $u_t(i)$ as center in image u_t ;

$\hat{\mathbf{u}}_t(i)$ Denoised Patch of size $\sqrt{K} \times \sqrt{K}$ with pixel $\hat{u}_t(i)$ as center in image \hat{u}_t (estimation of $\mathbf{u}_t(i)$);

Number of looks:

L_t Map of number of looks associated to image y_t ;

$L_t(i)$ Number of looks associated to pixel $y_t(i)$;

$\mathbf{L}_t(i)$ Patch of number of looks associated to patch $\mathbf{y}_t(i)$;

$\hat{\mathbf{L}}_t(i)$ Patch of (equivalent) number of looks associated to patch $\hat{\mathbf{u}}_t(i)$;

\hat{L}_t Map of (equivalent) number of looks associated to image \hat{u}_t ;

Examples:

$y(1)$ An example of intensity of pixel (it can be any pixel in the multi-temporal images);

$y(2)$ Another example of pixel;

$u(1)$ Noise-free value of pixel $y(1)$;

$\hat{u}(1)$ Denoised value of $y(1)$;

$L(1)$ Number of looks associated to pixel (1);

$\hat{L}(1)$ Equivalent number of looks associated to $\hat{u}(1)$.

Operators:

D_{pixel} Difference between two pixels;

R_{pixel} Ratio between two pixels;

$\mathbf{E}(y)$ Expectation of variable y ;

$\mathbf{Var}(y)$ Variance of variable y ;

$f(\cdot)$ Kernel function to map weights;

$S(y(i), y(j))$ Similarity of pixel $y(i)$ and pixel $y(j)$;

$S_{\text{GLR}}(\mathbf{y}(i), \mathbf{y}(j))$ Generalized likelihood ratio similarity between patch $\mathbf{y}(i)$ and $\mathbf{y}(j)$;

$S_{\text{KL}}(\hat{\mathbf{u}}(i), \hat{\mathbf{u}}(j))$ Kullback-Leibler divergence similarity between patch $\hat{\mathbf{u}}(i)$ and $\hat{\mathbf{u}}(j)$;

Chapter 1

Introduction

Remote sensing is the collection of information about the Earth features without making physical contact. Synthetic aperture radar (SAR), one of the remote sensing techniques, is well known as an all-weather and all-time operational active sensor. It has been used for a variety of applications ranging from urban monitoring to biomass study. A large number of methodologies for SAR have been developed in the community of remote sensing.

Nowadays more and more SAR sensors have been launched, which provide us a huge quantity of SAR images. For the same geographic areas, there are many SAR images acquired at different times with different sensor parameters (e.g. band, resolution, incidence angle etc.). They provide multi-temporal SAR images. This new availability of SAR data brings us new challenges. The main objective of this thesis is to fully exploit the information provided by the multi-temporal SAR images. This chapter presents the background and the main questions addressed by this thesis.

1.1 Context of the PhD

1.1.1 Development of SAR systems

The development of radar imaging systems dates back to the beginning of the 1950s. To balance the effect of ground permittivity and roughness, the wavelengths are usually in bands L, S, C or X (corresponding to 0.39~1.55GHz, 1.55~4.20GHz, 4.20~5.75GHz or 5.75~10.90GHz). Real aperture radar can not reach a spatial resolution of meters, since the length of the antenna is impracticable to be several kilometers for any spaceborne or airborne sensors. Synthetic aperture radar (SAR) invented by Carl A. Wiley in 1951 addresses this problem by a coherent registration and processing of the received radar echoes during the motion of the sensor. Since then, SAR systems have experienced a fast growth with drastic improvement of the spatial resolution and numerous launched sensors are now acquiring a huge amount of data.

SEASAT satellite was the first spaceborne platform of SAR sensors [Jordan, 1980]. After the success of SEASAT, more effort was made to develop spaceborne (including shuttleborne) SAR platforms, e.g. SIR-A SAR [Granger, 1983], SIR-B SAR [Cimino et al., 1986], ERS-1 SAR [Attema, 1991] etc. The SIR missions continued and more complex systems were equipped. SIR-C SAR could operate at multi-wavelength, X, C, L bands with full polarimetric mode [Jordan et al., 1995]. More recently, an increasing number of spaceborne SAR systems have been launched, e.g. ALOS-PALSAR by JAXA [Shimada, 2006], RADARSAT-1/2 by CSA [Moon et al., 2010], TerraSAR-X and TanDEM-X by DLR

[Krieger et al., 2010], ENVISAT-ASAR and Sentinel-1A by ESA, Cosmo-SkyMed by ASI etc.

The airborne SAR systems, meanwhile, have been well developed, for example AIR-SAR by NASA, E-SAR [Horn, 1996] and F-SAR [Horn et al., 2008] by DLR, RAMSES by ONERA [Dubois-Fernandez et al.], Pi-SAR by JAXA and so on. Compared with spaceborne SAR systems, airborne SAR systems usually operate at multi-frequency and full polarization mode with higher spatial resolution.

1.1.2 Challenges when dealing with multi-temporal SAR images

At the beginning of SAR image interpretation, various processors mainly dealt with the amplitude or intensity images. With the development of SAR systems and the interferometric and polarimetric modes, the additional potential information in phase and polarization has been exploited in the complex SAR images. More recently, multi-temporal images provide a considerable number of images of the same area by repeat passing of SAR sensors. Consequently, new challenges for the efficient use of these multi-temporal images have been raised. Let us precise here that we will not consider the differential interferometric case (D-InSAR) in this PhD, thus focusing on the general case of intensity or amplitude images combination. For D-InSAR, many approaches specially relying on permanent scatters have been proposed exploiting lying multi-temporal interferometric series.

Improved performance

Since multi-temporal images observe the objects many times, it is expected to exploit this increasing information to improve SAR image interpretation tasks. For example, it can be used to improve the performance of SAR image denoising, classification, segmentation, object recognition and tracking. Of course, appropriate approaches should be used to extract and utilize this information, otherwise no better or even worse performance might be obtained compared with using *single*-temporal image. Therefore, much effort has been made to develop and experiment new effective ways of extracting and fusing the information from different dates (images).

Exploitation of change information

Change detection is defined as “*a process of identifying differences in the state of an object or phenomenon by observing it at different times*” [Singh, 1989]. It is usually applied between two dates (two images). Change detection is helpful in locating and monitoring regions of interest, like urban growth, disaster evaluations etc. However, if we have multi-temporal SAR images with more than two dates/images, how can we get use of these images to improve the change detection between only two dates (any pair of images in the multi-temporal data set)?

To avoid confusion, we denote bi-temporal images as images at two dates only and multi-temporal images as images with more than two dates. Compared with the *bi*-temporal images, multi-temporal images provide us more information over the time about the objects. This temporal information has to be used to monitor and analyze the changing trend of natural objects, e.g. the vegetation change, the movements of the earth’s surface etc. However for changes in urban areas caused by human activities, people may need to define and recognize these long term changes (e.g. change classification etc.) and how it

can be used for further interpretation.

Big data challenges

SAR imagery is “*big data*“ from the day of its birth, since its size is much larger than usual natural images or pictures. Nowadays, multi-temporal SAR images with high spatial and temporal resolution make this be especially true. Like other big data problems, the data compression and storage of multi-temporal SAR images should be considered. In addition, how to quickly, efficiently and better interpret the new acquired images with the former multi-temporal images is also a challenge for SAR image interpretation. Although the problem of SAR compression will not be fully addressed in this thesis, some of the proposed methods will find applications for compression purposes.

Combination of various types of multi-temporal images

Fig.1.1 gives an illustration of the family of the available multi-temporal remote sensing images or data. It consists of a large number of different kinds of images. Even when only SAR images are concerned, multi-temporal images can be images acquired by different sensors, with different resolution, different polarimetric mode, different incidence angle, different ascending/descending mode etc. The challenges of using various types of multi-temporal images in a uniform framework is how to combine or fuse the information extracted from these images, which is a hot topic in the remote sensing community.

1.2 Purposes and contributions of this thesis

Our main objective in this PhD work is to fully exploit the available information provided by multi-temporal SAR images. In this thesis, we will focus on SAR images acquired from the same sensor with the same spatial resolution, the same incidence angle, the same ascending/descending mode and the same polarimetric mode, as shown in the red part of Fig.1.1. Although the data can be in interferometric configuration, differential interfere is out of the scope of our work. The three following subjects have been handled in the PhD.

Multi-temporal SAR images denoising

We will first address the problem of SAR image denoising, or more precisely SAR physical parameters estimation (like the reflectivity). The intensity of SAR data suffers from multiplicative noise called *speckle*. Denoising/despeckling is usually a pre-processing for many automatic interpretation tasks. When dealing with single SAR image, much effort has already been made in this community to limit the fluctuations. For multi-temporal SAR images with more images and more (redundant) information, the denoising/despeckling results are supposed to be better than using single SAR image. and multi-temporal averaging is used since the beginning of SAR. The first purpose of this thesis is to efficiently denoise multi-temporal SAR images using both spatial and temporal redundant information.

Non local means (NLM), a simple but efficient method, proposed by Buades et al. [2005a] has been successfully used in image denoising field. Inspired by the theory of NLM and its extension to single SAR image denoising (the probabilistic patch based method of Deledalle et al. [2009]), we extend non-local approaches for the denoising of multi-temporal SAR data. This approach improves single SAR image denoising while preserving the new

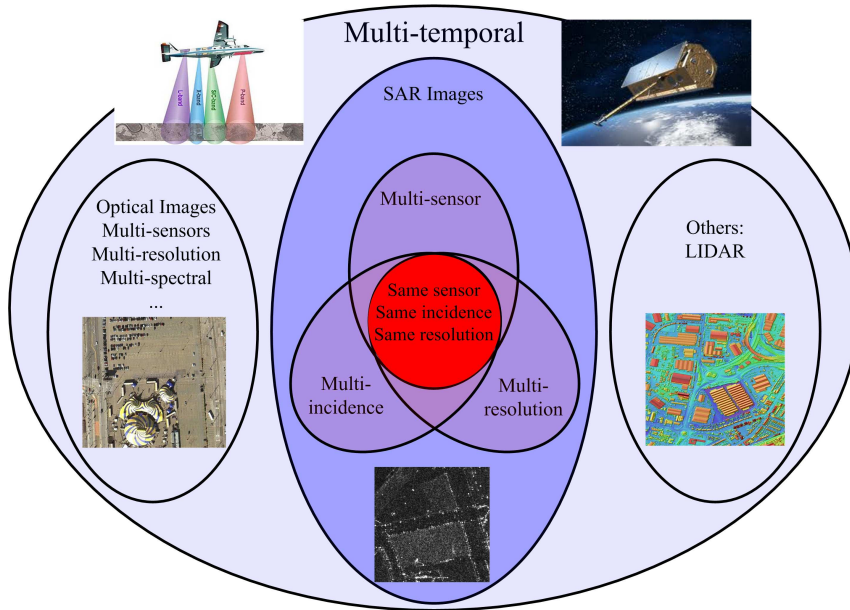


Figure 1.1: The data set studied in this thesis is multi-temporal SAR images with same sensor, same incidence angle, same resolution and same polarization. It is a small subset of the family of multi-temporal remote sensing images.

information in the multi-temporal data set. This first contribution is described in chapter 4 (Fig.1.2).

Change detection and change classification

The second problem we will focus on is the change detection problem between two SAR images. This problem has already been well studied but we will focus on change detection when a SAR multi-temporal series is available. Our purpose is to exploit the useful information of the whole multi-temporal SAR data set for change detection. We will propose two change criteria based on likelihood ratio test. They introduce the denoised images provided by our previously mentioned denoising filter using the whole multi-temporal data set into the computation of the likelihood probability.

Beyond change detection with bi-temporal images, the definition of changes in multi-temporal images is a major challenge for multi-temporal SAR data. Taking a boat in a port as example, it may go through a process of appearance, disappearance then reappearance over the time in the multi-temporal images. To extract and recognize this kind of long term change information, we propose to classify the changes according to their temporal behaviors. The proposed method is based on the analysis of the complete matrix of changes via a clustering approach. This change classification is the second main contribution (chapter 7).

Data compression and updating of denoised images and change information

Although compression was not the core of our work, we also investigate how the proposed approaches could be used in an operational way, when data are sequentially available and should be processed separately (a new data being processed using the available data base,

but not processing again the whole set of data). We thus develop a new compression approach. When a new image is acquired, the compressed data can be used to process the new image (e.g. denoising, change detection etc.), and comparable performance can be obtained than using uncompressed data.

1.3 Organization of this thesis

Fig.1.2 gives a global view of the organization of this thesis. Chapter 2 introduces the SAR fundamentals and the basic features of SAR images which will be used in the next chapters, e.g. the statistical features, the (equivalent) number of looks, the coherence features etc. Part I of this thesis presents our work on reflectivity estimation when dealing with multi-temporal SAR series. It consists of two chapters: chapter 3 reviews the state of the art of denoising methods and highlights the non local means approaches and their improvements; chapter 4 presents the proposed two-steps multi-temporal non local means filter for multi-temporal SAR images. In Part II, we first give a global review of change analysis in chapter 5. We then propose a likelihood ratio test based change criteria (chapter 6) and develop a change classification method (chapter 7). The challenge of updating reflectivity estimation, change detection and change classification when a new image is available is detailed in Part III (chapter 8). Conclusions and perspectives are discussed in chapter 9.

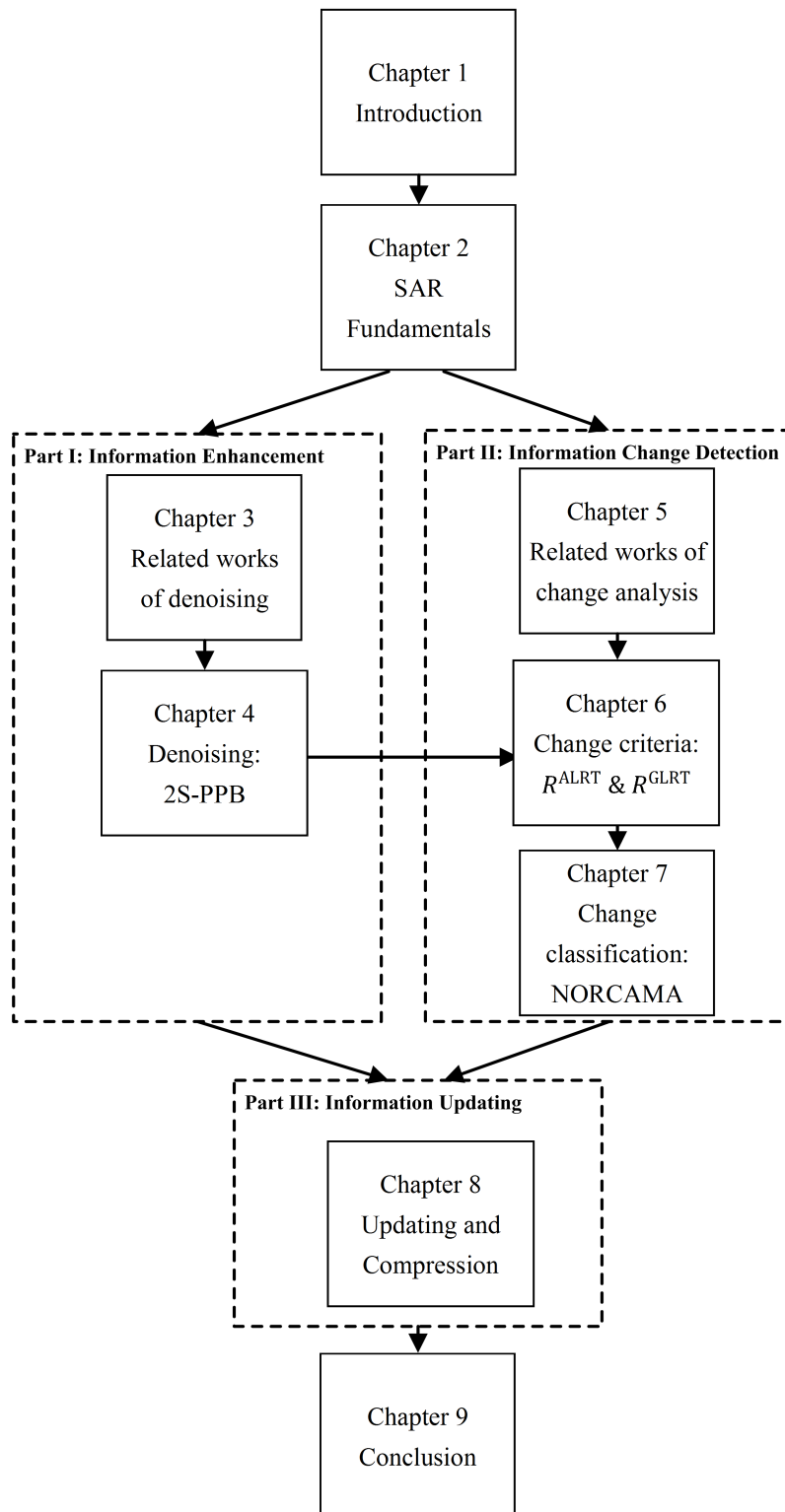


Figure 1.2: The organization of the manuscript

Chapter 2

SAR Fundamentals

A radar imaging system is a form of radar system used to create images of landscape. Like a common radar system, it emits an electromagnetic wave in a side looking way, as shown in Fig.2.1. When arriving on the ground, the wave is diffused and only part of the wave re-emitted in the emitting direction can be received by the sensor. The incidence angle θ , the angle of the side looking, is the angle between the radar beam direction (usually in the middle of the swath) and the nadir. In the range direction, the objects have different distances to the sensor. Resolution in the range dimension of the image is accomplished by emitting short pulses consisting of a carrier frequency and the necessary sidebands, or by using longer *chirp pulses* in which frequency varies (often linearly) with time in the bandwidth. The differing times and frequencies at which echoes return allow points at different distances to be distinguished. Thus, the sensor receives the backscattered waves at different times. After quantizing the time delay and applying adapted filtering, SAR can create one line of the image (the sum of individual scatterers received at certain time and frequency of the chirp contributes to one point on the line). Imaging system can create the image line by line in the same way.

In the azimuth direction each acquired line corresponds first to each emitted pulse during the sensor movement. The resolution is thus mainly linked to the size of the antenna, given a certain spaceborne or airborne radar sensor. Increasing the size of the antenna to obtain a fine resolution in azimuth direction is impracticable for spaceborne or airborne sensors. Synthetic aperture radar (SAR) *lengthens* artificially the antenna using digital signal processing techniques. SAR sensor is moving, thus each object can be illuminated during a time span (which is called integration time). SAR system records all the received signals during this time span and then integrates them by exploiting the Doppler shifts. The synthetic aperture can be considered as a synthetic antenna whose size is the displacement distance of the sensor during the integration time.

This chapter briefly introduces the SAR imagery and its statistical modeling.

2.1 SAR imagery

2.1.1 Single look SAR imagery

As explained in the beginning of this chapter, each point/pixel in the SAR image corresponds to a region of the ground, which is called a resolution cell. In reality, this resolution cell is larger than the wavelength, thus there are many backscattered waves in one resolution cell. In other words, all the returns from the resolution cell will contribute to the

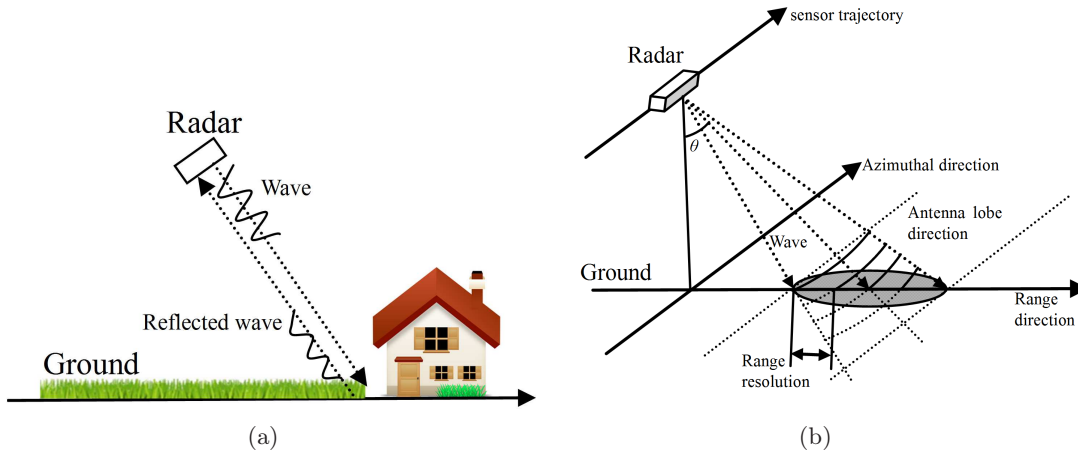


Figure 2.1: (a) The radar illuminates the scene in side looking geometry. (b) Principle of radar imaging system.

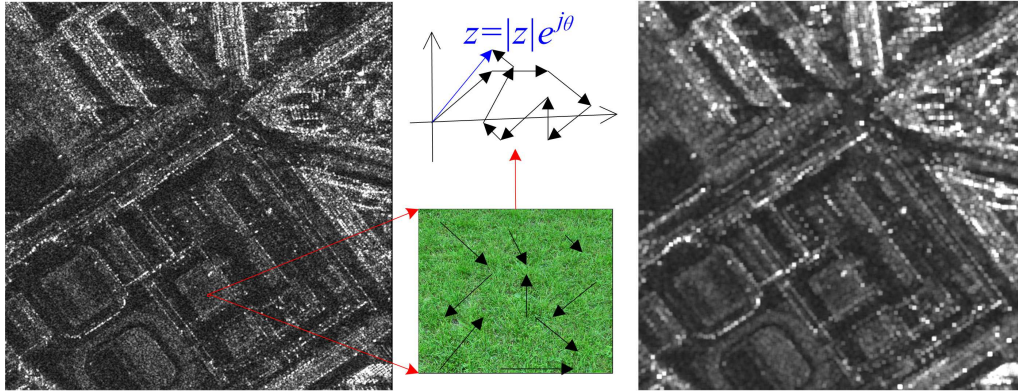


Figure 2.2: An illustration of single-look complex (SLC) SAR image and its multi-looked image. From left to right: the SLC SAR image, the illustration of coherence summation in a resolution cell and the 5×5 multi-look SAR image.

complex value of the pixel. Each backscattered wave has its own amplitude and phase. As shown in the middle of Fig.2.2, each backscattered wave is denoted as a vector with length (amplitude) and direction (phase). Thus, each pixel of the SAR imagery has two coefficients, amplitude and phase, which can be represented as a complex value $z = |z|e^{j\theta}$ (j is the imaginary number such that $j^2 = -1$). Single look complex (SLC) SAR image consists of a matrix of complex values z . The modulus $|z|$ is the amplitude, $|z|^2 = y$ is the intensity or reflectivity and $\theta = \arg z$ is the phase.

As shown in the middle of Fig.2.2, all the backscattered echoes contribute to the final z in an interferential way. It can be shown that the intensity images have very strong multiplicative noise, called speckle. The simplest way to reduce the speckle is spatially averaging in a small window, which is similar to the locally smoothing operator of the boxcar filter. This averaging operator is given by:

$$y = \frac{1}{L} \sum_{i=1}^L |z(i)|^2, \quad (2.1)$$

where L is referred to the number of looks. This operator is also known as the multi-looking operator. The right of Fig.2.2 presents the multi-looking result of the SAR image using a 5×5 smoothing window. Multi-looking operator (filter) indeed reduces the fluctuation of speckle, but with a loss of spatial resolution since there is a blurring of edges.

2.1.2 Interferometric SAR imagery

Interferometric SAR (InSAR) imagery is a SAR remote sensing technique using two SAR images to collect ground information using intensity, coherence and phase differences of the backscattered echoes. InSAR images are acquired using either single-pass interferometry or repeat-pass interferometry. They must have very close incidence angles such that the backscattered signals of the two images are almost the same. The time interval may vary from 0.1s to years. Moreover, when N ($N > 2$) co-registered SAR images are available in interferometric configuration, any pair of them can be used to build an interferogram. The quality of the interferogram is linked to the temporal delay between the two acquisitions, to the difference of incidence angles and possibly to ground changes. Lots of literature call them multi-interferometric SAR images. As mentioned in chapter 1, the multi-temporal SAR images studied in the thesis are from the same sensor, same incidence angle, same-resolution co-registered SAR images. They are usually in interferometric configuration, which is a special case (and favorable) of multi-temporal images. InSAR imagery can be used to generate maps of surface deformation or digital elevation using differences in the phase of the waves returning to the sensors [Zebker et al., 1997]. The minor changes (like centimeter-scale changes) in deformation can be detected. This technique has been applied to geophysical monitoring of natural disasters, for example earthquakes [Simons et al., 2002], volcanoes [Hooper et al., 2004], landslides [Riedel and Walther, 2008] and so on.

Interferometric SAR images

Taking z_t and $z_{t'}$ a pair of co-registered InSAR images, a pair of pixels $z_t(i)$ and $z_{t'}(i)$ are located at the same position i . Without loss of generality, we replace $z_t(i)$ and $z_{t'}(i)$ by a pair of pixels $z(1)$ and $z(2)$ to simplify the expressions. The covariance matrix is:

$$\begin{aligned} \Sigma &= \mathbf{E} \left[\begin{pmatrix} z(1) \\ z(2) \end{pmatrix} \begin{pmatrix} z(1)^\dagger & z(2)^\dagger \end{pmatrix} \right] \\ &= \begin{bmatrix} \mathbf{E}(|z(1)|^2) & \mathbf{E}(z(1)z(2)^\dagger) \\ \mathbf{E}(z(1)^\dagger z(2)) & \mathbf{E}(|z(2)|^2) \end{bmatrix} \\ &= \begin{bmatrix} R(1) & \sqrt{R(1)R(2)}D \exp(j\phi) \\ \sqrt{R(1)R(2)}D \exp(-j\phi) & R(2) \end{bmatrix} \end{aligned} \quad (2.2)$$

with

$$R(1) = \mathbf{E}(|z(1)|^2), R(2) = \mathbf{E}(|z(2)|^2), \quad (2.3)$$

$$\phi = \arg(z(1)z(2)^\dagger) \quad (2.4)$$

and

$$D = \frac{|\mathbf{E}(z(1)z(2)^\dagger)|}{\sqrt{\mathbf{E}(|z(1)|^2)\mathbf{E}(|z(2)|^2)}}. \quad (2.5)$$

$z(1)^\dagger$ is the complex conjugate of $z(1)$. D is called the coherence between the two pixels, ϕ is the actual interferometric phase. From a physical point of view, ϕ depends on the difference of the two propagation times (wave from the target to the sensor) [Graham, 1974] and is thus related to the elevation of the point. However, ϕ is known modulo 2π and contains some orbital fringes [Gens and Van Genderen, 1996], which make it difficult to recover the unwrapped phase. Many methods for phase unwrapping and orbital fringes removal have been proposed, for instance Goldstein et al. [1988], Rosen et al. [2000].

The simplest way to estimate Σ is to compute the empirical covariance matrix by averaging in a local square window (which is closely similar to the multi-looking operator but with complex values):

$$\begin{aligned} \mathbf{C} &= \frac{1}{L} \sum_{i=1}^L \begin{bmatrix} z(1, i) \\ z(2, i) \end{bmatrix} \begin{bmatrix} z(1, i)^\dagger & z(2, i)^\dagger \end{bmatrix} \\ &= \frac{1}{L} \begin{bmatrix} \sum_i z(1, i)z(1, i)^\dagger & \sum_i z(1, i)z(2, i)^\dagger \\ \sum_i z(2, i)z(1, i)^\dagger & \sum_i z(2, i)z(2, i)^\dagger \end{bmatrix}, \end{aligned} \quad (2.6)$$

where $z(1, i)$ is i -th neighbor of $z(1)$, and this average is performed in a square window with L pixels (L is also called the number of looks for interferometric estimation). \mathbf{C} is the empirical matrix which can be considered as the respective sample estimation of the covariance matrix Σ . Then, we can get:

$$\begin{aligned} \hat{D} \exp(j\hat{\phi}) &= \frac{\sum_i z(1, i)z(2, i)^\dagger}{\sqrt{\sum_i z(1, i)z(1, i)^\dagger} \sqrt{\sum_i z(2, i)z(2, i)^\dagger}}, \\ \hat{D} &= \frac{|\sum_i z(1, i)z(2, i)^\dagger|}{\sqrt{\sum_i z(1, i)z(1, i)^\dagger} \sqrt{\sum_i z(2, i)z(2, i)^\dagger}}, \\ \hat{\phi} &= \arg \left(\sum_i z(1, i)z(2, i)^\dagger \right). \end{aligned} \quad (2.7)$$

The quantity $\hat{D} \in [0, 1]$ denotes the similarity between $z(1)$ and $z(2)$ (and it is an estimation of the true coherence D). The larger \hat{D} the stronger correlation between $z(1)$ and $z(2)$, and it also denotes a higher reliability of the estimated interferometric phase $\hat{\phi} \in [-\pi, \pi]$. \hat{D} can also be considered as a criterion for similarity measurement (which will be discussed in section 4.1) and a change detection criterion (which will be discussed in section 5.1). Fig.2.3 shows an example of InSAR data.

Multi-interferometric SAR

We denote a multi-interferometric SAR series as $\{z_{t_1}, z_{t_2}, \dots, z_{t_N}\}$. A pixel series $\mathbf{z}(i) = \{z_{t_1}(i), z_{t_2}(i), \dots, z_{t_N}(i)\}$ is located at position i . Similarly, we take $\mathbf{z} = \{z(1), z(2), \dots, z(N)\}$ as a generic notation, the covariance matrix of this pixel series is:

$$\begin{aligned} \Sigma &= \mathbf{E}(\mathbf{z}\mathbf{z}^\dagger) = \mathbf{E} \left(\begin{pmatrix} z(1) \\ z(2) \\ \dots \\ z(N) \end{pmatrix} \begin{bmatrix} z(1)^\dagger & z(2)^\dagger & \dots & z(N)^\dagger \end{bmatrix} \right) \\ &= \mathbf{E} \left(\begin{bmatrix} z(1)z(1)^\dagger & z(1)z(2)^\dagger & \dots & z(1)z(N)^\dagger \\ z(2)z(1)^\dagger & z(2)z(2)^\dagger & \dots & z(2)z(N)^\dagger \\ \dots & \dots & \dots & \dots \\ z(N)z(1)^\dagger & z(N)z(2)^\dagger & \dots & z(N)z(N)^\dagger \end{bmatrix} \right), \end{aligned} \quad (2.8)$$

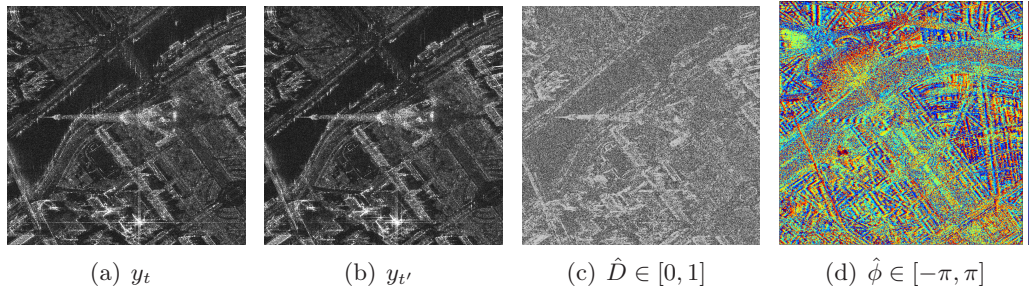


Figure 2.3: An example of InSAR imagery. (©DLR project LAN1746) (a) SAR image z_t , (b) SAR image $z_{t'}$, (c) The estimation $\hat{D} \in [0, 1]$ using Eq.(2.7), (d) The estimation $\hat{\phi} \in [-\pi, \pi]$ using Eq.(2.7). The coherence \hat{D} indicates the reliability of the estimated phase $\hat{\phi}$. When \hat{D} is close to 1 (bright in figure c), the phase difference $\hat{\phi}$ is highly reliable.

where $\mathbf{E}(z(m)z(n)^\dagger) = \sqrt{\mathbf{E}(|z(m)|^2)\mathbf{E}(|z(n)|^2)}D_{m,n} \exp(j\phi_{m,n})$ and \dagger indicates the hermitian transpose. $D_{m,n}$ and $\phi_{m,n}$ are the coherence and interferometric phase between pixel $z(m)$ and $z(n)$. The empirical matrix \mathbf{C} of the pixel series can be obtained by the similar expression of Eq.(2.6):

$$\mathbf{C} = \frac{1}{L} \sum_{i=1}^L \mathbf{z}(i)\mathbf{z}(i)^\dagger. \quad (2.9)$$

The term in the m -th row and n -th column of can be represented as $\frac{1}{L} \sum_i z(m, i)z(n, i)^\dagger$. The multi-look estimation of $D_{m,n}$ and $\phi_{m,n}$ can also be obtained using the same expression as in Eq.(2.7). Multi-interferometric SAR images can be used to reduce the uncertainty in estimation of surface elevation [Homer et al., 1996], and recover fine ground movement.

2.1.3 Polarimetric SAR and polarimetric interferometric SAR imagery

Polarimetric SAR (PolSAR) images provide more complete information on the imaged scene. They are obtained by sending and receiving waves with different polarization components (horizontal or vertical polarization). For example, z_{hv} denotes an echo emitted using horizontal polarization mode and received using vertical polarization mode. A pixel at position i in the full-polarization PolSAR imagery consists of a vector $\mathbf{z}(i) = \{z_{hh}(i), z_{hv}(i), z_{vv}(i)\}$, in which z_{vh} has been discarded because of the assumption of $z_{hv} = z_{vh}$ using mono-static polarimetry. The empirical matrix \mathbf{C} of PolSAR is given by the same expression as Eq.(2.9). It presents the complex hermitian product between each pair of different polarizations, which indicates the polarimetric information of the targets. Many works have been done to exploit the physical features of the targets from the empirical matrix \mathbf{C} .

For instance, Pauli decomposition [Cloude and Pottier, 1996] provides an interpretation of targets using single bounce (or odd bounces), double bounces (or even bounces) and orthogonal polarization, and more polarimetric decompositions like Krogager [Krogager, 1990], Freeman [Freeman and Durden, 1998], Huynen [Huynen, 1970], Barnes [Holm and Barnes, 1988], Cloude (also known as H/A/a and asymmetry) [Cloude and Pottier, 1997] have been proposed.

Polarimetric interferometric SAR (PolInSAR) imagery consists of a pair of polarimetric SAR imagery, which can provide both the interferometric and polarimetric information of the scene. The complex vector of each pixel can be represented as $\mathbf{z}(i) = \{z_{c-hh}(i), z_{c-hv}(i), z_{c-vv}(i), z_{c'-hh}(i), z_{c'-hv}(i), z_{c'-vv}(i)\}$, which can be considered as an extension of the PolSAR vector. The covariance matrix $\mathbf{\Sigma}$ and empirical matrix \mathbf{C} (the multi-looking estimation of $\mathbf{\Sigma}$) can also be obtained using Eq.(2.8) and Eq.(2.9). These notations can be extended to multi-temporal data.

2.2 Statistics of SAR data

2.2.1 Single SAR data

As explained in section 2.1.1, SAR imagery suffers from the speckle noise since z is the coherence summation of echoes in a resolution cell. To statistically model the speckle, Goodman [1976] proposed some assumptions in each resolution cell: 1) the phase and amplitude of each scatterer are independent and identically distributed (i.i.d.), 2) each echo is independent of the others; 3) the phases of echoes are uniformly distributed (rough surface). Under the central limit theorem, the probability of z follows a 2-dimensional multivariate normal distribution or a zero-mean circular complex Gaussian distribution:

$$p(z|\sigma^2) = p([\text{Re}(z) \ \text{Im}(z)]|\sigma^2) = \frac{1}{2\pi\sigma^2} \exp\left(-\frac{|z|^2}{2\sigma^2}\right). \quad (2.10)$$

Besides, $2\sigma^2$ represents the reflectivity of the imaged surface, which is the physical parameter related to the radar cross section (RCS). When the complex variable z changes to intensity value y ($y = |z|^2$), the probability density function (pdf) turns to be an exponential distribution given by:

$$p(y|u) = \frac{1}{u} \exp\left(-\frac{y}{u}\right), \text{ with } y \geq 0, \quad (2.11)$$

where $u = 2\sigma^2$ and in the following of this thesis u denotes the expectation of y ($\mathbf{E}(|z|^2) = \mathbf{E}(y) = u$). Further more, the multi-looking result (L looks) using Eq.(2.1) can be modeled by the Gamma distribution, which is given by:

$$p(y|u, L) = \frac{L^L y^{L-1}}{\Gamma(L)u^L} \exp\left(-\frac{Ly}{u}\right), \quad (2.12)$$

where $\Gamma(\cdot)$ is the Gamma function. Note that the exponential distribution given by Eq.(2.11) can be deduced from the Gamma distribution in Eq.(2.12) by setting $L = 1$. Fig.2.4.a gives an illustration of Gamma distributions with different parameters. The distribution marked in blue is Gamma distribution with $L = 1$ and also the exponential distribution. Eq.2.12 is obtained when the averaged values are i.i.d. in Eq.2.1. In practice, these values can be correlated. In this case the Gamma distribution still holds, but L has to be replaced by an equivalent number of looks.

The amplitude data $|z|$ can also be modeled. It follows a Nakagami-Rayleigh distribution given by:

$$p(|z||u) = \frac{2L^L |z|^{2L-1}}{\Gamma(L)u^L} \exp\left(-\frac{L|z|^2}{u}\right). \quad (2.13)$$

Figure 2.4.b shows the Nakagami-Rayleigh distributions with $u = 1$ and $L = \{0.5, 1, 2, 3, 5\}$.

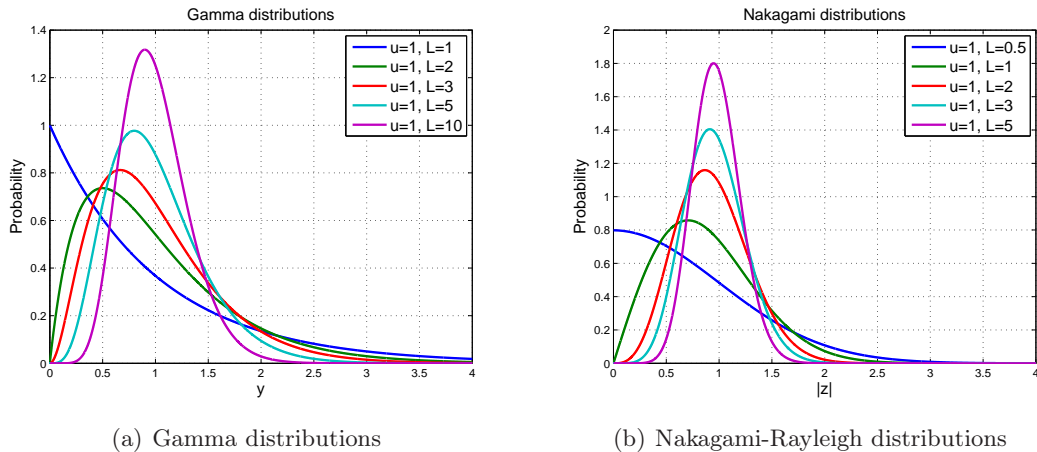


Figure 2.4: The distributions of intensity y and amplitude $|z|$ with different parameters. (a) Gamma distributions modeling y with $u = 1$ and different $L = \{1, 2, 3, 5, 10\}$, Gamma distribution with $L = 1$ is also the exponential distribution. (b) Nakagami-Rayleigh distributions modeling $|z|$ with $u = 1$ and different $L = \{0.5, 1, 2, 3, 5\}$.

Gamma distribution plays an important role in the SAR image processing, since it can model the intensity of SAR imagery. In this thesis, we will use this Gamma distribution in the denoising and change detection of the intensity of SAR images. Let us mention that other models exist like Weibull, log-normal, Fisher, Generalized Gamma distribution. They are more adapted for non-homogeneous areas and take into account some texture distribution representing the variations of the scene. More parameters are necessary, like the shape parameter of the scene, to define them.

2.2.2 Scattering vector \mathbf{z} of SAR imagery

Without loss of generality, we can denote all the previous types of SAR images introduced in section 2.1 by $\mathbf{z}(i) = \{z_1(i), z_2(i), \dots, z_N(i)\}$, with $N = 1$ for SLC images, $N = 2$ for InSAR images, $N = 3$ for PolSAR images, $N = 6$ for PolInSAR images and $N \in \mathbb{N}^*$ for multi-channel SAR images. The $N \times N$ complex covariance matrix Σ can be computed using Eq.(2.8). Under Goodman's model, the distribution of \mathbf{z} is a N -dimensional circular complex Gaussian distribution given by:

$$p(\mathbf{z}|\Sigma) = \frac{1}{\pi^N |\Sigma|} \exp\left(-\mathbf{z}^\dagger \Sigma^{-1} \mathbf{z}\right), \quad (2.14)$$

where $|\Sigma|$ is the determinant of matrix Σ . Note that the exponential distribution given by Eq.(2.11) can be deduced from the circular complex Gaussian distribution in Eq.(2.14) by setting $N = 1$.

2.2.3 Empirical matrix \mathbf{C} of SAR imagery

The empirical matrix \mathbf{C} of scattering vector \mathbf{z} computed by multi-looking operator in Eq.(2.9) (including Eq.(2.1) with $N = 1$ and Eq.(2.6) with $N = 2$) is usually used in SAR image processing. When $N = 1$ and $L = 1$, the distribution of \mathbf{C} simplifies to the

exponential distribution given by Eq.(2.11). When $N = 1$ and $L \geq 1$, the distribution will be the Gamma distribution given by Eq.(2.12).

When $N > 1$ and $L < N$, the matrix \mathbf{C} is singular and matrix $\mathbf{\Sigma} = \mathbf{E}(\mathbf{C})$ is also singular. Its distribution cannot be modeled by a pdf with inverse matrix of $\mathbf{\Sigma}$. However, modeling each term of \mathbf{C} respectively, instead of modeling \mathbf{C} in a united way, is one of the solutions. When $N > 1$ and $L \geq N$, matrix \mathbf{C} follows a complex Wishart distribution:

$$p(\mathbf{C}|\mathbf{\Sigma}) = \frac{L^{NL} |\mathbf{C}|^{L-N}}{\Gamma_N(L) |\mathbf{\Sigma}|^L} \exp [-L \text{tr} (\mathbf{\Sigma}^{-1} \mathbf{C})] , \quad (2.15)$$

where $\Gamma_N(L)$ is the multivariate gamma function.

2.3 Summary of SAR image

This chapter has briefly introduced the principles of SAR imagery and its main statistical models. The intensity of SAR images and its associated Gamma distribution have been highlighted. However, with the development of SAR sensors, the spatial resolution of SAR images has raised to meters or even centimeters. SAR images are full of edges, textures, which cannot be modeled by Gamma distributions anymore. But in the following chapters we will show that our proposed methods focus on local features (i.e. patches), to select samples following the same distribution, thus boiling down to the Gamma distribution of homogeneous area. In the following chapters, this Gamma distribution will be used to drive the proposed methods of denoising and change detection for multi-temporal SAR images.

Part I

Information Enhancement: Multi-Temporal Denoising (2S-PPB)

Chapter 3

State of the Art of Denoising

Both denoising of natural images and despeckling of SAR images have been well studied in the literature. The main purpose of denoising and despeckling is providing better estimation of physical parameters and better performance of automatic tools. Most algorithms of denoising consider the statistical models of noise, for example Gaussian distribution of noise in natural images and Gamma distribution of speckle in SAR intensity images. Thus, both the statistical models of noise and the denoising principles are discussed in this chapter.

Although this thesis focuses on multi-temporal SAR despeckling, the state of art of natural images denoising (usually with Gaussian noise) and single SAR image despeckling is worthy of review. This chapter begins with the review of noise models, including Gaussian and Gamma noise distributions. Following the brief introduction of main ideas of denoising (and despeckling), the non local means (NLM) theory [Buades et al., 2005a] is highlighted and various improvements and extensions of it are reviewed. Since the (patch) similarity plays an important role in the NLM theory, some similarity measurements are discussed and extended to a more general case: comparing patches with different noise level, which will be used in the proposed method in chapter 4.

3.1 Noise models

Image noise is random variation of brightness (color information, reflectivity or other physical quantity) in images. It can be produced by the imaging sensor or during the transmission. Different imaging systems produce different types of noise. Due to its irregular characteristic in both spatial and temporal spaces, image noises are usually represented by their statistical characteristics. In this section, we describe the most common statistical models used for different types of acquisition systems.

3.1.1 Independent additive Gaussian noise

In optical images, a typical model of image noise is a Gaussian, additive, independent (at each pixel) noise. Major causes of Gaussian noise in digital images arise during acquisition (sensor noise) caused by poor illumination or high temperature, and transmission (electronic circuit noise). Given an underlying true value u , the observed variable y can be considered as the sum of u (considered as a deterministic value here) and a Gaussian

independent random variable (noise) n :

$$y = u + n \quad (3.1)$$

where n is a zero-mean Gaussian random variable following the pdf $\mathbf{G}(0, \sigma^2)$:

$$p(n) = \frac{1}{\sqrt{2\pi}\sigma} \exp\left(-\frac{n^2}{2\sigma^2}\right), \quad (3.2)$$

with variance $\mathbf{Var}(n) = \sigma^2$. Figure 3.1.a shows some zero-mean Gaussian distributions with different σ . Given a Gaussian noise model for n , the pdf, expectation and variance of the observed variable y can be represented as:

$$\begin{aligned} p(y|u) &= p(n = y - u) = \frac{1}{\sqrt{2\pi}\sigma} \exp\left(-\frac{(y - u)^2}{2\sigma^2}\right), \\ \mathbf{E}(y) &= \mathbf{E}(u + n) = u, \\ \mathbf{Var}(y) &= \mathbf{Var}(u + n) = \sigma^2. \end{aligned} \quad (3.3)$$

In this model, no texture for u is taken into account. Figure 3.1.a and b show Gaussian distributions with different u and σ . σ can be considered as the noise level, as shown in Figure 3.1.c-e the larger σ denotes stronger noise in images.

3.1.2 Multiplicative (signal-dependent) speckle noise

As introduced in chapter 2, speckle universally exists in the coherent imagery systems, e.g. SAR, sonar and ultrasound images. The common model of multiplicative noise is given by:

$$y = u \cdot n, \quad (3.4)$$

where n is a Gamma random variable following a Gamma distribution $\Gamma(L, 1)$ when considering intensity data. The pdf of y is given by Eq.(2.12) in chapter 2. In SAR images, L is the number of looks and denotes the noise level of images. Fig.3.2 shows synthetic SAR images based on *Lena* with different number of looks.

3.1.3 Other noise models

There are other types of noise which exist in real images or just appear in the academic researches. For instance Poisson noise, it is caused by the variation in the number of photons sensed at a given exposure level. This noise is also known as photon shot noise. It follows a Poisson distortion with a root-mean-square value proportional to the square root of the image intensity. The pdf of Poisson noise is:

$$p(y|u) = \frac{u^y e^{-u}}{y!} \quad (3.5)$$

Its expectation and variance are $\mathbf{E}(y) = u$ and $\mathbf{Var}(y) = u$. Besides, impulse noise, salt-and-pepper noise and so on have also been studied in the image processing field. In reality, the noise existing in images could be more complicated. Poisson-Gaussian noise is an example in optical systems that can be described by the sum of two random variables (a Poisson noise and a Gaussian noise). However, in this thesis only Gamma noise in SAR images is considered.

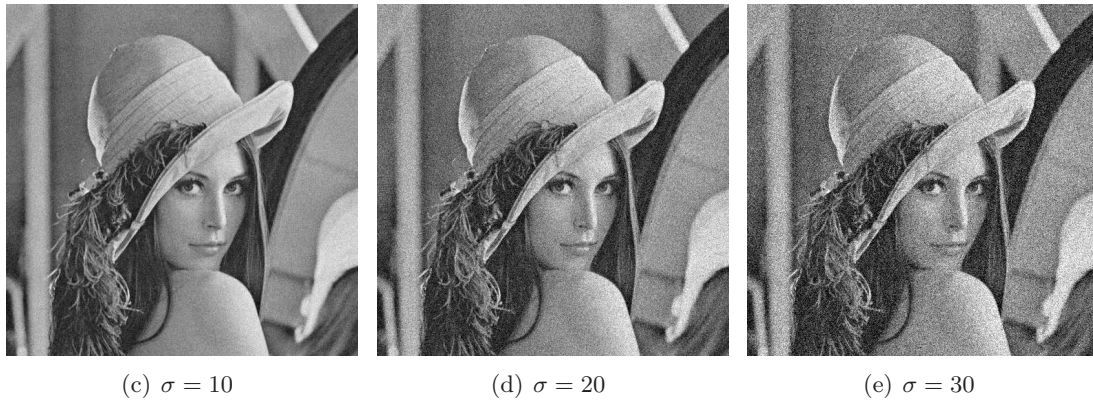
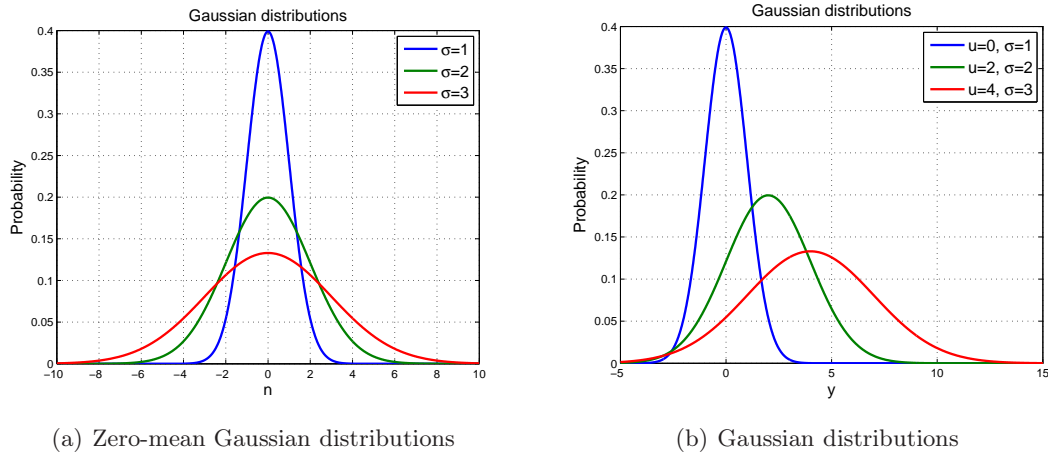


Figure 3.1: The additive Gaussian noise model. (a) Zero-mean Gaussian distributions with different $\sigma = 1, 2, 3$. (b) Gaussian distributions with different $\sigma = 1, 2, 3$ and different $u = 0, 2, 4$. (c) *Lena* picture with Gaussian noise $\sigma = 10$. (d) *Lena* picture with Gaussian noise $\sigma = 20$. (e) *Lena* picture with Gaussian noise $\sigma = 30$. σ can be considered as the noise level, larger σ means stronger noise.

3.2 Main approaches of denoising

Depending on the statistical features of noise, various noise removing methods have been proposed. This section will introduce the main approaches of denoising for a single image. Among these denoising approaches, the non local means based methods have been highlighted and deeply reviewed in section 3.3. Multi-temporal image denoising will be introduced in section 3.4.

3.2.1 Spatial domain approaches

Spatial averaging methods

When having a distribution linking independent and identically distributed observations $\{y(1), y(2), \dots\}$ and the searched for parameter u , a powerful framework is given by maximum likelihood (ML) estimation. The estimation \hat{u} is given by:

$$\hat{u}^{\text{ML}} = \underset{u}{\operatorname{argmax}} \log p(y(1), y(2), \dots | u), \quad (3.6)$$

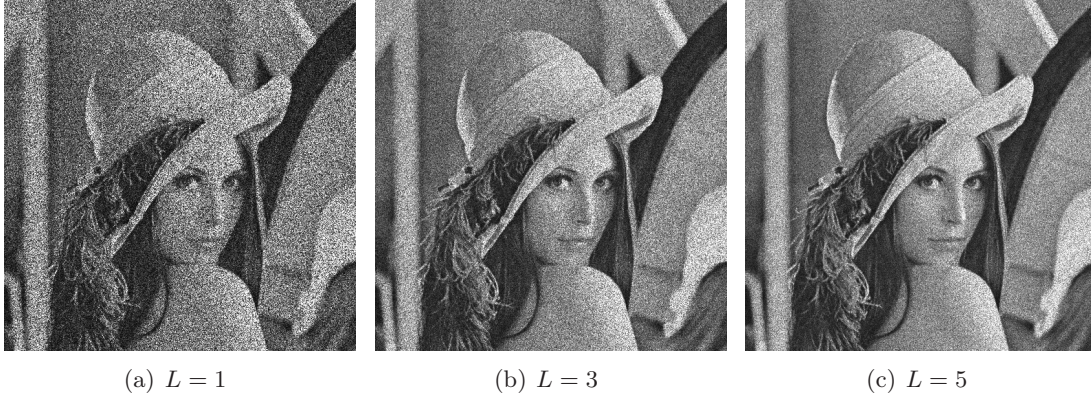


Figure 3.2: The synthetic noisy image with multiplicative (Gamma) noise (showing the amplitude values \sqrt{y}). (a) *Lena* picture with Gamma noise $L = 1$. (b) *Lena* picture with Gamma noise $L = 3$. (c) *Lena* picture with Gamma noise $L = 5$. L can be considered as the noise level, smaller L means stronger noise.

where $p(y(1), y(2), \dots | u)$ is the joint density function for all observations, given by:

$$p(y(1), y(2), \dots | u) = \prod_j p(y(j) | u) . \quad (3.7)$$

In the case of Gaussian distribution, the pdf $p(y(j) | u)$ is computed by Eq.(3.2). In the case of Gamma distribution, $p(y(j) | u)$ is given by Eq.(2.12).

When the observation are no longer identically distributed, weights can be introduced to select observations that are likely to be identically distributed. This leads to the weighted maximum likelihood (WML) estimate [Polzehl and Spokoiny, 2006]:

$$\hat{u}^{\text{WML}} = \operatorname{argmax}_u \sum_j w(j) \log p(y(j) | u) . \quad (3.8)$$

In the case of Gaussian and Gamma noise, we have a formula linking the observation y and the real u value:

$$\begin{aligned} \hat{u}(i) &= \frac{1}{Z} \sum_{j \in \Omega(i)} w(i, j) y(j) \\ Z &= \sum_{j \in \Omega(i)} w(i, j) , \end{aligned} \quad (3.9)$$

where $w(i, j)$ is the weight of candidate $y(j)$. The simplest case is to select the closer neighbors in a local region $\Omega(i)$, e.g. a square window. This will define the Box filter, as shown in Fig.3.3.a. A more adapted approach is to weight the neighbors depending on the distance from the processed pixel. This will be the Gaussian filter, as shown in Fig.3.3.b. Box filter is defined by constant weights and Gaussian filter is defined by weights depending on the distance between pixel i and j , as shown in the following:

$$\begin{aligned} \text{Box filter: } w(i, j) &= 1 , \\ \text{Gaussian filter: } w(i, j) &= \exp\left(\frac{-|i - j|^2}{2h^2}\right) . \end{aligned} \quad (3.10)$$

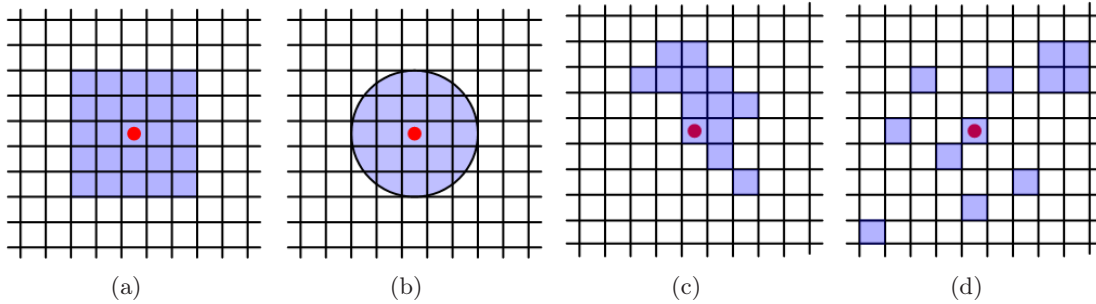


Figure 3.3: Illustration of averaging operators. (a) Averaging with a square window (Box filter). (b) Averaging with linear Gaussian weights in a pie (Gaussian filter). (c) Averaging with a shape-adaptive window. (d) Averaging with non-local principle.

Note that these filters reduce noise by averaging neighbor pixels given by Eq.(3.8), always with a loss of resolution (or details) of images, e.g. box-car filter, Gaussian filter. To restrict such loss, the selection could be performed only over similar pixels. Smith and Brady [1997] and Tomasi and Manduchi [1998] proposed a data adaptive weight definition, given by:

$$\text{Data adaptive weight: } w(i, j) = \exp\left(\frac{-|i - j|^2}{2h^2}\right) \exp\left(\frac{-|y(i) - y(j)|^2}{2h'^2}\right). \quad (3.11)$$

This weight function combining geometric and radiometric distances ensures that only the similar pixels in the neighborhood are contributing to the averaging and details like edges can be preserved. However, it may fail when the noise is strong.

To solve the same issue, adaptive windows instead of windows with fixed size are introduced, e.g. an example shown in the Fig.3.3.c. Lee [1981] used eight oriented windows which are of fixed size but with different orientations. In homogeneous areas the larger window would be used, however on the edges the windows whose orientation is along the edges are used. Park et al. [1999] applied windows with adaptive size (square windows but with different sizes). Moreover, Katkovnik et al. [2002] modified both the shape and the size of the windows. Vasile et al. [2006] suggest to build an intensity driven adaptive neighborhood.

More recently, the non local selection of pixels has been proposed, as shown in Fig.3.3.d. The selected pixels could be from non local areas and do not need to be connected to each other, thus this kind of approach is named non local means (NLM) [Buades et al., 2005a]. The estimation is computed again by the weighted average of the selected pixels. The main idea of this approach is to compute the similarity of two pixels by comparing two small patches around them. This patch comparison is very robust to noise and allow a very efficient selection. The weights are thus controlled by a similarity which is given by:

$$\text{Non local means: } w(i, j) = f(S[\mathbf{y}(i), \mathbf{y}(j)]) , \quad (3.12)$$

where $S[\mathbf{y}(i), \mathbf{y}(j)]$ is computed on patches $\mathbf{y}(i)$ and $\mathbf{y}(j)$ around pixel i and j . $f(\cdot)$ is a kernel function transforming the similarity to weight. Due to its simplicity and efficiency in denoising, NLM has become one of the powerful approach in image denoising. For this reason, we will focus on this approach which is described in details in section 3.3.

For SAR images, homomorphic approach consisting of applying a logarithmic transform can convert the multiplicative speckle noise in an additive one. In this case, most available filtering algorithms developed for additive white Gaussian noise can be used to denoise SAR images. However, due to the non linearity of the logarithmic transform, the statistical features of SAR images are changed (non-Gaussian distribution). Moreover, the log-transformed speckle is non-zero mean especially for images with high noise level. Thus, during the denoising process a post-processing step to remove the biased mean is needed.

Except homomorphic approach based methods, there are many state of the art approaches exploiting the multiplicative noise model to develop denoising algorithms, for instance stationary multiplicative speckle model (SMSM) filters e.g. Lee filter [Lee, 1980], Forst filter [Frost et al., 1982] and Kuan filter [Kuan et al., 1985], and non-stationary multiplicative speckle model (NSMSM) filters proposed in Lopes et al. [1990] and [Kuan et al., 1987]. Based on the stationarity assumption of the multiplicative speckle model, SMSM filters operate under a minimum mean-square error (MMSE) theory and can be described by a linear function of the covariance matrix of the signal and noise. On the contrary, NSMSM filters reduce speckle under the non stationarity multiplicative speckle model assumption. And the MMSE estimation is replaced by the maximum a posteriori (MAP) theory which, however, raises the problem of providing an accurate statistical description of the SAR image.

More recently, Alonso-González et al. [2012] denoised the PolSAR image with the use of binary partition trees, which represents the multi-scale homogeneous regions of the images. NLM theory has been introduced to SAR image denoising by probability patch-based filter [Deledalle et al., 2009] which considers the statistical distribution of speckle in the definition of weights in Eq.(3.12). The details about this NLM based approach can be found in section 3.3.

Regularization based approaches

Regularization methods deal with the denoising problem as solving an optimization problem. Their main principle is to introduce some spatial regularity for detail enhancement, i.e. edges, point targets. The optimization problem can be formalized with:

$$\hat{u} = \underset{u}{\operatorname{argmin}} \sum_i \mathcal{D}(y(i), u(i)) + \lambda \operatorname{Reg}(u) , \quad (3.13)$$

where $\mathcal{D}(y(i), u(i))$ is the data fidelity term which could be the L1, L2 distance for Gaussian noise assumption or ratio based distance for speckle model, and $\operatorname{Reg}(u)$ is the regularization term with λ controlling the contribution of regularity. To preserve details like edges and objects, a regularization term based on the gradient of u is proposed in the total-variation (TV) minimization method [Rudin et al., 1992]. Other norms of the regularization terms with different image priors can also be introduced to $\operatorname{Reg}(u)$, e.g. a local TV model [Louchet and Moisan, 2011]. Methods have been developed to solve the minimization problem given by Eq.(3.13), such as [Chambolle, 2004, Chambolle and Pock, 2011]. More recently, the TV regularization has been combined with the NLM approach to improve the drawback of NLM in dealing with rare patches in Louchet and Moisan [2011], Sutour et al. [2013].

3.2.2 Transform domain approaches

The basic idea of denoising in transform domain is that the signal and the noise could be separated in the transform domain, and thus it is easier to reduce the noise. For

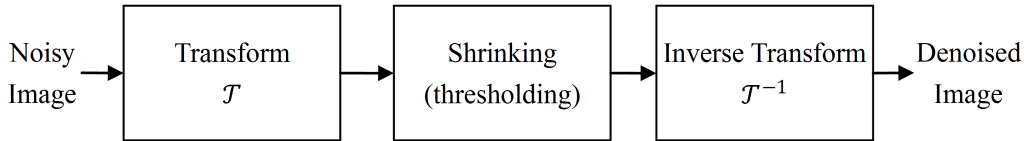


Figure 3.4: Principle of the processing chain in transform-based denoising methods.

instance, the noise in images generally presents itself as rapid changes in a smooth area and it has uniform power across the whole frequency band, while the signal changes slowly and usually only has power on lower frequencies. Then, the noise can be reduced by a processing chain: 1) transforming the noisy data to the transform domain; 2) shrinking the transform coefficients by hard-thresholding or soft-thresholding to suppress the effects of noise; 3) performing an inverse transform on the shrunk coefficients to the spatial domain. As shown in Fig.3.4, this processing chain is also the basic principle of most transform-domain denoising methods. The key issue of denoising in transform domain is the choice of the transform domain and suitable shrinking way without smoothing the details in the image.

Due to the space-frequency localization property and a large number of transform bases, wavelet has been the most popular choice for denoising methods. Portilla et al. [2003] proposed to model the wavelet coefficients by a scale mixture of Gaussian (GSM) model. Like the common processing of transform based filter, the noisy image is first decomposed into multiple sub-bands in the wavelet domain and the wavelet coefficients in each sub-band are modeled as a Gaussian scale mixture. For the shrinking step, Wiener filter is used to denoise the wavelet coefficients in a Bayesian least squares framework. In the final step, the denoised coefficients across sub-bands are then inversely transformed to form the denoised image. Lyu and Simoncelli [2009] improved the filter proposed in [Portilla et al., 2003] by using a global Gaussian Markov random field to model the local GSM models. However, the edges and textures in the images may be smoothed since they have similar characteristics with the noise in transform domain (for instance, both edges and noise correspond to the rapid changes in spatial domain and have uniform power in frequency domain). To solve this problem, some techniques of detail preservation and enhancement are proposed. For instance, geometric constraints added into the shrinking step are applied to preserve edges in [Rosito Jung and Scharcanski, 2003]. More recently, some high-level transformation methods, such as Principal Component Analysis [Zhang et al., 2010], K-SVD dictionary based methods [Elad and Aharon, 2006], have also been introduced to image denoising tasks. Dabov et al. [2007b] recently proposed a block-match in 3D transform-domain filter (BM3D), which combined the NLM theory and the wavelet transform based denoising (more details can be found in the introduction of NLM theory in section 3.3).

For SAR images, homomorphic approach with a logarithmic transform could also be used to develop these transform based denoising approaches to deal with speckle noise, such as the filters in [Guo et al., 1994] and [Gagnon and Jouan, 1997]. Considering the heavy-tailed feature of speckle distribution, a heavy-tailed model under Bayesian wavelet shrinkage is proposed in [Achim et al., 2003]. Recently, Ranjani and Thiruvengadam [2010] and Gleich et al. [2010] use spatial information to better preserve the edges and textures of SAR images based on spatially adaptive Wavelet analysis, Parrilli et al. [2012] extended the BM3D filter to SAR data (namely SAR-BM3D filter), Xu et al. [2014] introduced Prin-

Principal Component Analysis theory to SAR despeckling, and dictionary based despeckling approach has also been proposed in Tabti et al. [2014].

3.3 Non local means methods

Following the main approaches of denoising presented in section 3.2, this section deeply introduces the NLM based methods.

Given by Eq.(3.9), basic NLM filter exploits image redundancy by searching similar pixels and combines these similar pixels with different weights. As shown in Fig.3.5, to filter the center pixel $y(i)$ marked in red, the pixels in the search window (marked in yellow) are weighted averaged by:

$$\hat{u}(i) = \frac{1}{Z} \sum_{j \in \Omega(i)} w(i, j) y(j) , \quad (3.14)$$

$$w(i, j) = f(S[\mathbf{y}(i), \mathbf{y}(j)]) , \quad (3.15)$$

$$Z = \sum_{j \in \Omega(i)} w(i, j) . \quad (3.16)$$

The weight $w(i, j)$ depends on the similarity between patches $\mathbf{y}(i)$ (marked in red) and $\mathbf{y}(j)$ (marked in blue). NLM has been proved powerful in image denoising, however the challenges of applying NLM lie in selecting filter parameters, such as:

- $S[\mathbf{y}(i), \mathbf{y}(j)]$: the similarity between patch $\mathbf{y}(i)$ and $\mathbf{y}(j)$. The common similarity is defined as a value negatively related to the distance between $\mathbf{y}(i)$ and $\mathbf{y}(j)$. Different similarity measurements will be discussed in section 3.3.1;
- $f(\cdot)$: the kernel function transforming the similarity to weight. It was selected as an exponential function and other choices have also been proposed, which will be reviewed in section 3.3.2;
- the size of patches $\mathbf{y}(i)$ and $\mathbf{y}(j)$. Too small patch size may make NLM find wrong (dissimilar) patches, while too large patch size may lead to few or no similar patches found by NLM; the selection of patch and search window sizes will be discussed in section 3.3.4;
- the size and shape of search window $\Omega(i)$. In the original NLM theory, Ω_i should be the whole image, while in reality Ω_i is usually a square window to balance the algorithm time consumption and the denoising performance.

This section will discuss these issues and review the improvements and extensions of NLM.

3.3.1 The choice of similarity

Pixel similarity

The similarity between two pixels $y(1)$ and $y(2)$ can be measured by the negative value of the euclidean distance (i.e. under the additive Gaussian noise) or ratio operator (i.e. under the multiplicative speckle noise), as defined in the following:

$$\begin{aligned} D_{\text{pixel}}(y(1), y(2)) &= -(y(1) - y(2))^2, \quad D_{\text{pixel}} \in [-\infty, 0) \\ R_{\text{pixel}}[y(1), y(2)] &= \min \left[\frac{y(1)}{y(2)}, \frac{y(2)}{y(1)} \right], \quad R_{\text{pixel}} \in (0, 1] \end{aligned} \quad (3.17)$$

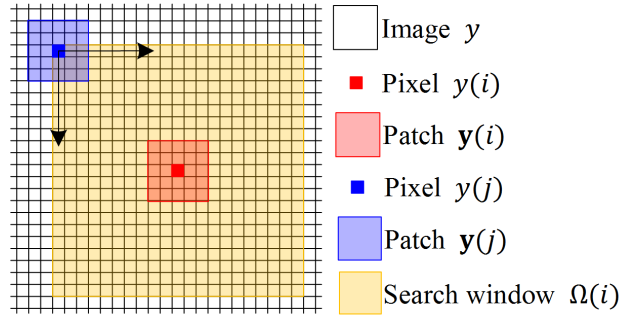


Figure 3.5: The non local means approach denoises each pixel $y(i)$ by weighted averaging these pixels (i.e. $y(j)$) in the search window $\Omega(i)$. The weights are calculated based on the similarity between patch $\mathbf{y}(i)$ and $\mathbf{y}(j)$.

where D_{pixel} denotes the similarity which is inversely proportional to the distance, while the R_{pixel} is proportional to the ratio. The higher similarity values, $y(1)$ and $y(2)$ are more similar. In reality, this measure is corrupted by noise data. For example, if $y(1) = u(1) + n(1)$ ($y(2) = u(2) + n(2)$) is the sum of noise-free value $u(1)$ ($u(2)$) and a zero-mean, σ^2 -variance Gaussian noise $n(1)$ ($n(2)$), the similarity of $y(1)$ and $y(2)$ will be:

$$\begin{aligned} -(y(1) - y(2))^2 &= -(u(1) - u(2) + n(1) - n(2))^2 \\ &= -(\Delta u + \Delta n)^2 \end{aligned} \quad (3.18)$$

where Δn is a zero-mean and $4\sigma^2$ -variance Gaussian noise. The ratio operator of two pixels is also affected by the Gamma distribution.

To reduce the effect of noise, the patch difference is usually used instead of pixel difference. Given the noisy patch $\mathbf{y}(1)$ with $\mathbf{y}(1) = \mathbf{u}(1) + \mathbf{n}(1)$, the patch difference between $\mathbf{y}(1)$ and $\mathbf{y}(2)$ is:

$$\begin{aligned} -\frac{1}{K} \sum_k [y(1, k) - y(2, k)]^2 &= -\frac{1}{K} \sum_k [u(1, k) - u(2, k) + n(1, k) - n(2, k)]^2 \\ &= -\frac{\sum_k (\Delta u + \Delta n)^2}{K} \end{aligned} \quad (3.19)$$

where K is the number of pixels in patch $\mathbf{y}(1)$. Assuming that Δu is constant, this patch difference is the expectation of pixel difference given by Eq.(3.18), which will have less variance.

Obviously, the patch similarity is not the same as the pixel similarity since the noise-free value u is not constant in the patch. However it is a more robust approximation and the similarity of the central pixels is strongly correlated to the similarity of the patches. Fig.3.6 shows the two-dimensional histogram of the Euclidean distance between noise-free pixels $|u(1) - u(2)|$ and the Euclidean distance between noise-free patches $\|\mathbf{u}(1) - \mathbf{u}(2)\|$ measured from the *house* image. From this histogram, an approximate proportional relation between $|u(i) - u(j)|$ and $\|\mathbf{u}(i) - \mathbf{u}(j)\|$ can be found. A discussion on patch similarity measures is presented in the following section.

Observed patch similarity

As explained in the former section, patch similarity is more robust than pixel similarity. Seven patch similarity criteria were presented in [Deledalle et al., 2012a] based on the

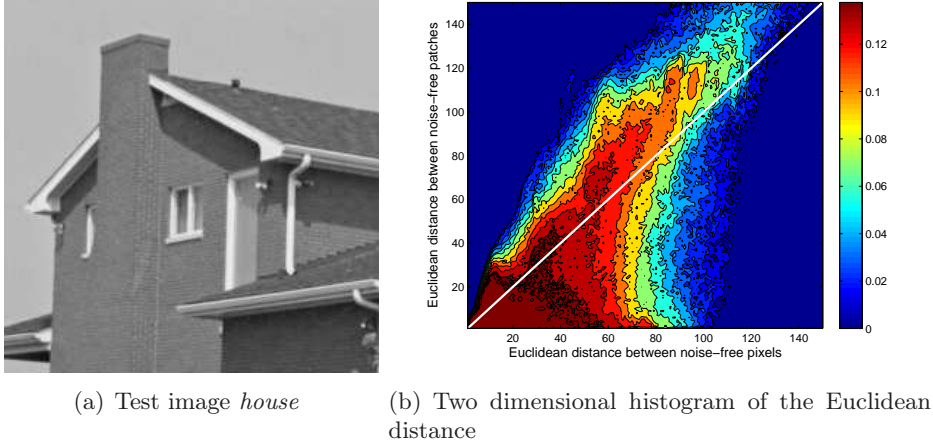


Figure 3.6: The two dimensional histogram of the Euclidean distance between noise-free patches K and noise-free pixels. The ideal case (the assumption that similar patches have similar central pixels [Duval et al., 2010]) is shown on the white line.

detection theory. As suggested in their works, for the despeckling application, the generalized likelihood ratio (GLR) criterion outperforms the other similarity measurements, especially in the strong noise cases. This similarity criterion has been successfully used in probability patch-based (PPB) filter [Deledalle et al., 2009]. Taking a pair of observed patches $\mathbf{y}(1)$ and $\mathbf{y}(2)$ as examples, they are similar when they have the same underlying noise-free patch $\mathbf{u}(1) = \mathbf{u}(2) = \mathbf{u}(12)$. The measurement of the similarity between $\mathbf{y}(1)$ and $\mathbf{y}(2)$ can be considered as a hypothesis test:

$$\begin{aligned} \mathcal{H}_0 : \mathbf{u}(1) = \mathbf{u}(2) = \mathbf{u}(12) & \text{ Similar (null) hypothesis} \\ \mathcal{H}_1 : \mathbf{u}(1) \neq \mathbf{u}(2) & \text{ Dissimilar (alternative) hypothesis.} \end{aligned}$$

Given the observed data $\mathbf{y}(1)$ and $\mathbf{y}(2)$, the optimal criterion which detects whether $\mathbf{u}(1)$ and $\mathbf{u}(2)$ are identical is the likelihood ratio:

$$\mathcal{R}(\mathbf{y}(1), \mathbf{y}(2)) = \frac{p(\mathbf{y}(1), \mathbf{y}(2) | \mathbf{u}(12), \mathcal{H}_0)}{p(\mathbf{y}(1), \mathbf{y}(2) | \mathbf{u}(1), \mathbf{u}(2), \mathcal{H}_1)}. \quad (3.20)$$

This likelihood ratio can not be directly used since we do not have any knowledge about the noise-free value u . The generalized likelihood ratio (GLR) solves this problem by replacing the u values by their ML maximum likelihood estimates. The ratio with estimates is:

$$\begin{aligned} \mathcal{R}^{\text{GLR}}(\mathbf{y}(1), \mathbf{y}(2)) &= \frac{p(\mathbf{y}(1), \mathbf{y}(2) | \hat{\mathbf{u}}^{\text{ML}}(12), \mathcal{H}_0)}{p(\mathbf{y}(1), \mathbf{y}(2) | \hat{\mathbf{u}}^{\text{ML}}(1), \hat{\mathbf{u}}^{\text{ML}}(2), \mathcal{H}_1)} \\ &= \prod_{k=1, \dots, K} \frac{p(y(1, k), y(2, k) | \hat{u}^{\text{ML}}(12, k), \mathcal{H}_0)}{p(y(1, k), y(2, k) | \hat{u}^{\text{ML}}(1, k), \hat{u}^{\text{ML}}(2, k), \mathcal{H}_1)} \end{aligned} \quad (3.21)$$

where $y(1, k)$ is the k -th pixel in patch $\mathbf{y}(1)$ (k is the index of pixel in patch, $y(2, k)$, $\hat{u}(1, k)$, $\hat{u}(2, k)$ and $\hat{u}(12, k)$ have the same case). The ML estimates for Gaussian or Gamma distributions are given by:

$$\hat{u}^{\text{ML}}(1, k) = y(1, k) \quad \text{and} \quad \hat{u}^{\text{ML}}(2, k) = y(2, k) \quad (3.22)$$

under the \mathcal{H}_1 hypothesis. Under the \mathcal{H}_0 hypothesis, the ML estimate of $\mathbf{u}(12)$ is given by:

$$\begin{aligned} \text{Gaussian distribution case: } \hat{u}^{\text{ML}}(12, k) &= \frac{\sigma(2, k)y(1, k) + \sigma(1, k)y(2, k)}{\sigma(1, k) + \sigma(2, k)}, \\ \text{Gamma distribution case: } \hat{u}^{\text{ML}}(12, k) &= \frac{L(1, k)y(1, k) + L(2, k)y(2, k)}{L(1, k) + L(2, k)}. \end{aligned} \quad (3.23)$$

$\sigma(1, k)$ or $L(1, k)$ is the variance or the number of looks associated to k -th pixel of $y(1, k)$ (for full generality we suppose that σ could be spatially varying).

Then, combined with the multiplicative speckle noise model in (2.12) and the additive Gaussian noise model in (3.3), the GLR turns to be:

Gaussian distribution case:

$$\begin{aligned} &\mathcal{R}^{\text{GLR}}(\mathbf{y}_1, \mathbf{y}_2) \\ &= \prod_{k=1, \dots, K} \exp \left(- \frac{\left[\frac{\sigma(1, k)y(1, k) + \sigma(2, k)y(2, k)}{\sigma(1, k) + \sigma(2, k)} - y(1, k) \right]^2}{2\sigma(1, k)^2} - \frac{\left[\frac{\sigma(1, k)y(1, k) + \sigma(2, k)y(2, k)}{\sigma(1, k) + \sigma(2, k)} - y(2, k) \right]^2}{2\sigma(2, k)^2} \right), \end{aligned} \quad (3.24)$$

Gamma distribution case:

$$\mathcal{R}^{\text{GLR}}(\mathbf{y}_1, \mathbf{y}_2) = \prod_{k=1, \dots, K} \left[\frac{L(1, k)y(1, k) + L(2, k)y(2, k)}{L(1, k) + L(2, k)} \right]^{-L(1, k) - L(2, k)} \frac{y(1, k)^{L(1, k)}}{y(2, k)^{-L(2, k)}}, \quad (3.25)$$

where $\mathcal{R}^{\text{GLR}}(\mathbf{y}_1, \mathbf{y}_2) \in (0, 1]$ in both Gaussian and Gamma distribution cases. The GLR based patch similarity is the log operation of Eq.(3.21):

$$S_{\text{GLR}}(\mathbf{y}(1), \mathbf{y}(2)) = \log [\mathcal{R}^{\text{GLR}}(\mathbf{y}(1), \mathbf{y}(2))] . \quad (3.26)$$

$S_{\text{GLR}}(\mathbf{y}(1), \mathbf{y}(2)) \in] -\infty, 0]$, in which the larger values (close to 0) denote $\mathbf{y}(1)$ and $\mathbf{y}(2)$ are more similar. Note that, when the noise level of two patches are the same, the patch similarity boils down to the similarity used in [Deledalle et al., 2009]. Taking Gamma distribution as example when $\mathbf{L}(1) = \mathbf{L}(2) = \mathbf{L}$ ($L(1, k) = L(2, k) = L|_{k=1, \dots, K}$), this GLR similarity criterion in Eq.(3.26) turns to be:

$$S_{\text{GLR}}(\mathbf{y}(1), \mathbf{y}(2)) |_{\mathbf{L}(1)=\mathbf{L}(2)} = - \sum_k \left[2L \log \left(\sqrt{\frac{y(1, k)}{y(2, k)}} + \sqrt{\frac{y(2, k)}{y(1, k)}} \right) - 2L \log 2 \right], \quad (3.27)$$

which is the same as the GLR criterion in [Deledalle et al., 2009]. And in the case of Gaussian distributions with constant σ , \mathcal{R}^{GLR} boils down to the euclidean distance in [Buades et al., 2005a].

Noise-free (denoised) patch similarity

In [Brox et al., 2008, Kervrann and Boulanger, 2006], the denoised patch similarity is used to improve the denoising performance especially for high noise level images. Deledalle et al. [2009] and Deledalle [2011] also proposed similar strategy for SAR images. In their work, the Kullback-Leibler (KL) divergence based patch similarity had better performance than simple Euclidean distance based similarity in selecting similar patches, and it also has been applied in the PPB filter Deledalle et al. [2009]. We thus recall the KL divergence similarity here and extend it to different noise levels cases.

For distributions $p(y|u(1), \Theta(1))$ and $p(y|u(2), \Theta(2))$ of a continuous random variable (where Θ is the distribution parameter, e.g. $\Theta = \sigma^2$ in Gaussian distribution and $\Theta = L$ in Gamma distribution), KL-divergence is defined to be the integral:

$$D^{\text{KL},1} = \int_{-\infty}^{+\infty} p(y|u(1), \Theta(1)) \ln \left[\frac{p(y|u(1), \Theta(1))}{p(y|u(2), \Theta(2))} \right] dy \quad (3.28)$$

The analytical expression can be derived in the case of Gamma distribution. We extend here the result of [Deledalle et al., 2009], when considering different number of looks for each pixels. Substituting the Gamma distribution $p(y|u, \Theta = L)$ given by Eq.(2.12) in the KL criterion with $y \leq 0$:

$$D^{\text{KL},1} = \int_0^{+\infty} p(y|u(1), L(1)) \ln [A \cdot B \cdot C] dy \quad (3.29)$$

where

$$A = \frac{\frac{1}{\Gamma(L(1))} \frac{L(1)}{u(1)}}{\frac{1}{\Gamma(L(2))} \frac{L(2)}{u(2)}}, B = \left(\frac{L(1)y}{u(1)} \right)^{L(1)-1} \left(\frac{L(2)y}{u(2)} \right)^{1-L(2)} \quad (3.30)$$

$$\text{and } C = \exp \left[\frac{L(2)y}{u(2)} - \frac{L(1)y}{u(1)} \right].$$

Then,

$$\begin{aligned} D^{\text{KL},1} &= \ln A \int_0^{+\infty} p(y|u(1), L(1)) dy \\ &\quad + \int_0^{+\infty} p(y|u(1), L(1)) \ln B dy \\ &\quad + \int_0^{+\infty} p(y|u(1), L(1)) \ln C dy . \end{aligned} \quad (3.31)$$

Since,

$$\begin{aligned} \int_0^{+\infty} p(y|u, L) dy &= 1 , \\ \int_0^{+\infty} p(y|u, L) \ln y dy &= E(\ln y) = \psi(L) + \ln(u) , \\ \int_0^{+\infty} p(y|u, L) y dy &= E(y) = u , \end{aligned} \quad (3.32)$$

where $\psi(L)$ is the digamma function. Thus,

$$\begin{aligned} D^{\text{KL},1} &= \ln A + (L(1) - 1) \ln \frac{L(1)}{u(1)} + (1 - L(2)) \ln \frac{L(2)}{u(2)} \\ &\quad + [L(1) - L(2)] [\psi(L(1)) + \ln(u(1))] + L(2) \frac{u(1)}{u(2)} - L_1 , \end{aligned} \quad (3.33)$$

with

$$D^{\text{KL},2} = \int_{-\infty}^{+\infty} p(y|u(2), L(2)) \ln \left[\frac{p(y|u(2), L(2))}{p(y|u(1), L(1))} \right] dy . \quad (3.34)$$

The KL-divergence criterion between two pixels is:

$$\begin{aligned} D^{\text{KL}}(u(1), u(2)) &= D^{\text{KL},1} + D^{\text{KL},2} \\ &= L(1) \frac{u(2)}{u(1)} + L(2) \frac{u(1)}{u(2)} - L(1) - L(2) \\ &\quad + [L(1) - L(2)] \left[\psi(L(1)) - \psi(L(2)) + \ln \frac{u(1)}{u(2)} \right]. \end{aligned} \quad (3.35)$$

Finally, the KL-divergence criterion between two patches is:

$$\begin{aligned} D^{\text{KL}}(\mathbf{u}(1), \mathbf{u}(2)) &= \sum_k L(1, k) \frac{u(2, k)}{u(1, k)} + L(2, k) \frac{u(1, k)}{u(2, k)} - L(1, k) - L(2, k) \\ &\quad + [L(1, k) - L(2, k)] \left[\psi(L(1, k)) - \psi(L(2, k)) + \ln \frac{u(1, k)}{u(2, k)} \right], \end{aligned} \quad (3.36)$$

where $D^{\text{KL}}(\mathbf{u}(1), \mathbf{u}(2)) \in [0, \infty[$.

For patches $\mathbf{u}(1)$ and $\mathbf{u}(2)$, the KL divergence similarity between them is:

$$S_{\text{KL}}(\mathbf{u}(1), \mathbf{u}(2)) = -D^{\text{KL}}(\mathbf{u}(1), \mathbf{u}(2)), \quad (3.37)$$

where $S_{\text{KL}}(\mathbf{u}(1), \mathbf{u}(2)) \in]-\infty, 0]$. The higher value means patches $\mathbf{y}(1)$ and $\mathbf{y}(2)$ are more similar.

When $\mathbf{L}(1) = \mathbf{L}(2) = \mathbf{L}$,

$$S_{\text{KL}}(\mathbf{u}(1), \mathbf{u}(2))|_{\mathbf{L}(1)=\mathbf{L}(2)} = \sum_k L(k) \left[2 - \frac{u(1, k)}{u(2, k)} - \frac{u(2, k)}{u(1, k)} \right], \quad (3.38)$$

which corresponds to the same expression as in [Deledalle et al., 2009].

When considering additive Gaussian noise, we can substitute the Gaussian distribution $p(y|u, \Theta = \sigma^2)$ given by Eq.(3.3) in the KL divergence given by Eq.(3.28), then we can get:

$$D^{\text{KL},1} = \int_{+\infty}^{+\infty} p(y|u(1), \Theta = \sigma(1)^2) \left[\ln \frac{\sigma(2)}{\sigma(1)} + \frac{|y - u(1)|^2}{2\sigma(1)^2} - \frac{|y - u(2)|^2}{2\sigma(2)^2} \right] dy. \quad (3.39)$$

Then, the final KL divergence similarity can be computed by:

$$\begin{aligned} S_{\text{KL}}(\mathbf{u}(1), \mathbf{u}(2)) &= - \sum_k D^{\text{KL},1} + D^{\text{KL},2} \\ &= - \sum_k \frac{|u(1, k) - u(2, k)|^2 + \sigma(2, k)^2}{2\sigma(1, k)^2} + \frac{|u(1, k) - u(2, k)|^2 + \sigma(1, k)^2}{2\sigma(2, k)^2} - 1 \end{aligned} \quad (3.40)$$

with $S_{\text{KL}}(\mathbf{u}(1), \mathbf{u}(2)) \in]-\infty, 0]$.

Coherence based similarity for SAR imagery We could wonder if the interferometric coherence could be used for image comparison. We show through a simple experiment that this information does not correspond to our objectives. As introduced in chapter 2, the interferometric coherence is a key indicator of the relation between two multi-temporal SAR images, which is usually used to detect the changes between two dates. When comparing two patches of SAR image, the coherence given by Eq.(2.7) can be used to measure the similarity since highly interrelated patches are similar to each other. To compare with the patch similarity given by Eq.(3.26), we calculate both the GLR patch similarity and the coherence on a pair of real SAR images (two single-look TerraSAR X-band images of Paris, France, as shown in Fig.3.7):

- The GLR patch similarity: Eq.(3.26) with $L = 1$, K is a 7×7 pixels patch;
- The coherence: Eq.(2.7) performed in a 7×7 pixels square window.

Fig.3.7 gives an illustration of the two similarity measurements. The coherence has good performance at buildings areas as well as the GLR criterion. However, it fails when the reflectivity is lower, for instance in the river and the public square etc. (as shown in Fig.3.8), since it will rely mostly on the phase information. We see that this indicator, although very useful for interferometric purposes, could not be applied for the combination of amplitude of images.

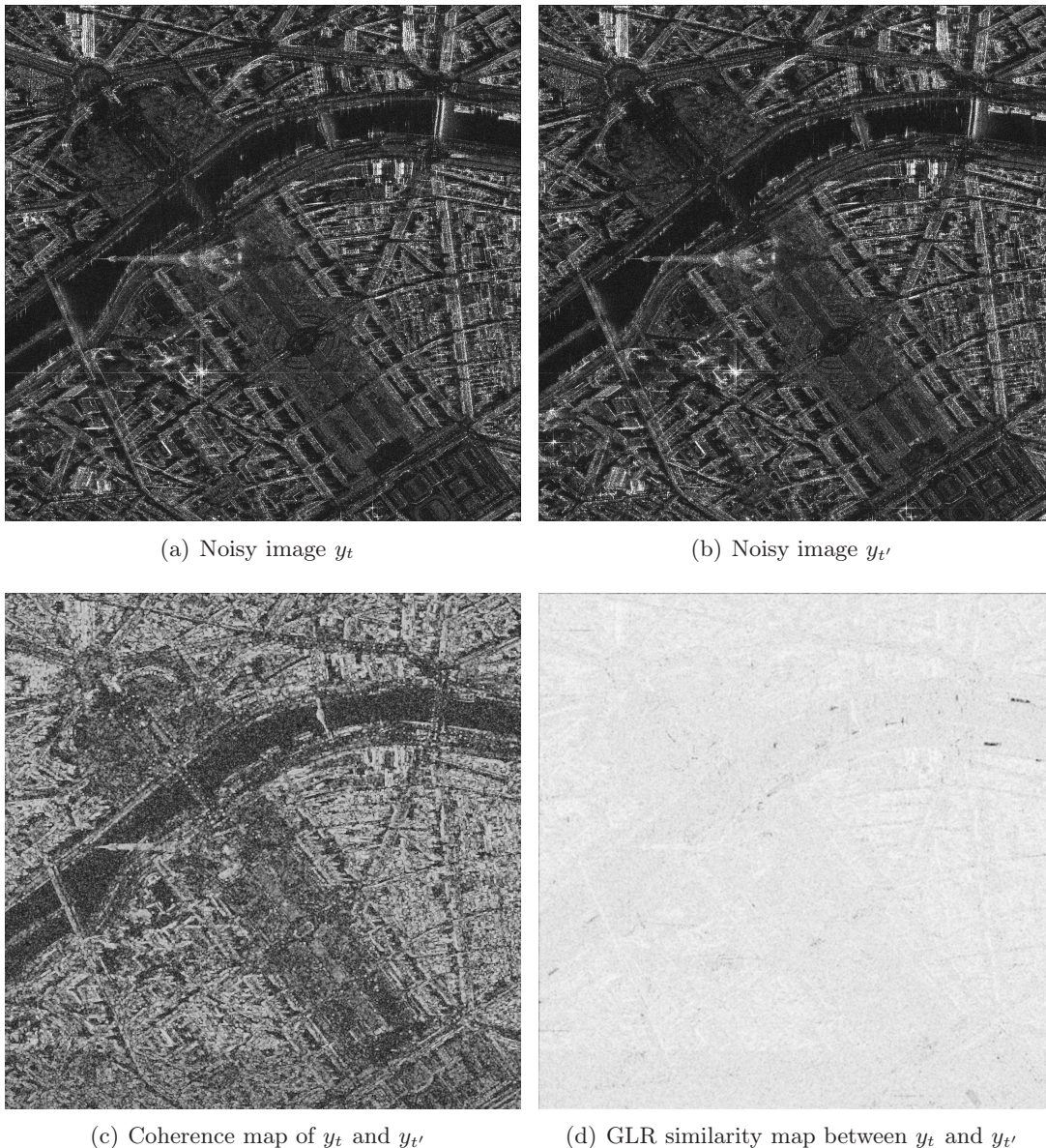


Figure 3.7: The coherence and GLR similarity of a pair of interferometric SAR images ©DLR project LAN1746.

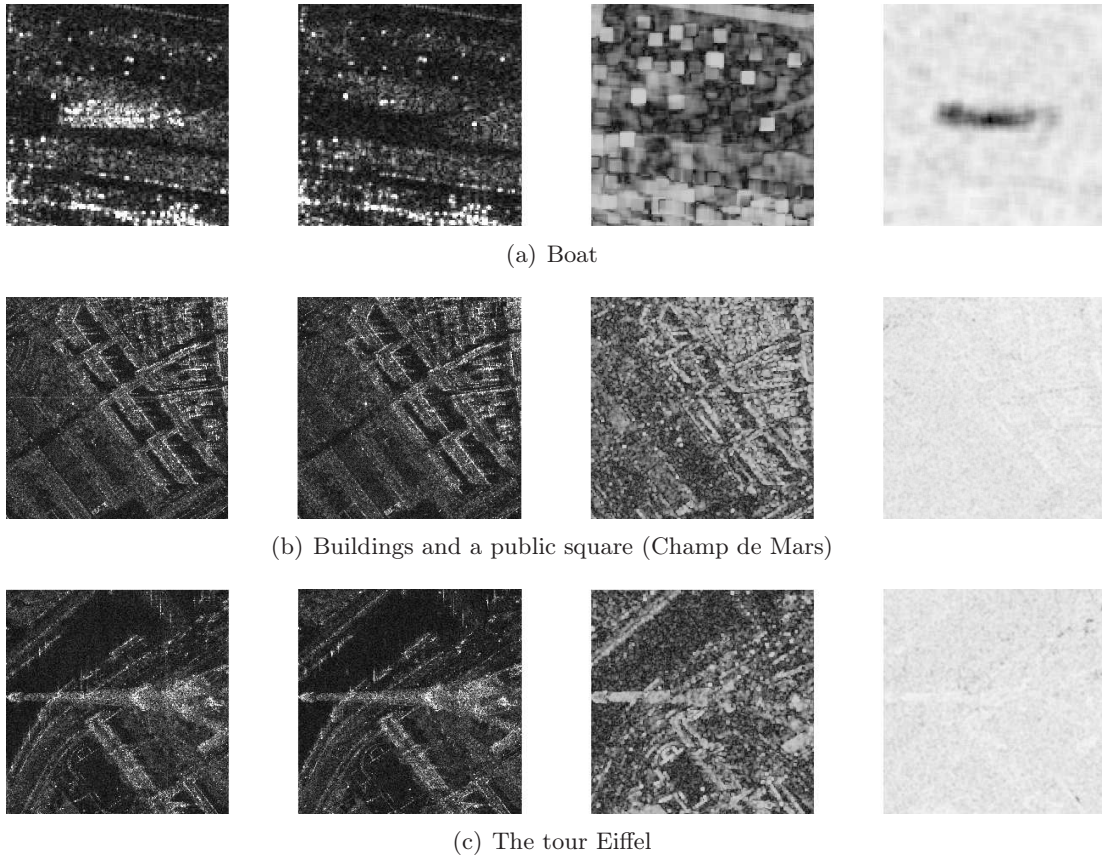


Figure 3.8: The coherence and GLR similarity of a pair of interferometric SAR images. From left to right: noisy image y_t and $y_{t'}$, the coherence map, the GLR similarity map. (Note that figure (a) is not of the same size as (b) and (c)).

In this section, we have developed the noisy/denoised patch similarity used in the PPB filter Deledalle et al. [2009]. They have been extended to a more general case (patches with different noise level), which will be useful for the proposed filter in chapter 4.

3.3.2 Kernel functions $f(\cdot)$

One of the key ingredients is the definition of the weights from the similarity. An exponential kernel is used to compute weights in [Buades et al., 2005a]:

$$w(i, j) = f(S[\mathbf{y}(i), \mathbf{y}(j)]) = \exp\left(\frac{S[\mathbf{y}(i), \mathbf{y}(j)]}{h^2}\right), \quad (3.41)$$

where h controls the decay of the weights. People usually select a single h as a general rule of thumb for the whole image denoising [Buades et al., 2005a,b]. As shown in figure 3.9, weights with higher h ($h \mapsto \infty$) tend to the same value, which is suitable for homogeneous region denoising. In the edge or texture regions, smaller h ($h \mapsto 0$) can keep more details. Kervrann and Boulanger [2006] proposed to choose h by considering the distribution of the similarity. Stein's unbiased risk estimate (SURE) is used in [Van De Ville and Kocher, 2009] to select h . For further improvement, Van De Ville and Kocher [2011] proposed an estimation by a linear combination of NLMs with different parameters and SURE is also

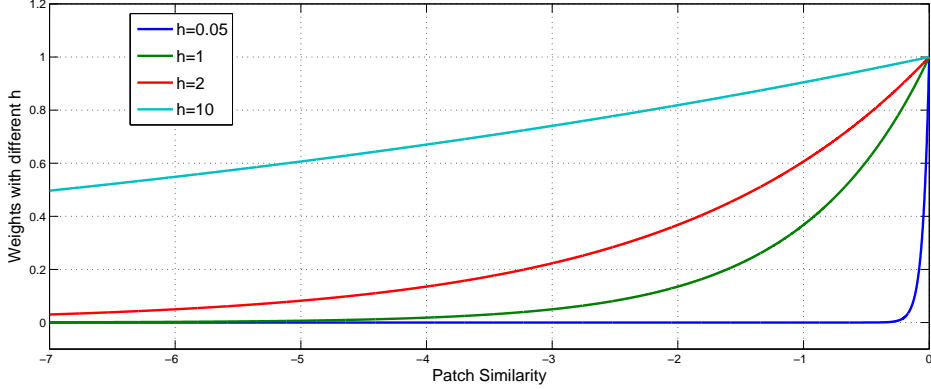


Figure 3.9: Exponential weights with different parameter h . When $h \mapsto 0$, the denoising results will be the noisy data itself. When $h \mapsto \infty$, the denoising will smooth all the pixels in the searching window.

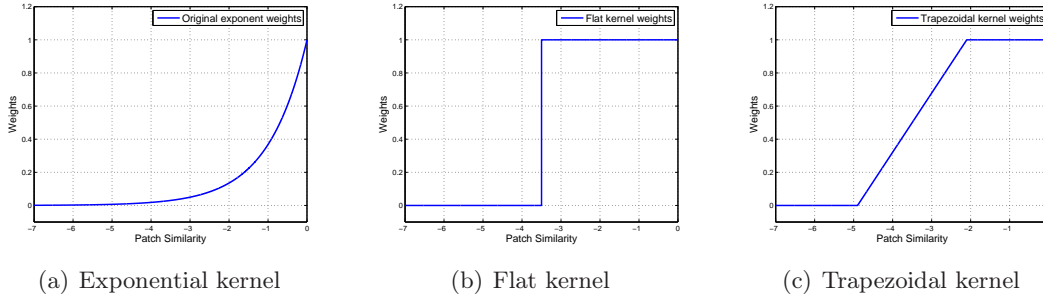


Figure 3.10: Different kernels for weights.

used to optimize the combination. More generally, local selection of h has been proposed by Duval et al. [2011] using SURE for Gaussian noise. For PolSAR denoising, Hondt et al. [2014] selected the filter parameters by comparing a guess of the filtering error under the theory of unbiased risk estimation.

Compared with the exponential kernel, Buades et al. [2011] and Salmon and Strozecki [2010] show that flat kernels or trapezoidal kernels can provide better or competitive results. Figure 3.10 gives an illustration of different kernels for weights. Flat kernels weights are binary (1 and 0, or other values) which reduce the computational cost. Cosine function is also used to define the weights [Salih et al., 2013]. Tracey et al. [2014] used a combined kernel by the weighted sum of the individual NLM kernels.

Salmon [2010] claimed that the NLM is semi-local rather than non local since a large searching window size (such as using the whole image as the searching window) would not provide a better denoising results. In fact, one of the reason is that the larger searching window will introduce more incorrect pixels to the averaging and cause more bias, since by Eq.(3.41) the dissimilar pixels also have non-zero weights (no matter how dissimilar they are, they can still contribute to the averaging). To avoid the contribution of the dissimilar pixels, Duval et al. [2011] proposed a truncation on the exponential weights:

$$w(i, j) = \begin{cases} \exp\left(\frac{S(\mathbf{y}(i), \mathbf{y}(j))}{h^2}\right) & \text{if } |y(i) - y(j)| \leq \tau, \\ 0 & \text{else.} \end{cases} \quad (3.42)$$

When $\tau = \text{maximum}$, the algorithm is equivalent to the usual NLM. Eq.(3.42) can reduce the bias of the estimation by removing the pixels with high patch similarity but very different central values. Thus, the truncated weights are insensitive to the increase of the search window. Based on the same motivation, Zhang et al. [2014] proposed to combine the patch and pixel similarity to preserve the high-contrast particle details in magnetic resonance image denoising. Deledalle et al. [2014] introduced a new way to define weights with a learned kernel that impose the distribution of weights in homogeneous regions. This distribution model is learned from a homogeneous area.

3.3.3 Weight of the center pixel

In Eq.(3.26), the similarity between $\mathbf{y}(i)$ and itself is maximum. Thus the weight of pixel $y(i)$ in Eq.(3.41) will also be maximum ($w(i, i) = 1$). This may let the center pixel bring strong noise in the denoising. Thus, $w(i, i)$ is replaced by the maximal weight in the searching window (except $w(i, i)$) in [Salmon, 2010]:

$$w(i, i) = \max \left[\max_{j \in \Omega_i, j \neq i} w(i, j) \right] . \quad (3.43)$$

In most methods, the weight of the center pixel is linked to the selection of the kernel function. Given $w(i, j)$ defined by Eq.(3.26), Salmon [2010] considered the noise level when setting $w(i, i)$:

$$w(i, i) = \max \left[\max_{j \in \Omega_i, j \neq i} w(i, j) , \varphi \left(-\frac{\sigma^2}{h} \right) \right] . \quad (3.44)$$

In the comparison experiments in [Salmon, 2010], $w(i, i)$ in Eq.(3.43) should be used in higher noise level images and Eq.(3.44) is suggested being used in more moderate noise level. In [Deledalle et al., 2014], the center weight is $w(i, i) = 1$.

3.3.4 Selection of searching window and patch size

The searching window $\Omega(i)$ in Eq.(3.9) is usually selected as a $\sqrt{|\Omega(i)|} \times \sqrt{|\Omega(i)|}$ square region with pixel $y(i)$ as center. The size of $\Omega(i)$ has been discussed in [Salmon, 2010, Duval et al., 2010, Kervrann and Boulanger, 2006]. Salmon [2010] suggested that an appropriate size of $\Omega(i)$ is 21×21 [Buades et al., 2005a], since larger or smaller searching window would not get better results in his experiments. Rather than searching in a square window, a spiral searching path (a disk searching region) is used in [Deledalle et al., 2014] to deal with different window size. Kervrann and Boulanger [2006] proposed to locally select the size of $\Omega(i)$ based on a point-wise rule. Moreover, Berkovich et al. [2013] proposed a content-based search region for NLM, which is defined by a pixel based classification (segmentation). Chan et al. [2013] search the similar pixels in the whole image but with a Monte Carlo sampling. Duval et al. [2010] chose to overcome the selection of $\Omega(i)$ size by using a larger size combined with a local h setting algorithm, insensitive to the size of $\Omega(i)$.

As explained in section 3.3.1, the patch similarity can be used to represent the similarity of pixels if the similarity between two patches is strongly related to the similarity between their center pixels. Small patch size $\sqrt{|K|} \times \sqrt{|K|}$ tends to increase the correlation between the similarity of patches and the similarity of central pixels. However it is very sensitive

to noise and more dissimilar pixels are selected to denoise. Large patch size will exactly find similar pixels but few (or even no) similar pixels will be found. Generally, a patch is a small square window and its size depends on the size of objects in the images (or on the spatial resolution of images). To improve the performance in strong noise cases, Deledalle et al. [2009] proposed to use an increasing size of patch in an iterative denoising. Moreover, locally adaptive shape and size of patch is proposed in [Deledalle et al., 2012b].

3.3.5 NLMs with iteration strategy

Kervrann and Boulanger [2006] proposed an iterative framework which renews the weights with pre-estimated images. The same idea has been used in [Brox et al., 2008, Dabov et al., 2007b]. Goossens et al. [2008] proposed a post-processing filter after the NLM to remove remaining noise in regions with non-repetitive structures. Deledalle et al. [2009] defined the weights using both noisy image and pre-denoised image:

$$w(i, j) = \exp \left[\frac{S_{\text{GLR}}(\mathbf{y}(i), \mathbf{y}(j))}{h^2} + \frac{S_{\text{KL}}(\hat{\mathbf{u}}(i), \hat{\mathbf{u}}(j))}{h'^2} \right], \quad (3.45)$$

$S_{\text{KL}}(\hat{\mathbf{u}}(i), \hat{\mathbf{u}}(j))$ is computed using denoised patches $\hat{\mathbf{u}}(i)$ and $\hat{\mathbf{u}}(j)$, which is given by Eq.(3.37). This approach has been extended to SAR images [Deledalle et al., 2011] and Poisson noise images [Deledalle et al., 2010a].

3.3.6 NLMs in non-spatial domains

The basic NLMs find similar pixels and average them in spatial domain for estimation. This processing can also be done or considered in transformed domains.

Patch domain

Rather than the center pixel of patches, Coupé et al. [2008] proposed to estimate the noise-free patches. This estimator has similar expression as Eq.(3.9):

$$\hat{\mathbf{u}}(i) = \frac{1}{Z} \sum_{j \in \Omega_i} w(i, j) \mathbf{y}(j), \quad (3.46)$$

Weight $w(i, j)$ can also be calculated by Eq.(3.41) or Eq.(3.45). This patch/block-wise idea has been investigated more clearly in [Tschumperlé and Brun, 2011]. Then the value $\hat{u}(i)$ in pixel i is defined by combining the most significant patches together.

Transform domains

Block Matching 3-D (BM3D) algorithm [Dabov et al., 2007b] considers that an image has a locally sparse representation in the transform domain. Fig.3.11 shows the filtering processing of BM3D. The first step of BM3D (the first line in Fig.3.11) groups similar noisy patches (2D) into 3D groups. Then, a collaborative filtering produced individual estimates of all the grouped patches by filtering them jointly (through hard-thresholding in transform-domain). The second step (the second line in Fig.3.11) has the same stages like in step one, but it is performed on the basic estimation obtained by the step one instead of the noisy image. Both steps need an aggregation stage to reconstruct the estimated image, which transforms patches to image (the invert-grouping stage). Many extensions of BM3D have been proposed, such as BM3D with shape-adaptive PCA [Dabov et al., 2009], BM3D with PCA local pixel grouping [Zhang et al., 2010], video-BM3D [Dabov et al., 2007a]

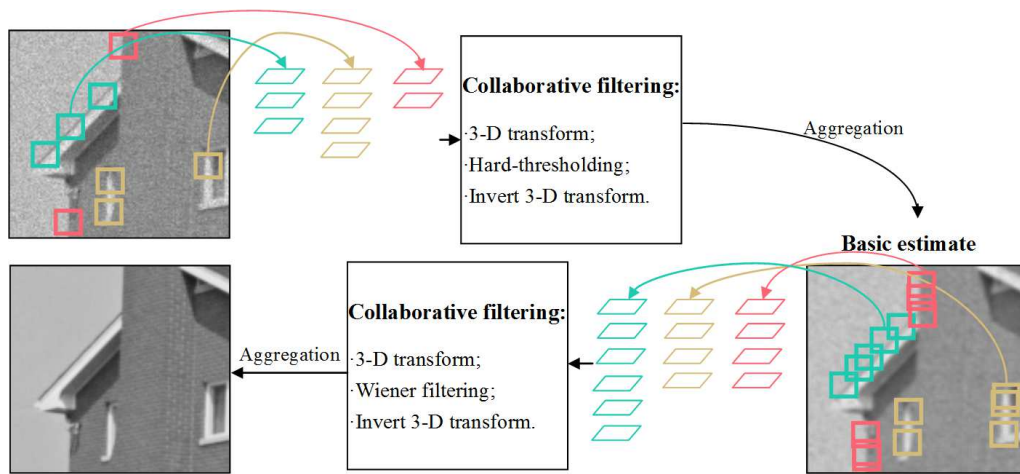


Figure 3.11: The sketch map of BM3D algorithm [Dabov et al., 2007b].

and BM4D [Maggioni et al., 2011] for video denoising, SAR-BM3D [Parrilli et al., 2012] and SAR-BM3D with a variable-size search area [Cozzolino et al., 2014] for SAR image denoising.

Image neighborhood (patches) used in the non-local means algorithm are projected onto a lower-dimensional subspace using principal component analysis (PCA) [Tasdizen, 2009, Zhang et al., 2010]. Consequently, patch similarity weights for NLM are computed using distances in this PCA subspace rather than the full (original) space. And this idea has been extended to Poisson noise reduction (photon-limited image reconstruction) by Salmon et al. [2014] and Gamma noise (speckle noise in SAR images) by Xu et al. [2014].

Mairal et al. [2009] further developed the locally sparse representation idea using unfixed dictionaries (compared with various types of wavelets which can be considered as fixed dictionaries). These unfixed dictionaries are over-complete and learned in the training data by K-SVD [Elad and Aharon, 2006], PCA [Tasdizen, 2009] or clustering method [Chatterjee and Milanfar, 2009, Dong et al., 2011].

3.4 Multi-temporal images denoising

Following the introduction of the denoising approaches dealing with single image in section 3.2 and 3.3, this section reviews some main approaches of multi images denoising, for instance video data, multi-temporal images and multi-channel images. Most of these methods are extended from the filters introduced in section 3.2 and 3.3.

According to the ways of extension, this section classifies the multi-image denoising methods into two groups:

- extension of denoising range, for instance extending the 2D searching window to a 3D searching cube may entitle NLM to deal with multi-image denoising;
- extension of denoising model, for instance Deledalle et al. [2011, 2014] developed the patch similarity from Gamma distributed noise model to complex Wishart distributed noise model for multi-channel SAR images.

Some state-of-the-art algorithms, including video denoising, multi-channel image (i.e. interferometric/polarimetric SAR images) denoising and multi-temporal images (i.e. SAR

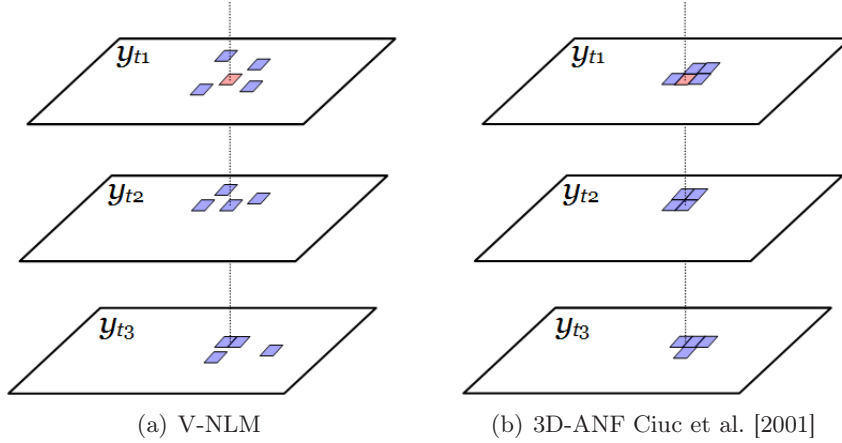


Figure 3.12: The illustration of extension of denoising range of NLM and the sketch map of 3D-ANF. NLM finds non local similar pixels/patches, while 3D-ANF only uses the connected pixels for estimation.

images) denoising, are introduced in this section.

3.4.1 Extension of denoising range

3D-ANF

Ciuc et al. [2001] proposed a 3D adaptive-neighborhood filter (3D-ANF) based on sigma-filter idea [Lee, 1983]. It uses both spatial and temporal neighbors of the current pixel for estimation. However, unlike the non local principle, this approach adaptively finds neighboring regions (only neighbors whose value is within a range is selected and this range depends on the current pixel value), as shown in Fig.3.12.b. These neighborhood pixels connected to each other should be involved in the denoising.

Video NLM

Buades [2006] extended the NLM from single image to multi-image (video) case by enlarging the spatial searching window to a spatial and temporal searching zone:

$$\hat{u}_t(i) = \frac{1}{Z} \sum_{t'} \sum_{j_{t'} \in \Omega(i_{t'})} w(i_t, j_{t'}) \cdot y_{t'}(j), \quad (3.47)$$

where, $w(i_t, j_{t'}) = f [S(\mathbf{y}_t(i), \mathbf{y}_{t'}(j))]$.

$y_t(i)$ denotes the pixel located at i in image y_t (at time t). $S(\mathbf{y}_t(i), \mathbf{y}_{t'}(j))$ is the similarity between patch $\mathbf{y}_t(i)$ and $\mathbf{y}_{t'}(j)$. Video NLM takes a spatial searching window at position i in each image and looks for all similar blocks in temporal searching windows, as shown in Fig.3.12.a. Note that no motion estimate or optical flow estimate has been performed in Buades [2006], since the NLM finds the *similar* pixels for denoising instead of the *same* pixels, there is no need to have the explicit estimation of motions. Following the idea in [Buades, 2006, Cheung et al., 2008] that there is no need for the NLM framework to have motion estimation, Mahmoudi and Sapiro [2005] applied a pre-classifying processing to video denoising. They firstly classified the image blocks according to fundamental characteristics (average gray values and gradient orientation). Then, only blocks with similar characteristics are used in the denoising (with non-zero weights). This pre-processing can

reduce the computational complexity and diminish the influence of dissimilar pixels in the denoising.

Most videos are highly temporally consistent. That is why the NLM without motion estimation between two frames can get satisfying results. However, many real noisy videos have structured noise that makes NLM failing. In contrast with [Buades, 2006, Cheung et al., 2008], Liu and Freeman [2010] claimed that high-quality video denoising, especially when structured noise is taken into account, needs reliable motion estimation. An optical flow algorithm with spatial regularity was used to estimate temporal correspondence between two frames. To reduce the computational complexity of NLM, an approximate K-nearest neighbor patch matching algorithm is used to search for similar patches in the entire image.

V-BM3D

BM3D has also been developed to denoise video by Dabov et al. [2007a], named video-BM3D (V-BM3D). A predictive-search block-matching is used to group similar patches both in the spatial and temporal domain of the video. It is similar to the techniques used for grouping in BM3D, but also has the facility to estimate the motion between two frames.

Others

Alonso-González et al. [2014] also extended the binary partition trees based PolSAR filter [Alonso-González et al., 2012] to PolSAR temporal series. It constructs the PolSAR series as a set of spatio-temporal homogeneous regions and estimates the polarimetric parameters within them. Le et al. [2014] proposed an adaptive filter based on a change detection matrix for SAR time series. Coefficient of variation is used to determine the change/un-change, which is the ratio of standard deviation to the mean of noisy image. The unchanged pixels in temporal domain have been averaged, however no spatial filtering process follows this temporal averaging.

3.4.2 Extension of denoising model

BM4D

Contrary to V-BM3D, BM4D does not group blocks, but mutually similar spatiotemporal volumes according to a non local search procedure. As shown in Fig.3.13, the V-BM3D groups patches, while the BM4D searches similar volumes (a series of patches). More recently, Sutour et al. [2014] adapted their method to video denoising by using 3D patches instead of 2D patches.

Spatial-temporal filters for SAR amplitude images

Quegan and Le Toan [1998], Quegan et al. [2000] denoised the multi-temporal SAR images by a weighted sum based on the covariance matrix. Quegan and Yu [2001] proposed a texture compensation multi-channel filter based on Kuan filter [Kuan et al., 1985]. Kuan filter is firstly applied on each image and obtained the texture compensation. It considers the estimation of each pixel as the linear combination of its temporal neighbors, and the weights of this combination (or summation) depend on the ratio of the texture compensations. The main idea of the time-space filter in Coltuc et al. [2000] is to apply a DCT transform along temporal domain to separate the signal from the noise and remove the noise in the transform domain.

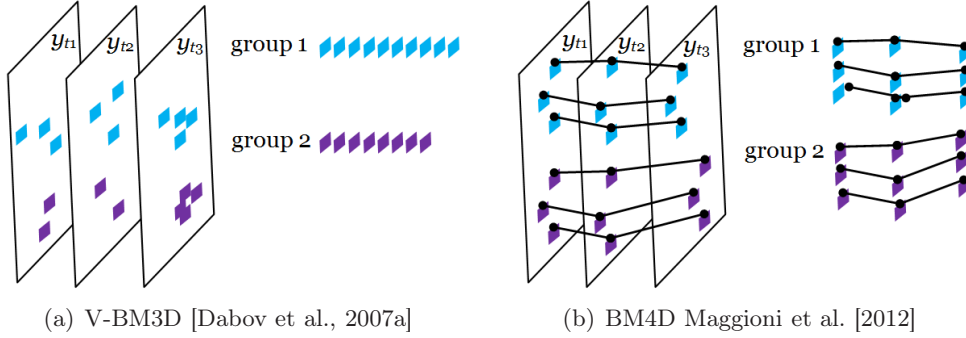


Figure 3.13: The sketch map of grouping steps in V-BM3D and BM4D. V-BM3D: grouping 2D patches, BM4D: grouping series of patches (spatiotemporal volumes, 3D patches).

Non-local means for InSAR, PolSAR and PolInSAR images

Non local means have also been applied to InSAR [Deledalle et al., 2011], PolSAR [Deledalle et al., 2010b, Liu and Zhong, 2014] and PolInSAR images Deledalle et al. [2014]. Deledalle et al. [2014] proposed an unified non-Local framework for multi SAR images, including InSAR, PolSAR and PolInSAR images by developing the weighted maximum likelihood estimation from Gamma distribution to complex Wishart distribution.

Similarly to Eq.(3.9), the estimation $\hat{\Sigma}$ can be calculated by:

$$\hat{\Sigma}(i) = \frac{1}{Z} \sum_{j \in \Omega(i)} w(i, j) \mathbf{C}(j). \quad (3.48)$$

The weight $w(i, j)$ is the averaging weight based on the similarity between $\mathbf{C}(i)$ and $\mathbf{C}(j)$. Deledalle et al. [2012a] defined this similarity according to the comparison between two patches with i and j as center respectively. Like the computation of similarity in the PPB algorithm, the comparison of two patches is also based on the detection theory, the generalized likelihood ratio (GLR), given by:

$$S_{\text{GLR}}(\mathbf{C}(i), \mathbf{C}(j)) = \sum_k -\log \frac{|\frac{1}{2}[\mathbf{C}(i, k) - \mathbf{C}(j, k)]|^{2L}}{|\mathbf{C}(i, k)|^L |\mathbf{C}(j, k)|^L} \quad (3.49)$$

where $\mathbf{C}(i + k)$ is the k -th neighbor of $\mathbf{C}(i)$ (in spatial domain). This averaging operator is performed on a square patch with size of $\sqrt{K} \times \sqrt{K}$ pixels. When $M = 1$, this GLR similarity turns to be the expression given in Eq.(3.27). Then, the weight based on the similarity can also be given by Eq.(3.41).

3.5 Evaluation of denoising

This section presents some common approaches of evaluating the denoising methods.

Mean squared error (MSE) related evaluations

Mean squared error (MSE) measures the Euclidean distance between the "true" signals and the estimated signals. The expression of MSE is:

$$\text{MSE}(\hat{u}, u) = \sum_i (\hat{u}(i) - u(i))^2. \quad (3.50)$$

The lower the MSE, the better the estimation.

Signal-to-noise ratio (often abbreviated SNR or S/N) is a measure comparing the level of a desired signal to the level of background noise. It is defined as the power ratio between the signals and the noise. Since the signals usually have a very wide dynamic range, SNR is often expressed using the logarithmic decibel scale. For images, SNR measures the difference between the noise-free image u and the estimated image \hat{u} :

$$\text{SNR}(\hat{u}, u) = 10 \log_{10} \frac{\text{Var}(u)}{\frac{1}{N} \text{MSE}(\hat{u}, u)}, \quad (3.51)$$

where $\text{Var}(u)$ is the variance pixel values in image u . N is the number of pixels of image u . For the seek of simplicity, the peak signal-to-noise ratio can be used to measure the denoising quality:

$$\text{pSNR}(\hat{u}, u) = 10 \log_{10} \frac{[\max(u) - \min(u)]^2}{\frac{1}{N} \text{MSE}(\hat{u}, u)} \quad (3.52)$$

where $\max(u)$ and $\min(u)$ are the maximum and minimum pixel value of image u .

MSE-related evaluations can accurately measure the difference between noise-free u and the estimation \hat{u} . However, they can only measure the performance when the noise-free u is available, which is impossible in reality (for instance, the real SAR images have no noise-free data available).

Difference/ratio map

When the noise-free images are not available, the evaluation of denoising quality can be done by analyzing the difference map $\hat{u} - y$ between the estimation \hat{u} and the observed data y (for multiplicative noise like speckle, the ratio map $\frac{y}{\hat{u}}$ should be used). Obviously, in the ideal case ($\hat{u} = u$), the difference/ratio map will be pure noise. Thus the better denoising results have purer noise in the difference/ratio maps. In other words, the less structured information is left in the difference/ratio map, the better is the performance the denoising technique. Fig.3.14 and Fig.3.15 respectively show the difference and ratio maps of denoising results.

Equivalent number of looks for denoised SAR images

As explained in chapter 2, the number of looks L can denote the speckle noise level of SAR images. The higher the number of looks, the less speckle noise will exist. In other words, the reduction of speckle is equivalent to increasing the number of looks. Thus, the estimation of number of looks L of denoised SAR images can be considered as an evaluation of SAR denoising. This estimation is named equivalent number of looks (ENL), which can be calculated by the square ratio of mean and variance:

$$\text{ENL} = \frac{E(\hat{u})^2}{\text{Var}(\hat{u})} \quad (3.53)$$

where the mean $E(\hat{u})$ and variance $\text{Var}(\hat{u})$ are calculated in an homogeneous square window. ENL is usually used to evaluate SAR image quality and needs no noise free images.

3.6 Summary of image denoising

We have reviewed some state of the art methods for the image and multi-image denoising tasks. Among these approaches, the non local means (NLM) have been highlighted and will

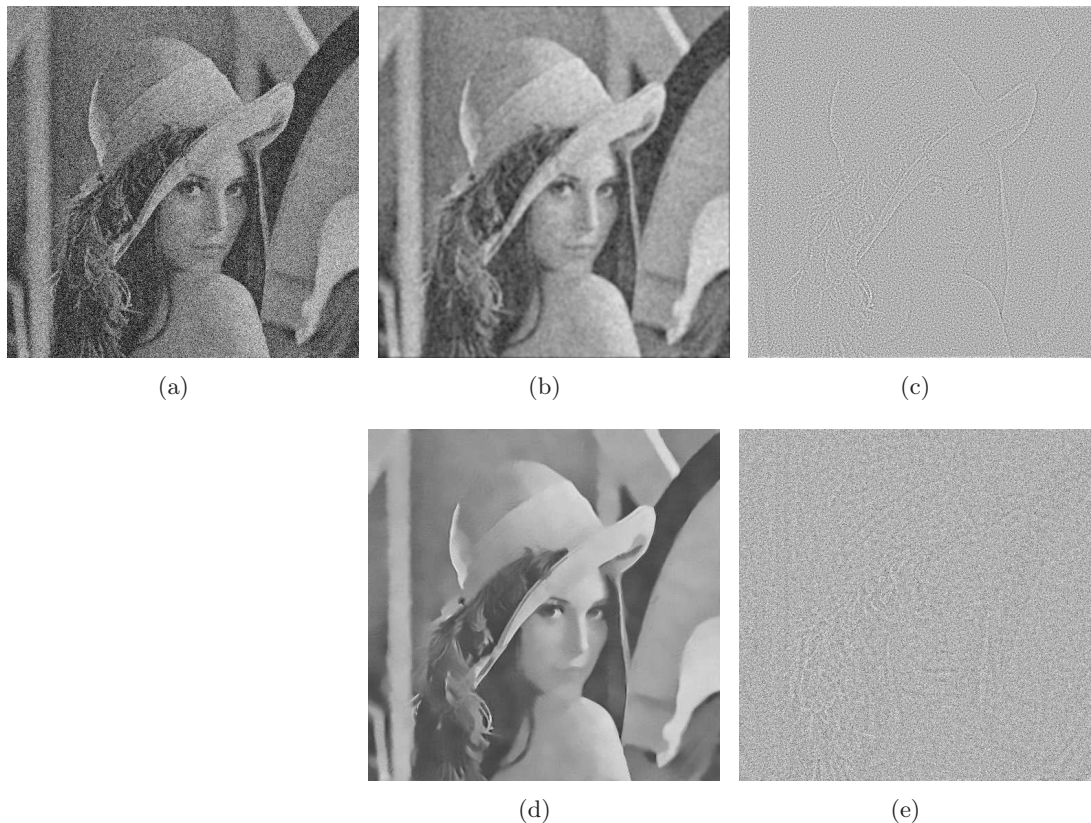


Figure 3.14: Difference maps of denoising results (additive Gaussian noise). (a) The noisy image *Lena* with additive Gaussian noise $\sigma = 30$. (b) The denoising result by a linear Gaussian filter. (c) The difference map between a and b. (d) The denoising result by the non local means filter [Buades et al., 2005a]. (e) The difference map between a and d. There are less structures left in e, thus the non local means filter has better performance than the linear Gaussian filter.

be applied to our multi-temporal SAR image denoising task due to its efficiency. Various improvements and extensions of NLM have been proposed, especially for the SAR image denoising, for instance the generalized likelihood ratio (GLR) similarity of noisy patches and the Kullback-Leibler (KL) divergence similarity of denoised patches are introduced. In this chapter we have proposed some extensions of both GLR and KL similarities by considering patches with different noise levels, and full expressions of the improved GLR and KL have been given. Based on these works on NLM, we will present in the next chapter how these approaches can be used for multi-temporal SAR intensity estimation.

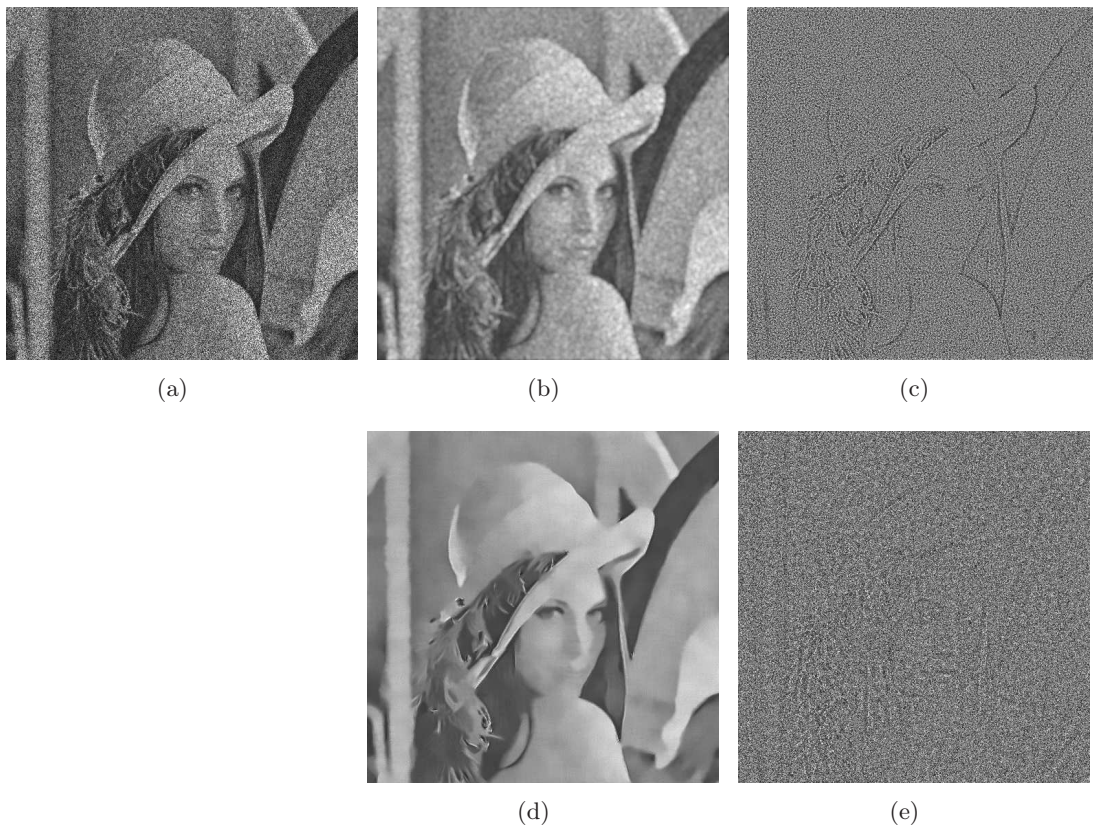


Figure 3.15: Difference maps of denoising results (multiplicative speckle noise). (a) The noisy image *Lena* with multiplicative speckle noise $L = 1$. (b) The denoising result by a linear Gaussian filter. (c) The difference map between a and b. (d) The denoising result by the PPB filter [Deledalle et al., 2009]. (e) The difference map between a and d. There are less structures left in e, thus the PPB filter has better performance than the linear Gaussian filter.

Chapter 4

Two Steps Non-Local Means for Multi-temporal SAR images

In this chapter we will present how non local means theory can be applied to multi-temporal SAR images. The proposed method is an extension of the probabilistic patch-based (PPB) filter by Deledalle et al. [2009] presented in details in the previous chapter. The main idea of the proposed approach is to deal with the spatial and temporal information of the time series respectively. Inspired by the works in [Buades, 2006, Cheung et al., 2008], we firstly present a direct extension of PPB for multi-temporal SAR images. An interesting comparison experiment is then introduced to propose our motivation, which is followed by the details of the proposed 2S-PPB filter. At the end of this chapter, we will present an extension of the proposed filter to miss-registered multi-temporal SAR images.

4.1 Direct Extension of PPB

As introduced in chapter 3, the key idea of the PPB denoising in [Deledalle et al., 2009] (and also the NLM) is to estimate actual pixel intensity with image redundancy. The way to exploit image redundancy is the search of similar pixels in a search window and averaging those similar pixels with different weights. For multi-temporal data, a direct extension of PPB can be the definition of a cube search window, by aggregating all the search windows of the different dates, like the extension of NLM to video denoising in [Buades, 2006, Cheung et al., 2008]. Considering a SAR time series $\{y_{t_1}, y_{t_2}, \dots, y_{t_N}\}$, the temporal PPB filter can be defined on a cube $\mathbf{C}(i) = \Omega(i) \times \{t_1, t_2, \dots, t_N\}$ of all pixel indexes i . Meanwhile, the direct temporal extension of PPB (we will name it T-PPB) to estimate the *true* value $u_t(i)$ is:

$$\hat{u}_t(i) = \frac{1}{Z} \sum_{j_{t'} \in \mathbf{C}(i)} w(i_t, j_{t'}) \cdot y_{t'}(j) \quad (4.1)$$

where $w(i_t, j_{t'})$ is given by Eq.(3.45).

4.1.1 Comparison of PPB method

To analyze the interest of this direct extension for the temporal case, we have tested it on a synthetic set of multi-temporal images $\{y_{t_1}, y_{t_2}, y_{t_3}\}$. These images are synthesized

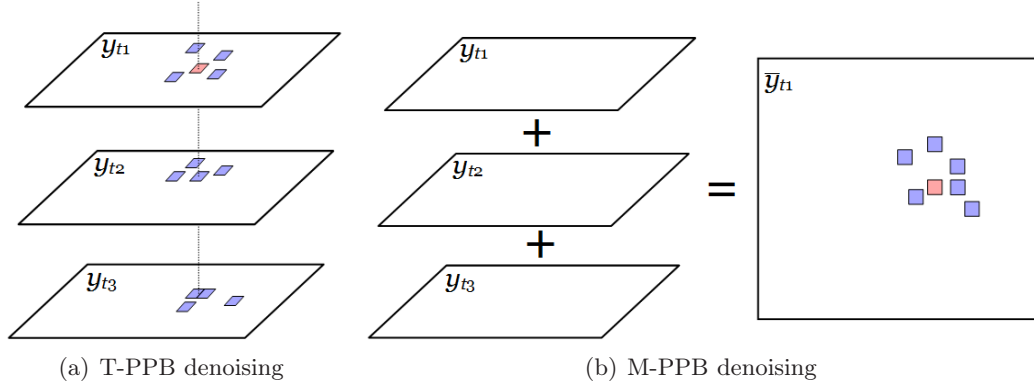


Figure 4.1: The sketch map of temporal PPB (T-PPB) and mean PPB (M-PPB). (a) Denoise y_{t_1} using the set of temporal images $\{y_{t_1}, y_{t_2}, y_{t_3}\}$ by temporal PPB approach (Eq.(4.1)). (b) Firstly get the mean values \bar{y} of the set of multi-temporal images $\{y_{t_1}, y_{t_2}, y_{t_3}\}$. Then denoise this average image \bar{y} using PPB approach.

supposing no change in time (stable case) and temporally , therefore giving 3 realizations of the same scene. They have been denoised using three methods:

- **Method i (PPB)**: Denoise the single image y_{t_1} without using images y_{t_2} and y_{t_3} by PPB approach.
- **Method ii (T-PPB)**: Denoise y_{t_1} using the set of temporal images $\{y_{t_1}, y_{t_2}, y_{t_3}\}$ by temporal PPB approach (Eq.(4.1)).
- **Method iii (M-PPB)**: Firstly get the mean values \bar{y} of the set of multi-temporal images $\{y_{t_1}, y_{t_2}, y_{t_3}\}$. Then denoise this average image \bar{y} using PPB approach.

Note that method **i** uses only one image, while method **ii** uses the whole image set (3 images). Although methods **ii** and **iii** share the same input noisy images, method **iii** firstly temporally averages the 3 temporal images. Because the denoising approach of the three methods is PPB and the main difference among them is the input, one can easily predict that method **i** has the poorest results and Methods **ii** and **iii** should have comparable performances.

Fig.4.2 shows the three results. As expected, by using three 1-look noisy images, the denoising performance of T-PPB in Fig.4.2.d has been improved compared with the result of PPB in Fig.4.2.b (in terms of the SNR values). However, it is not sufficient, because M-PPB Fig.4.2.f has significantly outperformed T-PPB, in spite of the same input noisy images.

4.1.2 Analysis and motivation

In order to analyze the results, we present the map of weights $w(i_t, j_{t'})$. Fig.4.3 shows the weight maps of several interesting pixels for the three methods. In the noise-free image, we can easily find the similar pixels. However, in method **ii** more dissimilar pixels have been assigned large weights (bright points in the weight map) than those in method **iii**. More weights are computed but they are less accurate. Thanks to the temporal average before denoising, method **iii** reduces the risk when searching similar pixels.

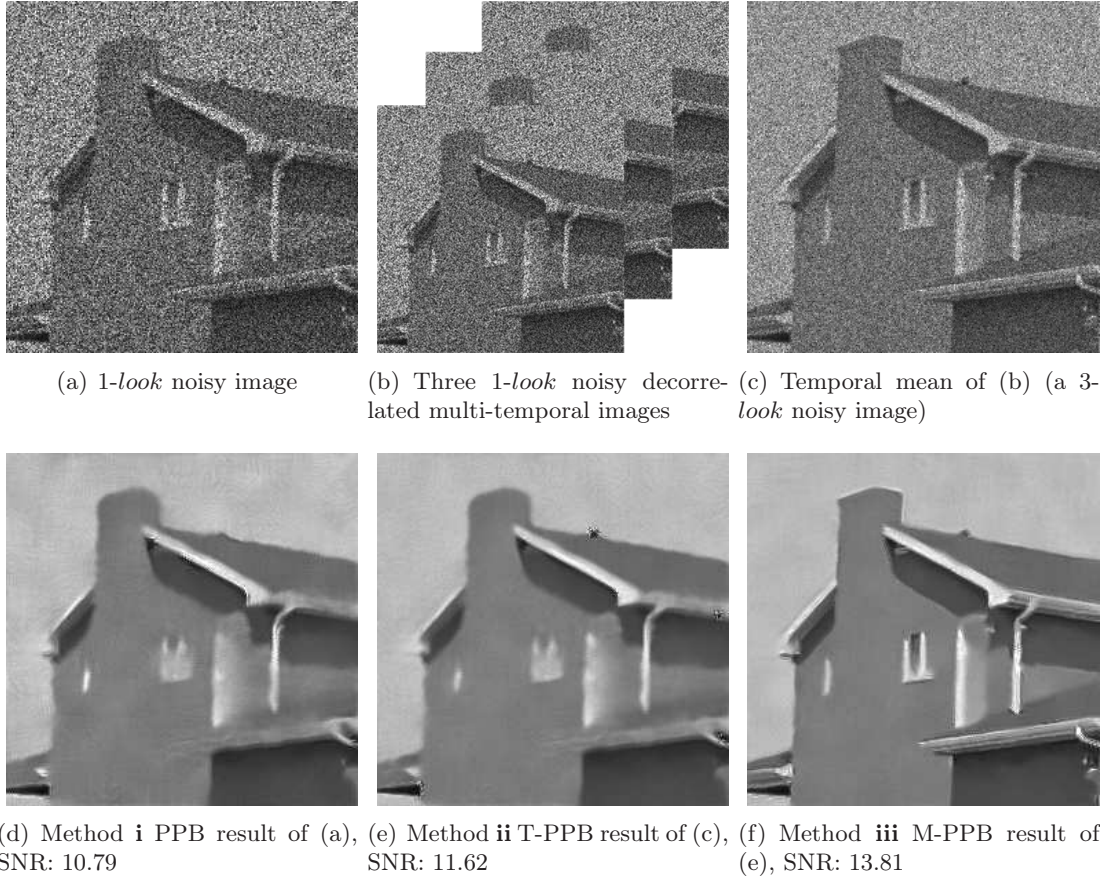


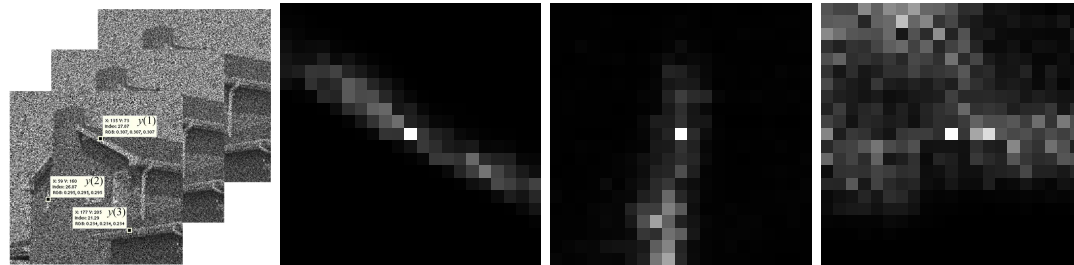
Figure 4.2: Denoising results of synthetic images with multiplicative speckle noise (top: input noisy images; bottom: denoising results).

A first solution could be the modification of the kernel that transforms similarity in weights. Indeed, it is shown in [Duval et al., 2011] that truncated weights for NLM (instead of exponential function) could improve the selection. However for 1-look image, the improvement is not sufficient.

Averaging in temporal domain (multi-looking) is considered as the efficient and best unbiased estimator for the hypotheses of independent and identical distribution. Thus, method **iii** naturally performs better than method **i** and **ii** in the situation of no-change and decorrelated images. The purpose of this experiment was to illustrate the improvement of the introduction of multi-looking into PPB. In this chapter we combine the advantages of both approaches (multi-looking and PPB) to define a multi-temporal denoising method.

4.2 Two-steps non-local means (2S-PPB)

Let us go back to the simple comparison experiment in Section 4.1.1. Method **iii** (in Fig.4.2.c and f) firstly temporally averages noisy images, which reduces the noise level and improves the weights, as shown in Fig.4.3. Although the real SAR images or video data may encounter changes due to miss-registration (or motion) and temporal changes, there are still lots of cases that can be temporally combined. Taking inspire from the Method **iii**, we propose to divide the denoising process into two steps, which deal with temporal



(a) 3 1-look noisy images

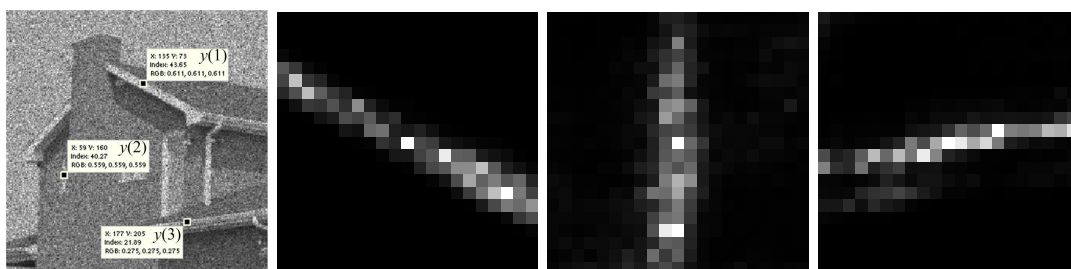
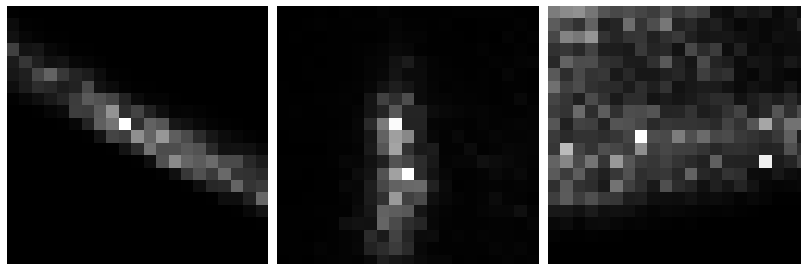
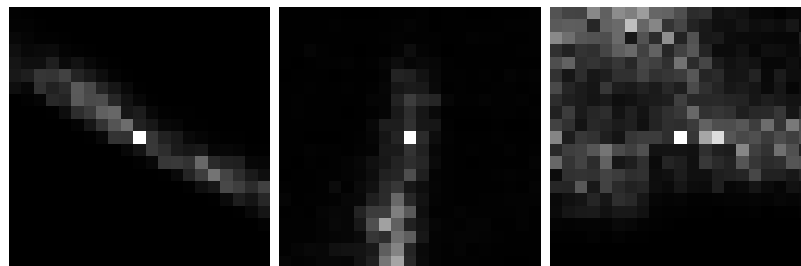
(b) Temporal mean of (a)
(3-look noisy image)

Figure 4.3: Weight maps. (a) three 1-look noisy images; (b) temporal mean of (a). *Right:* the corresponding weight maps. 1-look noisy images have more similar pixels found by similarity measurement, but they are not accurately selected.

and spatial information respectively. The main purpose of multi-temporal denoising is exploiting all the available information for temporally stable pixels while keeping the new information as much as possible. Note that in this part all the multi-images are considered as well registered, and only the change detection problem is considered in this section.

In case of stable pixels (no change over time and well registered), the method **iii** illustrates the usefulness of temporal averaging. The proposed denoising framework namely two-step (2S-PPB) approach based on NLM and PPB is to exploit similar pixels in the temporally average image \bar{y} rather than in the stack $\{y_{t_1}, \dots, y_{t_N}\}$ (the premise is that there is no change taking place among multi-images). If pixels located at the same position but at different times (like $y_t(i)$ and $y_{t'}(i)$) have not changed (in other words, they share a same *true* value $u_t(i) = u_{t'}(i)$), they can be averaged together to estimate $u_t(i)$. From a probability point of view, this equally weighted average can be considered as an estimation using prior information (relative to the estimate using likelihood information in [Deledalle et al., 2009]). This temporal average can be seen as a preliminary multi-looking operation. However, the main problem lying in this temporal denoising is the use of only stable pixels. We thus have to use efficient change detection, which will be detailed in the following.

4.2.1 Criteria of change

Usually, most change detection methods are concerned about the changes between different terrestrial objects, like *rivers*, *buildings* and other artificial objects. However in image denoising, we theoretically combine the observed pixels from the same true value or reflectivity (coming from the same distribution). Hence here the *changes* are defined as samples coming from different distributions.

As mentioned in section 3.3.1, several similarity criteria for noisy patches are compared in [Deledalle et al., 2012a]. They can also be used to detect changes. For instance, the GLR proposed for non-Gaussian noise can be used to detect changes in times. Another criterion, the KL divergence criterion in denoised images [Deledalle et al., 2009] can also be used to improve the performance of the GLR criterion computed in noisy images. As shown in the previous chapter these criteria are very efficient. Therefore, we have decided to study both criteria, GLR on noisy images and KL divergence on denoised data for similar pixel selection.

Fig.4.4 illustrates the performance of the GLR criterion in the noisy image and the KL criterion in the denoised image (using PPB on each image) to find the similar pixels. The results show that the KL criterion in denoised images is more efficient to select similar pixels than the GLR criterion in noisy image. However, this comparison experiment is not fair, because of the different noise level in Fig.4.4.a and c. What is more, the KL criterion in denoised images has an inevitable drawback that the used denoising approaches have great influence on the quality of the selections.

To balance the advantages against the disadvantages of both the GLR in noisy images and the KL criterion in denoised images, we propose to employ both of them to detect the changes between temporal images. This suggestion has similar consideration as in [Deledalle et al., 2009], which proposed that the denoising weights are coming from both the noisy images (by GLR criterion) and the previous denoised images (by KL divergence).

For the sake of simplicity, we use Eq.(4.2) as a binary criterion to define the temporal

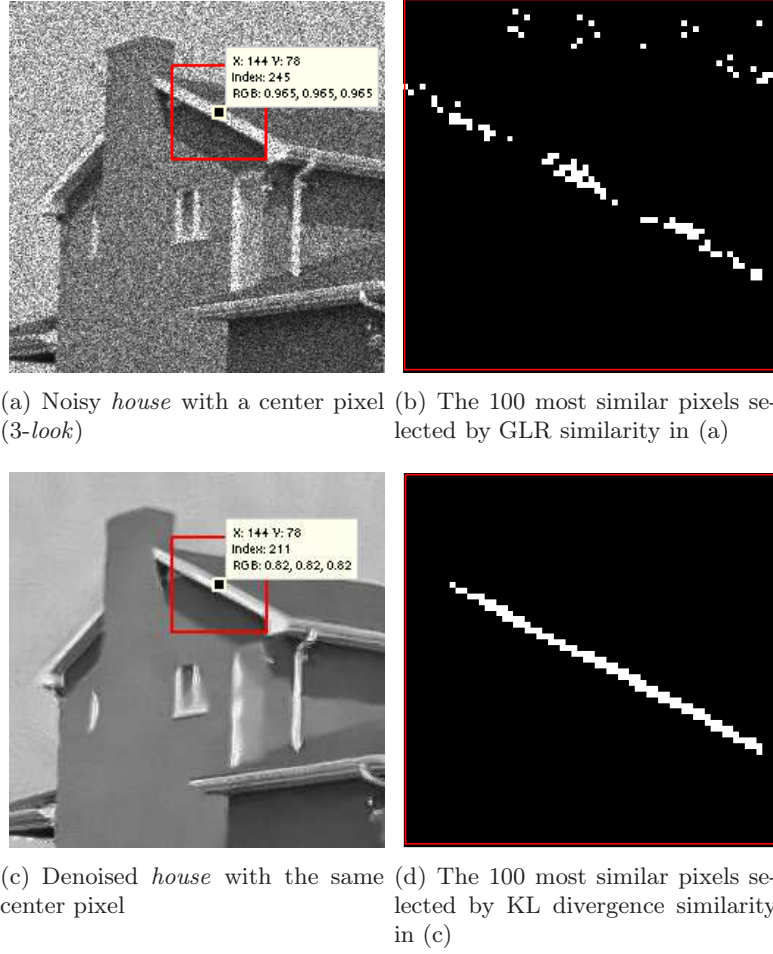


Figure 4.4: Selected similar pixels by the GLR criterion and the KL divergence criterion. (a) the 3-look noisy *house* image and the pixel that will be used to illustrate the distributions, the red rectangle is the search window; (b) selections by GLR criterion; (c) PPB denoising result of (a); (d) selections by KL criterion. The KL criterion in denoised images is more efficient to select similar pixels than the GLR criterion in noisy image.

relation between the pixel values at i_t and the pixel value at $j_{t'}$ as

$$f^b(S(y_t(i), y_{t'}(j))) = \begin{cases} 1, & \text{if } S(y_t(i), y_{t'}(j)) > -2 \\ 0, & \text{otherwise} \end{cases} \quad (4.2)$$

$$S(y_t(i), y_{t'}(j)) = \frac{S_{\text{GLR}}(\mathbf{y}_t(i), \mathbf{y}_{t'}(j))}{h^b} + \frac{S_{\text{KL}}(\hat{\mathbf{u}}_t^{\text{PPB}}(i), \hat{\mathbf{u}}_{t'}^{\text{PPB}}(j))}{h'^b} \quad (4.3)$$

where, $S(y_t(i), y_{t'}(j)) \in]-\infty, 0]$, $\hat{\mathbf{u}}_t^{\text{PPB}}(i)$ and $\hat{\mathbf{u}}_{t'}^{\text{PPB}}(j)$ are patches extracted in the denoised result respectively in y_t and $y_{t'}$ using PPB filter. In order to ensure that both GLR and KL criterion have same contribution on the change detection, we normalize the GLR and KL terms in Eq.(4.2) by parameters $h^b = |\text{quantile}(S_{\text{GLR}}, \alpha)|$ and $h'^b = |\text{quantile}(S_{\text{KL}}, \alpha)|$ respectively, where for any similarity measure S , $\text{quantile}(S, \alpha)$ denotes the α -quantile of the *pure* distribution of S (i.e., the distribution when patches

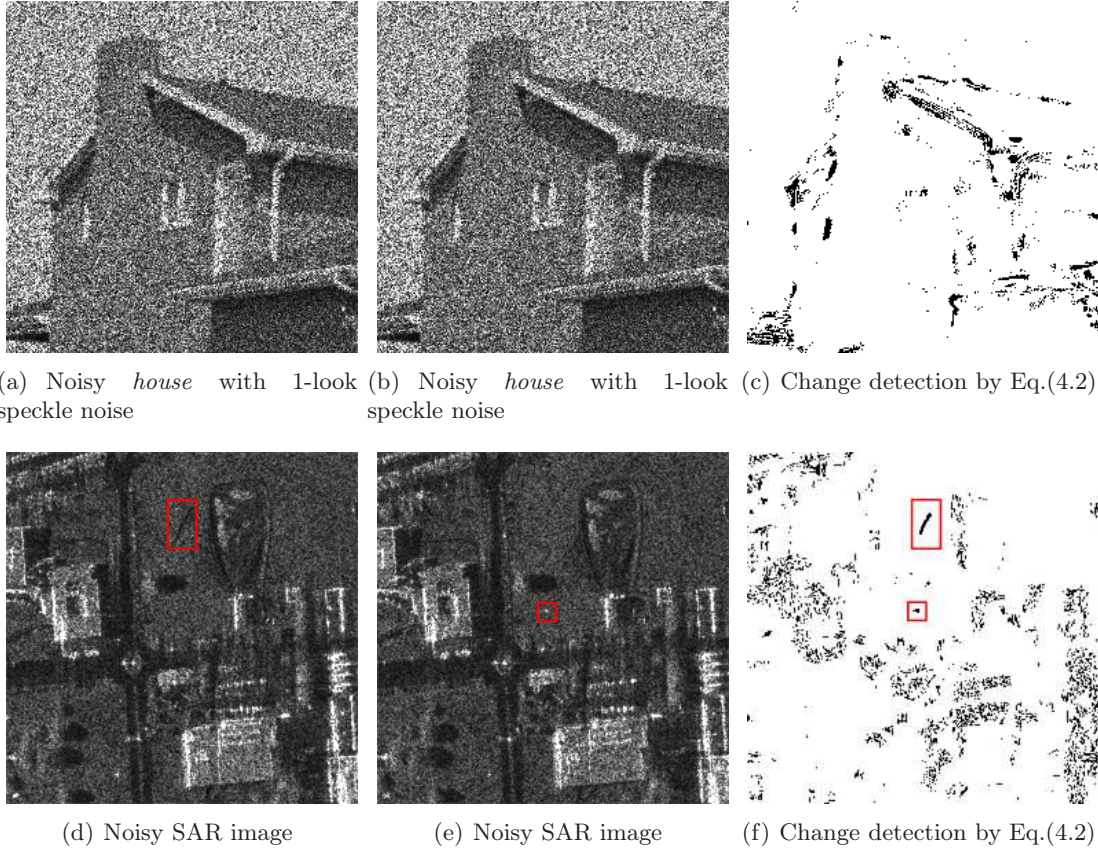
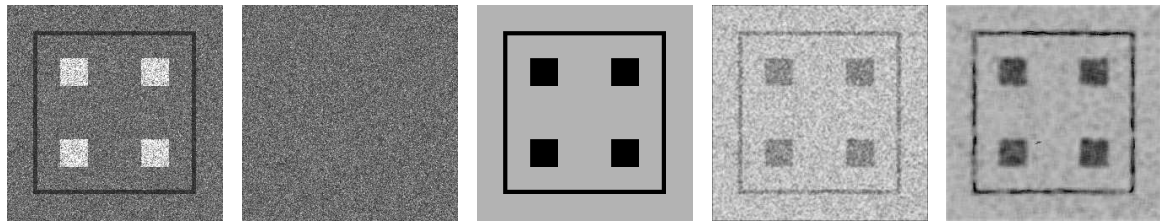


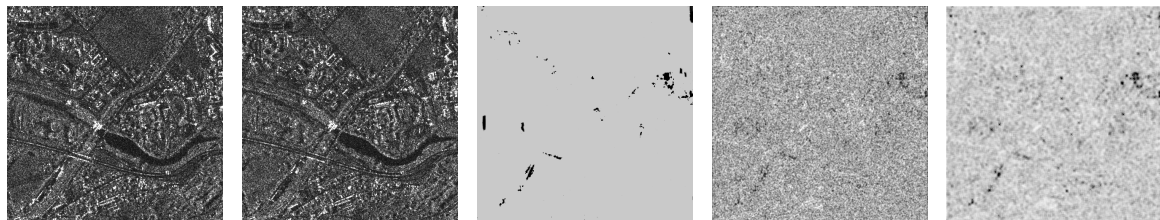
Figure 4.5: Change detection by the KL divergence and the GLR criterion. (a, b) the noisy house images with 1-look speckle noise; (c) change detection results between (a) and (b); (d, e) the noisy SAR images, the red rectangles denote the changes between (d) and (e); (f) change detection results between (d) and (e). Changes in red rectangles have been found out in detection results.

have the same underlying reflectivity). More discussion about the α -quantile based threshold can be found in section 5.4. In practice, here we have chosen $\alpha = 0.99$, such that a binary weight $f^b(S(y_t(i), y_{t'}(j))) = 1$ means that pixel $y_t(i)$ and $y_{t'}(j)$ have a high probability to be realizations coming from the same underlying reflectivity. If α is kept constant, thresholds lower than '-2' will add more changed pixels in the temporal step. On the contrary, the smaller threshold may neglect some similar (unchanged) pixels in the temporal step.

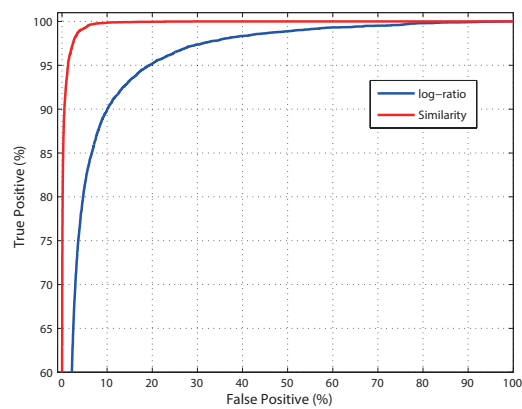
We compare this *change detection* criterion with the log-ratio, a criterion widely used in SAR images. Synthetic images and real SAR images are used in this comparison experiment, 1) synthetic SAR images corrupted by a multiplicative 1-look speckle noise in Fig.4.6.a, 2) two real SAR images (TerraSAR images of Saint-Gervais-les-Bains, France) sensed in 2009 and 2011 respectively in Fig.4.6.b. The reference maps of changes are shown in the middle of Fig.4.6.a and b (for the real SAR images, we manually label the changes taking place between date 1 and date 2). The right of Fig.4.6.a and b shows log-ratio criterion and our similarity-based change detection criterion. The similarity criterion has higher ROC curves in the False-positive and True-positive curves in Fig.4.6.c and d.



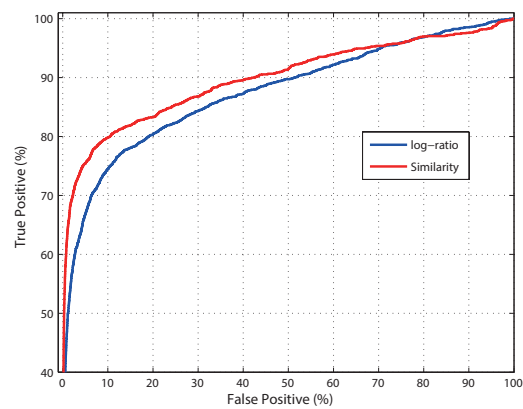
(a) Synthetic images. From left to right: image at date t , image at date t' , reference map of changes, log-ratio criterion map and the proposed similarity criterion map.



(b) *Saint-Gervais-les-Bains* images. From left to right: image at date t , image at date t' , reference map of changes, log-ratio criterion map and the proposed similarity criterion map.



(c) Change detection results (True positive and false positive curves) of synthetic images



(d) Change detection results (True positive and false positive curves) of *Saint-Gervais-les-Bains* images

Figure 4.6: Change detection criterion comparison. a) synthetic SAR images, b) real SAR images (TerraSAR images of Saint-Gervais-les-Bains, France). From left to right, noisy image y_t , noisy image $y_{t'}$, the reference maps of changes, the log-ratio criterion map and our similarity-based change detection criterion map. c) and d) Change detection results (True positive and false positive curves).

4.2.2 Two Steps Denoising

Based on this change criterion we propose the following framework for temporal denoising named 2S-PPB.

Temporal step. The following formula shows the temporal averaging process with the change criterion (binary weights):

$$\tilde{y}_t(i) = \frac{1}{Z} \sum_{t' \in [t_1, t_N]} f^b(S(y_t(i), y_{t'}(j))) \cdot y_{t'}(i) \quad (4.4)$$

where $Z = \sum_{t' \in [t_1, t_N]} f^b(S(y_t(i), y_{t'}(j)))$.

Denoising on the temporal estimate $\tilde{y}_t(i)$ is comparable to Eq.(4.1). However, different pixels $\tilde{y}_t(i)$ may have different (equivalent) number of *looks* depending on the number of averaged data. The resulting number of *looks* is temporally and spatially varying and is given by:

$$\tilde{L}_t(i) = \sum_{t' \in [t_1, t_N]} f^b(S(y_t(i), y_{t'}(j))) \cdot L_{t'} \quad (4.5)$$

in which $L_{t'}$ is the original spatially-invariant (equivalent) number of *looks* of the image $y_{t'}$.

Discussion on the equivalent number of looks and pixel correlation. In the temporal step, the number of looks $\tilde{L}_t(i)$ associated to the averaged pixel $\tilde{y}_t(i)$ only depends on the number of candidate pixels in Eq.(4.4). However for interferometric images, the *real* number of looks is also linked to the coherence between the concerned pixel $y_t(i)$ and the candidate pixel $y_{t'}(i)$. In the ideal case, the coherence between $y_t(i)$ and $y_{t'}(i)$ is 0 (they are thus decorrelated), then the number of looks $\tilde{L}_t(i)$ can be given by Eq.(4.5). However, when the coherence is non-zero, the *real* $\tilde{L}_t(i)$ will be lower than the value given by Eq.(4.5), due to the coherence of noise. This case mainly takes place in the building areas and other artifact objects, as shown in Fig.3.7.c.

Spatial step. Now working on the image $\tilde{\mathbf{y}}_t$, the similarity between patches $\tilde{\mathbf{y}}_t(i)$ and $\tilde{\mathbf{y}}_t(j)$ has to be modified to take into account the spatially varying number of *looks*. For any pair of patches in the temporal mean image $\tilde{\mathbf{y}}_t$, the GLR similarity is given by:

$$\begin{aligned} S_{\text{GLR}}(\tilde{\mathbf{y}}_t(i), \tilde{\mathbf{y}}_t(j)) = & - \sum_{k \in K} \left[\left(\tilde{L}_t(i, k) + \tilde{L}_t(j, k) \right) \log \left[\tilde{L}_t(i, k) \tilde{y}_t(i, k) + \tilde{L}_t(j, k) \tilde{y}_t(j, k) \right] \right. \\ & - \left(\tilde{L}_t(i, k) + \tilde{L}_t(j, k) \right) \log \left(\tilde{L}_t(i, k) + \tilde{L}_t(j, k) \right) \\ & \left. - \tilde{L}_t(i, k) \log [\tilde{y}_t(i, k)] - \tilde{L}_t(j, k) \log [\tilde{y}_t(j, k)] \right] \end{aligned} \quad (4.6)$$

which is deduced from Eq.(3.26). KL divergence similarity can also be computed by Eq.(3.37). Then, the estimate $\hat{u}_t(i)$ using $\tilde{\mathbf{y}}_t$ will be:

$$\hat{u}_t(i) = \frac{1}{Z} \sum_{j \in \Omega(i)} w(i, j) \tilde{\mathbf{y}}_t(j) . \quad (4.7)$$

It is similar to NLM filtering given by Eq.(3.9), but applies on the temporally improved image $\tilde{\mathbf{y}}_t$ instead of original noisy image y_t . The weights are also iteratively defined based

Algorithm 1 The proposed 2S-PPB algorithm.

Input:

Well registered temporal SAR images $\{y_{t_1}, y_{t_2}, \dots, y_{t_N}\}$.
 A date t_1 of interest.

Output:

\hat{u}_{t_1} : the denoising result of image y_{t_1} .

—————**Step 1 (Temporal step):**—————

- 1: **for** each y_t in $\{y_{t_1}, y_{t_2}, \dots, y_{t_N}\}$ **do**
- 2: denoise y_t using PPB approach; (Section 3.3)
- 3: obtain pre-denoised results \hat{u}_t^{PPB} ;
- 4: **for** each pixel index i **do**
- 5: compute change criterion $f^b(S(y_t(i), y_{t'}(j)))$; (Eq. 4.2)
- 6: **end for**
- 7: **end for**
- 8: **for** each pixel index i **do**
- 9: initialize $\tilde{y}_{t_1}(i) = 0, \tilde{L}_{t_1}(i) = 0$;
- 10: **for** each y_t in $\{y_{t_1}, y_{t_2}, \dots, y_{t_N}\}$ **do**
- 11: $\tilde{y}_{t_1}(i) = \tilde{y}_{t_1}(i) + f^b(S(y_t(i), y_{t'}(j))) y_t(i)$; (Eq. 4.4)
- 12: $\tilde{L}_{t_1}(i) = \tilde{L}_{t_1}(i) + f^b(S(y_t(i), y_{t'}(j))) L_t$
- 13: **end for**
- 14: $\tilde{y}_{t_1}(i) = \tilde{y}_{t_1}(i) / \tilde{L}_{t_1}(i)$; (Eq. 4.4)
- 15: **end for**

—————**Step 2 (Spatial step):**—————

- 16: denoise $\tilde{y}_{t_1}(i)$ using Eq. (4.7) and (4.8) in Section 4.2.2. This denoising step is similar to the PPB approach.

- 17: **return** Denoised result \hat{u}_{t_1} ;
-

on the combination of GLR similarity from \tilde{y}_t and KL similarity from previous denoised image, as given by:

$$w(i_t, j_{t'}) = \exp\left(\frac{S_{\text{GLR}}(\tilde{\mathbf{y}}_t(i), \tilde{\mathbf{y}}_t(j))}{h} + \frac{S_{\text{KL}}(\hat{\mathbf{u}}_t(i), \hat{\mathbf{u}}_t(j))}{h'}\right). \quad (4.8)$$

The parameters h and h' are also selected by the α -quantile of the pure distribution of S_{GLR} and S_{KL} in image \tilde{y}_t . Algorithm 1 summarizes the steps to denoise temporal SAR images by the proposed 2S-PPB method.

4.3 Experiments of denoising

For all the following experiments, we use the parameters as suggested by Deledalle *et al.* in Deledalle et al. [2009]. The search window Ω and patch size K enlarge with the increase of the number of iterations, $\Omega \in \{3 \times 3, 7 \times 7, 11 \times 11, 21 \times 21\}$ and $K \in \{1 \times 1, 3 \times 3, 5 \times 5, 7 \times 7\}$ for all experiments.

The experiments are taken under the MATLAB environment on an Intel(R) Core(TM)2 Quad CPU Q9550@2.83GHz 64bit computer. The consuming time of the proposed method

is about 400s¹ for a 3-date 256×256 temporal image set (PPB needs about 15s for a 256×256 image).

4.3.1 Synthetic Images

We present visual and numerical results obtained on synthetic images corrupted by multiplicative Goodman’s speckle noise. Classical noise-free images are used: *house*, *lena*, *barbara*, *boat* and *peppers*. We use the same noise-free image to synthesize a temporal image set, which means there is no temporal changes and that the pixels are fully decorrelated (no interferometric correlation). Besides the proposed 2S-PPB filter, the comparisons that have been tested here are PPB only on single image y_{t_1} (Method **i**: PPB), 3D adaptive neighborhood filter (3D-ANF, it is self-implemented) Ciuc et al. [2001] on the multi-temporal image set $\{y_{t_1}, \dots, y_{t_N}\}$ and Temporal PPB on the multi-temporal image set $\{y_{t_1}, \dots, y_{t_N}\}$ (Method **ii**: T-PPB). For the 3D-ANF filter, we use 3×3 median filter in the first step of 3D-ANF and 50×50 as the maximum size of adaptive neighborhood in the last step of 3D-ANF.

Fig.4.7 only shows the denoising results of the *house* images corrupted by $L = 1$ multiplicative speckle noise. There are 3 noisy images in the temporal data set. The image obtained by the T-PPB filter are well smoothed compared with the PPB filter. However, the edge and shape preservation has limited improvement. The proposed 2S-PPB filter provides more details of edges as the eaves and windows of *house*, while smooth regions are comparable. 3D-ANF has less loss of structural information in stable cases (shown in the ratio map in Fig.4.7.b), while it has poor noise reduction in homogeneous regions.

To quantify the denoising qualities, Tab. 4.1 presents numerical results for images corrupted by multiplicative speckle noise with different number of looks $L = 1, 3, 5$ and 10 and different number of dates (different number of images in temporal data set) $N = 1, 2, 3$ and 5. Note that when $N = 1$, there are no T-PPB and 2S-PPB denoising results. The used performance criterion is the signal to noise ratio (SNR) given by Eq.(3.51). We observe that the 2S-PPB filter improves on the T-PPB filter for high noise level images (i.e. $L = 1$), particularly when N is large. However, for low noise level images (i.e. $L > 5$), 2S-PPB has only limited improvement. This is because the similarity of noisy patches in low noise level images is efficient enough, and the improvement of patch similarity using temporal average is relatively less important.

4.3.2 Realistic SAR Synthetic Images

This part presents denoising results of realistic SAR synthetic images. It is a 100-look SAR acquisition identified as *Toulouse* of the CNES in Toulouse (France) sensed by RAMSES and provided by the CNES. We corrupt this 100-look *Toulouse* image by 1-look multiplicative speckle noise to form 3 temporal images $\{y_{t_1}, y_{t_2}, y_{t_3}\}$. In order to simulate the changes in the multi-temporal images, a dark *line* and a bright *target* are added to y_{t_1} , labeled by red rectangles (Region #1 and #2) in Fig.4.9.a. y_{t_2} and y_{t_3} are corrupted by different multiplicative speckle noise without the dark *line* and the bright *target* (Fig.4.9.e and i). Note again that in this case the temporal pixels are decorrelated.

Fig.4.9 presents the obtained denoising results for the *Toulouse* images. The results of the proposed 2S-PPB filter have better edge and shape preservation with comparable

¹This time consumption contains the computation of parameters, such as h^b , h'^b , h and h' . If these parameters have been obtained, the time consumption is about 50s.

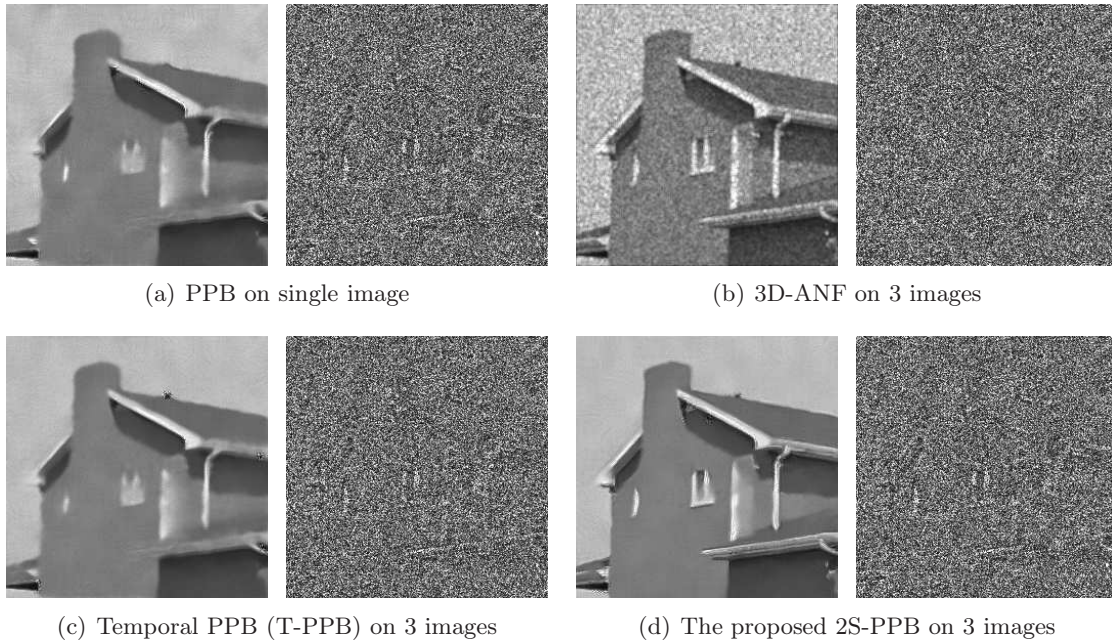


Figure 4.7: Denoising results for the *house* images corrupted by multiplicative speckle noise with $L = 1$. From left to right: the denoising results and the ratio of noisy image to the denoised image. (a) PPB filter; (b) 3D-ANF, (c) T-PPB filter; (d) the proposed 2S-PPB filter.

smoothed regions than PPB and T-PPB filters (ENL in Tab.4.2). Structural information of new objects (changes) is also better preserved as shown in Fig.4.9.a (Region #1 and #2). Stable objects, as the dark lines in Region #3 and #4, have been better restored in the results of 2S-PPB than PPB and T-PPB filters.

4.3.3 Real Multi-Temporal SAR Images

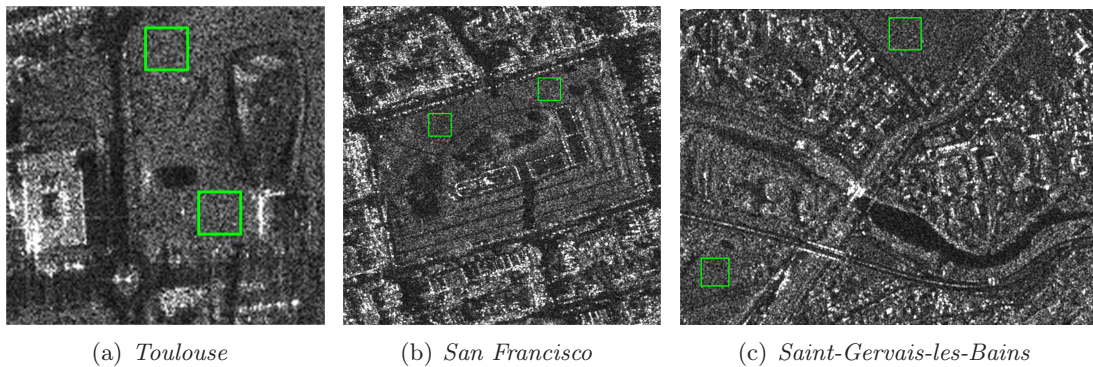


Figure 4.8: *Toulouse*, *San Francisco* and *Saint-Gervais-les-Bains* noisy images (regions in green rectangles are used to calculate the ENL values).

We also tested 2S-PPB on real multi-temporal SAR data:

- *San-Francisco* (well-registered) ©IGARSS: 6 single-look TerraSAR images of San

<i>peppers</i>					<i>barbara</i>				
	$L = 1$	$L = 3$	$L = 5$	$L = 10$		$L = 1$	$L = 3$	$L = 5$	$L = 10$
$N = 1$	10.39 6.58	13.21 9.08	14.29 10.07	15.81 10.97	$N = 1$	10.71 6.58	13.47 8.88	14.89 9.68	16.69 10.39
$N = 2$	8.16 10.43 11.51	10.35 13.68 13.73	10.97 14.99 14.69	11.52 16.80 16.20	$N = 2$	8.15 11.00 12.15	9.91 13.91 14.53	10.38 15.02 15.53	10.79 16.62 16.79
$N = 3$	9.09 11.33 12.15	10.86 13.99 14.48	11.32 15.37 15.52	11.73 17.19 16.84	$N = 3$	8.91 11.77 13.10	10.29 14.41 15.06	10.68 15.60 15.99	10.95 17.29 17.40
$N = 5$	10.03 11.87 12.99	11.32 14.45 15.20	11.62 15.74 16.25	11.90 17.73 17.62	$N = 5$	9.68 12.29 13.97	10.65 14.77 15.83	10.89 15.89 16.78	11.06 18.28 18.16
<i>lena</i>					<i>boat</i>				
	$L = 1$	$L = 3$	$L = 5$	$L = 10$		$L = 1$	$L = 3$	$L = 5$	$L = 10$
$N = 1$	12.37 6.89	14.83 10.64	16.05 12.32	17.60 14.18	$N = 1$	9.50 6.01	11.61 9.15	12.62 10.39	14.14 11.77
$N = 2$	9.29 12.90 13.31	12.81 15.21 15.63	14.23 16.60 16.70	15.66 17.81 18.07	$N = 2$	8.01 9.75 10.75	10.78 11.87 12.75	11.77 13.29 13.76	12.66 15.25 15.22
$N = 3$	10.62 13.28 14.14	13.93 15.59 16.13	15.11 16.77 17.18	16.32 18.07 18.63	$N = 3$	9.12 9.99 11.05	11.59 12.62 13.39	12.32 13.89 14.34	13.00 15.67 15.78
$N = 5$	12.26 13.37 14.80	15.11 15.82 16.89	16.07 16.80 17.94	16.86 18.91 19.18	$N = 5$	10.41 10.97 12.37	12.34 12.78 14.21	12.86 14.27 15.24	13.35 16.41 16.50

Table 4.1: SNR value of estimated images using PPB, 3D-ANF, T-PPB and 2S-PPB filter for images corrupted by multiplicative speckle noise with different equivalent numbers of looks $L = 1, 3, 5, 10$ and different numbers of images $N = 1, 2, 3, 5$ in temporal data set.

Francisco (USA) provided by IGARSS Fusion Contest 2012 (three images are sensed in 2007 and the other three in 2011).

- *Saint-Gervais-les-Bains* (well-registered): 26 single-look TerraSAR images in Saint-Gervais-les-Bains (France) Terra-SAR-X images (project MTH0232) (13 images are sensed in 2009 and the other 13 images in 2011).

Both of them have been finely registered using the sensor parameters.

We assessed the performance of noise reduction in real SAR images by measuring the equivalent number of looks (ENL) given by Eq.(3.53). The denoising results are shown in Fig.4.10. Compared with PPB and T-PPB filters, 2S-PPB filter reduces the speckle effect comparably in *San-Francisco* (well-registered). Moreover, dark and thin streets have been better preserved.. We also compare the 2S-PPB filter with the classical temporal filtering method, multi-looking approach in *Saint-Gervais-les-Bains*. Generally, 2S-PPB filter gets smoother results than multi-looking,, as the Region #1 in Fig.4.10.c and d. More than that, the changes over time can be restored by 2S-PPB, as the changes in the Region #2 in Fig.4.10.c and d. Multi-looking ignores the temporal changes (loss of temporal

resolution), while 2S-PPB filter can well preserve both the spatial and temporal resolution and reduce the speckle effect. Tab.4.2 shows the ENL calculated in homogeneous regions (green rectangles in Fig.4.8). In general, the proposed filter has higher ENL than other filters.

4.4 Extension of 2S-PPB for miss-registered images

The two-step multi-temporal NLM proposed in previous section deals with multi-temporal SAR images which have been finely registered. However in practice, it is not always easy to get accurately registered images, because of the lack of accuracy of sensor parameters or of terrain deviation. In this section, we propose an adaptation of the two-step multi-temporal NLM to deal with miss-registered temporal SAR images. We assume that there is a coarse registration between images, but that a residual offset for each pixel may exist ².

4.4.1 Estimation of miss-registration

From the simple comparison experiment in section 4.1.1, we have seen that the direct extension of 2-D denoising approaches to well-registered temporal SAR images is not optimal. Hence, unlike in Buades et al. [2008], we try to consider the *offset* caused by miss-registration between temporal SAR images using patch similarity. This offset between remote sensing SAR images caused by miss-registration is much simpler than the complex scenes changes in video. Besides, our aim is not accurate registration, but only accurate detection of similar pixels to perform temporal averaging.

Let y_t and $y_{t'}$ denote two temporal images without registration, and $y_t(i)$ and $y_{t'}(i)$ are the i -th pixel in y_t and $y_{t'}$ respectively. Note that $y_t(i)$ and $y_{t'}(i)$ are both located at i in images, but they do not denote the same position in the geographic coordinate system before image registration. Suppose that $y_{t'}(i + \vec{v}_{tt'}(i))$ is the $[i + \vec{v}_{tt'}(i)]$ -th pixel in $y_{t'}$ which shares the same geographic location with $y_t(i)$ in y_t , and $\vec{v}_{tt'}(i)$ denotes the offset between $y_t(i)$ and $y_{t'}(i + \vec{v}_{tt'}(i))$. If no change takes place, $y_{t'}(i + \vec{v}_{tt'}(i))$ should be the most similar pixel of $y_t(i)$ in image $y_{t'}$. Consequently, the idea to estimate this offset

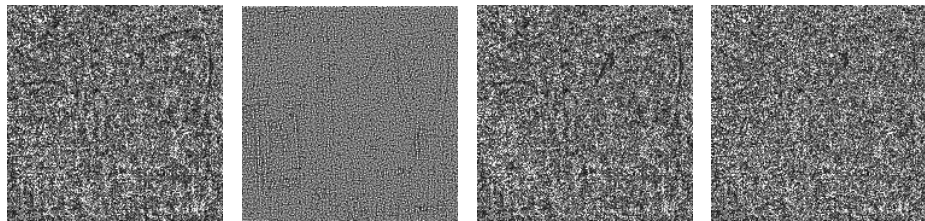
²As it was the case for the *San Francisco* data set of the data fusion contest IGARSS 2012, in section 4.3.3

Table 4.2: ENL of **noisy images** and estimated images using **PPB**, **3D-ANF**, **T-PPB** and **2S-PPB** filters for real SAR images.

ENL	<i>Toulouse</i>	<i>San Francisco</i>	<i>Saint-Gervais-les-Bains</i>
	0.83	0.94	0.93
Left green Region in Fig.4.8	56.97	41.87	41.48
	13.37	10.70	10.79
	89.81	52.31	54.99
	66.78	65.15	497.25
	0.85	0.97	0.92
Right green Region in Fig.4.8	169.90	16.44	8.79
	21.73	11.78	5.83
	252.33	38.31	13.58
	328.61	69.38	190.08



(a) Image y_{t_1} (1-look). From left to right: noisy image, PPB result, 3D-ANF result, T-PPB result and 2S-PPB result.



(b) Ratio map of noisy images to denoised images in a. From left to right: PPB, 3D-ANF, T-PPB and 2S-PPB.

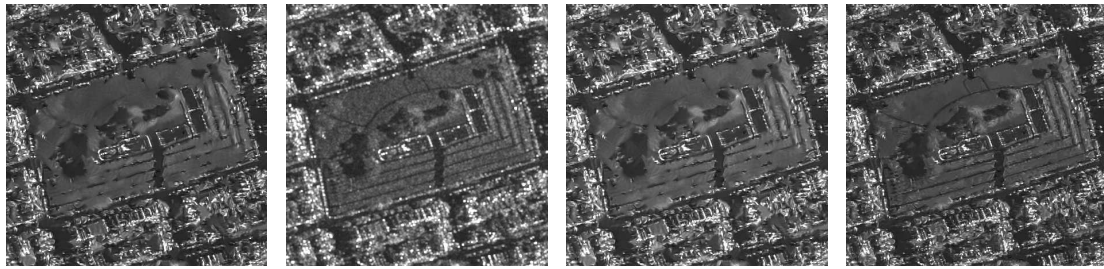


(c) Noisy image y_{t_2} (1-look). From left to right: noisy image, PPB result, 3D-ANF result, T-PPB result and 2S-PPB result.

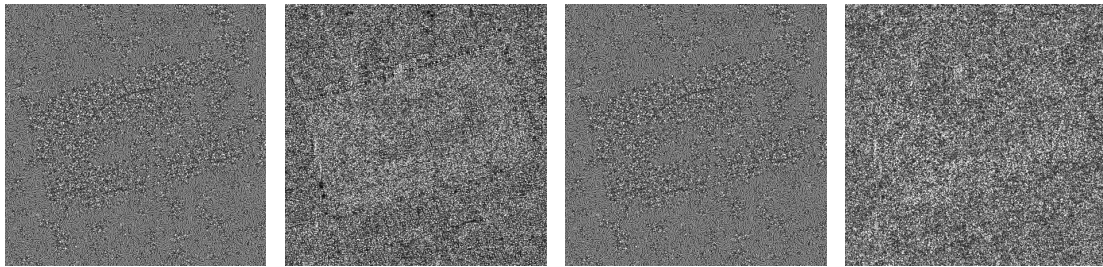


(d) Noisy image y_{t_3} (1-look). From left to right: noisy image, PPB result, 3D-ANF result, T-PPB result and 2S-PPB result.

Figure 4.9: Denoising results on a zoom of *Toulouse* ©DGA ©ONERA. From left to right, noisy image with 1-look multiplicative speckle noise, results by PPB on single image, results by 3D-ANF on temporal images, results by T-PPB on temporal images, results by 2S-PPB on temporal images. From top to bottom, image y_{t_1} with new objects (a dark *line* in Region #1 and a bright *target* in Region #2), ratio maps of noisy images to denoised images, image y_{t_2} without new objects, image y_{t_3} without new objects.



(a) *San Francisco* denoising results. From left to right: PPB on single image, 3D-ANF, T-PPB and 2S-PPB



(b) Ratio map of *San Francisco* images. From left to right: PPB on single image, 3D-ANF, T-PPB and 2S-PPB



(c) *Saint-Gervais-les-Bains* images. From left to right: noisy image, denoising result by multi-looking, denoising results by PPB on single image.



(d) *Saint-Gervais-les-Bains* images. From left to right: 3D-ANF, denoising result by T-PPB on temporal images, denoising results by 2S-PPB on temporal images.

Figure 4.10: Denoising results of well-registered *San Francisco* ©IGARSS and *Saint-Gervais-les-Bains*. (a) *San Francisco* denoising results. From left to right: PPB on single image, 3D-ANF, T-PPB and 2S-PPB, (b) Ratio map of *San Francisco* images. From left to right: PPB on single image, 3D-ANF, T-PPB and 2S-PPB, (c) *Saint-Gervais-les-Bains* images. From left to right: noisy image, denoising result by multi-looking, denoising results by PPB on single image, (d) *Saint-Gervais-les-Bains* images. From left to right: 3D-ANF, denoising result by T-PPB on temporal images, denoising results by 2S-PPB on temporal images. Stable region #1 in *Saint-Gervais-les-Bains* and changed region #2 in *Saint-Gervais-les-Bains*.

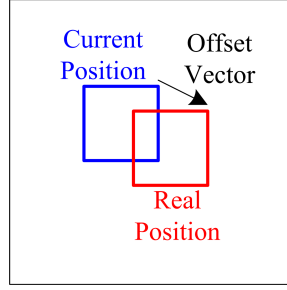


Figure 4.11: Assumption of image registration. In the intensity images registration, all pixels in a small patch share a same offset to their real position.

$\vec{v}_{tt'}(i)$ caused by miss-registration is to use the pixel similarity, supposing that changes are quite 'rare' on the image.

Using the conclusion of Section 4.2.1, we combine the KL divergence and the GLR criterion as the similarity between patches, as given by Eq. (4.3). Note that this KL divergence criterion is computed from the PPB denoising results on each image. For each pixel $y_t(i)$ in y_t , we measure the similarity between $y_t(i)$ and pixels in region $A_{t'}(i)$ (an image patch with $y_{t'}(i)$ as center in $y_{t'}$, shown in Fig.4.12). The similarity between $y_t(i)$ and $y_{t'}(j)$ is $d_{1st}(i_t, j_{t'})$. Each pair of pixel $y_t(i+n)$ in y_t and region $A_{t'}(i+n)$ in $y_{t'}$ has a similarity map $M_{tt'}(i+n)$ ($0 \leq n \leq N_A - 1$, N_A is the size of the region A), as shown in the top right of Fig.4.12.

$$M_{tt'}(i) = \{S(y_t(i), y_{t'}(j))\}_{j_{t'} \in A_{t'}(i)} , \quad (4.9)$$

where $S(y_t(i), y_{t'}(j))$ is given by Eq.(4.3).

The offset $\vec{v}_{tt'}(i)$ should be the offset between the center of map $M_{tt'}(i)$ and the position of maximum value in $M_{tt'}(i)$. However, it leads to a poor performance because of noise. Based on the assumption in Fig.4.11, we suggest that the offset $\vec{v}_{tt'}(i)$ caused by miss-registration can be estimated from an average similarity map $\bar{M}_{tt'}(i)$, which is the mean of similarity maps $M_{tt'}(i+n)$ ($1 \leq n \leq N_A$). The estimation of offset $\vec{v}_{tt'}(i)$ is from the center of map $\bar{M}_{tt'}(i)$ to the position of maximum value in $\bar{M}_{tt'}(i)$.

$$\begin{aligned} \bar{M}_{tt'}(i) &= \{\bar{S}(y_t(i), y_{t'}(j))\}_{j_{t'} \in A_{t'}(i)} \\ \bar{S}(y_t(i), y_{t'}(j)) &= \sum_{i_t \in A_t(i)} S(y_t(i), y_{t'}(j)) \end{aligned} \quad (4.10)$$

We test the miss-registration estimation on real SAR images. Fig.4.14.(b) is the temporal average without fine image registration or miss-registration estimation, which is blurred. After miss-registration estimation, the temporal average is illustrated in Fig.4.14.(c).

4.4.2 Two-steps non-local means on miss-registered images

The miss-registration estimation entitles the proposed 2S-PPB denoising approach to deal with miss-registered multi-temporal images. The denoising process is exactly the same as detailed in Section 4.2, except that the candidate pixels $y_{t'}(i)$ are replaced by $y_{t'}(i + \vec{v}_{tt'}(i))$ found out by the miss-registration estimation. Algorithm 2 summarizes the steps to denoise miss-registered temporal SAR images by the proposed 2S-PPB method.

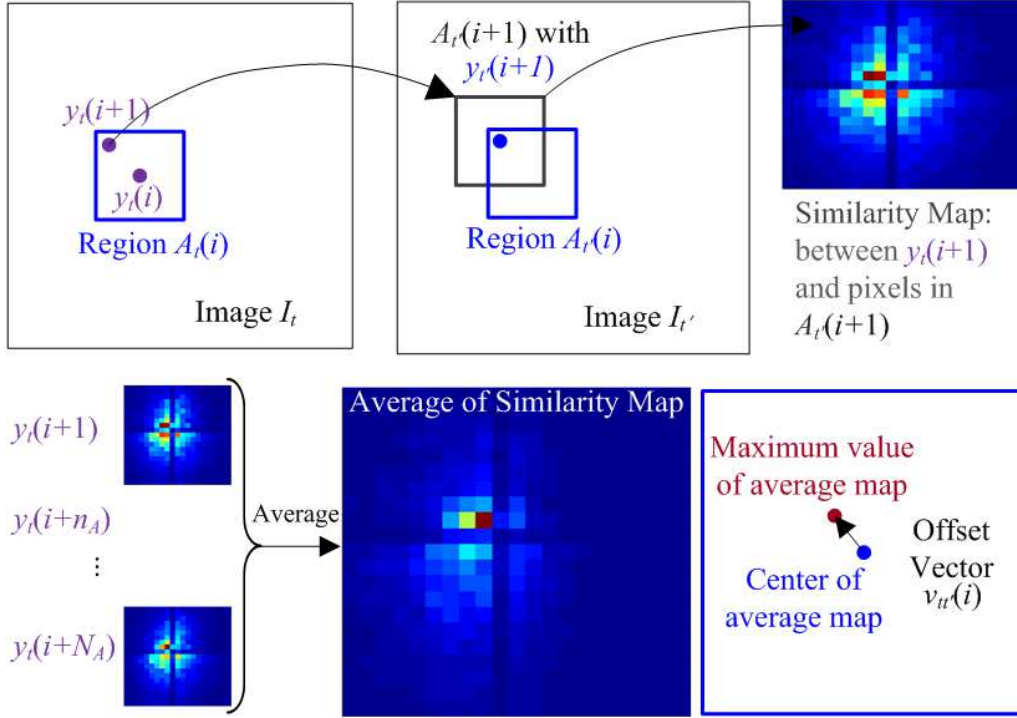


Figure 4.12: The sketch map of the miss-registration estimation for miss-registered images.

4.4.3 Experiments of denoising on miss-registered images

We compare our offset estimation with the offset estimation using the intensity tracking method. Intensity tracking with correlation has been widely used in glacier motion estimation tasks on multi-temporal SAR images Gray et al. [2001], Strozzi et al. [2002]. In this comparison experiment, we simulate a multi-temporal image set with an offset $\vec{v}_{tt'} = (3, 3)$ pixels between them, as shown in Fig.4.13.a and b.

For the offset estimation using the intensity tracking, it is self-implemented in our comparison experiments and it also has a local averaging process like the one in the proposed method to reduce the effect of speckle noise. The patch size is 7×7 pixels and the test area is 21×21 pixels. To illustrate the performances, the estimation error is calculated using the Euclidean distance between the true offset $\vec{v}_{tt'} = (3, 3)$ and the estimated offset. Fig.4.13.c and d show that the proposed offset estimation has less estimation error than the log-ratio similarity.

The real temporal SAR images provided by IGARSS (data information in section 4.3) are tested here. The difference is that we manually coarsely register those temporal images without using the accurate sensor parameters. The miss-registration between two images is about 4~7 pixels (shown in Fig4.14.b, the temporal mean of the temporal images illustrates the un-registration). These miss-registered temporal images are identified as *San-Francisco* (miss-registered). In the miss-registration estimation, the search region $A_t(i)$ is a 21×21 pixels window. Patch size is 7×7 pixels, h and h' have been chosen identical to the filtering step. After miss-registration estimation, the proposed 2S-PPB filter is applied with the same parameters as those used in Section 4.3.

The temporal mean after miss-registration estimation in Fig.4.14.c shows the performance of the miss-registration estimation. Similarly, for the thin and dark streets in

Algorithm 2 The proposed 2S-PPB algorithm (Un-registered temporal images).

Input:

Un-registered temporal SAR images $\{y_{t_1}, y_{t_2}, \dots, y_{t_N}\}$.
 A date t_1 of interest.

Output:

\hat{u}_{t_1} : the denoising results of image y_{t_1} .

—————**Miss-Registration estimation:**—————

- 1: **for** each y_t in $\{y_{t_1}, y_{t_2}, \dots, y_{t_N}\}$ **do**
- 2: denoise y_t using PPB approach; (Section 3.3)
- 3: obtain pre-denoised results \hat{u}'_t ;
- 4: **end for**
- 5: **for** each pixel index i **do**
- 6: **for** each image y_t in $\{y_{t_1}, y_{t_2}, \dots, y_{t_N}\}$ **do**
- 7: $\bar{M}_{t_1 t}(i) = 0$;
- 8: **for** each pixel index $i + n$ in region $A_{t_1}(i)$ **do**
- 9: compute similarity map $M_{t_1 t}(i + n)$; (Eq. 4.10)
- 10: $\bar{M}_{t_1 t}(i) = \bar{M}_{t_1 t}(i) + M_{t_1 t}(i + n)$;
- 11: **end for**
- 12: find the offset vector $\vec{v}_{t_1 t}(i)$ in similarity map $\bar{M}_{t_1 t}(i)$;
- 13: **end for**
- 14: **end for**

—————**Step 1 (Temporal step):**—————

- 15: compute \tilde{y}_{t_1} using Eq. (4.2), (4.4) by taking into account the vector field $\vec{v}_{t_1 t}$. This denoising step is similar to the one in Algorithm 1 where i_t is substituted to $i_t + \vec{v}_{t_1 t}(i)$.

—————**Step 2 (Spatial step):**—————

- 16: denoise $\tilde{y}_{t_1}(i)$ using Eq. (4.7) and (4.8) in Section 4.2.2. This denoising step is similar to the PPB approach.

- 17: **return** Denoised result \hat{u}_{t_1} ;
-

San-Francisco (miss-registered), the proposed 2S-PPB preserves more details than PPB and T-PPB. However, its performance is not as good as the one on well-registered *San-Francisco* (in Fig.4.14.f), because of the insufficient estimation of miss-registration. In addition, the miss-registration estimation will fail when the offset between temporal images is too large. Indeed larger offset estimation needs larger search region $A_t(i)$, but this increases the risk of finding wrong similar pixels.

4.5 Conclusion

A spatial-temporal filter was proposed for the estimation of same-sensor, same-incidence and same-ascending/descending multi-temporal SAR images. It is an extension of the non local means [Buades et al., 2005a] and patch-based weighted maximum likelihood estimation (PPB) [Deledalle et al., 2009]. We proposed to deal with the spatial and temporal information respectively: 1) the first step (the temporal step) averages the similar pixels only in the temporal domain with binary weights; 2) the second step (the spatial step) ap-

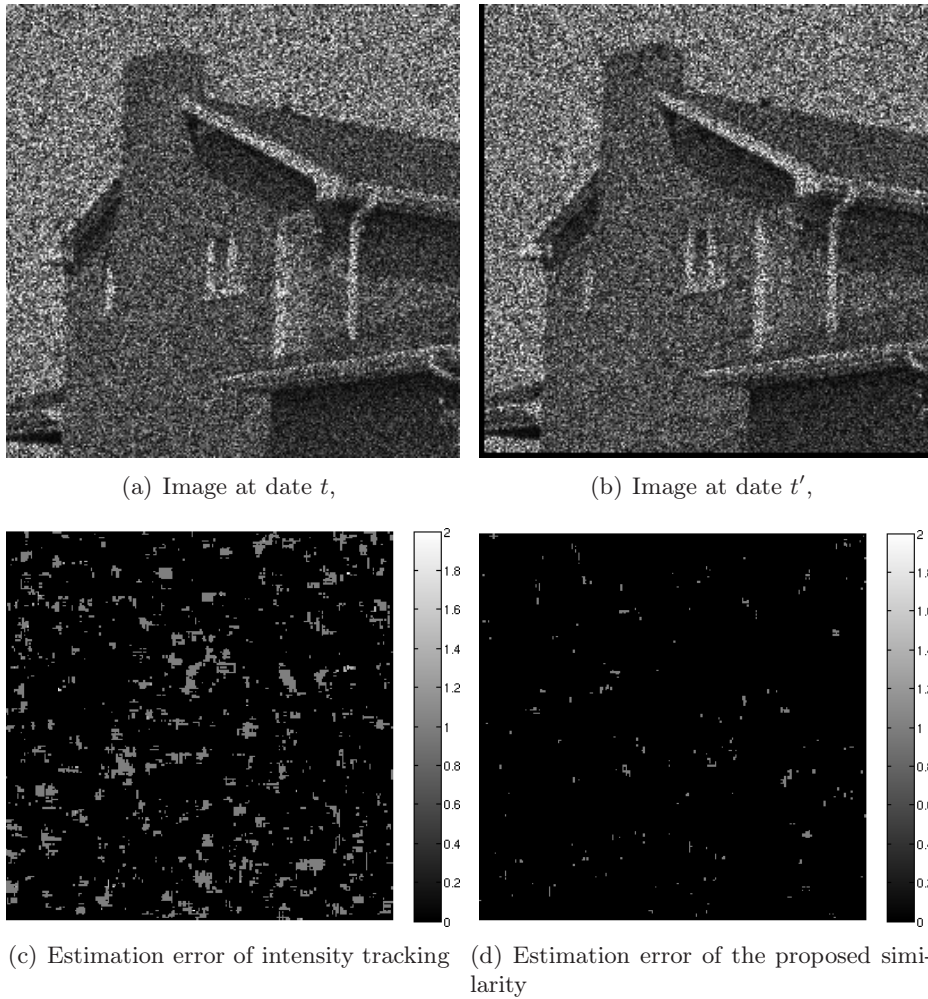
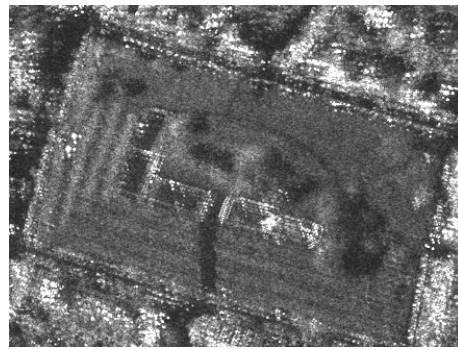


Figure 4.13: Offset estimation. a) Noisy image 1, b) Noisy image 2 (with an offset $\vec{v}_{tt'} = (3, 3)$ with image 1), c) Estimation error of intensity tracking [Gray et al., 2001, Strozzi et al., 2002] (the distance between intensity tracking offset estimation results and the true offset $\vec{v}_{tt'} = (3, 3)$), d) Estimation error of the proposed similarity (the distance between the proposed offset estimation results and the true offset $\vec{v}_{tt'} = (3, 3)$).

plies the PPB filter with more general expression of similarity criteria (the GLR similarity and KL divergence). The proposed filter out-performs the state-of-the-art spatial-temporal SAR filters. This is the first contribution of this PhD and has been published in [Su et al., 2012, 2014b]. We have also extended the proposed framework to the case of miss-registered images by adding an offset estimation set. In the next part of this PhD, we will focus on the change detection and classification of multi-temporal SAR images, in which the proposed 2S-PPB filter will be used.

(a) y_{t1} , One of the noisy images (1-look)

(b) Temporal average without miss-registration estimation



(c) Temporal average with miss-registration estimation



(d) Temporal PPB (T-PPB) using 6 miss-registered SAR images



(e) The proposed 2S-PPB (with miss-registration estimation) using 6 miss-registered SAR images



(f) The proposed 2S-PPB using 6 well-registered SAR images

Figure 4.14: Denoising results of miss-registered *San Francisco* ©IGARSS. (a) y_{t1} , one of the noisy images (1-look); (b) the temporal average of the multi-temporal SAR images, which shows that the temporal images are miss-registered; (c) the temporal average of the multi-temporal SAR images after miss-registration estimation; (d) denoising results by T-PPB on miss-registered temporal images; (e) denoising results by 2S-PPB on miss-registered temporal images; (f) denoising results by 2S-PPB on well-registered temporal images.

Part II

Information Change Analysis: Change Detection and Change Classification (NORCAMA)

Chapter 5

State of the Art of Change Analysis

The second issue concerned in this thesis is change analysis of multi-temporal SAR images. It is a processing required by many applications using SAR images, such as rapid mapping of disaster, land-use and land-cover monitoring and so on. One of the main topics of change analysis is change detection, which is defined as "a process of identifying differences in the state of an object or phenomenon by observing it at different times" [Singh, 1989]. Given different modes of images (i.e. optical images, SAR images), different algorithms of change detection have been defined. Beyond detecting changes, other interesting research topics, e.g. change classification, long-term series change detection and analysis, are also introduced in this chapter.

5.1 General methods of change detection

Change detection in remote sensing images is the process of identifying differences in regions of interest by observing them at different dates [Singh, 1989]. In spite of different types of images used for change detection, a general architecture of change detection can be built as shown in Fig.5.1. Used input images are first pre-processed, e.g. radiometric cor-

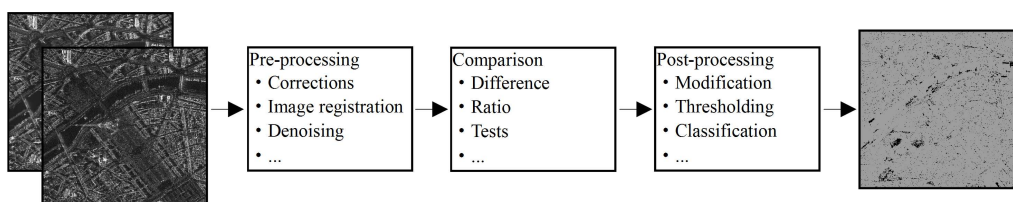


Figure 5.1: The general architecture of change detection process.

rection, geometric correction, image registration, noise reduction etc. Then, the improved images are compared using various criteria. To get the final change detection results, the comparison criteria usually are binarized by a threshold or machine learning methods. The image registration in pre-processing steps can be suppressed (or reduced) when using criteria robust to registration errors. In this section, we just focus on the comparison and the thresholding parts.

Due to the difference in statistics, we divided the following section for optical and SAR data. We suppose that the data have been finely registered ¹ and from the same sensor.

¹Concerning the registration of data, significant progress have been done using the accuracy of sensor

However, change analysis using multi-modality images (especially images from different sensors) has also been studied in the domain of data fusion. Nevertheless, difficulties lie in the geometric and radiometric differences (or distortions), image registration and so on. In this PhD we just focus on the data from the same sensor.

5.1.1 Change criteria for optical images

Difference operator

1) *Single channel case.* The most widely used comparison between two images is difference operator, which is close to the difference similarity presented in section 3.3.1. Let us consider two candidate pixels $y(1)$ and $y(2)$, which could be any pair of pixels $y_t(i)$ and $y_{t'}(i)$ in two co-registered images y_t and $y_{t'}$. The difference between them can be written as following:

$$D_d = y(1) - y(2) + C, \quad (5.1)$$

where C is a constant to produce positive results of D_d ($C = -\min(y(1) - y(2))$). Fig.5.2 gives an illustration of the difference operator using synthetic images with Gaussian noise and Gamma noise. [Coppin and Bauer, 1994, Gianinetto and Villa, 2011] proposed to normalize the difference D_d to $[-1, 1]$. They calculate the difference as following:

$$D_{Nd} = \frac{y(1) - y(2)}{y(1) + y(2)}, \quad (5.2)$$

where value 0 denotes unchanged case, value -1 or 1 indicates the changed case (increase and decrease of reflectivity respectively).

In the regression methods of change detection, value $y(2)$ is assumed to be a linear function of $y(1)$. $y(1)$ is also considered as *reference* pixel and $y(2)$ is a *subject* pixel. The least-squares regression, one of the popular regression methods, *estimates* $y(2)$ by:

$$\hat{y}(2) = ay(1) + b, \quad (5.3)$$

where a and b are estimation parameters, which can be learned from the un-changed areas and constant in the whole image. Then, the change index D_{Rd} is calculated by subtracting regressed pixel $\hat{y}(2)$ from the observed pixel $y(2)$ [Lunetta et al., 1999]:

$$D_{Rd} = y(2) - \hat{y}(2). \quad (5.4)$$

This criterion will be useful to reduce the impact of atmospheric, sensor and environmental differences.

2) *Multi-channel case.* When dealing with multi-temporal or hyperspectral data, a vector is available. A first category of approaches, especially dealing with vegetation, first converts this vector in a useful scalar and then applies the previous one-channel criteria. In particular, vegetation indices are designed to evaluate the impact of vegetation in multi-spectral images $\{y_t^{b1}, y_t^{b2}, \dots\}$ at time t and $\{y_{t'}^{b1}, y_{t'}^{b2}, \dots\}$ at time t' (b is the index of band). Usually, only two bands in the multi-spectral images are used, which are the red band the

parameters. For the same sensor like TerraSAR-X, very accurate registrations can be obtained.

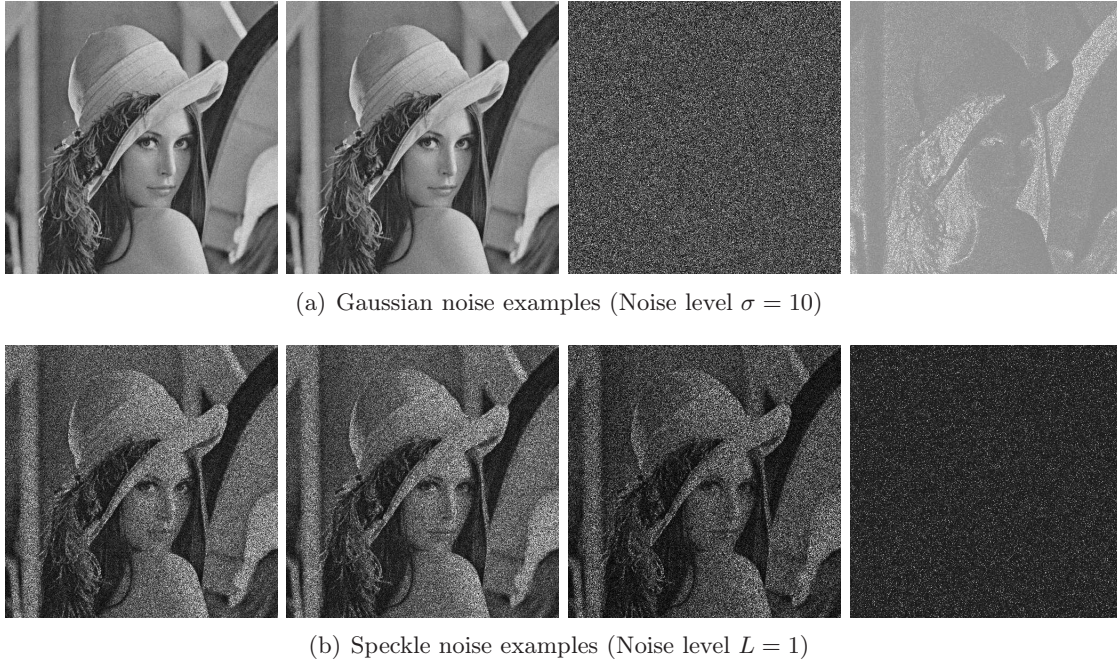


Figure 5.2: The difference operator and the ratio operator. From left to right, the noisy image y_t and $y_{t'}$ with $\sigma = 10$ Gaussian noise or $L = 1$ speckle noise, the difference map using Eq.(5.1) between y_t and $y_{t'}$, the ratio map using Eq.(5.8) between y_t and $y_{t'}$. There is no change between y_t and $y_{t'}$, thus the change criteria map should reflect only the noise contribution.

near-infrared band (denoted as y_t^{red} and y_t^{near}). Vegetation indices y_t^{VI} are calculated from y_t^{red} and y_t^{near} given by (taking the images at time t as example):

$$\begin{aligned}
 y_t^{\text{VI}}(i) &= \frac{y_t^{\text{near}}(i)}{y_t^{\text{red}}(i)} && \text{Ratio vegetation index,} \\
 y_t^{\text{VI}}(i) &= \frac{y_t^{\text{near}}(i) - y_t^{\text{red}}(i)}{y_t^{\text{near}}(i) + y_t^{\text{red}}(i)} && \text{Normalized vegetation index,} \\
 y_t^{\text{VI}}(i) &= \sqrt{\frac{y_t^{\text{near}}(i) - y_t^{\text{red}}(i)}{y_t^{\text{near}}(i) + y_t^{\text{red}}(i)}} + 0.5 && \text{Transformed vegetation index.}
 \end{aligned} \tag{5.5}$$

Then, the changes can be detected on the difference of vegetation indices y_t^{VI} and $y_{t'}^{\text{VI}}$:

$$D_{\text{VI}d} = y_t^{\text{VI}}(i) - y_{t'}^{\text{VI}}(i), \tag{5.6}$$

or other comparison methods such as Eq.(5.2) and Eq.(5.4). Based on the ratio vegetation index and normalized vegetation index, Unsalan [2007] recently proposed a bi-temporal time-dependent vegetation indices.

More generally, the second family of approaches exploits all the bands in the multi-spectral images for change detection. For instance Malila [1980] proposed a change vector criterion which calculates the magnitude and direction of changes. Bovolo and Bruzzone [2007] improved this idea and introduced a more theoretical definition of changes in the polar domain to describe the change information. Given two multi-spectral pixel stacks

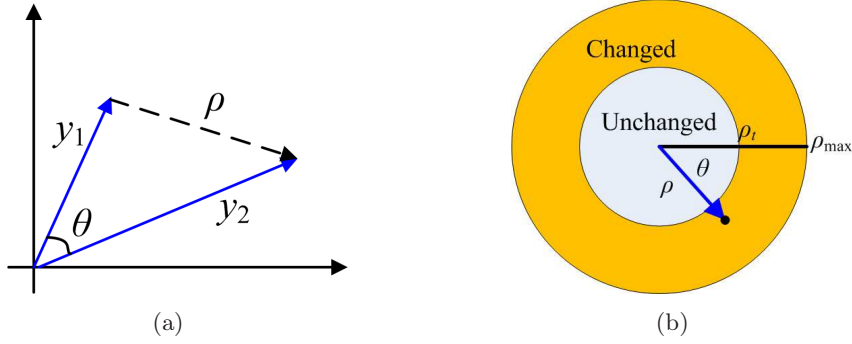


Figure 5.3: Representation of change information in the polar domain. (a) \mathbf{y}_1 and \mathbf{y}_2 in the rectangular coordinate system ($K = 2$); (b) the difference $\{\rho, \theta\}$ between \mathbf{y}_1 and \mathbf{y}_2 in polar domain.

$\{y_t^{b1}(i), y_t^{b2}(i), \dots\}$ and $\{y_{t'}^{b1}(i), y_{t'}^{b2}(i), \dots\}$ acquired at different time, the change vector criterion can be calculated as:

$$\rho = \sqrt{\sum_{k=1}^K (y_t^{bk}(i) - y_{t'}^{bk}(i))^2}$$

$$\theta = \arccos \frac{\sum_{k=1}^K y_t^{bk}(i) y_{t'}^{bk}(i)}{\sqrt{\sum_{k=1}^K y_t^{bk}(i)^2} \sqrt{\sum_{k=1}^K y_{t'}^{bk}(i)^2}} \quad (5.7)$$

ρ is defined by the euclidean distance between both vectors. By analyzing the distribution of changed and unchanged pixels in the polar domain, they propose the disk with $\{\rho, \theta : 0 \leq \rho < \rho_t \text{ and } 0 \leq \theta < 2\pi\}$ as unchanged pixels and the annulus with $\{\rho, \theta : \rho_t \leq \rho < \rho_{\max} \text{ and } 0 \leq \theta < 2\pi\}$ as changed pixels. The quantity of θ denotes the direction information of changes which has been used to classify the changes. In other works, only ρ is computed in some works e.g. [Xian et al., 2009, Xian and Homer, 2010, Demir et al., 2013].

Instead of using accurate angle to present the direction of the changes, Michalek et al. [1993] used a binary array $\{\theta^{b1}, \theta^{b2}, \dots\}$ to denote direction (sector coding), where $\theta^{bk} = -1$ when $y_t^{bk}(i) < y_{t'}^{bk}(i)$ and $\theta^{bk} = 1$ when $y_t^{bk}(i) \geq y_{t'}^{bk}(i)$. Thus $\{\theta^{b1}, \theta^{b2}, \dots\}$ has 2^K possible types of directions. Chen et al. [2003] presented the direction of change vector in the cosine space, given by $\{\frac{y_t^{b1} - y_{t'}^{b1}}{\rho}, \frac{y_t^{b2} - y_{t'}^{b2}}{\rho}, \dots\}$ (since $\frac{y_t^{bk} - y_{t'}^{bk}}{\rho}$ is the cosine value of the angle between the change vector and the k -th axis).

5.1.2 Change criteria for SAR images

Ratio and log-ratio operators

The difference operator has been proved effective in optical images, because of the assumption of additive noise model. However due to the multiplicative noise in SAR images, the ratio operator demonstrates to outperform the difference one in SAR images

[Singh, 1989]:

$$R_R = \frac{y(1)}{y(2)}, \quad (5.8)$$

$$R_{L-R} = \log R_R = \log y(1) - \log y(2).$$

Fig.5.2 gives an illustration of the ratio operator using synthetic noisy images with Gaussian noise and Gamma noise. Transforming the ratio into a subtraction by the logarithmic operation, the log-ratio comparison has also been widely used in SAR image change detection [Rignot and van Zyl, 1993, Bovolo and Bruzzone, 2005, Bazi et al., 2005]. In order to reduce the effect of speckle noise, the ratio or log-ratio of local means in a patch is usually performed instead of the ratio of single pixels. The ratio operator can be normalized by $R_R = \min \left\{ \frac{y(1)}{y(2)}, \frac{y(2)}{y(1)} \right\}$ to gather increase and decrease of radiometric value.

Hypothesis tests

Hypothesis tests have been presented in section 3.3.1 to measure the similarity between patches. However, they can also be used in the change detection task. Let us recall the hypotheses to describe a change detection problem between two observed data $\mathcal{Y}(1)$ and $\mathcal{Y}(2)$ (note that the observed data \mathcal{Y} could just be the noisy pixel value y , or the data set consisting of y and other observed data, i.e. denoised data \hat{u} acquired by our filter): 1) hypothesis of un-changed case, these observed pixels share the same reflectivity $u(1) = u(2) = u(12)$ (underlying noise-free value), 2) hypothesis of changed case, these observed pixels have different underlying reflectivities. They can be given by:

$$\begin{aligned} \mathcal{H}_0 : u(1) = u(2) = u(12) & \quad \text{Unchanged (null) hypothesis;} \\ \mathcal{H}_1 : u(1) \neq u(2) & \quad \text{Changed (alternative) hypothesis.} \end{aligned} \quad (5.9)$$

Eq.(5.9) has the same expression as the Eq.(3.20) but with different meanings. To decide between the changed and unchanged hypotheses, the likelihood ratio test (LRT) can be used, which is given by:

$$\mathcal{R}^{\text{LR}} = \frac{p(\mathcal{Y}(1), \mathcal{Y}(2) | u(12), \mathcal{H}_0)}{p(\mathcal{Y}(1), \mathcal{Y}(2) | u(1), u(2), \mathcal{H}_1)}. \quad (5.10)$$

Compared with the expression given by Eq.(3.20) used for patch comparison in section 3.3.1, Eq.(5.10) is a more general form of likelihood ratio which considers the observed data beyond noisy pixel values. However, when noisy pixel value is the only observed data, the likelihood ratio given by Eq.(5.10) is the same as Eq.(3.20).

As explained in section 3.3.1, due to the lack of knowledge about the noise-free value u , some estimations have to be used instead of the original likelihood ratio. For instance the generalized likelihood ratio is used in [Lombardo and Oliver, 2001], the unknown u being replaced by its maximum likelihood (ML) estimate. Taking a pair of pixels $y(1)$ and $y(2)$ as example, the ML estimate of $u(1)$ is computed in a patch $\mathbf{y}(1)$ (supposing the homogeneity in the patch) and given by $\hat{u}^{\text{ML}}(1) = \frac{1}{K} \sum_k y(1, k)$, while under the unchanged hypothesis, the noise-free value $u(12)$ is estimated using both $\mathbf{y}(1)$ and $\mathbf{y}(2)$ and given by $\hat{u}^{\text{ML}}(12) = \frac{1}{2K} \sum_k y(1, k) + \frac{1}{2K} \sum_k y(2, k)$. In this work, it is supposed that the used patches for ML estimation are homogeneous. Combined with the gamma noise assumption in Eq.(2.12), the *generalized* likelihood ratio can be extended by:

$$\mathcal{R}^{\text{gLR}} = \frac{p(\mathcal{Y}(1), \mathcal{Y}(2) | \hat{u}^{\text{ML}}(12), \mathcal{H}_0)}{p(\mathcal{Y}(1), \mathcal{Y}(2) | \hat{u}^{\text{ML}}(1), \hat{u}^{\text{ML}}(2), \mathcal{H}_1)} \quad (5.11)$$

Eq.(5.11) can be computed by Eq.(3.25), which is given by:

$$\mathcal{R}^{\text{gLR}} = \frac{\sum_k y(1, k) \cdot \sum_k y(2, k)}{(\sum_k y(1, k) + \sum_k y(2, k))^2}, \quad (5.12)$$

However, \mathcal{R}^{gLR} is usually computed by the ratio between the geometric and arithmetic means [Lombardo and Oliver, 2001], which is given by:

$$\mathcal{R}^{\text{gLR}} = \frac{2\sqrt{\sum_k y(1, k) \cdot \sum_k y(2, k)}}{\sum_k y(1, k) + \sum_k y(2, k)}. \quad (5.13)$$

Given multi-temporal SAR images, \mathcal{R}^{gLR} can be calculated by:

$$\mathcal{R}^{\text{gLR}} = \frac{N \sqrt[N]{\prod_n (\sum_k y_{t_n}(i, k))}}{\sum_n \sum_k y_{t_n}(i, k)}. \quad (5.14)$$

When the patch $\mathbf{y}(1)$ is reduced to one pixel (patch size $K = 1$), $\mathcal{R}^{\text{gLR}}|_{K=1} = \frac{N \sqrt[N]{\prod_n y_{t_n}(i)}}{\sum_n y_{t_n}(i)}$. $\mathcal{R}^{\text{gLR}} \in [0, 1]$, value 1 denotes the unchanged case and value 0 is the changed case. The logarithmic version of this generalized likelihood ratio is given by:

$$\mathcal{R}^{\text{L-gLR}}|_{K=1} = \log \mathcal{R}^{\text{gLR}}|_{K=1} = \frac{1}{N} \sum_{t=t_1}^{t_N} \ln y_t(i) - \ln \left(\frac{1}{N} \sum_{t=t_1}^{t_N} y_t(i) \right), \quad (5.15)$$

which has been used in [Bujor et al., 2004] to detect changes. Except using amplitude or intensity values of SAR, PolSAR data also has been used to detect changes with hypothesis test, e.g. Conradsen et al. [2003]. To reduce the speckle noise, Liu et al. [2014] applied a NLM based filter in PolSAR change detection.

Instead of the ratio of the geometric and arithmetic means, Quin et al. [2013] proposed to calculate the ratio of the geometric and quadratic means named MIMOSA, which can be given by (for two pixels):

$$\mathcal{R}^{\text{MIMOSA}} = \frac{\sqrt{y(1)y(2)}}{\sqrt{\frac{y(1)^2 + y(2)^2}{2}}}, \quad (5.16)$$

This ratio has also been extended to multi-temporal SAR images (more than 2 images):

$$\mathcal{R}^{\text{MIMOSA}} = \frac{\sqrt[N]{\prod_{t=t_1}^{t_N} y_t(i)}}{\sqrt{\frac{1}{N} \sum_{t=t_1}^{t_N} y_t(i)^2}}. \quad (5.17)$$

if $N = 2$ (the bi-temporal images case), Eq.(5.17) boils down to Eq.(5.16).

Beyond the likelihood ratio test computed directly on the image pixels, Krylov et al. [2012] proposed to construct a likelihood ratio test on a Wilcoxon statistic W of pixels values, which is calculated from the Wilcoxon rank-sum test [Lehmann and Romano, 2006]. Given two independent pixel values $y(1)$ and $y(2)$, the Wilcoxon rank-sum test verifies two hypotheses:

$$\begin{aligned} \mathcal{H}_0 : p(y(1) < y(2)) &= \frac{1}{2} && \text{Unchanged (null) hypothesis} \\ \mathcal{H}_1 : p(y(1) < y(2)) &\neq \frac{1}{2} && \text{Changed (alternative) hypothesis .} \end{aligned} \quad (5.18)$$

This test is applied in two patches $\mathbf{y}(1)$ and $\mathbf{y}(2)$. All the pixels in patches $\mathbf{y}(1)$ and $\mathbf{y}(2)$ are sorted in ascending or descending order (according to their values). Each pixel $y(1, k)$ in patch $\mathbf{y}(1)$ has a rank number in this ascending order, for instance $r(1, k)$ is the rank number of pixel $y(1, k)$ in patch $\mathbf{y}(1)$ with $1 \leq r(1, k) \leq 2K$. The Wilcoxon statistic W is given by:

$$W = \frac{\sum_k r(1, k) - \frac{K(2K+1)}{2}}{\sqrt{\frac{K^2(2K+1)}{12}}} . \quad (5.19)$$

W converges to the standard normal distribution when the patch size $K \rightarrow \infty$ [Lehmann and Romano, 2006]. Thus W is called as the rank-sum (W can also be computed in patch $\mathbf{y}(2)$). To compare $y(1)$ and $y(2)$, a likelihood ratio test on W verifies the null hypothesis (unchanged case) $W \sim N(\mu_0, \sigma_0^2)$ with an alternative hypothesis (changed case) $W \sim N(\mu_1, \sigma_1^2)$, where μ_0, σ_0^2 are estimated using the whole images and μ_1, σ_1^2 are estimated using the local windows.

Kullback-Leibler divergence

As introduced in section 3.3.1, Kullback-Leibler (KL) divergence has been applied to measure the similarity between two denoised patch in our multi-temporal filter. In probability theory and information theory, KL divergence however is a non-symmetric measure of the difference between two probability distributions. Thus it can also be applied to decide whether two noisy pixels $y(1)$ and $y(2)$ come from the same distribution, which can be considered as a change detection problem. Given the pdfs $p_1(y)$ and $p_2(y)$ describing the probabilities of $y(1)$ and $y(2)$ respectively, the Kullback-Leibler (KL) divergence between pdfs $p_1(y)$ and $p_2(y)$ is given by:

$$D_{\text{KL}} = \int \log \frac{p_1(y)}{p_2(y)} p_1(y) dy + \int \log \frac{p_2(y)}{p_1(y)} p_2(y) dy , \quad (5.20)$$

which has the same expression as the (denoised) patch similarity given by Eq.(3.28) and Eq.(3.35), but dealing with change detection problem. To calculate the divergence D_{KL} , the pdfs $p_1(y)$ or $p_2(y)$ must be known, while they are not in the real situation (because of the unknown model and/or the unknown parameters). When the pdfs are known to belong to a given parametric model, parameters are usually estimated using a moving window. In [Inglada and Mercier, 2007], an analytical expression of the KL divergence is estimated using a fourth-order Taylor-like series Gaussian models. KL divergence criterion has also been applied to the optical images in [Tian et al., 2014]'s work, in which combined with height difference measured by digital surface models, the KL divergence is used to detect building changes in urban areas.

Coherence change detection

Most change detection algorithms with SAR images aims at identifying changes in the mean backscatter power (intensity value of images). Since SAR is a coherent imaging system as explained in chapter 2, the changes may take place not only in the intensity values but also the phase values. Coherent changes are defined as the changes in both intensity and phase of SAR images (incoherent changes are the changes only in intensity) [Preiss and Stacy, 2006]. According to this definition, coherent change detection can detect more subtle changes than incoherent change detection. These approaches can be used only

when dealing with interferometric data where the phase of each pixel can be supposed when computing the hermitian product.

The true underlying complex cross correlation coefficient $D \exp(j\phi)$ of two complex SAR images is given by Eq.(2.2) in chapter 2. The interferometric phase ϕ is determined by the baseline between the repeat-pass sensors and the terrain topography and possible displacement during the two dates. Changes in the phase caused by the terrain topography displacement can be used to monitor the subsidence and deformations of surface that commonly take place in the earthquakes [Zebker, 2000, Preiss and Stacy, 2006]. Changes can also be detected according to the coherence coefficient D , which denotes the correlation between two images. The value of D is in the range 0 to 1 and is sensitive to relatively small changes within a resolution cell [Preiss and Stacy, 2006]. Moreover, Cha et al. [2014] proposed to detect changes in SAR using a processing chain which combines an incoherent change detection of SAR intensity and a coherent change detection of interferometric coherence D .

In this work we will mostly deal with amplitude images, therefore not exploiting the phase information for change detection.

5.1.3 General criteria for change detection

Structure based criteria

Contrary to most change criteria measuring the difference between pixel values as introduced in section 5.1.1 and 5.1.2, Marin and Bruzzone [2013] detected the changes with the help of 3D models of buildings. The expected backscattering properties of buildings simulated using the 3D models are combined with the log-ratio criterion from SAR images to detect the changes of buildings (the new and fully destroyed buildings). Similarly, Tao et al. [2013] applied SAR 3D simulation based on the LiDAR data to detect changes between two SAR images with different incidence angles. Dellinger et al. [2014] proposed to describe the structures of buildings by scale-invariant feature transform (SIFT) [Lowe, 2004] for optical images or SAR-SIFT [Dellinger et al., 2012] for SAR images. The changes can be detected locally by comparing the number of detected keypoints and the number of the matched keypoints of two images using a contrario approach (they could be optical or SAR images).

Change detection in transform domain

Kauth-Thomas transformation [Kauth and Thomas, 1976] is a fixed linear transformation of multi-spectral (or multi-band) images. Its output represents the greenness, brightness and wetness of the images. The change can be measured based on these values [Crist, 1985].

Principal component analysis (PCA) differs from Kauth-Thomas transformation in terms that it is an unfixed transformation. The output are the eigenvectors usually sorted in decreasing order. From the first eigenvector (or principal component) to the last one, each eigenvector expresses the next largest amount of information of the data. When dealing with change detection problem, principal components are learned from two dates separately then applied to some comparison techniques [Byrne et al., 1980] (such as image differencing in Eq.(2.5)). Another approach based on PCA is to merge the input images into one set then principal components are learned from this merged set [Ingebritsen and Lyon, 1985]. The principal components with negative correlation correspond to change.

Wiemker [1997] improved this idea by an iterative PCA to reduce the influence of changed pixels. Other transformation theories, such as dual-tree complex wavelet transform [Celik and Ma, 2010], curvelet transform [Schmitt et al., 2009] etc. are also applied to detect changes.

Instead of transformation of the input images, Celik and Ma [2011] proposed to apply an undecimated discrete wavelet transform on the difference map (for optical images) or log-ratio map (for SAR images). Similarly, in [Jha and Unni, 1994]’s work, the PCA was used as a preliminary step to reduce the dimensionality before change extraction.

Regularization for change detection

In the last years, spatial contextual information and multi-scale information have been taken into account in the change detection methods. For example a *changed* pixel is likely to be surrounded by *changed* pixels. This context information is widely modeled by Markov random fields [Bruzzone and Prieto, 2000b]. Bruzzone et al. [2004b], Bruzzone and Prieto [2000a], Bovolo [2009] model the context information by multi-temporal parcels. Hazel [2001], Brunner et al. [2010], Molinier et al. [2007], Carlotto [2005], Yamamoto et al. [2001] consider the context information at the object level. For very high resolution images, low resolution level leads to introduce global information more easily, such as multi-level or multi-scale approaches in [Bovolo, 2009, Dalla Mura et al., 2008, 2010, Bovolo and Bruzzone, 2009]. Gong et al. [2014] also applied the Markov model with a regularization taking into account the number of neighborhood pixels with the same class.

5.1.4 Thresholds for change detection

Section 5.1.1 and 5.1.2 mainly reviewed the change criteria used in change detection of optical and SAR images. However, these criteria are usually followed by thresholding methods or decision techniques to detect regions of change. The threshold value is critical, since a low (or high) value will cause too much false alarm, while too high (or low) value may suppress significant changes. This section thus reviews and discusses some main thresholding methods.

Global thresholds

The most common approach to carry out the change detection results from a change criterion (it could be any one of these introduced in section 5.1.1 and 5.1.2) is to find a global threshold to differentiate change from no-change. The values associated to the changed pixels can be identified on the right (or left) side of the criterion histogram [Bruzzone and Prieto, 2002] with the assumption that the values associated to unchanged pixels gather together on one side of the histogram, while the values of changed pixels gather together on the other side or are evenly distributed in the histogram. However, selecting an appropriate threshold in this way is generally not easy since the real distribution of the analyzed criterion is unknown. Therefore, thresholds are usually selected according to empirical strategies [Fung and LeDrew, 1988] or manual trial-and-error procedures.

Another common way to select thresholds is based on the assumption that only a few changes occurred in the studied area between the two considered dates [Bruzzone and Prieto, 2000b]. Under this assumption, the distribution of the criterion associated to unchanged pixels can be confused with the histogram of the values in the computed criterion map. The values located far away from the mean in this histogram are defined as change, in particular the threshold is set at $n\sigma$ from the mean value of the criterion

map (n : a real number derived by a trial-and-error procedure; σ : the standard deviation of the criterion map). Bruzzone and Prieto [1999] have experimentally studied the effects of different n values on the accuracy of detection results. Neagoe et al. [2014] selected the threshold based on the clustering of the spectral change vectors (derived according to the standard change vector analysis).

More generally, the criteria images are modeled by Gaussian distributions in [Bruzzone and Prieto, 2000b] and generalized Gaussian distributions in [Bazi et al., 2007], in which the Expectation-Maximization algorithm is applied to estimate the statistical parameters of the distributions. Then, the thresholding processing turns to be a decision of each criterion value between the *unchanged* distribution and the *changed* distribution under a Bayesian decision rule (e.g., minimum error, minimum cost, etc.).

In [Kervrann and Boulanger, 2006], the authors proposed to set the threshold according to the quantiles of the criterion value when it is subject to identical and independent distributed random variables. Although this thresholding method is used to select filter parameter for NLM (as explained in section 3.3), it can also be applied to select thresholds for change detection. Pursuing this idea, the change detection threshold can be set by:

$$\tau = \text{quantile}(\mathcal{R}, \alpha) , \quad (5.21)$$

where \mathcal{R} is a change criterion (or a similarity criterion in NLM algorithms). Since it is not easy to obtain the distribution of \mathcal{R} , it can be simulated using synthetic data (or real data with known groundtruth data). For instance, any noise-free picture can be used to generate multi-temporal images using the expected statistical distribution for the noise. Note that all the synthetic multi-temporal noisy images use the same *true* image, which guarantees no changes among them. Then, the criterion is computed using these synthetic images. The histogram of the criterion from the synthetic images is considered as an estimation of the distribution of \mathcal{R} . Finally, the threshold τ can be obtained by Eq.(5.21) with the simulated distribution of \mathcal{R} . Compared with modeling the real distribution of the criterion by Gaussian or other distributions, this quantiles method can be easily extended to various change criteria since it is highly data dependent (or data driven) and can simply control the false alarm rate by setting the value of α . Nevertheless the former method may fail when the real noise distribution is complex and departs from the assumed distributions.

Local thresholds and machine learning based decision

Quin et al. [2013] proposed to select the threshold for the criterion given by Eq.(5.17) in a scatterplot plane (horizontal axis: the geometric mean $m_0 = \sqrt{y(1)y(2)}$, vertical axis: the quadratic mean $m_2 = \sqrt{\frac{1}{2}(y(1)^2 + y(2)^2)}$). The joint probability $p(m_0, m_2)$ combined with the conditional probability $p(m_2|m_0)$ is used to describe the 2D distribution of pair $\{m_0, m_2\}$ in the scatterplot plane. Thus, given a rate α (false alarm rate) i.e. $\alpha = 0.01$, a boundary can be found in the scatterplot plane, inside which the probabilities are higher than α and outside the probabilities are lower than α . This boundary can be considered as the threshold and $\{m_0, m_2\}$ pairs located outside it are defined as changes. Since this threshold is spatially variable depending on different m_0 values, it can be seen as a local thresholding method.

Instead of thresholding the change criteria, lots of methods apply the machine learning approaches to make decision, i.e. artificial neural networks (ANN) [Dai and Khorram, 1997, Nemmour and Chibani, 2006a], support vector machine (SVM) [Nemmour and Chibani, 2006b, Volpi et al., 2013]. Bovolo et al. [2008] performed transductive SVM for change

detection with a Bayesian selective thresholding method [Bruzzone and Prieto, 2000b] that allows the unsupervised application of this classifier. The one-class SVM is also applied to detect changes [Bovolo et al., 2010, Li et al., 2011]. In [Huo et al., 2012]’s work, the SVM was applied on the SIFT features extracted from the input images instead of the pixel values to detect changes.

5.1.5 Change detection Evaluations

To evaluate the change detection results, both qualitative/visual and quantitative methods can be used.

Visual evaluation

When dealing with radiometrically calibrated data, the main visual evaluation used for change detection corresponds to the display of a flicker animation [Berger et al., 2000, Radke et al., 2005]. It is a short movie file that has only two frames (the analyzed two images y_t and $y_{t'}$). Because of the persistence of vision, people see a steady scene in the unchanged areas, and the changed areas appear to flicker. The visual comparison of the flicker areas and the detection results is a reliable approach for evaluation. In some cases, it is a method to display the changes.

Quantitative evaluation

Since it is not easy to get ground truth data of the real SAR images, the quantitative evaluation is more challenging. Usually, an approximate ground truth is provided by manually labeled map by experts, but it is still not perfectly accurate. Different experts may have different view of changes, and even the same one may give different determination at different times. Thus, in the quantitative evaluation of SAR change detection, two kinds of data sets are usually used:

- Synthetic multi-temporal images. The changes are known (the ground truth data is exactly accurate, such as the widely used synthetic images and the benchmark data set in [Cui, 2014]), but the context of the images is not real (e.g. excessively simple or complex objects, biased statistic model of noise etc.).
- Real multi-temporal images with manually labeled ground truth data. The ground truth data is not perfectly accurate.

Once the ground truth has been obtained, several measurements to compare the ground truth and a detection results can be used:

- 1) The number of true positive (TP): the number of changed pixels correctly detected;
- 2) The number of false positive (FP): the number of unchanged pixels detected as change;
- 3) The number of true negatives (TN): the number of unchanged pixels correctly detected;
- 4) The number of false negatives (FN): the number of changed pixels detected as no change.

FP is also known as the false alarm. True positive rate (or sensitivity) and false positive

rate (or false alarm rate) can be calculated by:

$$\begin{aligned} R_{\text{TP}} &= \frac{\text{TP}}{\text{TP} + \text{FN}} , \\ R_{\text{FP}} &= \frac{\text{FP}}{\text{FP} + \text{TN}} . \end{aligned} \tag{5.22}$$

A receiver operating characteristic (ROC) or simply ROC curve can be created by plotting the true positive rate versus the false positive rate at various threshold settings. The higher ROC curves (at the same false positive rate, the higher true positive rate) indicates the better algorithms.

5.2 Change pattern classification

Unlike the change/un-change detection, multi-class change detection identifies changes of different classes. Each changed area (or pixel) is associated with a specific type, e.g. the land-cover transition etc.

Unsupervised methods

Lombardo and Pellizzeri [2002] presented two detectors for the discrimination between constant and step change pattern in the temporal domain for SAR images. Based on the change vector analysis in polar domain as shown in Fig.5.3, Bovolo and Bruzzone [2007] classified the changed pixels according to θ of the samples in the polar domain. Changes of *Burned area* and *lake enlargement area* have been identified in the change detection map. The coefficients of variation, amplitude and coherence identify objects dominated by volume scatterers, rough surfaces and smooth surfaces respectively. Schulz et al. [2010] proposed to display a pair of SAR images using these coefficients as RGB visualization, as shown in Fig.5.4.b. Yellow regions in Fig.5.4.b are the moving objects (e.g. cars, airplanes), green parts are the forest or dense bushes. Similarly, Amitrano et al. [2014] presented another RGB composition of multi-temporal SAR images, in which the coherence map (R channel) combined with original image y_t (G channel) and image image $y_{t'}$ (B channel) were used. Lu [2014] considered the land-cover transitions when classifying the changes. As shown in Fig.5.4.c, the regions with yellow color are the changes from farmlands to buildings, red regions are areas where water changes to farmlands, etc.

Supervised methods

Camps-Valls et al. [2008] considered the change detection problem as a pre-classification enhancement or a post-classification comparison [Singh, 1989]. In the post-classification comparison, the images of two dates are independently classified and co-registered, and after comparing the classification results those pixels whose predicted labels change between dates are changed.

Bruzzone and Serpico [1997] explicitly identified land-cover transitions (changes among *Bare soil*, *Corn*, *Soybean*, *Sugar beet*, *Wheat*) in multi-temporal remote-sensing images based on supervised classification. Unlike post-classification comparison, Bruzzone and Serpico [1997] took into account the time dependency by a prior probabilities of classes. Bruzzone et al. [2004a] detected land-cover transitions by means of a multiple classifier system (developed in the framework of the compound classification decision rule). Sluiter and de Jong [2007] identified different types of soil using aerial photographs.

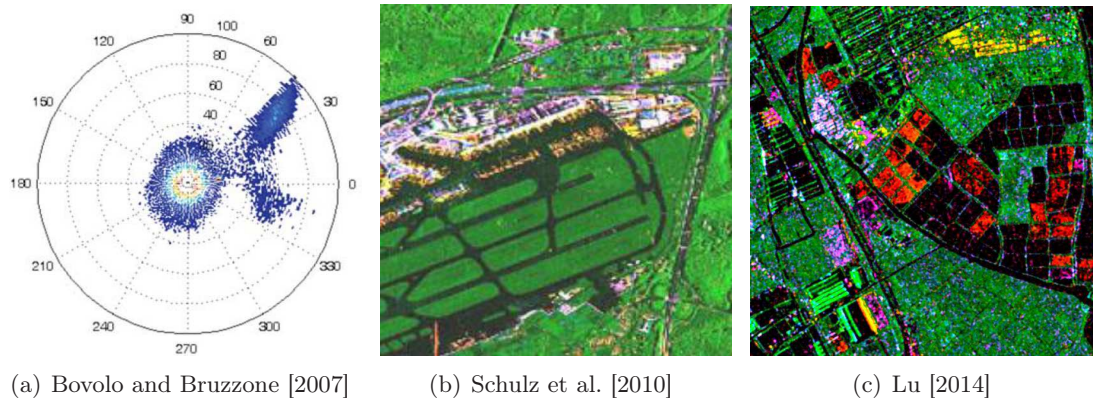


Figure 5.4: Various approaches of change classification. (a) Change classification using the position of change vector in the polar domain Bovolo and Bruzzone [2007]; (b) Change classification using the coefficient of variation, amplitude and coherence Schulz et al. [2010]; (c) Change classification using the class transform of objects Lu [2014].

5.3 Long-term Change analysis

Long-term Change Detection detects or monitors the seasonal changes (vegetation dynamic changes) and slow accumulated changes (trends detection). It implies a set of images, covering a long time period.

Julea et al. [2011] proposed a crop monitoring using satellite image time series (SITS) by considering both spatial and temporal dimensions. A grouped frequent sequential pattern dedicated to groups of pixels sharing common temporal patterns and satisfying a minimum spatial connectivity is defined.

A generic change detection approach is proposed by [Verbesselt et al., 2010a] for time series by detecting and characterizing breaks for additive seasonal and trend contributions. It integrates the decomposition of time series into trend, seasonal, and remaining components within a long-term time series. An improved harmonic seasonal model which requires fewer observations has been presented in [Verbesselt et al., 2010b]. De Jong et al. [2011] analyzed the normalized difference vegetation index time series data based on fast Fourier transform. Martínez and Gilabert [2009] used a multi-resolution analysis based on Wavelet transform to deal with the normalized difference vegetation index time series. To compare time series data with miss samples (due to meteorological phenomena, like clouds) in optical images, Petitjean et al. [2012] proposed to use dynamic time warping [Petitjean et al., 2011] to compare time series data with different lengths.

5.4 Summary of change analysis

In this chapter, the main change criteria applied to optical and SAR images have been reviewed. Most of them include an assumption of the noise in the analyzed images, i.e. additive Gaussian noise model for optical images and multiplicative Gamma noise for SAR images. Among them, the likelihood ratio test (LRT) have been widely used. However, the composite hypothesis problem (due to the lack of the knowledge of noise-free value u) leads to approximations of the likelihood ratio, like generalized likelihood ratio. Contrary to the popular methods in which u is estimated by the mean inside a moving window,

we propose to use the multi-temporal denoising results obtained with our 2S-PPB filter to solve the composite hypothesis problem. The next chapter thus presents two change criteria based on LRT for SAR images using 2SPPB filtering results.

Chapter 6

Likelihood Ratio Test based Change Detection

Based on the likelihood ratio test (LRT) introduced in section 5.1.2, this chapter proposed two change criteria for multi-temporal SAR images. Thanks to the expected estimation of SAR reflectivity achieved by our 2S-PPB filter, we can solve the composite hypothesis problem of the LRT using the denoising results. Contrary to most likelihood ratio tests which only use noisy data, both the denoised data and the noisy data are involved in the proposed criteria.

6.1 Approximate likelihood ratio test

Recall that the noise-free values u in the likelihood ratio given by Eq.(5.10) are unknown. To estimate the noise free value u , we propose to use the denoised results \hat{u} provided by our multi-temporal filter 2SPPB presented in chapter 4, instead of the noisy data y usually used in the literature. The noise-free value u is simply replaced by the denoised data \hat{u} , as shown in the following:

$$\begin{aligned} u(1) &= \hat{u}(1), \\ u(2) &= \hat{u}(2), \\ u(12) &= \frac{\hat{L}(1)\hat{u}(1) + \hat{L}(2)\hat{u}(2)}{\hat{L}(1) + \hat{L}(2)}, \end{aligned} \tag{6.1}$$

where $\hat{L}(1)$ is the equivalent number of looks of pixel $\hat{u}(1)$, which is estimated by Eq.(3.53). According to Eq.(5.10), the *change* criterion between $y(1)$ and $y(2)$ using likelihood ratio can be defined as (combined with the Gamma probability density function):

$$\begin{aligned} \mathcal{R}^{\text{ALRT}}(y(1), y(2)) &= \frac{p(y(1), y(2)|u(12), \mathcal{H}_0)}{p(y(1), y(2)|u(1), u(2), \mathcal{H}_1)} \tag{6.2} \\ &= \left[\frac{1}{4} \left(\frac{\hat{u}(2)}{\hat{u}(1)} + \frac{\hat{u}(1)}{\hat{u}(2)} + 2 \right) \right]^{-L} \exp \left[L \left(\frac{y(1)}{\hat{u}(1)} + \frac{y(2)}{\hat{u}(2)} - \frac{2y(1) + 2y(2)}{\hat{u}(1) + \hat{u}(2)} \right) \right] \tag{6.3} \end{aligned}$$

where L is the original number of looks of $y(1)$ and $y(2)$. Note that the approximate likelihood ratio $\mathcal{R}^{\text{ALRT}}$ highly depends on the denoised values $\hat{u}(1)$ and $\hat{u}(2)$, since $\mathcal{R}^{\text{ALRT}}(y(1), y(2)) \equiv 1$ when $\hat{u}(1) = \hat{u}(2)$ whatever $y(1)$ and $y(2)$.

6.2 Generalized likelihood ratio test

In a more accurate way, we can take into account the denoised values to define the observed data and consider the likelihood probability of \mathcal{H}_0 and \mathcal{H}_1 as $p(y(1), y(2), \hat{u}(1), \hat{u}(2)|\mathcal{H}_0)$ and $p(y(1), y(2), \hat{u}(1), \hat{u}(2)|\mathcal{H}_1)$. To simplify this likelihood probability, we can assume that $\{y(1), \hat{u}(1)\}$ and $\{y(2), \hat{u}(2)\}$ are independent, although this assumption is not well justified (since, typically $y(1)$ can intervene in the estimation of $\hat{u}(1)$). Thus,

$$\begin{aligned} p(y(1), y(2), \hat{u}(1), \hat{u}(2)|\mathcal{H}_0) &= p(y(1), \hat{u}(1)|u(12), \mathcal{H}_0)p(y(2), \hat{u}(2)|u(12), \mathcal{H}_0) \\ p(y(1), y(2), \hat{u}(1), \hat{u}(2)|\mathcal{H}_1) &= p(y(1), \hat{u}(1)|u(1), \mathcal{H}_1)p(y(2), \hat{u}(2)|u(2), \mathcal{H}_1) . \end{aligned}$$

The likelihood ratio test is then given by:

$$\mathcal{R}^{\text{GLRT}}(y(1), y(2)) = \frac{p(y(1), \hat{u}(1) | u(12), \mathcal{H}_0)p(y(2), \hat{u}(2) | u(12), \mathcal{H}_0)}{p(y(1), \hat{u}(1) | u_1, \mathcal{H}_1)p(y(2), \hat{u}(2) | u_2, \mathcal{H}_1)} . \quad (6.4)$$

Since $u(12)$, $u(1)$ and $u(2)$ are not available, they can be replaced by their maximum likelihood (ML) estimation, exploiting both $y(i)$ and $\hat{u}(i)$ this time:

$$\begin{aligned} u(1) &= \frac{Ly(1) + \hat{L}(1)\hat{u}(1)}{L + \hat{L}(1)} \\ u(2) &= \frac{Ly(2) + \hat{L}(2)\hat{u}(2)}{L + \hat{L}(2)} \\ u(12) &= \frac{Ly(1) + Ly(2) + \hat{L}(1)\hat{u}(1) + \hat{L}(2)\hat{u}(2)}{2L + \hat{L}(1) + \hat{L}(2)} . \end{aligned} \quad (6.5)$$

L , $\hat{L}(1)$ and $\hat{L}(2)$ are the number of looks associated to y , $\hat{u}(1)$ and $\hat{u}(2)$ respectively. Note that this is very similar to [Lombardo and Oliver, 2001]. Nevertheless, the multi-temporal denoised values used in the proposed approach can provide more accurate estimation without loss of spatial resolution. It was not the case in [Lombardo and Oliver, 2001] where spatial partitioning and averaging were introduced as post-processing steps. In case of Gamma distributions with different number of looks, each probability term $p(y, \hat{u}|u)$ in Eq.6.4 can be approximated under conditional independence assumption by:

$$\begin{aligned} p(y, \hat{u}|u) &= p(y|u)p(\hat{u}|u) \\ &= \frac{y^{-1}\hat{u}^{-1}}{\Gamma(L)\Gamma(\hat{L})} \frac{(Ly)^L(\hat{L}\hat{u})^{\hat{L}}}{u^{L+\hat{L}}} \exp\left(-\frac{Ly + \hat{L}\hat{u}}{u}\right) . \end{aligned} \quad (6.6)$$

Finally, the change criterion given by the generalized likelihood boils down to:

$$\begin{aligned} \mathcal{R}^{\text{GLRT}}(y(1), y(2)) &= \left(\frac{Ly(1) + \hat{L}(1)\hat{u}(1)}{L + \hat{L}(1)}\right)^{L+\hat{L}(1)} \left(\frac{Ly(2) + \hat{L}(2)\hat{u}(2)}{L + \hat{L}(2)}\right)^{L+\hat{L}(2)} \\ &\quad \left(\frac{2L + \hat{L}(1) + \hat{L}(2)}{Ly(1) + \hat{L}(1)\hat{u}(1) + Ly(2) + \hat{L}(2)\hat{u}(2)}\right)^{2L+\hat{L}(1)+\hat{L}(2)} \end{aligned} \quad (6.7)$$

Unlike $\mathcal{R}^{\text{ALRT}}$, the generalized likelihood ratio $\mathcal{R}^{\text{GLRT}}$ does not rely so much on the denoised values $\hat{u}(1)$ and $\hat{u}(2)$. Indeed, even when $\hat{u}(1) = \hat{u}(2)$, $\mathcal{R}^{\text{GLRT}}$ still depends on the noisy values $y(1)$ and $y(2)$.

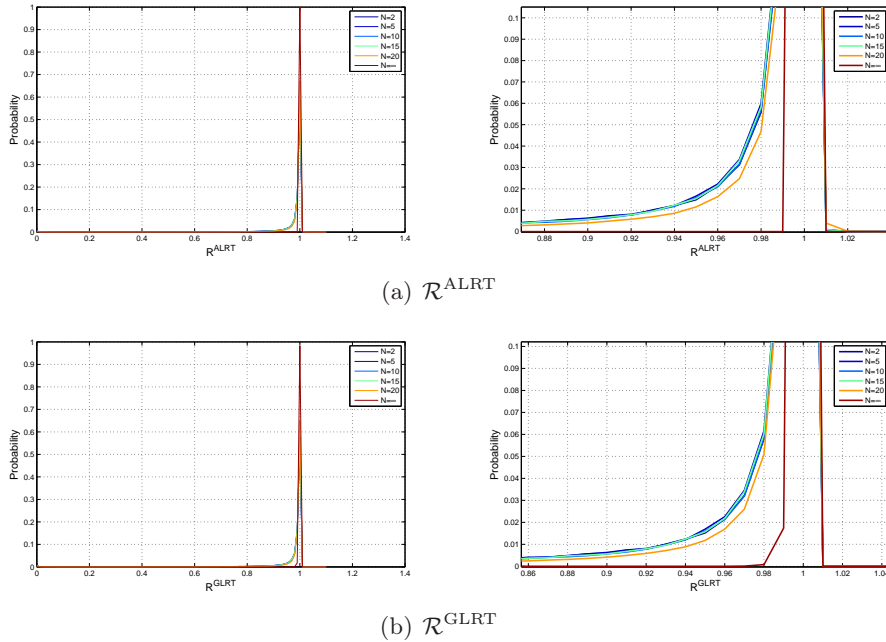
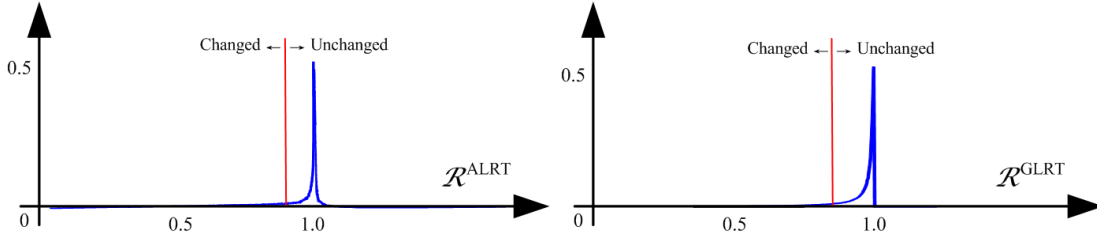


Figure 6.1: The simulated histograms of $\mathcal{R}^{\text{ALRT}}$ and $\mathcal{R}^{\text{GLRT}}$ with different number of images (N) using synthetic images. When $N \rightarrow \infty$, the values of $\mathcal{R}^{\text{ALRT}}$ and $\mathcal{R}^{\text{GLRT}}$ gather together.

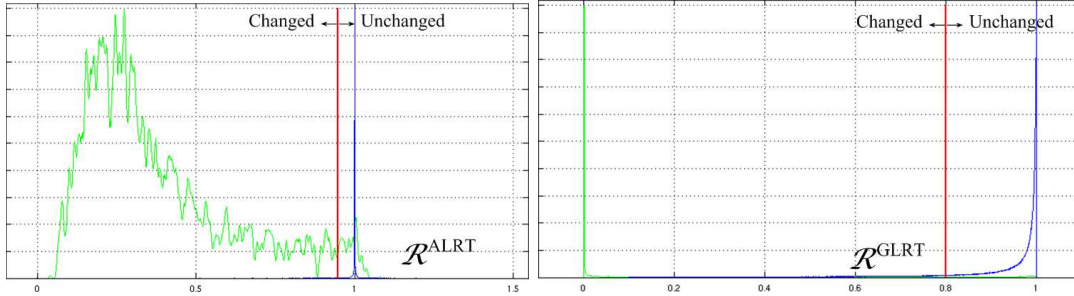
6.3 Thresholds for change detection

Distributions of $\mathcal{R}^{\text{ALRT}}$ and $\mathcal{R}^{\text{GLRT}}$. It is not easy to analytically obtain the distributions of $\mathcal{R}^{\text{ALRT}}$ and $\mathcal{R}^{\text{GLRT}}$ since they depend on the number of looks of noisy images, the number of images used in the denoising process and all the parameters of multi-temporal filter (such as h , h' , search window size, patch size and so on as described in chapter 3). Taking the number of images as example, Fig.6.1 shows the simulated histograms of $\mathcal{R}^{\text{ALRT}}$ and $\mathcal{R}^{\text{GLRT}}$ with different numbers of images using the synthetic images. For our purpose of simulating the histograms, any picture can be used to generate multiple speckle images with no change although it is preferable to use an image with a content similar to a SAR image (strong scatterers, bright lines...). Note that all the synthetic multi-temporal noisy images use the same *true* image, which guarantees no changes among them. The histograms vary with different numbers of images N (the denoised image is the noise-free image when $N = \infty$). The more images used to computed $\mathcal{R}^{\text{ALRT}}$ and $\mathcal{R}^{\text{GLRT}}$ ($N \rightarrow \infty$), the *sharper* are the histograms. They are then used as approximations of the distribution of $\mathcal{R}^{\text{ALRT}}$ and $\mathcal{R}^{\text{GLRT}}$.

Thresholding the histograms. As introduced in section 5.1.4, the quantiles of the change criteria can be selected as the thresholds without the complete modeling of the distribution of the criteria. We therefore propose to choose the thresholds according to the quantiles of the distributions of $\mathcal{R}^{\text{ALRT}}$ and $\mathcal{R}^{\text{GLRT}}$ computed on synthetic images. The change detection threshold can then be set by $\tau^{\text{ALRT}} = \text{quantile}(\mathcal{R}^{\text{ALRT}}, \alpha = 0.01)$ (and $\tau^{\text{GLRT}} = \text{quantile}(\mathcal{R}^{\text{GLRT}}, \alpha = 0.01)$), which means the false alarm rate is fixed to 1% for ideal signals. As shown in Fig.6.2.a, the histograms of $\mathcal{R}^{\text{ALRT}}$ and $\mathcal{R}^{\text{GLRT}}$ are truncated by the thresholds (red lines) with false alarm 1%. The parts on the right of the thresholds



(a) Thresholds in the simulated histograms. The simulated histograms of $\mathcal{R}^{\text{ALRT}}$ and $\mathcal{R}^{\text{GLRT}}$ using synthetic images are the blue lines. The red lines are thresholds τ^{ALRT} and τ^{GLRT} with false alarm 1%.



(b) Examples of the normalized histograms (peak normalization) of $\mathcal{R}^{\text{ALRT}}$ and $\mathcal{R}^{\text{GLRT}}$ using real SAR images *Paris* (detailed in section 6.4). The red lines are thresholds τ^{ALRT} and τ^{GLRT} with false alarm 1%. The blue lines are the histograms of unchanged $\mathcal{R}^{\text{ALRT}}$ and $\mathcal{R}^{\text{GLRT}}$. The green lines are the histograms of changed $\mathcal{R}^{\text{ALRT}}$ and $\mathcal{R}^{\text{GLRT}}$.

Figure 6.2: The selection of the thresholds for change detection.

are considered as unchanged case, the left part is changed case. Fig.6.2.b shows the $\mathcal{R}^{\text{ALRT}}$ and $\mathcal{R}^{\text{GLRT}}$ histograms of changed and unchanged pixels in real SAR data *Paris* (image information detailed in section 6.4). Those changed pixels are labeled manually.

6.4 Experiments of change detection

The proposed methods are evaluated on both synthetic images and real multi-temporal SAR images.

6.4.1 Data Set

Synthetic images: Fig.6.3.a shows the noisy synthetic images y_t and $y_{t'}$ corrupted by single-look multiplicative speckle noise respectively and the ground truth of changes between them. The four squares are 32×32 pixels with true value 128. The darker frame is 8 pixels width with 32 as true value and the true value of background is 64.

Realistic SAR synthetic images: A denoised image of 21 single-look TerraSAR X-band images in Paris (France) sensed in 2011 is considered as the noise-free image (multi-temporal denoising approach of section 4.2.2), as shown in Fig.6.3.b. Two single-look noisy images y_t and $y_{t'}$ are generated with changes added in $y_{t'}$. These changed regions are about 15-25 pixels width and length, for instance a 20×20 pixels patch of vegetation is replaced by a same size patch of building and so on. The right of Fig.6.3.b shows the ground truth of changes.

Real SAR images 1: 26 single-look TerraSAR images in Saint-Gervais-les-Bains (France) (13 images are sensed in 2009 and the other 13 images in 2011) are shown in

Name	Reference	Description
Log-Ratio GLRT	Rignot and van Zyl [1993] Lombardo and Oliver [2001]	Log-Ratio operator Generalized likelihood ratio test
Wilcoxon	Krylov et al. [2012]	Change detection using a Wilcoxon Test
MIMOSA	Quin et al. [2013]	Method for generalIzed Means Ordered Series Analysis
$\mathcal{R}^{\text{ALRT}}$	-	The proposed approximate likelihood ratio test
$\mathcal{R}^{\text{GLRT}}$	-	The proposed generalized likelihood ratio test

Table 6.1: The change detection methods used in the comparison experiments.

Fig.6.4.a, identified as *Saint-Gervais-les-Bains*. Reference Ground truth of changes is labeled manually in the right of Fig.6.4.a.

Real SAR images 2: Experiment in Fig.6.4.b uses 21 single-look TerraSAR X-band images identified as *Paris* in Paris (France) sensed in 2011. We label the ground truth of changes manually, as shown in right of Fig.6.4.b.

Real SAR images 3: Experiment in Fig.6.6 uses 24 CARABAS-II magnitude images acquired in Vidsel, Sweden 2002, identified as *CARABAS* [Sensor Data Management System (SDMS) Public web site, 2008]. We only detect the changes between image v02_2_1_1 and image v02_4_1_1, while all the 24 images are used in the multi-temporal denoising process.

Real SAR images 4: Experiment in Fig.6.7 uses 9 single-look TerraSAR X-band images identified as *Sendai* in Sendai Harbor (Japan) sensed in 2011. Fig.6.7.a and b show the images acquired respectively on May 6, 2011 and June 8, 2011. All the 9 images are used in the multi-temporal denoising step.

6.4.2 Change detection methods

The proposed change criteria approximate likelihood ratio test $\mathcal{R}^{\text{ALRT}}$ and generalized likelihood ratio test $\mathcal{R}^{\text{GLRT}}$ are compared with some state-of-the-art methods, such as Log-Ratio operator [Rignot and van Zyl, 1993], the generalized likelihood ratio test (GLRT) proposed in [Lombardo and Oliver, 2001], Wilcoxon Test based change criterion [Krylov et al., 2012] and Method for generalIzed Means Ordered Series Analysis (MIMOSA) [Quin et al., 2013], summarized in Tab.6.1.

6.4.3 Results

The change detection results are assessed by the True-Positive versus False-Positive curves using the reference map of changes as shown in Fig.6.3.c and Fig.6.4.c. The proposed methods $\mathcal{R}^{\text{ALRT}}$ and $\mathcal{R}^{\text{GLRT}}$ can generally obtain higher receiver operating characteristic (ROC) curves than others. For the sake of visual evaluation of those change criteria, we select a fixed true positive rate to compare the false positive rate. Fig.6.5 shows the change criteria thresholded by the fixed true positive rates¹ (or change detection results with fixed true positive rate). The proposed change criteria $\mathcal{R}^{\text{ALRT}}$ and $\mathcal{R}^{\text{GLRT}}$ (on the

¹Note that these fixed true positive rates may vary for different data sets, which is for the sake of visual evaluation.

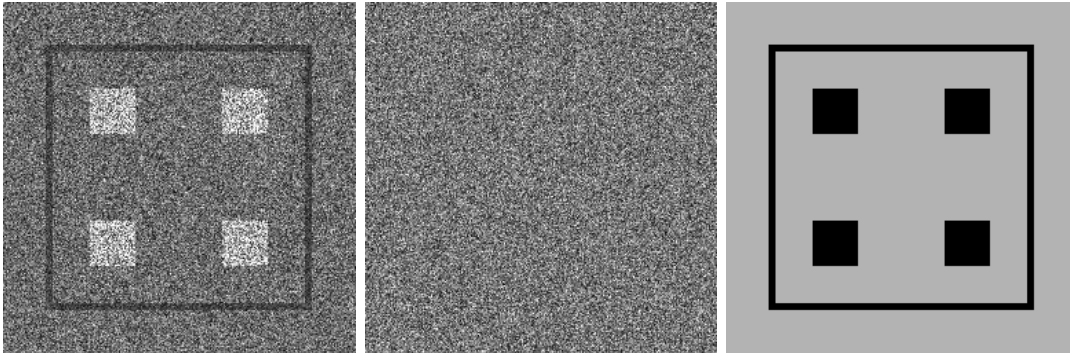
right of Fig.6.5) have less noise in the results, which means they have lower false positive rates.

The experiments on *CARABAS* and *Sendai* data in Fig.6.6 and 6.7 show that the proposed GLRT change detection has comparable performance with MIMOSA [Quin et al., 2013]. $\mathcal{R}^{\text{ALRT}}$ and $\mathcal{R}^{\text{GLRT}}$ outperform other change criteria, but the latter is more reliable than the former (the ROC curves of $\mathcal{R}^{\text{GLRT}}$ are higher than $\mathcal{R}^{\text{ALRT}}$ in Fig.6.3 and 6.4).

6.5 Conclusion

Based on the likelihood ratio test (LRT), two change criteria, approximated LRT $\mathcal{R}^{\text{ALRT}}$ and generalized LRT $\mathcal{R}^{\text{GLRT}}$ have been proposed in this chapter. They attempt to solve the composite hypothesis problem of LRT by using the multi-temporal denoising results. Thresholds selected by the quantiles of the change criteria are used to isolate the change regions. Experiments demonstrate the proposed change detection methods have higher accuracy and less noise compared with some state of the art change detection methods. Besides, the proposed criteria could be used with other filtering methods, but an associated number of looks should be provided for each pixel. Although using a pre-filtering process can be seen as a limit of our approach, it increases the reliability of our criterion and fully exploits the available information. This part of work has been published in [Su et al., 2013].

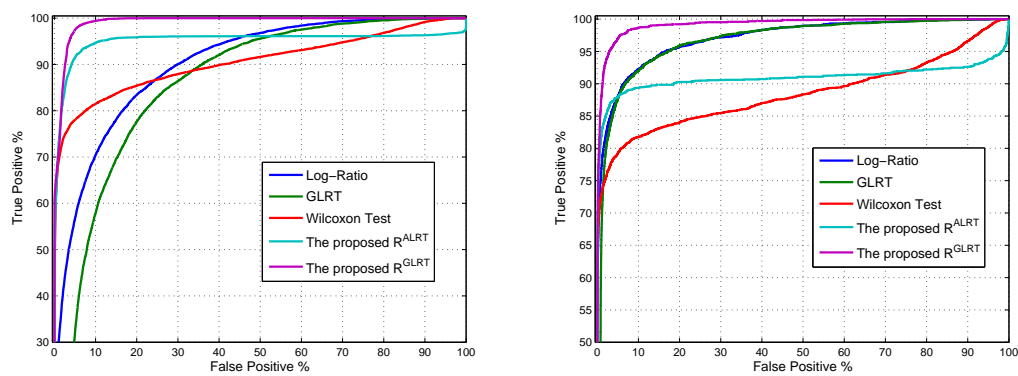
Change detection recognizes the change information only by two patterns, change and no-change. More change patterns exploiting the temporal information of the changes will be introduced in the next chapter.



(a) Synthetic images. From left to right: synthetic image y_t , Synthetic image $y_{t'}$ and the reference map of changes.

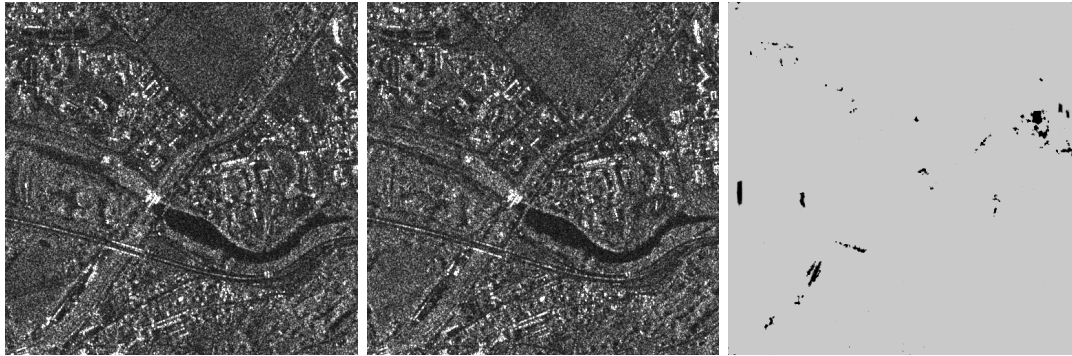


(b) Realistic SAR synthetic images. From left to right: synthetic image y_t , Synthetic image $y_{t'}$ and the reference map of changes.



(c) False positive alarm vs true positive curves of synthetic images and realistic SAR synthetic images

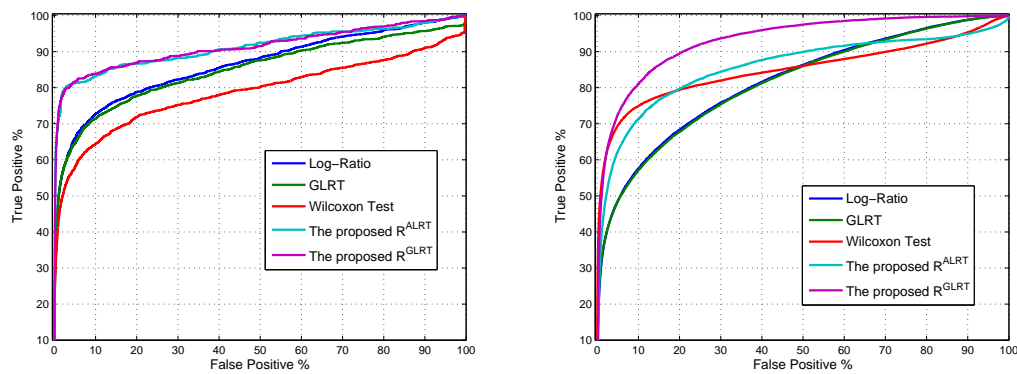
Figure 6.3: Change detection results for synthetic SAR images.



(a) *Saint-Gervais-les-Bains* data set. From left to right: noisy image y_{t_1} , noisy image $y_{t_{26}}$ and the reference map of changes.

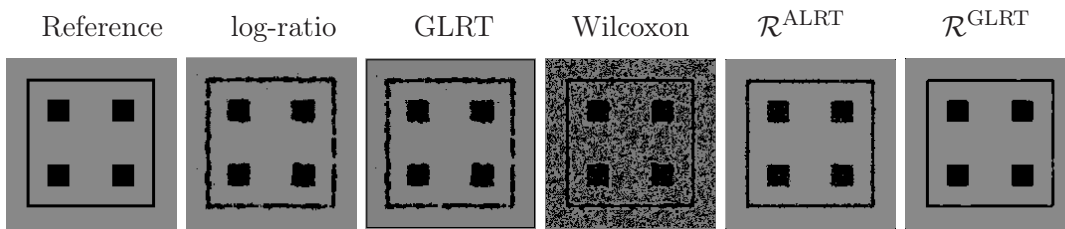


(b) *Paris* data set. From left to right: noisy image y_{t_1} , noisy image $y_{t_{26}}$ and the reference map of changes.

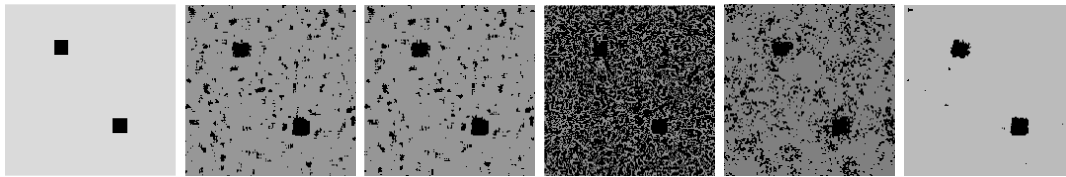


(c) False positive alarm vs true positive curves of *Saint-Gervais-les-Bains* and *Paris* data set.

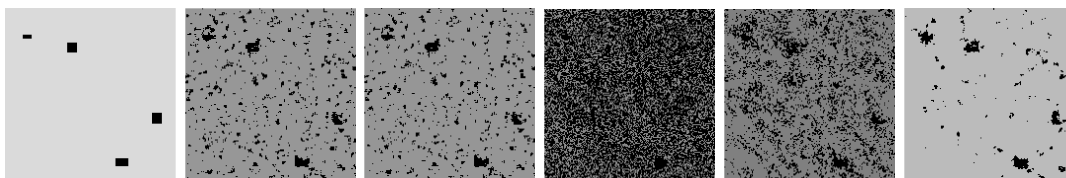
Figure 6.4: Change detection results for real SAR images *Saint-Gervais-les-Bains* and *Paris* data set.



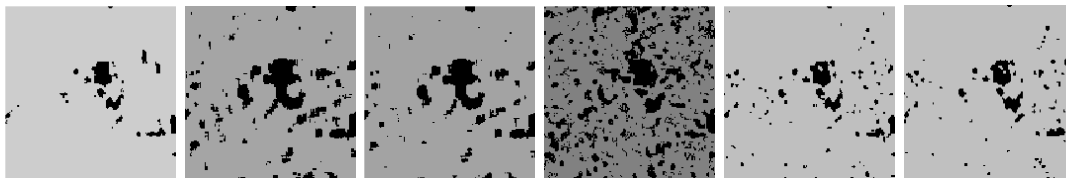
(a) Change detection results of Fig.6.3.a with True Positive rate 95%.



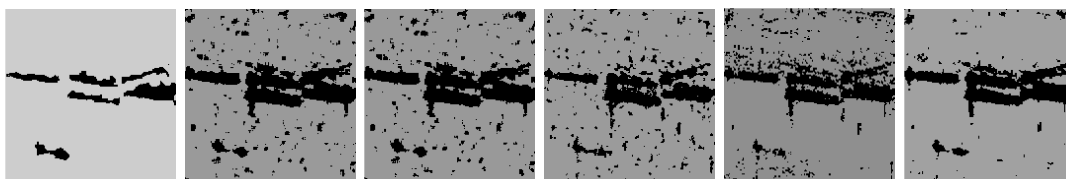
(b) Change detection results of Fig.6.3.b with True Positive rate 90%.



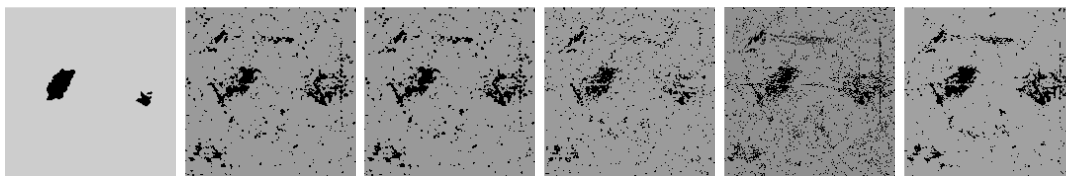
(c) Change detection results of Fig.6.3.b with True Positive rate 90%.



(d) Change detection results of *Saint-Gervais-les-Bains* data set with True Positive rate 80%.



(e) Change detection results of *Paris* data set with True Positive rate 75%.



(f) Change detection results of *Paris* data set with True Positive rate 75%.

Figure 6.5: Change detection results.

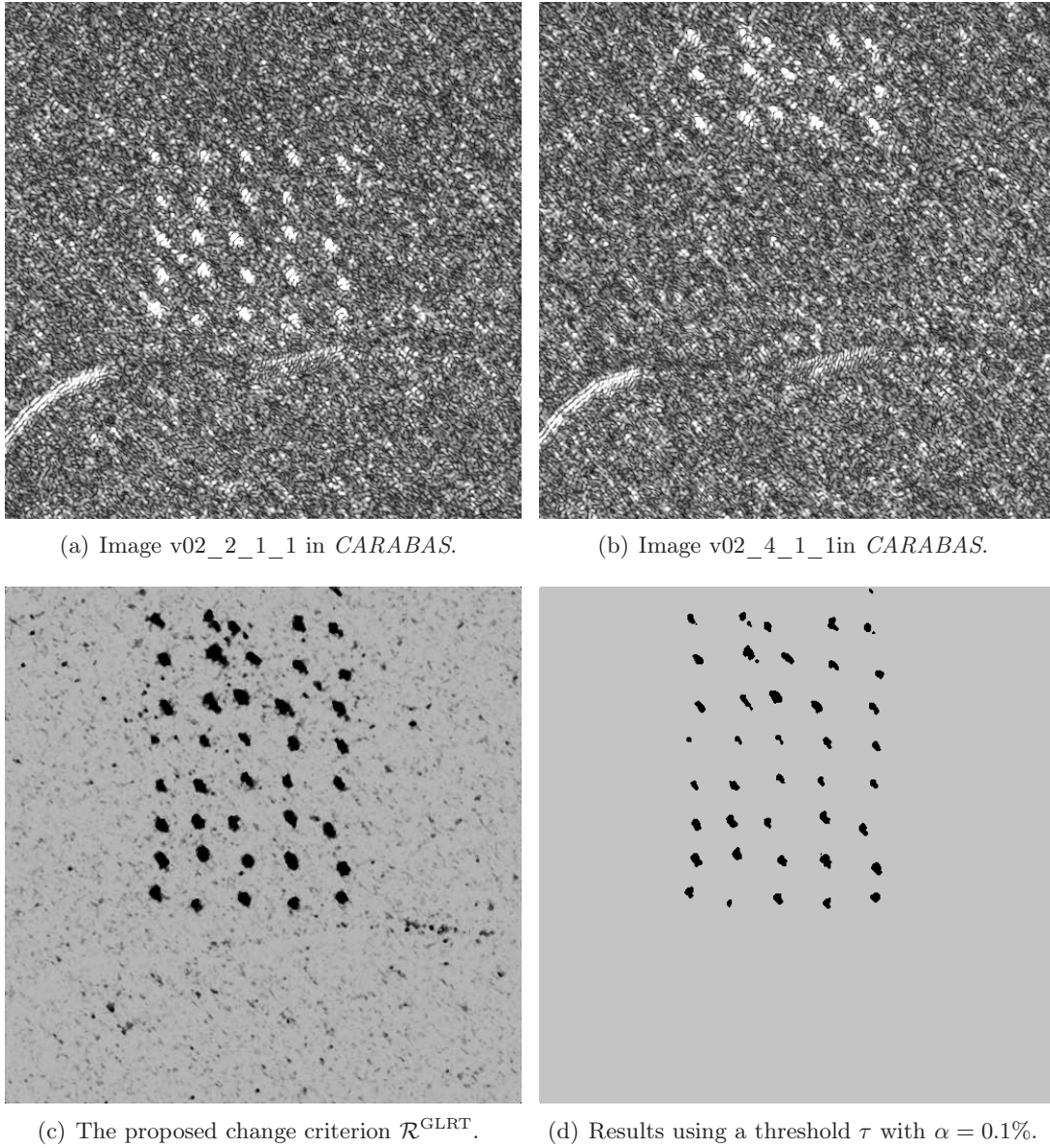
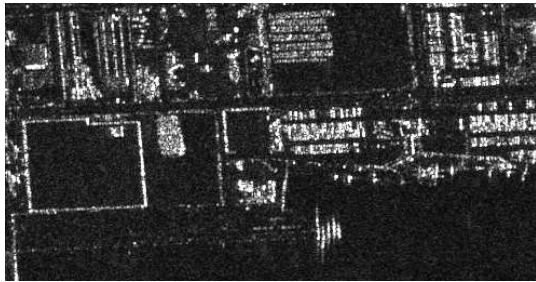
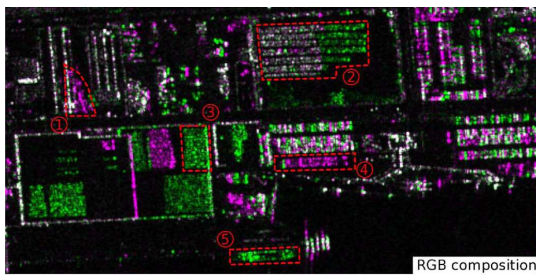
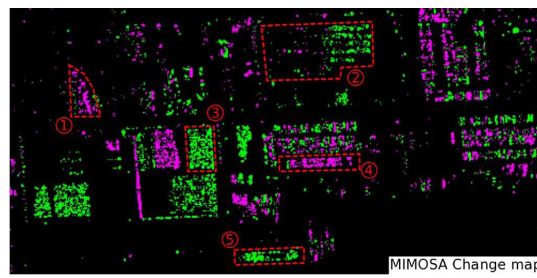


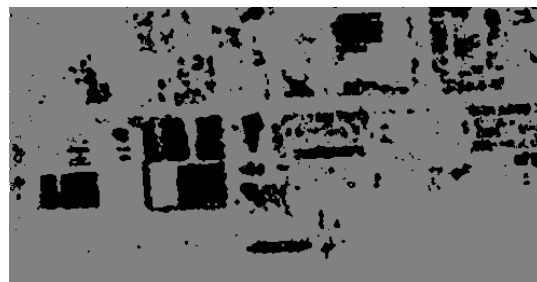
Figure 6.6: Change detection results of real SAR images *CARABAS* [Sensor Data Management System (SDMS) Public web site, 2008].

(a) Image on 06/05/2011 in *Sendai* data.(b) Image on 08/06/2011 in *Sendai* data.

(c) The RGB composition between a and b by MIMOSA [Quin et al., 2013].



(d) The change detection results by MIMOSA (a prior FAR is 1%) [Quin et al., 2013].

(e) The proposed change criterion $\mathcal{R}^{\text{GLRT}}$.(f) Results using a threshold τ with $\alpha = 0.1\%$.Figure 6.7: Change detection results of real SAR images *Sendai*.

Chapter 7

Change Classification: NORCAMA

In chapter 6, we focused on the bi-temporal SAR images and aimed at detecting a binary pattern (change or no-change). When dealing with a multi-temporal data set (more than 2 dates), the analysis among them is much more complex. As said in chapter 1, we will define the changes with more than two patterns (change or no-change). More patterns, such as *step* change, *impulse* change, *cycle* change, have been defined here according to the temporal behaviors of changes, unlike the work in [Lombardo and Pellizzeri, 2002] in which only the step changes are detected. It is very useful to exploit these temporal features of changes, since for instance the temporal behaviors of a new building usually can be considered as a *step* change, which means that comparing the oldest date with other dates, it was unchanged at the beginning but it changed since a certain date (shown in Fig. 7.1.a). Similarly, we can define the boats in rivers or cars on the roads as *impulse* changes (Fig. 7.1.b). These change information can be used in the multi-temporal image interpretation tasks.

To represent the change information, the change criteria proposed in chapter 6 have been used to form a *change criterion matrix* (CCM) which consists of the full change information among the time series. Then, a clustering-and-recognizing method is proposed to classify the changes. It has two steps, clustering using normalized cut on a *change criterion matrix* (to assign a same label to similar or unchanged temporal pixels) and classification according to their temporal behaviors. Note that although change information exploited here is no longer change or no-change problem as people usually focus on, it is still limited to binary changes, which means that we will not take into account continuous changes. For instance, in Zhu and Woodcock [2014]’s work, the continuous seasonal change is modeled by sines and cosines. The proposed change classification is well adapted for few time series and urban applications. It can also be seen as a preliminary step of screening before improved classification of continuous changes.

7.1 Change criterion matrix

At position i of a multi-temporal SAR series $\{y_{t_1}, \dots, y_{t_N}\}$, we have the two pixel series $\{y_{t_1}(i), \dots, y_{t_N}(i)\}$ (original noisy data), $\{\hat{u}_{t_1}(i), \dots, \hat{u}_{t_N}(i)\}$ (denoised data by multi-temporal filter of chapter 4) and associated equivalent number of looks $\{\hat{L}_{t_1}(i), \dots, \hat{L}_{t_N}(i)\}$.

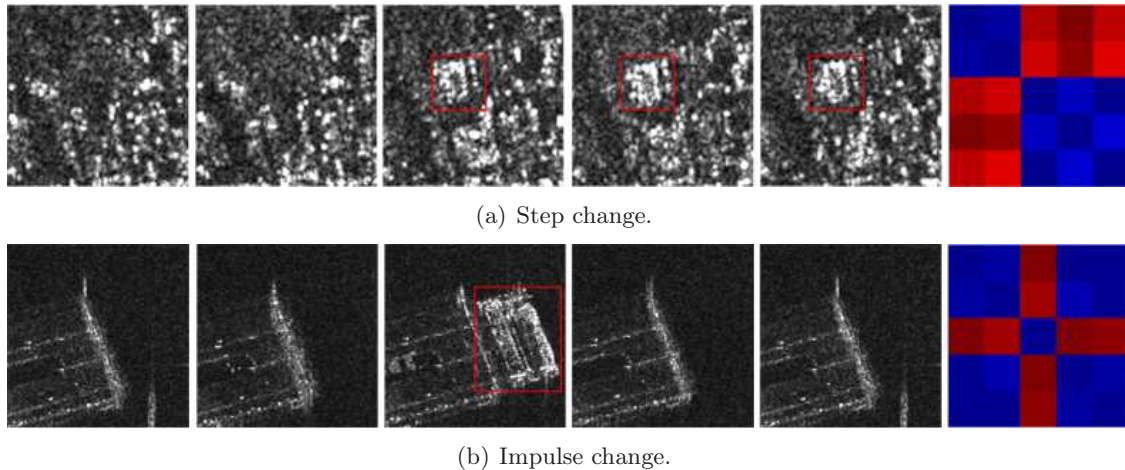


Figure 7.1: Examples of *step* changes and *impulse* changes. From left to right: original multi-temporal SAR images at time t_1, t_2, t_3, t_4, t_5 , change criterion matrix of a pixel in the red rectangle (cold color - high similarities: unchanged; warm color - weak similarities: changed).

The change criterion matrix (CCM) at position i is defined as:

$$\mathcal{M}(i) = \begin{bmatrix} \mathcal{R}(y_{t_1}(i), y_{t_1}(i)) & \mathcal{R}(y_{t_1}(i), y_{t_2}(i)) & \dots & \mathcal{R}(y_{t_1}(i), y_{t_N}(i)) \\ \mathcal{R}(y_{t_2}(i), y_{t_1}(i)) & \mathcal{R}(y_{t_2}(i), y_{t_2}(i)) & \dots & \mathcal{R}(y_{t_2}(i), y_{t_N}(i)) \\ \dots & \dots & \dots & \dots \\ \mathcal{R}(y_{t_N}(i), y_{t_1}(i)) & \mathcal{R}(y_{t_N}(i), y_{t_2}(i)) & \dots & \mathcal{R}(y_{t_N}(i), y_{t_N}(i)) \end{bmatrix} \quad (7.1)$$

where $\mathcal{R}(y_{t_n}(i), y_{t_m}(i))$ denotes the proposed change criterion ($\mathcal{R}^{\text{ALRT}}$ or $\mathcal{R}^{\text{GLRT}}$ in chapter 6) between pixel $y_{t_n}(i)$ and $y_{t_m}(i)$. Note that $\mathcal{R}(y_{t_n}(i), y_{t_m}(i)) = 1$ when $n = m$. Contrary to the multi-date divergence matrix in [Atto et al., 2013] performing at the image or sub-image level, the CCM presents the change information at pixel level. Each CCM $\mathcal{M}(i)$ denotes the temporal behavior of the pixel series at position i .

7.2 Normalized cut on change criterion matrix

Normalized cut (N-Cut) as one of the spectral clustering techniques makes use of the similarity matrix of the data to perform clustering. It is simple to implement, can be solved efficiently by standard linear algebra software, and very often outperforms traditional clustering algorithms such as the K-Means algorithm [Von Luxburg, 2007]. Since the CCM can be considered as a similarity matrix of the time series, spectral clustering method can be easily applied on the CCM to cluster the temporal pixels. In this case, no more similarity measurements is needed compared with other clustering methods (like K-Means algorithm for which new similarity to cluster center has to be computed).

7.2.1 Normalized cut

Spectral clustering has become one of the most popular modern clustering algorithms. Given a set of data (i.e. pixels) $\{y(1), y(2), \dots, y(N)\}$, a similarity graph $\mathcal{G} = (\mathcal{V}, \mathcal{R})$ is used to present the relation among these pixels. Each vertex $\mathcal{V}(i)$ in this graph represents

a pixel $y(i)$. Two vertices $y(i)$ and $y(j)$ are connected and $\mathcal{R}(i, j)$ is the weight of the edge between $y(i)$ and $y(j)$. This graph can also be presented by a $N \times N$ similarity matrix \mathcal{M}^S , in which element at i -column and j -line is the similarity $\mathcal{R}(i, j)$ between $y(i)$ and $y(j)$.

Spectral clustering performs on this similarity graph \mathcal{G} and it wants to find a partition of the graph such that vertices in the same cluster have high weights (meaning they are similar to each other) and vertices in different clusters have low weights (dissimilar to each other). The main processing chain of spectral clustering consists of 1) computing the Laplacian matrix \mathcal{M}^L ; 2) eigenvalue decomposition of \mathcal{M}^L ; 3) K-Means clustering on eigenvectors with $K = p$ the number of clusters.

Laplacian matrices

The popular ways to construct the similarity graph \mathcal{G} from the data set are to 1) connect the vertex pair with similarity more than a certain threshold, 2) connect each vertex with its k nearest neighbors or, 3) fully connect every pair of vertex. To fully represent the relation information, the third one should be used. There are many several expressions to compute the Laplacian matrix \mathcal{M}^L from the similarity matrix \mathcal{M}^S :

$$\begin{aligned} \mathcal{M}^L &= \mathcal{M}^D - \mathcal{M}^S && \text{Unnormalized Laplacian matrix,} \\ \mathcal{M}^L &= \mathcal{I} - \mathcal{M}^{D^{-\frac{1}{2}}} \mathcal{M}^S \mathcal{M}^{D^{-\frac{1}{2}}} && \text{Normalized Laplacian matrix [Chung, 1997],} \\ \mathcal{M}^L &= \mathcal{I} - \mathcal{M}^{D^{-1}} \mathcal{M}^S && \text{Normalized Laplacian matrix [Shi and Malik, 2000].} \end{aligned} \quad (7.2)$$

\mathcal{M}^D is the degree matrix, in which the non-diagonal elements are zero and the diagonal element at i -column is $\sum_j \mathcal{R}(i, j)$. In the minimization step, unnormalized Laplacian matrix cannot simultaneously minimize the disassociation across the partitions while maximizing the association within the cluster [Chung, 1997, Shi and Malik, 2000]. Therefore, normalized Laplacian matrix usually has better results in practice. In addition, in [Von Luxburg, 2007]'s work, the normalized Laplacian matrix presented in [Shi and Malik, 2000] is suggested since the one presented in [Chung, 1997] may be problematic if the eigenvectors contain particularly small entries.

Eigenvalue decomposition and K-Means clustering

The eigenvalue decomposition is applied on the Laplacian matrix \mathcal{M}^L . The eigenvalues $\{\lambda(1), \lambda(2), \dots, \lambda(N)\}$ are sorted in the ascending order, which are associated to eigenvectors $\{\mathbf{v}(1), \mathbf{v}(2), \dots, \mathbf{v}(N)\}$. In [Shi and Malik, 2000]'s work, a K -way cut is suggested due to the simplicity of the computation. The first p generalized eigenvectors $\{\mathbf{v}(1), \mathbf{v}(2), \dots, \mathbf{v}(p)\}$ are selected for the partition. These selected eigenvectors are used to form a new matrix (each line is a eigenvector). Then, this new matrix is split into vectors, while each column is a new vector $\mathbf{v}'(i)$, as shown in Fig.7.2. New vectors $\{\mathbf{v}'(1), \mathbf{v}'(2), \dots, \mathbf{v}'(N)\}$ are considered as N samples and have been classified into p clusters by K -means. The output labels $\{l(1), l(2), \dots, l(N)\}$ are the clustering results of the data set $\{y(1), y(2), \dots, y(N)\}$.

In the normalized cut algorithm, p is a important parameter controlling the number of the clusters. Choosing the number of clusters p is a general problem for all clustering algorithms, and a variety of successful methods have been devised (more details in [Von Luxburg, 2007]). Eigengap heuristic is one of them and particularly designed for spectral clustering. The main idea is to choose the number p such that all eigenvalues $\lambda_1, \dots, \lambda_p$ are very small, but λ_{p+1} is relatively larger (all eigenvalues are sorted in ascend-

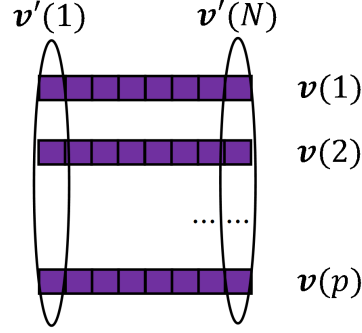


Figure 7.2: The selected eigenvectors $\{\mathbf{v}(1), \mathbf{v}(2), \dots, \mathbf{v}(p)\}$ are used to form a matrix (each line is an eigenvector). Each column of this matrix is a new vector $\mathbf{v}'(i)$.

ing order). However, this heuristic fails when the clusters of the data are overlapping (possibly because of noise).

7.2.2 Clustering using CCM

This section applies the normalized cut proposed by Shi and Malik [2000] to cluster the temporal pixel series $\{y_{t_1}(i), y_{t_2}(i), \dots, y_{t_N}(i)\}$, which can be summarized in Algorithm 3. In this algorithm, the normalized Laplacian matrix $\mathcal{M}^u(i)$ is computed by:

$$\mathcal{M}^L(i) = \mathcal{I} - \mathcal{M}^D(i)^{-1} \mathcal{M}(i) \quad (7.3)$$

$$\mathcal{M}^D(i) = \begin{bmatrix} \sum \mathcal{R}(y_{t_1}(i), y_{t_n}(i)) & 0 & \dots & 0 \\ 0 & \sum \mathcal{R}(y_{t_2}(i), y_{t_n}(i)) & \dots & 0 \\ \dots & \dots & \dots & \dots \\ 0 & 0 & \dots & \sum \mathcal{R}(y_{t_N}(i), y_{t_n}(i)) \end{bmatrix}$$

$$\sum \mathcal{R}(y_m, y_n) = \sum_{n=1, \dots, N} \mathcal{R}(y_m, y_n)$$

To estimate the number of clusters p , eigengap heuristic method has been applied here. However, to solve the overlapping problem of the eigengap, we binarize the CCM $\mathcal{M}(i)$ using the threshold used in the proposed change detection method, as shown in the following:

$$\mathcal{M}^b(i) = \begin{bmatrix} \mathcal{R}^b(y_{t_1}(i), y_{t_1}(i)) & \mathcal{R}^b(y_{t_1}(i), y_{t_2}(i)) & \dots & \mathcal{R}^b(y_{t_1}(i), y_{t_N}(i)) \\ \mathcal{R}^b(y_{t_2}(i), y_{t_1}(i)) & \mathcal{R}^b(y_{t_2}(i), y_{t_2}(i)) & \dots & \mathcal{R}^b(y_{t_2}(i), y_{t_N}(i)) \\ \dots & \dots & \dots & \dots \\ \mathcal{R}^b(y_{t_N}(i), y_{t_1}(i)) & \mathcal{R}^b(y_{t_N}(i), y_{t_2}(i)) & \dots & \mathcal{R}^b(y_{t_N}(i), y_{t_N}(i)) \end{bmatrix} \quad (7.4)$$

$$\mathcal{R}^b(y_m, y_n) = \begin{cases} 0 & \text{if } \mathcal{R}(y_m, y_n) < \tau \\ 1 & \text{if } \mathcal{R}(y_m, y_n) \geq \tau \end{cases}$$

The Eigengap heuristic performed on the binary change criterion matrix $\mathcal{M}^b(i)$ can easily be used to estimate the number of clusters p (see the example shown in Fig. 7.3). The toy model in Fig. 7.3.a has 2 clusters. Using CCM $\mathcal{M}(i)$ in 7.3.b, the difference between eigenvalues λ_2 and λ_3 is not large enough compared with the one between λ_1 and λ_2 . It is very easy to find the best estimation of p using the binary CCM $\mathcal{M}^b(i)$ in 7.3.c because

Types	p	Label series $\{l_{t_1}(i), \dots, l_{t_N}(i)\}$
Unchanged	1	$\{1, 1, \dots\}$
Step	2	$\{1, 1, \dots, 2, 2, \dots\}$
Impulse	2	$\{1, 1, \dots, 2, 2, \dots, 1, 1, \dots\}$
Cycle	2	$\{1, 1, \dots, 2, 2, \dots, 1, 1, \dots, 2, 2, \dots\}$
Complex	≥ 3	$\{1, 1, \dots, 2, 2, \dots, 3, 3, \dots, 4, 4, \dots\}$

Table 7.1: The identifications of different types of change.

of the large gap between λ_2 and λ_3 . It is obvious that this estimation of p highly depends on the choice of the thresholds. However, the robustness of the proposed change criteria (especially $\mathcal{R}^{\text{GLRT}}$ shown in Fig.6.2) can guaranty the estimation accuracy of p .

Algorithm 3 Clustering of the pixel series (Normalized spectral clustering [Shi and Malik, 2000])

Input:

A change criterion matrix $\mathcal{M}(i)$ of pixel series $\{y_{t_1}(i), \dots, y_{t_N}(i)\}$, number p of clusters to construct.

Output:

The clustering labels $\{l_{t_1}(i), \dots, l_{t_N}(i)\}$ for pixel series $\{y_{t_1}(i), \dots, y_{t_N}(i)\}$

- 1: Compute the normalized Laplacian matrix $\mathcal{M}^u(i)$ using Eq.7.3.
 - 2: Compute the first p generalized eigenvectors $\mathbf{v}_1, \dots, \mathbf{v}_p$ of $\mathcal{M}^u(i)$ ($\mathcal{M}^u(i)\mathbf{v} = \lambda\mathbf{I}\mathbf{v}$).
 - 3: Let \mathbf{v}' be the matrix containing the vectors $\mathbf{v}(1), \dots, \mathbf{v}(p)$ as columns.
 - 4: Consider each row of \mathbf{v}' as a sample, $\mathbf{v}' = \{\mathbf{v}'(1), \dots, \mathbf{v}'(N)\}$.
 - 5: Cluster the samples $\mathbf{v}'(1), \dots, \mathbf{v}'(N)$ with the k-means algorithm into clusters with $K = p$ as the number of clusters. The cluster labels of $\mathbf{v}'(1), \dots, \mathbf{v}'(N)$ are $l(1), \dots, l(n), \dots, l(N)$ ($l(n) \in \{1, \dots, p\}$).
 - 6: **return** Cluster labels $l(1), \dots, l(n), \dots, l(N)$
-

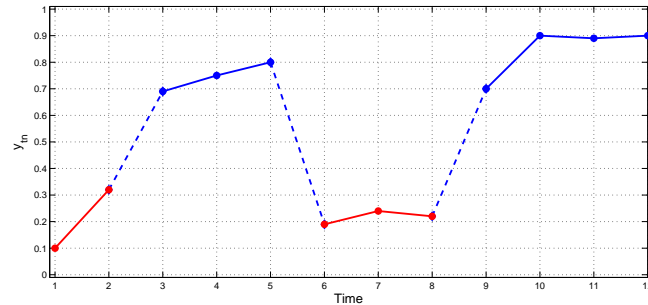
7.3 Recognition of change patterns

After clustering, each pixel series $\{y_{t_1}(i), \dots, y_{t_N}(i)\}$ has a cluster label series $\{l_{t_1}(i), \dots, l_{t_N}(i)\}$, in which $l_{t_n} \in \{1, \dots, p\}$. We can identify different types of change according to the transformation in the cluster label series $\{l_{t_1}(i), \dots, l_{t_N}(i)\}$. For example, if $p = 1$, there is no change among this pixel series. If $p = 2$ with cluster label series $\{1, 1, \dots, 1, 2, 2, \dots, 2\}$, it is a step change. Impulse change usually has $p = 2$ and cluster label series is $\{1, 1, \dots, 1, 2, 2, \dots, 2, 1, 1, \dots, 1\}$. When $p \geq 3$, the transformation is complex and changes are defined as complex cases. According to these identifications (details in Table 7.1), changes can be classified into several classes.

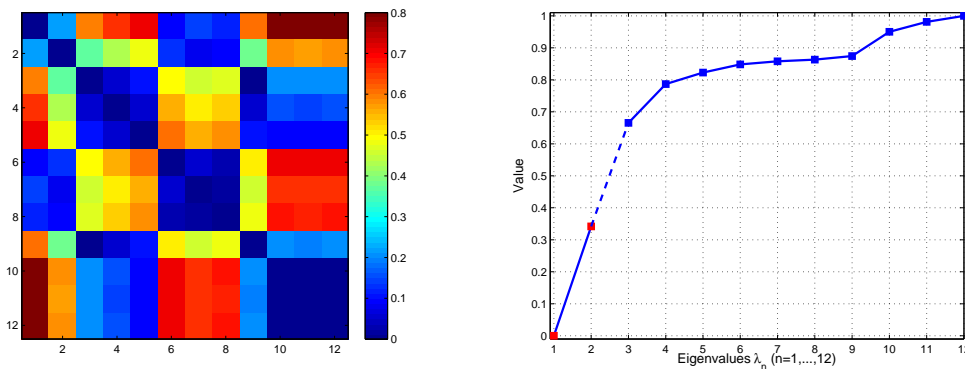
7.4 Experiments of Change Classification

7.4.1 Test on realistic SAR synthetic images

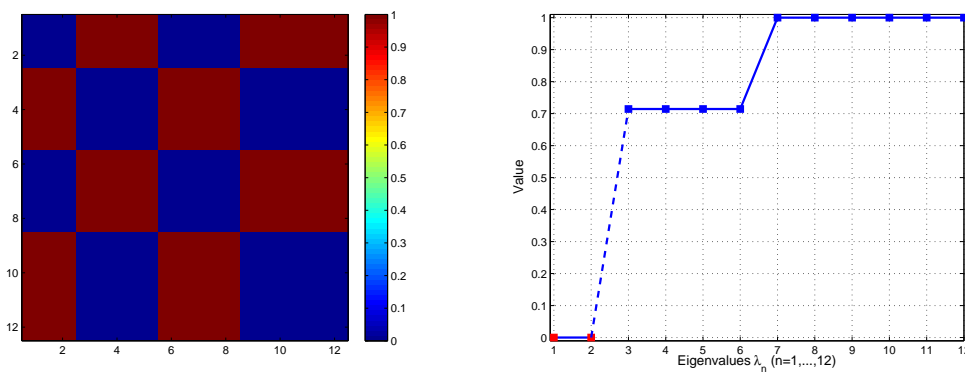
This experiment uses one denoised image of 21 single-look TerraSAR X-band images of Paris (France) sensed in 2011 as the noise-free image (multi-temporal denoising approach in



(a) A pixel series $\{y_{t_1}(i), \dots, y_{t_{12}}(i)\}$ which should be clustered into 2 groups (red and blue).



(b) CCM $\mathcal{M}(i)$ and its eigenvalues.



(c) Binary CCM $\mathcal{M}^b(i)$ and its eigenvalues.

Figure 7.3: Estimation of the number of clusters. (a) A pixel series $\{y_{t_1}(i), \dots, y_{t_{12}}(i)\}$ which should be clustered into 2 groups; (b) estimation of the number of clusters using CCM $\mathcal{M}(i)$, the gap between λ_2 and λ_3 is not obvious; (c) estimation of the number of clusters using binary CCM $\mathcal{M}^b(i)$, the gap between λ_2 and λ_3 is larger.

Confusion Matrix (%)		Classification results				
		Unch.	Step	Impl.	Cyc.	Comp.
Actual class	Unch	99.42	0.17	0.12	0.17	0.11
	Step	11.52	78.71	3.12	4.05	2.60
	Impl.	6.25	4.50	80.25	5.63	3.38
	Cyc.	17.50	2.92	1.58	75.58	2.42
	Comp.	4.27	5.52	2.85	6.23	81.14

Table 7.2: Confusion matrix of change classification results. Unch.: unchanged, Step: step change, Impl.:impulse change, Cyc.: cycle change and Comp.: complex change.

chapter 4), as shown in Fig.7.4.a. 6 single-look images are generated with different changes added in them. As shown in Fig.7.4.b, different kinds of changes have been introduced, such as step change (in red), impulse change (in green) and cycle change (in blue). Fig.7.4.c shows the change classification result by $\mathcal{R}^{\text{GLRT}}$. The confusion matrix in Tab.7.2 shows the good performance of the proposed classification method.

7.4.2 Test on real SAR images

We have 21 single-look TerraSAR X-band images identified as *Paris* in Paris (France) sensed in 2011 and 6 single-look TerraSAR X-band images identified as *San-Francisco* sensed in San-Francisco, U.S.A. 2007 and 2011. These images have been accurately registered using the sensor parameters. Fig.7.5.a and b only show the first noisy image and its denoising result. Fig.7.5.c shows the results of the change classification approach by $\mathcal{R}^{\text{GLRT}}$, in which red regions denote step changes, green are impulse changes and blue are cycle changes. We can observe that many boats in the river have been classified as impulse change. Fig.7.6 gives an illustration of examples of step change, impulse change; cycle change and complex change with the corresponding optical images ©Google (but the dates of the optical images are not exactly the same as the SAR images).

We can see that the step changes might correspond to some facilities in the stadium, impulse changes and complex changes are boats moored at piers, the cycle changes are the river bank. The proposed method has good performance in classifying these *interrupt* changes, however for the continuous changes, like the growth of vegetation, the proposed method probably considers them as complex changes.

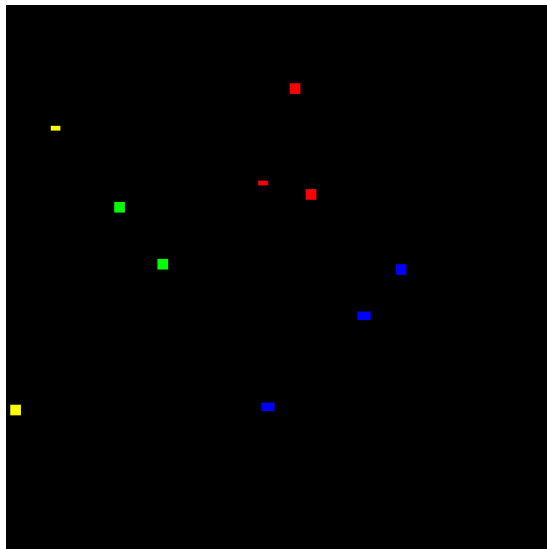
7.5 Conclusion

Based on the change criteria approximated LRT $\mathcal{R}^{\text{ALRT}}$ and generalized LRT $\mathcal{R}^{\text{GLRT}}$ presented in chapter 6, a change classification method has been introduced here. The purpose of this classification is to exploit the temporal behavior information of the changes. It applies a normalized cut algorithm to cluster the temporal pixel series, then classifies the pixel series by the clustering labels. After classification, pixel series are labeled as step change, impulse change, cycle change and complex change associated to step, impulse, cycle and complex fluctuation of intensity in the temporal domain.

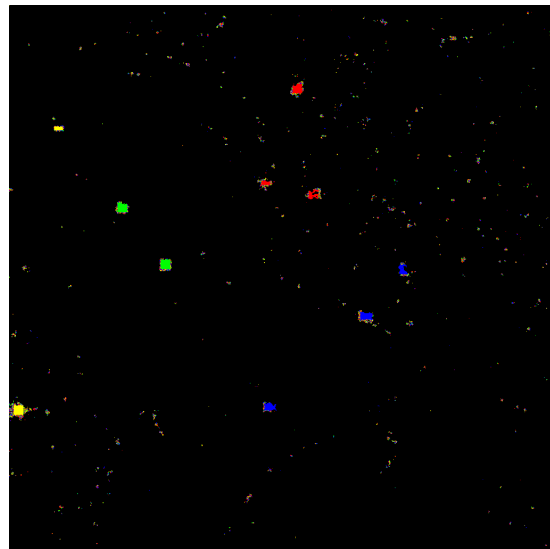
This is the second contribution of this PhD and has been published in [Su et al., 2014a, 2015]. In the next part of this PhD, we will extend the proposed 2SPPB filter, change criteria and change classification methods to the application of the SAR image compression and SAR change information updating.



(a) "Noise-free" image with synthetic changes (only 1 image has been shown).

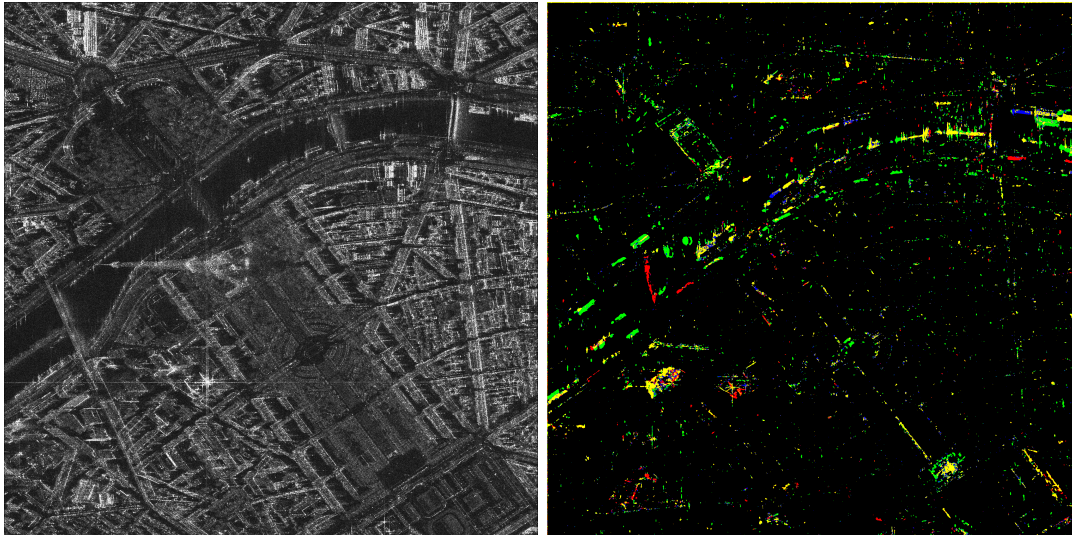


(b) Ground-truth map of changes

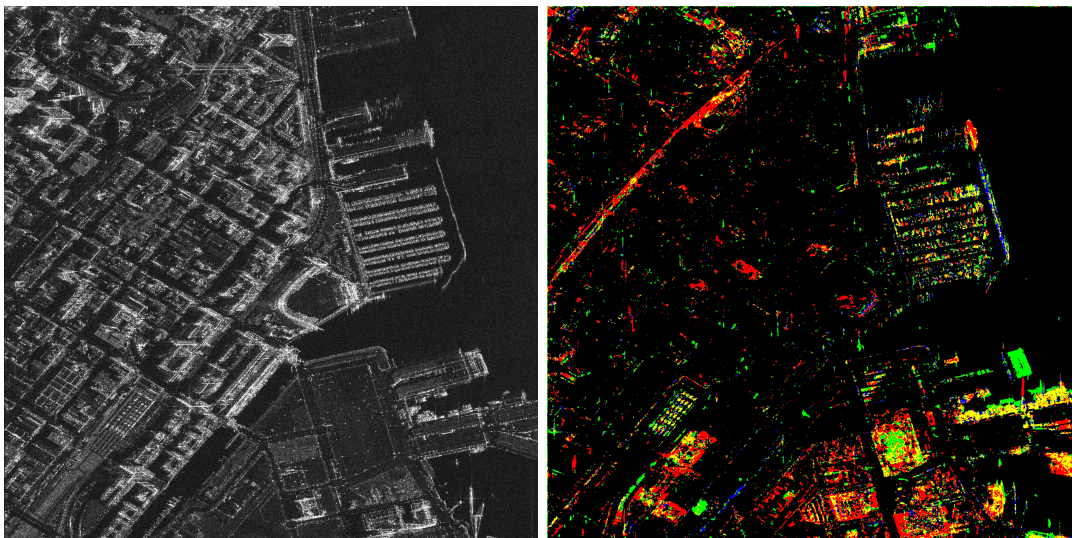


(c) Change classification results by $\mathcal{R}^{\text{GLRT}}$

Figure 7.4: Change classification of synthetic SAR images (6 single-look SAR images). (a) "noise-free" image with synthetic changes (only 1 image has been shown); (b) ground-truth map of changes; (c) change classification results by $\mathcal{R}^{\text{GLRT}}$ (black: no change, red: step change, green: impulse change, blue: cycle change and yellow: complex change).

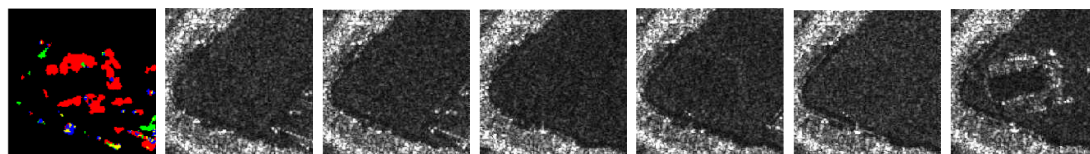


(a) *Paris*, 21 single-look TerraSAR-X images

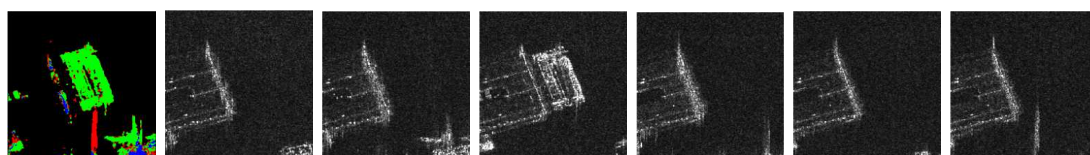


(b) *San-Francisco*, 6 single-look TerraSAR-X images

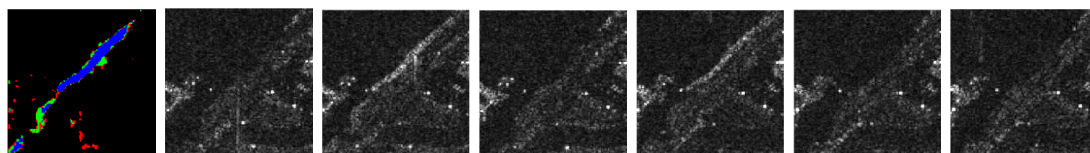
Figure 7.5: Change classification on Real SAR images. From top to bottom: *Paris*, 21 single-look TerraSAR-X images and *San-Francisco*, 6 single-look TerraSAR-X images. From left to right: noisy image y_{t_1} and change classification results by criterion $\mathcal{R}^{\text{GLRT}}$ (black: no change, red: step change, green: impulse change, blue: cycle change yellow: complex change.).



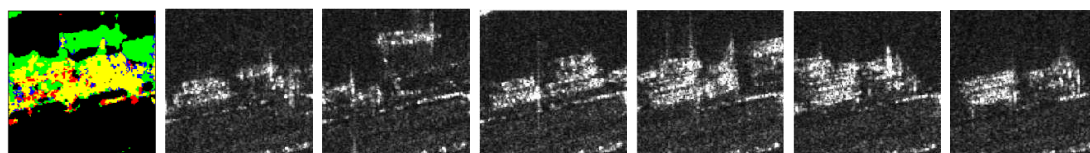
(a) The AT&T park in San-Francisco. Example of step change in *San-Francisco*. From left to right, the change classification results, the noisy image from date t_1 to t_6 .



(b) The Pier 48 in San-Francisco. Example of impulse change in *San-Francisco*. From left to right, the change classification results, the noisy image from date t_1 to t_6 .



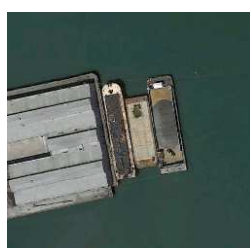
(c) The bank of the river in the Mission Creek Garden. Example of cycle change in *San-Francisco*. From left to right, the change classification results, the noisy image from date t_1 to t_6 .



(d) The Pier 50 in San-Francisco. Example of complex change in *San-Francisco*. From left to right, the change classification results, the noisy image from date t_1 to t_6 .



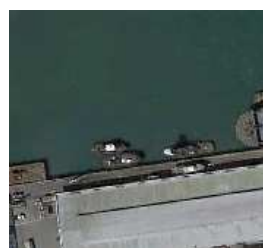
(e)



(f)



(g)



(h)

Figure 7.6: Details of change classification results of *San-Francisco* data set. (a-d) from top to bottom: from left to right: the AT&T park, the Pier 48, the bank of the river in the Mission Creek Garden and the Pier 50. They are step change, impulse change; cycle change and complex change. (black: no change, red: step change, green: impulse change, blue: cycle change and yellow: complex change). (e-h) the optical images ©Google Earth (imagery data 2014.02.24) corresponding to images (a-d).

Part III

Information Updating and
Compression

Chapter 8

Information Updating of SAR Time Series

The quantity of multi-temporal SAR images is experiencing a rapid growth, especially after the launch of some recent and new sensors like TanDEM-X (revisit cycle of 11 days) combined with TerraSAR-X, Sentinel-1 (revisit cycle of 12 days with Sentinel-1A, 6 days with the combination of Sentinel-1A and Sentinel-1B), etc. New challenges related to big data processing then raise: 1) how to compress the data to reduce the storage space, and 2) how to rapidly exploit useful information in this big data. We propose two compression methods for the multi-temporal SAR images in this chapter, *pixel-level* compression and *patch-level* compression, to solve these big data problems for further processing like denoising or change classification as seen in the previous chapters. We propose in this chapter to exploit our classification results to define a compression scheme, which can then be used for filtering updating, or classification updating. The main idea is to store only on representative value for a set of unchanged values. We present two 'compression' approaches one defined at the pixel-level, and the other one at the patch-level, which is the main structure of our processings as explained previously. In the implementation, the similar pixels/patches are found by a normalized cut clustering based on the change criterion matrix (CCM) presented in chapter 7, and compressed by simple averaging. A Huffman encoding algorithm is then applied to further compress the data.

Basically, the pixel-level compression scheme produces higher compression ratio, but it needs to be followed by a patch reconstructing step when the compressed data are used in patch-based applications, e.g. our 2S-PPB filter. Instead the patch-level compression stores the averaged patches, thus the compressed data can be rapidly used in patch-based applications but at the price of a lower compression ratio. These two approaches will be described and compared in the following chapters. Then with these compressed and stored data, when a new SAR image is acquired, we apply the proposed 2S-PPB filter to denoise the new image and NORCAMA change detection method to update the change classification results using the compressed data. After the processing, the stored compressed data are updated with the information extracted from the new image.

Fig.8.1 shows the main framework of the proposed compression and updating processes in this chapter. This chapter will firstly present the compression method (pixel-level and patch-level compressions) and then the updating method (denoising and change detection of the newly acquired SAR image). The experiments will compare the 2S-PPB filtering and NORCAMA change detection results using the compressed data and the original SAR

time series.

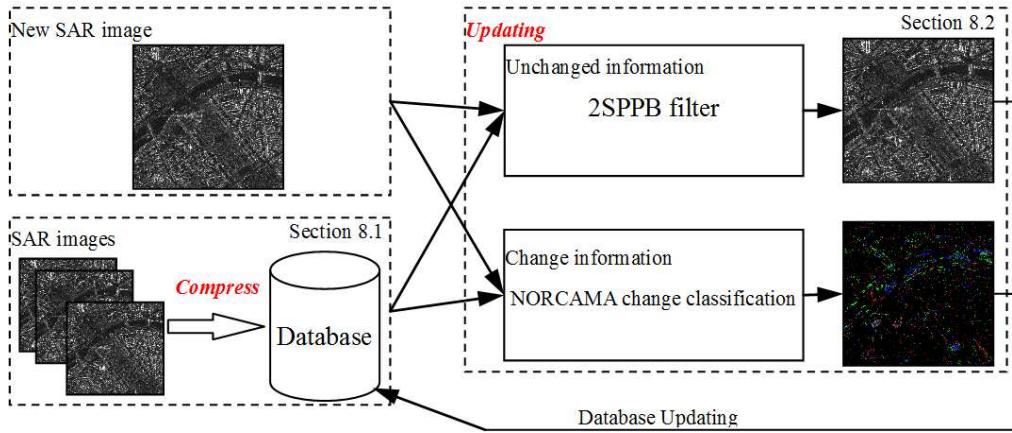


Figure 8.1: The problem of SAR data updating considered in this chapter.

8.1 Concept and method of compression

The pixel/patch-level compression consists of a lossy compression followed by a lossless compression, as shown in Fig.8.2.a and b. The lossy compression is performed on each pixel series. It finds the *similar* pixels or patches in the temporal domain by the normalized-cut clustering presented in chapter 7. The pixel-level compression computes the average of the pixels in a cluster (corresponding to the center of the cluster), as shown in the middle of Fig.8.2.a. Instead, the patch-level compression considers both the pixels and their neighbors (the patches surrounding them), and stores the averaged patches, as shown in the middle of Fig.8.2.b. Both the pixel-level and patch-level compressions finally have a Huffman encoding step to further compress the clustering labels and the averaged pixels/patches. The two approaches and their advantages and drawbacks are now described in details.

8.1.1 Pixel-level compression

The denoised images $\{\hat{u}_{t_1}, \hat{u}_{t_2}, \dots, \hat{u}_{t_N}\}$ associated to SAR image series $\{y_{t_1}, y_{t_2}, \dots, y_{t_N}\}$ are firstly obtained by the proposed 2S-PPB filter presented in chapter 4. The compression is applied pixel by pixel. At each position i , the pixel series $\{y_{t_1}(i), y_{t_2}(i), \dots, y_{t_N}(i)\}$ and the associated denoised pixel series $\{\hat{u}_{t_1}(i), \hat{u}_{t_2}(i), \dots, \hat{u}_{t_N}(i)\}$ are considered. As shown in Fig.8.2.a, the lossy compression step consists in storing the labels of the clusters for the different dates of the series, and a unique filtered intensity value $y_{c_m}(i)$ for each cluster. All these steps based on the previous chapters are described in Algorithm 4. Then, a Huffman compression is applied on the clustering labels $\{l_{t_1}(i), l_{t_2}(i), \dots, l_{t_N}(i)\}$ and clustering centers $\{y_{c_1}(i), y_{c_2}(i), \dots, y_{c_M}(i)\}$ to further compress the data.

Discussion about the compression ratio.

The data type of SAR intensity is *Float* (32 bits). Thus, the storage space (or the file size) O_o of the original SAR time series can be computed by:

$$O_o = 32N_t N_p \text{ bit} \quad (8.2)$$

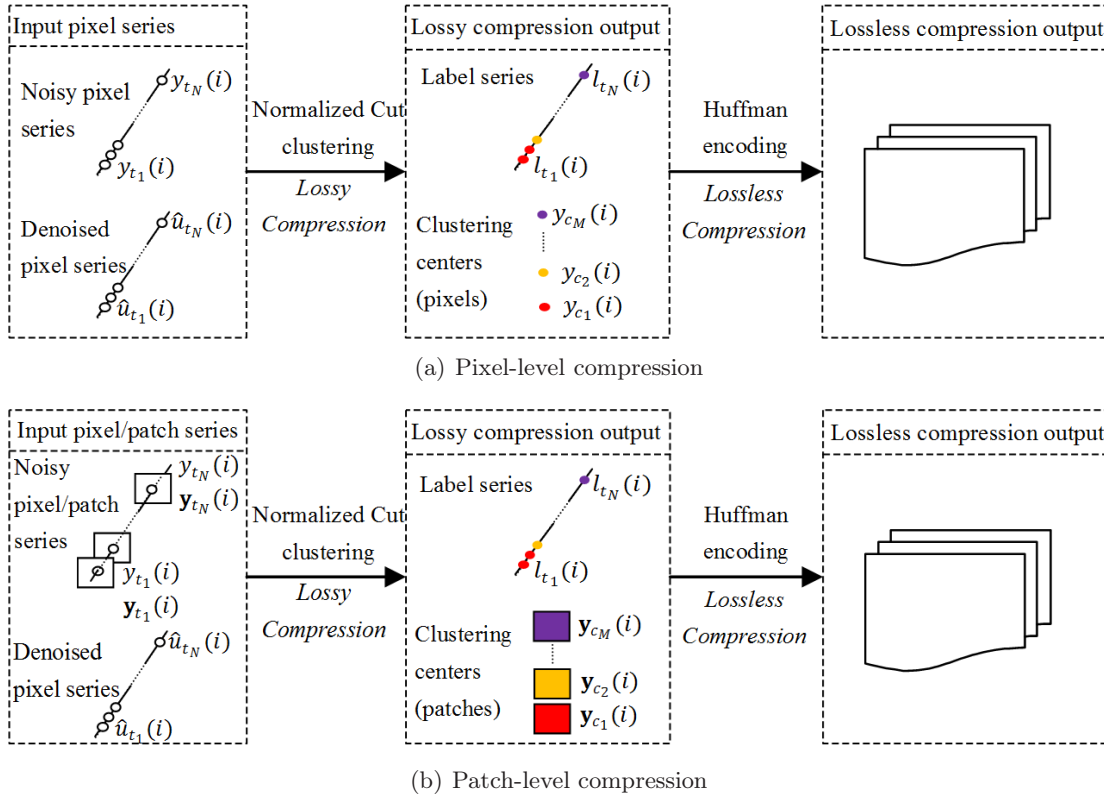


Figure 8.2: The compression processing. Each pixel series $\{y_{t_1}(i), y_{t_2}(i), \dots, y_{t_N}(i)\}$ (with associated denoised pixel series $\{\hat{u}_{t_1}(i), \hat{u}_{t_2}(i), \dots, \hat{u}_{t_N}(i)\}$) is firstly clustered by a normalized-cut algorithm presented in chapter 7. Pixel-level compression (a) keeps clustering centers (averaged pixels), while patch-level compression (b) keeps the clustering centers and their neighbors (averaged patches). Then the clustering results (both the labels and clustering centers) are further compressed by a Huffman encoding algorithm.

where N_t is the number of images in the SAR time series and N_p is the number of pixel in each image. The compression ratio is the ratio of O_o and the storage space of compressed data O_c :

$$r = \frac{O_o}{O_c} \quad (8.3)$$

$$O_c = O_l + O_v \quad (8.4)$$

where O_l is storage space of the (lossless compressed) labels and O_v for the (lossless compressed) centers of clusters.

1) O_l : This value depends on the change arising between the different dates. The worst case would be a full change of the whole image from one date to the next one. Since we can not model it theoretically, we propose to use an empirical study to give a general behaviour. In the Huffman encoding, the average description length \bar{b} to represent the labels can be calculated by:

$$\bar{b} = \sum_{l=1}^{M-1} p(l)l + p(M)(M-1) \quad (8.5)$$

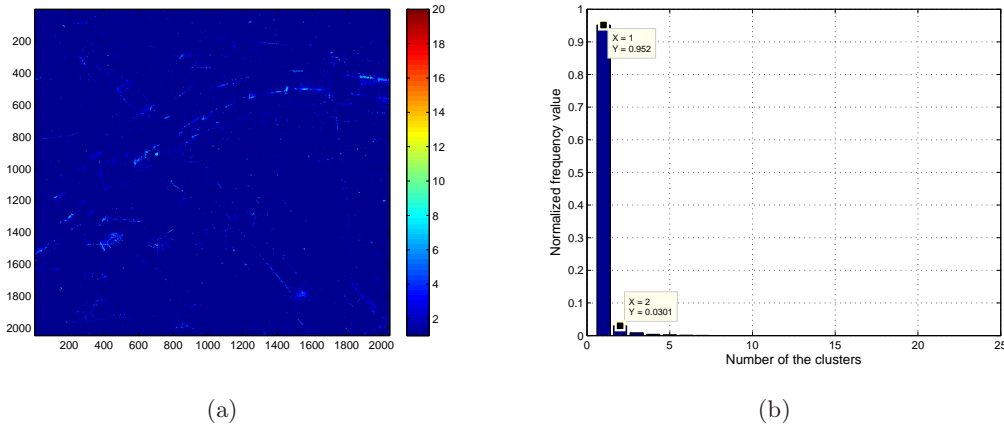


Figure 8.3: (a) Number of clusters and (b) Normalized histogram (distribution) of number of clusters. For this example and 20 dates, pixel series usually has only 1 or 2 clusters after the lossy compression.

algorithms which can better handle the distribution of labels could be used to improve this compression. However, we still use the Huffman encoding here for the convenience of implementation.

2) O_v : Given a certain SAR time series, the size of O_v depends on the number of the clusters of each pixel series, or the *new* pixels containing in each image compared with previous images. However the number of new pixels is difficult to estimate, thus we also use the number of new pixels empirically counted from the *Paris* data set to give some numerical intuition. On average, 0.7%~1% pixels in each image are new. Without any compression, the storage space for the clustering centers will be:

$$O'_v \approx 32N_p(1 + 1\%N_t) \quad (8.8)$$

Note that the computation of O'_v in Eq.(8.8) does not consider any compression, while in reality a Huffman compression has been applied. Therefore, the real storage space O_v will be smaller than O'_v given by Eq.(8.8).

So far, we can approximately estimate O_c by combining O'_l given by Eq.(8.7) and O'_v given by Eq.(8.8):

$$O_c \approx O'_l + O'_v = 1.0244N_tN_p + 32N_p(1 + 1\%N_t) . \quad (8.9)$$

The approximate compression ratio r can thus computed by:

$$\begin{aligned} r &\approx 32N_tN_p : [1.0244N_tN_p + 32N_p(1 + 1\%N_t)] \\ &= \frac{32N_t}{1.3444N_t + 32} \end{aligned} \quad (8.10)$$

The blue line in Fig.8.4.a shows the approximate compression ratio r against the number of images N_t . However, it must be clear that the computation of r given by Eq.(8.10) is not strict since O'_v is larger than what it is in reality. The real compression ratio should be higher than this approximate compression ratio, as shown by the green line (the real compression ratio computed using *Paris* data set) in Fig.8.4.a. But we can still conclude a qualitative result that when N_t increasing, the compression ratio r will correspondingly

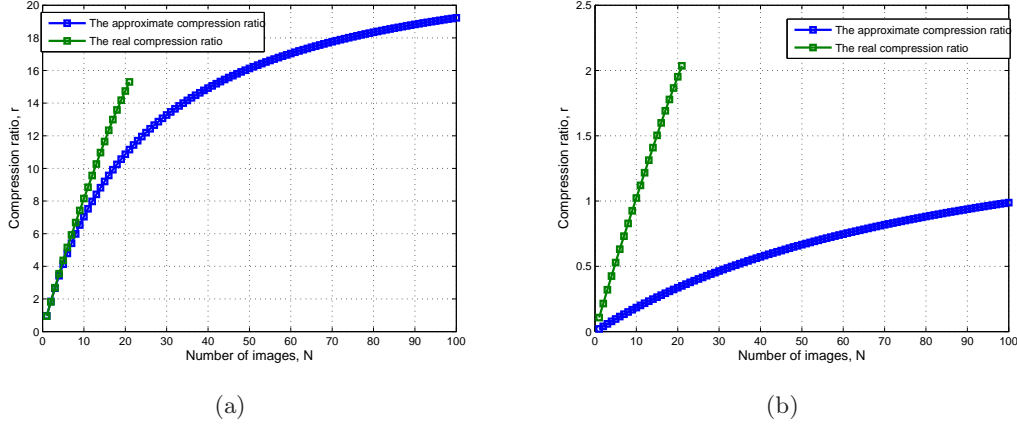


Figure 8.4: The real and approximate compression ratio against the number of images N_t . (a) Pixel-level compression and (b) patch-level compression. The blue line is the approximate estimation of compression ratio, while the green line is the real compression ratio tested on the *Paris* data set.

increase. The green line also shows the same trend than the approximate compression ratio as the blue line with the increase of N_t . It should be noted that for few images, the "compressed" size is bigger than the storage size.

Reconstructing patches from the compressed data

As explained before, we need to reconstruct a patch $\mathbf{y}'_{c_m}(i)$ surrounding pixel $y_{c_m}(i)$ when comparing $y_{c_m}(i)$ with pixels in a new arriving SAR image. Taking pixel $y_{c_m}(i)$ as an example, the reconstruction of patch $\mathbf{y}'_{c_m}(i)$ for pixel $y_{c_m}(i)$ can be summarized as the following steps (as shown in Fig.8.5):

- reconstruct the label patch for each label in the label series $\{l_{t_1}(i), l_{t_2}(i), \dots, l_{t_N}(i)\}$, e.g. the k -th neighbor of label $l_{t_n}(i)$ is $l_{t_n}(i+k)$ which can be found in label series $\{l_{t_1}(i+k), l_{t_2}(i+k), \dots, l_{t_N}(i+k)\}$;
- replace the labels by their associated clustering centers, for instance, $l_{t_n}(i+k)$ is replaced by value $y'_{c_{m'}}(i)$ with $m' = l_{t_n}(i+k)$;
- patch $\mathbf{y}'_{c_m}(i)$ is then defined as the patch with the averaged values (center pixel label $l_{t_n}(i)$ is m).

Patch $\mathbf{y}'_{c_m}(i)$ can be considered as an *averaged* surrounding of $y_{c_m}(i)$, which will be used in the patch comparison of 2S-PPB. Note that different pixels in patch $\mathbf{y}'_{c_m}(i)$ may have different number of looks, which depend on the number of looks of the added candidates.

8.1.2 Patch-level compression

Since the patch reconstruction step will cost extra time in the pixel-level compression, we present in this section another compression scheme to reduce this time consumption. It has the same processing steps as the pixel-level compression in Algorithm 4, but the only difference is that in step 5 of Algorithm 4 pixel $y_{t_n}(i)$ is replaced by its associated patch $\mathbf{y}_{t_n}(i)$. Thus, the averaged result will be a patch $\mathbf{y}_{c_m}(i)$, as shown in Fig.8.2.b.

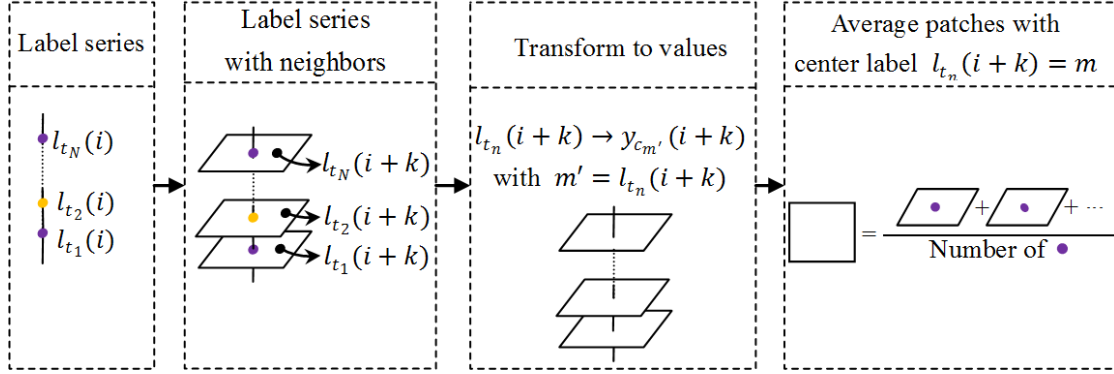


Figure 8.5: The reconstruction of patch for pixel $y_{c_m}(i)$. From left to right, 1) the label series $\{l_{t_1}(i), l_{t_2}(i), \dots, l_{t_N}(i)\}$, 2) reconstruct the label patches for each label $l_{t_n}(i)$, 3) transform the label patches to value patches, 4) average these value patches with the same center label m .

Taking pixel $y_{c_m}(i)$ as example, it is given by Eq.(8.1) in the pixel-level compression. In the patch-level compression, $\mathbf{y}_{c_m}(i)$ is computed by the same way:

$$\mathbf{y}_{c_m}(i) = \frac{1}{Z} \sum_{n=1}^N w(n) \mathbf{y}_{t_n}(i)$$

$$w(n) = \begin{cases} 1 & \text{if } l_{t_n} = m \\ 0 & \text{otherwise} \end{cases} \quad (8.11)$$

$$Z = \sum_{n=1}^{n=N} w(n)$$

Assuming the number of looks of $\mathbf{y}_{t_n}(i)$ is L , the number of looks of $\mathbf{y}_{c_m}(i)$ is a constant value, ZL , which is different from the varying number of looks in reconstructed patch $\mathbf{y}'_{c_m}(i)$. Label l_{t_n} is the same as the one in the pixel-level compression. Consequently, patches $\mathbf{y}_{c_m}(i)$ instead of just center pixel $y_{c_m}(i)$ are stored in the patch-level compression. Of course the Huffman compression is also applied to obtain the final compressed data.

Using the same approximate computation, the compression ratio of the patch-level compression is shown in Fig.8.4.b. Since the blue line (the approximate compression ratio) does not consider the lossless compression of the clustering centers, the real compression ratio (in green line) of *Paris* data set is significantly higher than the approximate compression ratio.

Compared with the pixel-level compression, the patch-level compression can directly use the stored patches and needs less time when dealing with patches. However the price is larger storage space for patch-level compression (it can be seen by the comparison of compression ratios in Fig.8.4.a and b).

Beyond the time and space consumptions, the difference between the two compression schemes is the difference of the patch $\mathbf{y}_{c_m}(i)$ and the reconstructed patch $\mathbf{y}'_{c_m}(i)$. Both $\mathbf{y}_{c_m}(i)$ and $\mathbf{y}'_{c_m}(i)$ are the neighbors of pixel $y_{c_m}(i)$, while they may present different values. It is difficult to measure the difference between $\mathbf{y}_{c_m}(i)$ and $\mathbf{y}'_{c_m}(i)$ in a theoretical way. We thus propose to do an empirical study of the difference computed in the real SAR data, *Paris* data set. The difference between $\mathbf{y}_{c_m}(i)$ and $\mathbf{y}'_{c_m}(i)$ is measured by

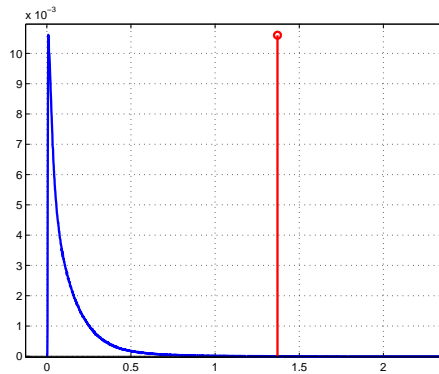


Figure 8.6: The normalized histogram of difference between $\mathbf{y}_{c_m}(i)$ and $\mathbf{y}'_{c_m}(i)$ is shown in blue line. If considering the comparison of $\mathbf{y}_{c_m}(i)$ and $\mathbf{y}'_{c_m}(i)$ as a change detection problem, the threshold selected by the quantiles with $\alpha = 0.01$ shown in red line (the left part is unchanged and the right part is changed).

$S_{\text{GLR}}(\mathbf{y}_{c_m}(i), \mathbf{y}'_{c_m}(i))$ given by Eq.(3.26). The blue line in Fig.8.6 shows the histogram of this difference. The comparison between $\mathbf{y}_{c_m}(i)$ and $\mathbf{y}'_{c_m}(i)$ can also be seen as a change detection problem. Therefore, change detection threshold has been calculated using synthetic data by the same method used in our proposed change detection method in chapter 6. We can find that most pairs of $\mathbf{y}_{c_m}(i)$ and $\mathbf{y}'_{c_m}(i)$ are *unchanged* (lower than the threshold). Thus, pixel-level compression and patch-level compression will lead to similar performance in the patch comparison, which will also be illustrated in the 2S-PPB denoising experiments in section 8.3.2.

8.1.3 The relation with usual data compression schemes

Compression of audio, images and video data has been well studied in communication field and lots of mature algorithms and compression standards have been proposed. They can be divided into two groups: lossless compression and lossy compression. Lossless compression usually exploits the statistical redundancy and represents data without losing any information. Lempel-Ziv compression methods, Huffman coding and Burrows-Wheeler transform [Burrows and Wheeler, 1994] are the most popular algorithms for lossless storage. Lossy compression represents data with loss of some information, but the loss must be acceptable under some conditions. For instance, the human eye is more sensitive to subtle variations in luminance than it is to variations in color. Based on this fact, JPEG image compression [Pennebaker and Mitchell, 1993] rounds off bits for nonessential information. Of course, there is a corresponding trade-off between preserving information and reducing data size. JPEG image compression is also used in video compression, like H.264/MPEG-4 AVC [Wiegand et al., 2003] and H.265/HEVC [Sullivan et al., 2012]. More recently, Donoho [2006] proved that compressed sensing can compress and reconstruct a signal (audio, images or video) with even fewer samples than the sampling theorem requires, if the signal is sparse.

In summary, most ordinary data compression methods (lossy compression) aim at reducing the size of data for easy storage and real-time transport. They find a balance in the trade-off between visual performance and reducing data size. Unlike the visual perfor-

mance considered by ordinary data compression methods, our proposed compression has to preserve information that can be used in SAR reflectivity estimation and change detection. Besides, our main purpose in this chapter is to speed up the processing steps when dealing with long time series.

8.2 Updating method

After the compression of SAR time series, at each position i we have the label series $\{l_{t_1}(i), l_{t_2}(i), \dots, l_{t_N}(i)\}$, the clustering centers $\{y_{c_1}(i), y_{c_2}(i), \dots, y_{c_M}(i)\}$ and associated reconstructed patches $\{\mathbf{y}'_{c_1}(i), \mathbf{y}'_{c_2}(i), \dots, \mathbf{y}'_{c_M}(i)\}$ (pixel-level compression) or associated surrounding patches $\{\mathbf{y}_{c_1}(i), \mathbf{y}_{c_2}(i), \dots, \mathbf{y}_{c_M}(i)\}$ (patch-level compression). For the sake of simplicity, we denote in the following both the patches from pixel-level and patch-level compression as $\{\mathbf{y}_{c_1}(i), \mathbf{y}_{c_2}(i), \dots, \mathbf{y}_{c_M}(i)\}$ without loss of generality. This section will present how the compressed data can be used to update the stable information by 2S-PPB filter and the unstable information by the proposed change detection/classification methods.

8.2.1 2S-PPB filtering for stable information updating

When a new SAR image $y_{t_{N+1}}$ is acquired, we firstly find similar information in the database to denoise it. Taking a pixel $y_{t_{N+1}}(i)$ as an example, the original 2S-PPB filter finds similar pixels in the pixel series $\{y_{t_1}(i), y_{t_2}(i), \dots, y_{t_N}(i)\}$ by comparing patch $\mathbf{y}_{t_{N+1}}(i)$ with patch series $\{\mathbf{y}_{t_1}(i), \mathbf{y}_{t_2}(i), \dots, \mathbf{y}_{t_N}(i)\}$. While with the compressed data, 2S-PPB filter will apply this searching among the clustering centers $\{y_{c_1}(i), y_{c_2}(i), \dots, y_{c_M}(i)\}$. Patch $\mathbf{y}_{t_{N+1}}(i)$ thus is compared with $\{\mathbf{y}_{c_1}(i), \mathbf{y}_{c_2}(i), \dots, \mathbf{y}_{c_M}(i)\}$, and this comparison can be given by:

$$S(\mathbf{y}_{t_{N+1}}(i), \mathbf{y}_{c_m}(i)) = S_{\text{GLR}}(\mathbf{y}_{t_{N+1}}(i), \mathbf{y}_{c_m}(i)) \quad (8.12)$$

where $S_{\text{GLR}}(\cdot)$ is the generalized likelihood ratio (GLR) based similarity given by Eq.(3.26). Like the temporal step of 2S-PPB filter, $S(\mathbf{y}_{t_{N+1}}(i), \mathbf{y}_{c_m}(i))$ is thresholded to determine if $\mathbf{y}_{c_m}(i)$ is similar with (or unchanged compared with) $\mathbf{y}_{t_{N+1}}(i)$. The center pixels associated to the similar/unchanged patches $\mathbf{y}_{c_m}(i)$ are then combined with the new pixel $y_{t_{N+1}}(i)$ with the following expressions:

$$\begin{aligned} \tilde{y}_{t_{N+1}}(i) &= \frac{1}{Z} \left[L_{t_{N+1}}(i) y_{t_{N+1}}(i) + \sum_{m=1}^M f^b(S(\mathbf{y}_{t_{N+1}}(i), \mathbf{y}_{c_m}(i))) L_{c_m}(i) y_{c_m}(i) \right], \\ Z &= L_{t_{N+1}}(i) + \sum_{m=1}^M f^b(S(\mathbf{y}_{t_{N+1}}(i), \mathbf{y}_{c_m}(i))) L_{c_m}(i), \end{aligned} \quad (8.13)$$

where

$$f^b(S(\mathbf{y}_{t_{N+1}}(i), \mathbf{y}_{c_m}(i))) = \begin{cases} 1, & \text{if } S(\mathbf{y}_{t_{N+1}}(i), \mathbf{y}_{c_m}(i)) > \tau, \\ 0, & \text{otherwise} \end{cases} \quad (8.14)$$

$\tilde{y}_{t_{N+1}}(i)$ is the temporal estimation and Eq.(8.13) is also the temporal step of the 2S-PPB using the compressed data. Z is the normalization parameter and corresponding to the number of looks $\tilde{L}_{t_{N+1}}(i) = Z$ associated to $\tilde{y}_{t_{N+1}}(i)$. The threshold τ is selected by the same way as presented in section 4.2.1. Note that the threshold τ varies pixel by pixel,

since it depends on the number of looks of patch $\mathbf{y}_{t_{N+1}}(i)$ and $\mathbf{y}_{c_m}(i)$. The temporal mean image $\tilde{y}_{t_{N+1}}$ is obtained by applying Eq.(8.13) on each pixel of the new image. We can finally get the 2S-PPB denoising result by applying the spatial denoising step of 2S-PPB on the temporal mean image $\tilde{y}_{t_{N+1}}$ (details presented in section 4.2.2).

The change criterion given by Eq.(8.12) consists of only the GLR similarity, instead of the combination of GLR similarity and KL similarity of the original 2S-PPB presented in section 4.2.1. The reason for only using GLR similarity is to reduce the time consumption of the denoising step.

8.2.2 Change detection for updating

To detect changes between the new image $y_{t_{N+1}}$ and one of the previous images y_{t_n} using the change detection method presented in chapter 6, we need to reconstruct image y_{t_n} . The reconstructing process is the same as to obtain the reconstructed patches illustrated in Fig.8.5. Each label $l_{t_n}(i)$ (associated to pixel $y_{t_n}(i)$) at time t_n is replaced by the associated clustering center $y_{c_m}(i)$ with $m = l_{t_n}(i)$ ($y_{c_m}(i)$ is the center pixel of patch $\mathbf{y}_{c_m}(i)$ or $\mathbf{y}'_{c_m}(i)$). We then have the reconstructed image y'_{t_n} (associated to y_{t_n}), which consists of pixels $y_{c_m}(i)$ with different number of looks. The changes between image y'_{t_n} and new image $y_{t_{N+1}}$ can be detected by the following steps:

- denoise y'_{t_n} by the spatial step of the 2S-PPB filter;
- denoise $y_{t_{N+1}}$ by the 2S-PPB filter presented in section 8.2.1;
- calculate the change criterion $\mathcal{R}^{\text{ALRT}}$ given by Eq.(6.3) or $\mathcal{R}^{\text{GLRT}}$ given by Eq.(6.7) presented in section 6.1 and 6.2 respectively;
- threshold the change criterion using the quantiles method presented in section 6.3.

8.2.3 Change classification for updating

Following the idea of change detection in previous section, we can also apply the change classification on the compressed data when a new SAR image is acquired. The processing chain are given in the following:

- reconstruct each previous image y'_{t_n} (associated to original image $y_{t_n}, n = 1, 2, \dots, N$);
- denoise each y'_{t_n} by the spatial step of the 2S-PPB filter;
- denoise $y_{t_{N+1}}$ by the 2S-PPB filter presented in section 8.2.1;
- calculate the change criterion matrix of each position i by Eq.(7.1) presented in section 7.1;
- classify the changes by the NORCAMA algorithm presented in chapter 7.

8.2.4 Database updating

After dealing with a newly acquired SAR image, the stable and unstable information should be added to the database (or the compressed data) for the processing of next new images. According to the change classification results (the new label series $\{l_{t_1}(i), l_{t_2}(i), \dots, l_{t_N}(i), l_{t_{N+1}}(i)\}$ of each pixel i), we can find that:

- if $l_{t_{N+1}}(i)$ is a new label ($l_{t_{N+1}}(i) \neq l_{t_n}(i)|_{n=1,2,\dots,N}$), a new clustering center $y_{c_{M+1}}(i) = y_{t_{N+1}}(i)$ or $\mathbf{y}_{c_{M+1}}(i) = \mathbf{y}_{t_{N+1}}(i)$ will be added to the database.
- if $l_{t_{N+1}}(i) = l_{t_n}(i)$, the associated clustering center $y_{c_m}(i)$ or $\mathbf{y}_{c_m}(i)$ ($m = l_{t_n}(i)$) will be updated by:

$$\begin{aligned}
 y_{c_m}(i) &= \frac{L_{t_{N+1}}(i)y_{t_{N+1}}(i) + L_{c_m}(i)y_{c_m}(i)}{L_{t_{N+1}}(i) + L_{c_m}(i)}, \text{ for pixel-level compression,} \\
 \mathbf{y}_{c_m}(i) &= \frac{L_{t_{N+1}}(i)\mathbf{y}_{t_{N+1}}(i) + L_{c_m}(i)\mathbf{y}_{c_m}(i)}{L_{t_{N+1}}(i) + L_{c_m}(i)}, \text{ for patch-level compression.}
 \end{aligned} \tag{8.15}$$

8.3 Experiments of compression and updating

We test our compression and updating methods on both synthetic images and real SAR time series.

8.3.1 Time and space consumptions

Compression. We apply the proposed compression method on the *Paris* data set, 21 single-look TerraSAR images. Only the first 20 images are used in the compression and the last image is considered as the newly acquired image which will be used in the updating step. Each image in the *Paris* data set has 2048×2048 pixels and the data type of SAR intensity value is *Float*. The saved labels are integer and we save them as Integer data type. Table 8.1 shows the time consumption using Intel Core 2 Quad CPU (Q9550) 2.83GHz and the compression ratio of the proposed patch level and pixel level compression compared with MAT format (a lossless data compression applied by the *Save* function of MATLAB, Versions 7.3 or later)¹. The patch size in the patch level compression is selected as 7×7 the same size as used in 2S-PPB filter.

The higher compression ratio denotes less cost of storage space. About the time consuming of the compression, since it performs pixel by pixel some parallel algorithms can be used to speed up the compressing step.

	File size (MB)	Time consumption	Compression ratio
Original data	320.00	-	1:1
MAT@MATLAB	108.00	2.5s	2.963:1
Patch-level compression	163.95	54.21mn	1.952:1
Pixel-level compression	21.71	50.38mn	14.75:1

Table 8.1: The time consumption and compression ratio of the proposed patch-level and pixel-level compression compared with MAT @MATLAB lossless compression.

Denosing and change classification. We compare the time consumption of 2S-PPB filter and NORCAMA change classification using compressed data and original SAR time series. Table .8.2 shows the details. Note that the time consumption here does not include the compression process. The SAR time series tested here is the *Paris* data set with the last image as the newly acquired image. The time consumption of change detection

¹The save function of MATLAB uses GZIP (level-3) compression to save variables to files. GZIP is based on the DEFLATE algorithm, which is a combination of LZ77 and Huffman coding. http://www.mathworks.com/help/pdf_doc/matlab/matfile_format.pdf

includes the denoising process of the two images and the change classification also includes the denoising of all the images. All of these processes are pixel by pixel, some parallel algorithms can be used to reduce the cost of time.

	2S-PPB denoising	Change detection	Change classification
Original SAR data	28.57h	30h	58.12h
Patch-level compression	1.38h	2.75h	27.75h
Pixel-level compression	1.89h	3.21h	29.56h

Table 8.2: The time consumption of 2S-PPB filtering, change detection between 2 dates and change classification using all dates.

8.3.2 Updating results

Denoising. We first test on synthetic images corrupted by multiplicative single-look speckle noise. in which the classical noise-free image *house* is used. We use the same noise-free image to synthesize a temporal image set, which means there is no temporal changes. The synthetic multi-temporal images have 10 dates (images) and the first 9 images are used in the compression step, the last one is considered as the *new* image. The denoising results of the new image are shown in Fig.8.7. The visual performance and the numerical results (SNR) show that 2S-PPB filter using patch/pixel-level compression data has comparable performance with 2S-PPB using original SAR time series. However, the time consumption is much less than using original SAR time series (note that the time consumption does not count the compression time consuming).

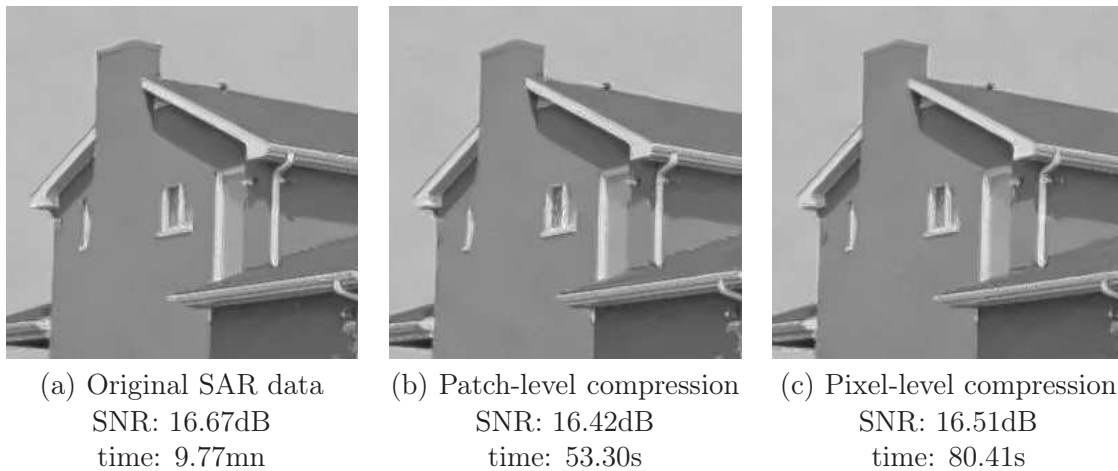


Figure 8.7: 2S-PPB denoising using (a) original SAR time series, (b) patch-level compression data and (c) pixel-level compression data.

Paris data set has also been tested here. The last image in *Paris* is considered as the new one and Fig.8.8 shows the denoising results. Comparing with 2S-PPB using original SAR time series, the visual performance 2S-PPB using patch or pixel level compressed data can achieve comparable results. Some regions have been shown in Fig.8.9. The result using patch-level compressed data is close to using pixel-level compressed data. Using original SAR time series, homogeneous regions have less variance than using pixel/patch-

level compressed data, while in regions rich of texture or edges, the three results have comparable visual performance.

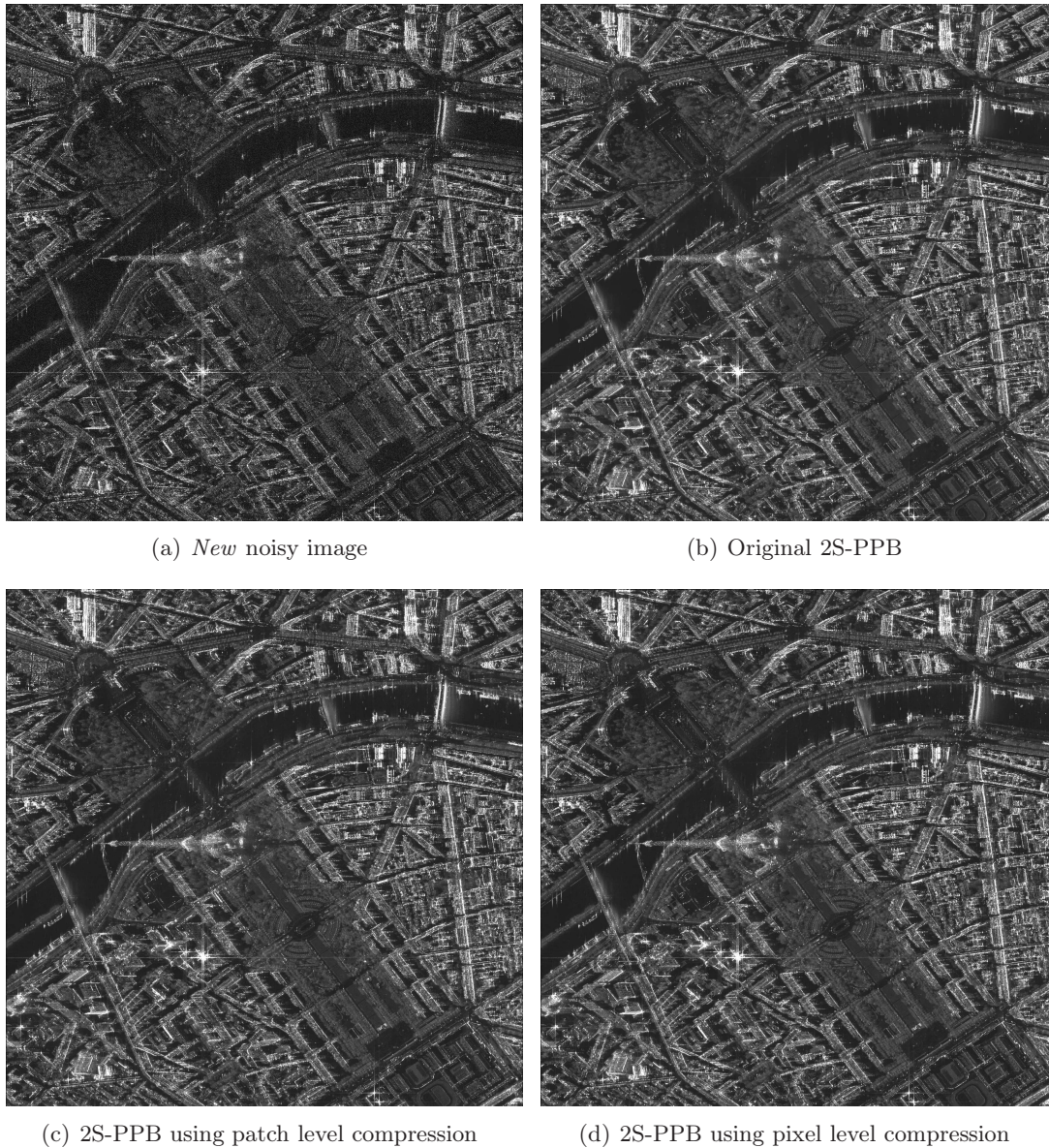
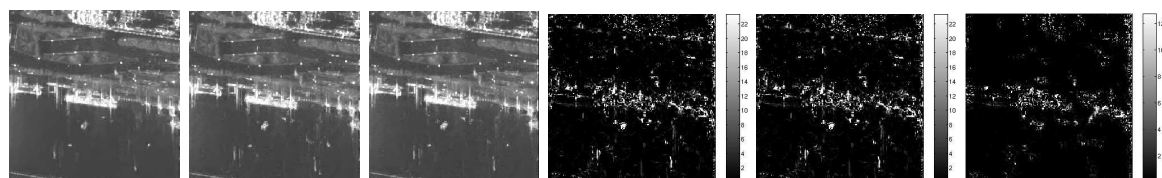


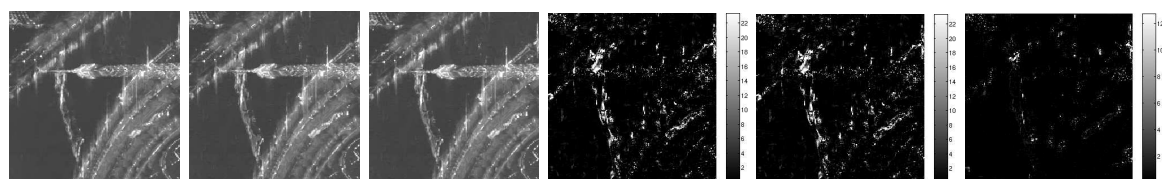
Figure 8.8: 2S-PPB denoising using original SAR time series (b), patch level compression data (c) and pixel level compression data (d).

Change classification. After the compression, the change classification of *Paris* data set can be obtained and shown in Fig.8.10.a. When the new image (the last image of *Paris*) is acquired, the change classification results using pixel-level compression data will be updated and shown in Fig.8.10.b.

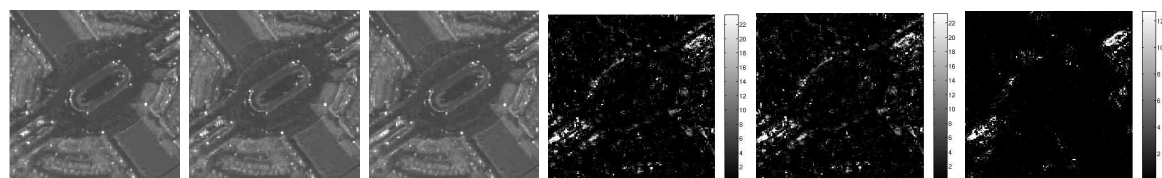
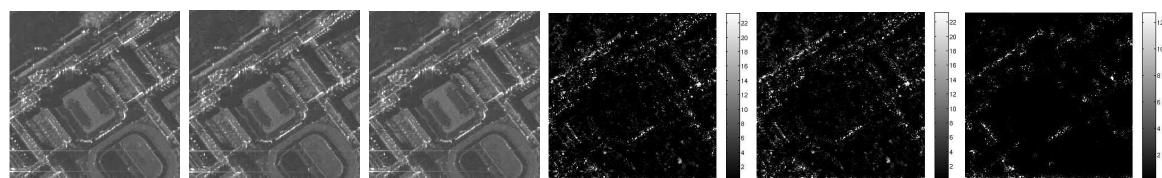
To analyze the classification results, we select some interesting patch series (7×7 pixels) and plot their mean of the intensity values by using time as coordinate axis X , as shown in Fig.8.11. The 21 values associated to 21 dates and the last one is associated to the new image. In Fig.8.11.a, there is a boat in the river representing itself as impulse change without the new information of the new date, however after the updating it turns to be



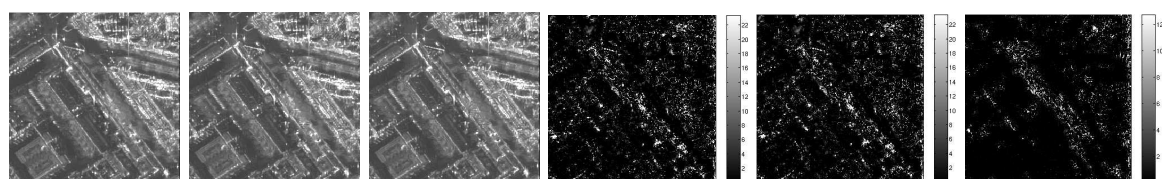
(a) Boats in the river.



(b) Metro crossing the river and the Eiffel tower.

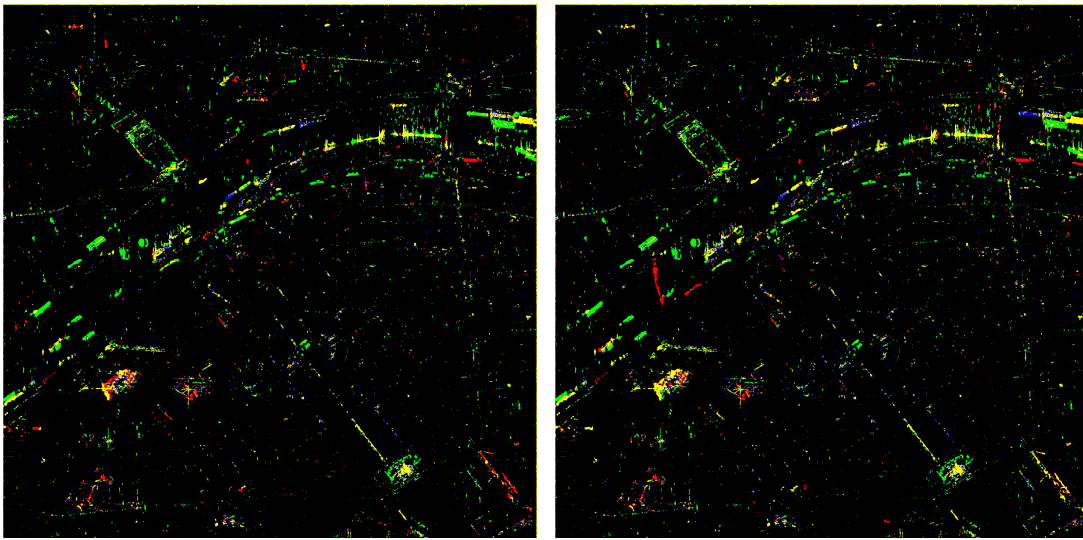
(c) Square (*Champ de Mars*).

(d) Paris Military school (1).



(e) Paris Military school (2).

Figure 8.9: 2S-PPB denoising results of *Paris* data set. From left to right, 2S-PPB using original SAR time series, 2S-PPB using patch-level compression data, 2S-PPB using pixel-level compression data, the difference map ($|y_1 - y_2|$) between first and second image, the difference map between first and third image, the difference map between second and third image.



(a) Change classification by NORCAMA of the first 20 images of *Paris* (b) Updating of change classification with the new image (the 21-th image) of *Paris*

Figure 8.10: Change classification updating of *Paris*. (a) Classification results by NORCAMA presented in chapter 7. (b) Updating of classification with the pixel-level compressed data.

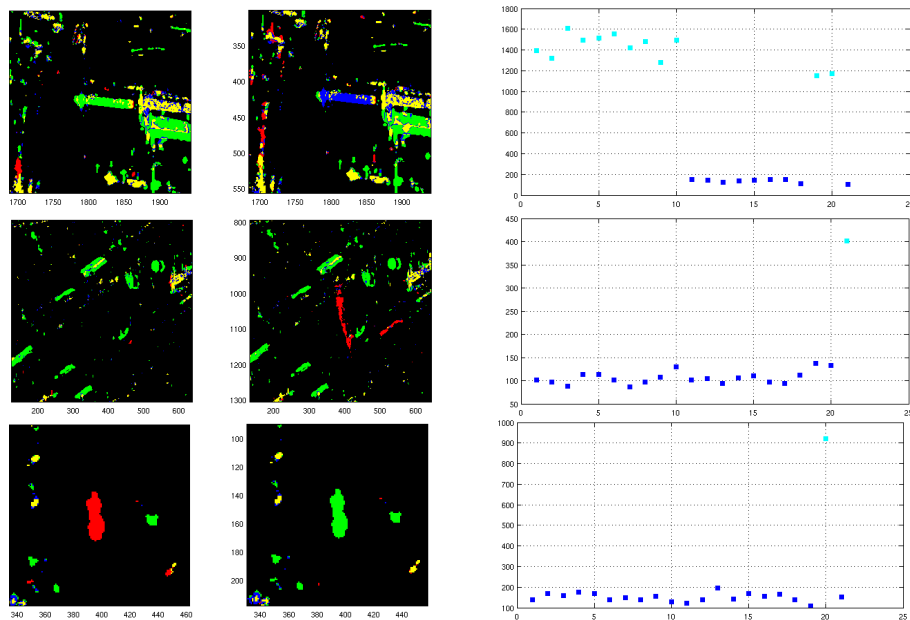


Figure 8.11: Change classification updating of *Paris*. From top to bottom: Boat in the river (impulse change \rightarrow circle change); Moving trains (no change \rightarrow step change); Moving Car on the street (step change \rightarrow impulse change).

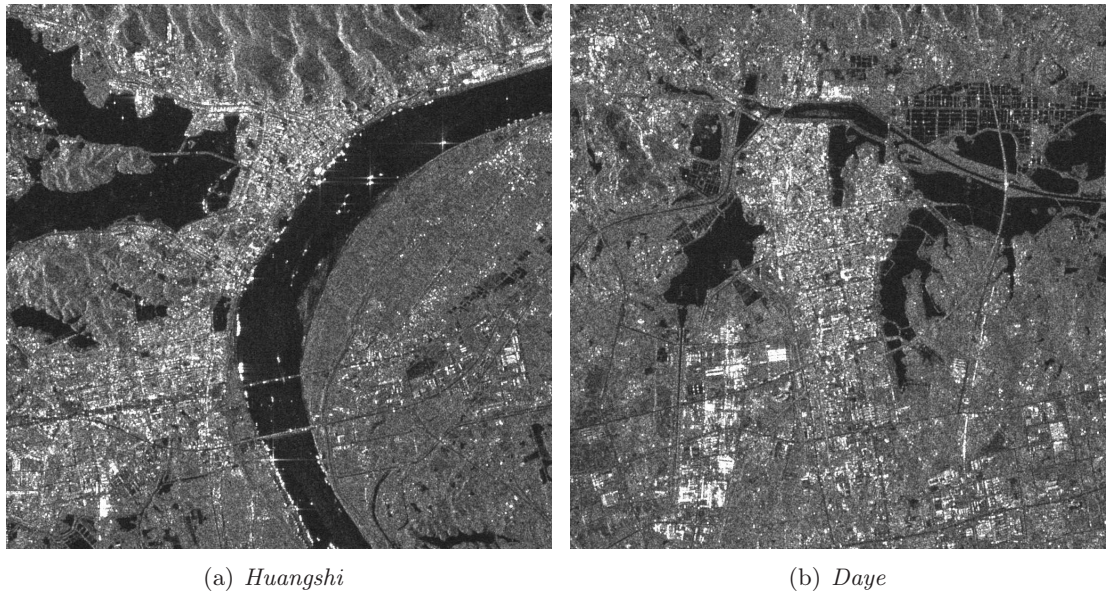


Figure 8.12: Sentinel-1 images of *Huangshi* and *Daye* in Hubei province, China acquired at 8th October 2014.

circle change since its repeated showing up.

8.4 Experiments of Sentinel-1 images

Sentinel-1A, the first Sentinel-1 satellite launched in April 2014, carries a C-band SAR sensor. Sentinel-1 (combination of Sentinel-1A and Sentinel-1B) can provide continuous radar mapping of the earth with enhanced revisit frequency (6 days) and long time series². The data used in this experiment is Level-1 Ground Range Detected (GRD) product, which has been projected to ground range using an Earth ellipsoid model such as WGS84. Thus, these multi-temporal images can be easily registered to each other manually (or with the help of some ground control points [Sester et al., 1998]).

Fig.8.12 shows two regions acquired at 8th October 2014 of *Huangshi* city and *Daye* city in Hubei province, China. There are 7 images of the two regions acquired at 8th October 2014, 20th October 2014, 1st November 2014, 13th November 2014, 25th November 2014, 7th December 2014 and 19th December 2014 respectively. The spatial resolution is $5\text{m} \times 5\text{m}$. The proposed methods (2S-PPB filter, NORCAMA change detection and classification and updating) have been tested on the Sentinel-1 images.

Multi-temporal denoising of Sentinel-1 images

The patch size is selected as 5×5 pixels since the spatial resolution is lower than the SAR images tested in chapter 4. Fig.8.13 compares the 2S-PPB denoising results using original time series (7 images) and the 2S-PPB denoising results using the compressed data. The difference map shows that the two results have close performance in homogeneous areas. More details can be found in Fig.8.14.

²More information can be found in <https://directory.eoportal.org/web/eoportal/satellite-missions/c-missions/copernicus-sentinel-1>

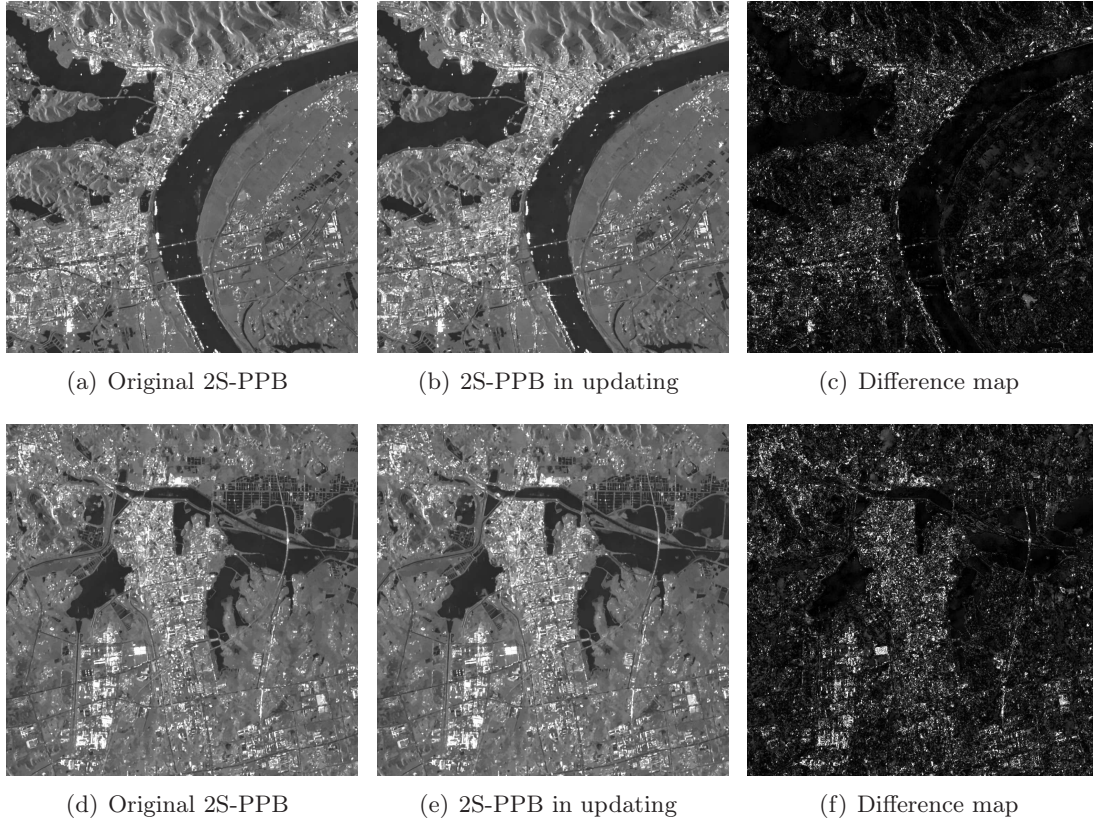


Figure 8.13: Multi-temporal denoising results. From left to right: 2S-PPB filtering results using original time series, 2S-PPB denoising results using the compressed data and difference between the former two results.

Change detection of Sentinel-1 images

We applied the proposed change detection method ($\mathcal{R}^{\text{GLRT}}$) on two Sentinel-1 images acquired at 8th October 2014 and 19th December 2014 respectively. The change criterion maps are shown in Fig.8.15. Since the time interval between the two images is not long, the changes between the two dates mainly takes place at river (due to the boats) and paddy fields. Fig.8.17 also show some details of the change detection results. In the right of Fig.8.17, the changes are detected by thresholding the change criterion $\mathcal{R}^{\text{GLRT}}$ with $\tau = \text{quantile}(\mathcal{R}, 0.001)$.

Change classification of Sentinel-1 images

The first 6 images in the time series are considered as images acquired at previous dates, and the last image acquired at 19th December 2014 is seen as the *new* image. Fig.8.16.b and e show the change classification results using the previous images (before updating). When the new images are acquired, the change classification results are updated, as shown in Fig.8.16.c and f. Since most changes are boats, these changes are classified as impulse or complex changes (marked in green and yellow color). More details can be found in Fig.8.18.

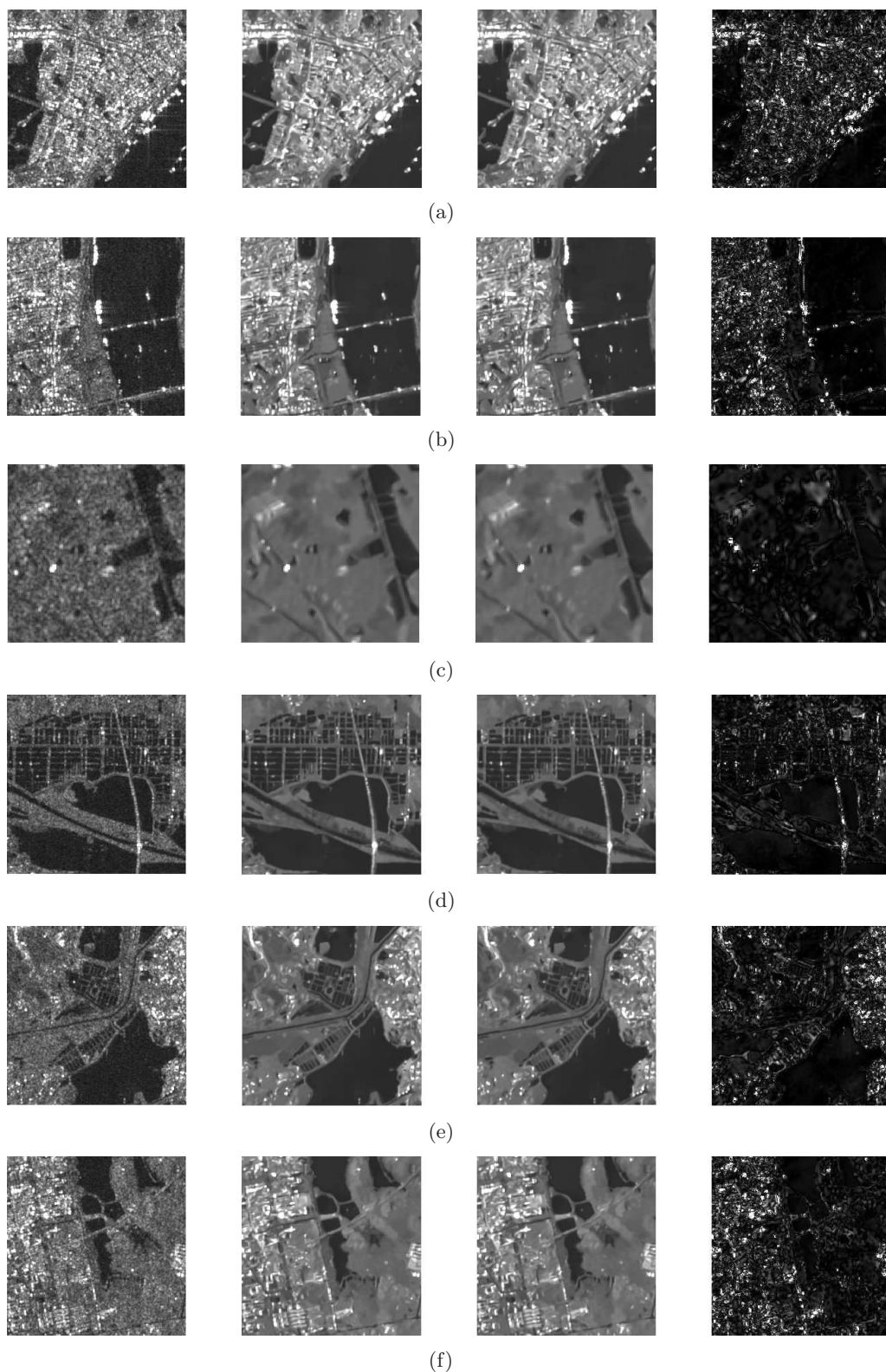


Figure 8.14: Multi-temporal denoising results. From left to right: noisy images, 2S-PPB filtering results using original time series, 2S-PPB denoising results using the compressed data and difference between the former two results.

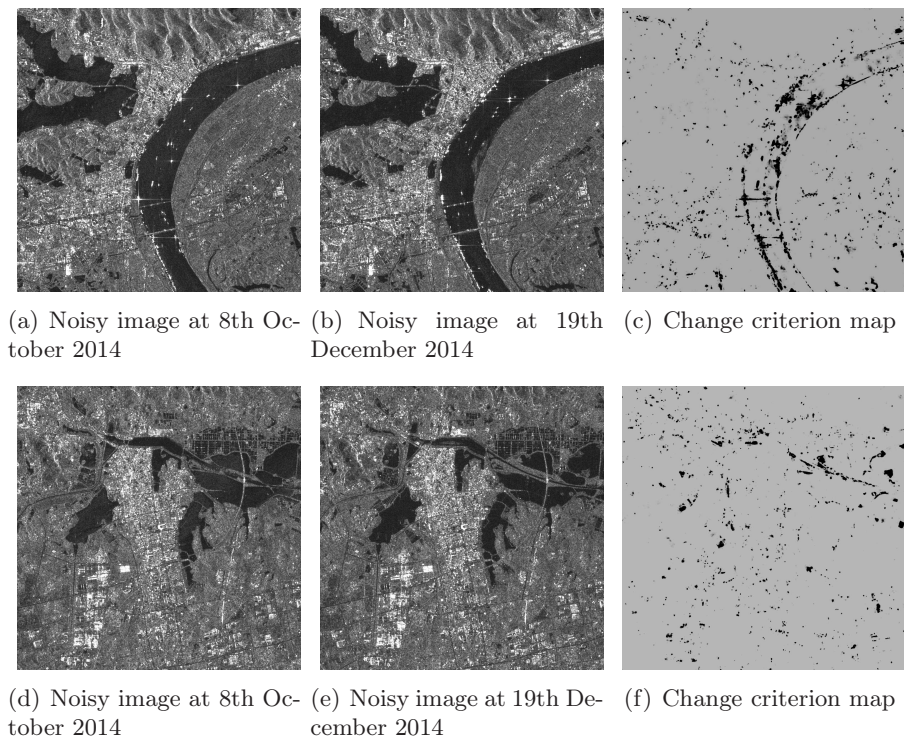


Figure 8.15: Multi-temporal denoising results. From left to right: 2S-PPB filtering results using original time series, 2S-PPB denoising results using the compressed data and difference between the former two results.

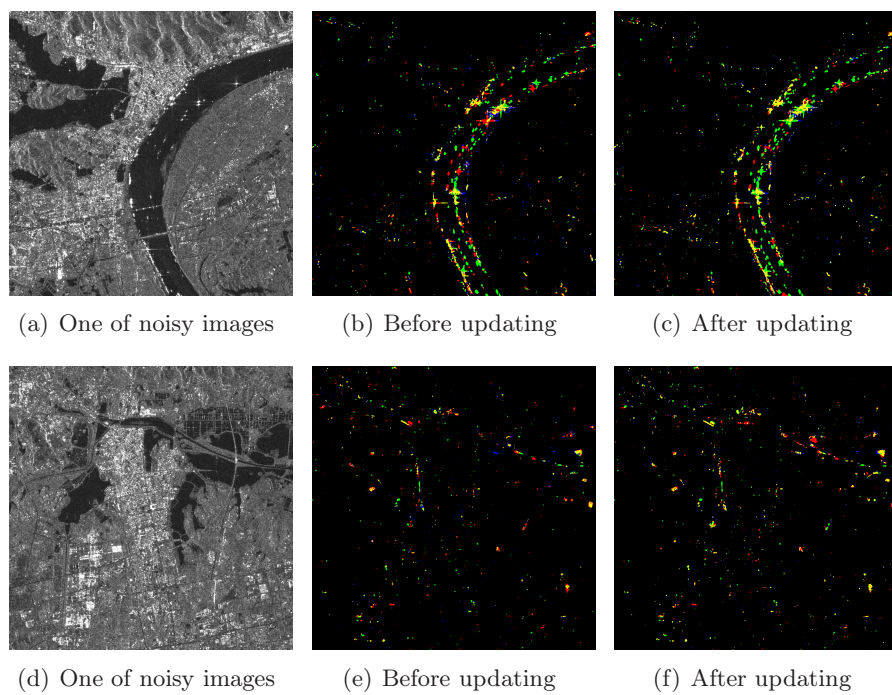


Figure 8.16: Updating of change classification results. From left to right: one of the noisy images, the change classification results using the first 6 images, the updated change classification results with the new image acquired at 19th December 2014.

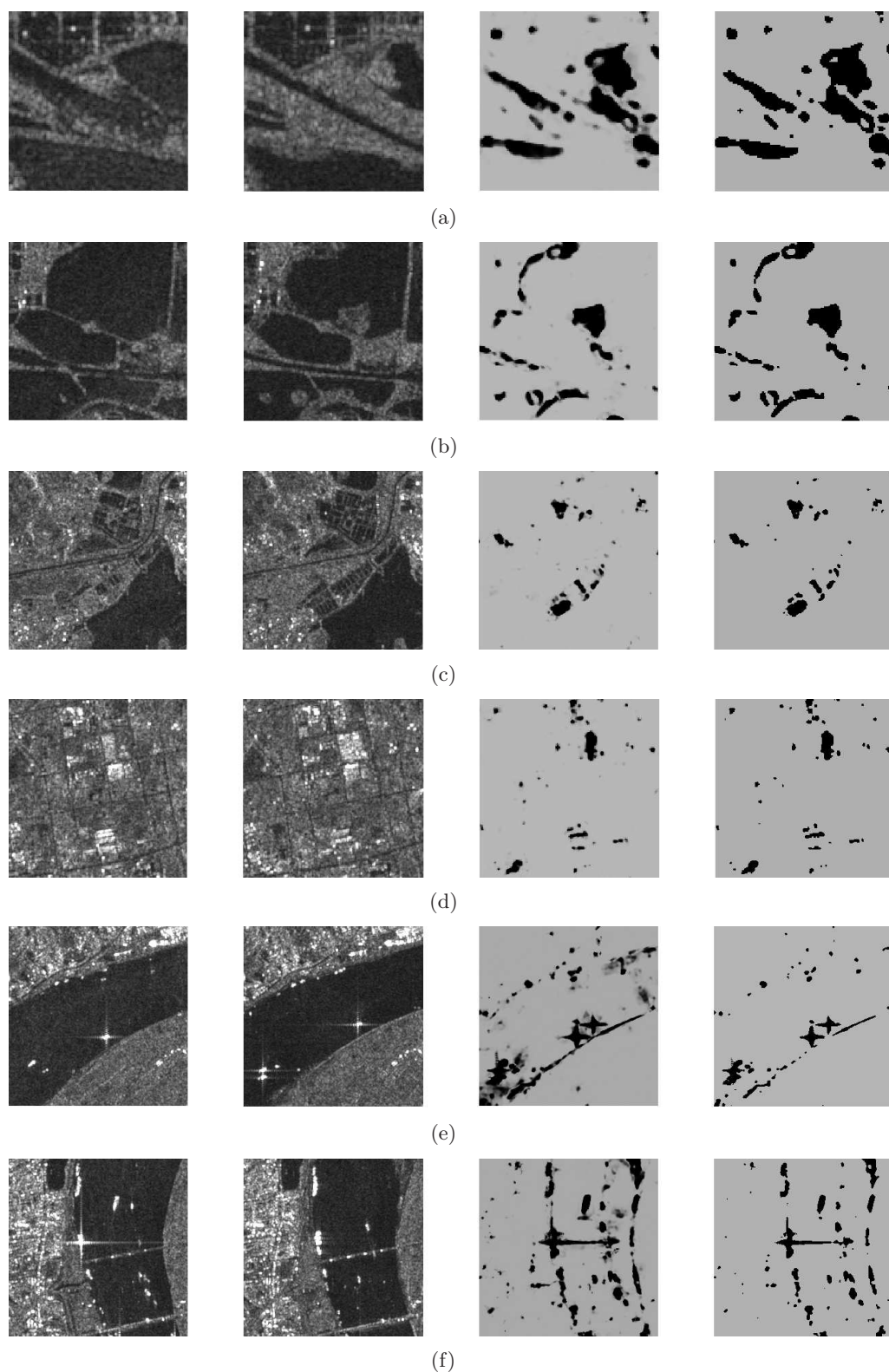


Figure 8.17: Change detection between date 8th October 2014 and 19th December 2014. From left to right: noisy image acquired at 8th October 2014, noisy image acquired at 19th December 2014, change criterion maps ($\mathcal{R}^{\text{GLRT}}$), and change detection results with threshold $\tau = \text{quantile}(\mathcal{R}, 0.001)$.

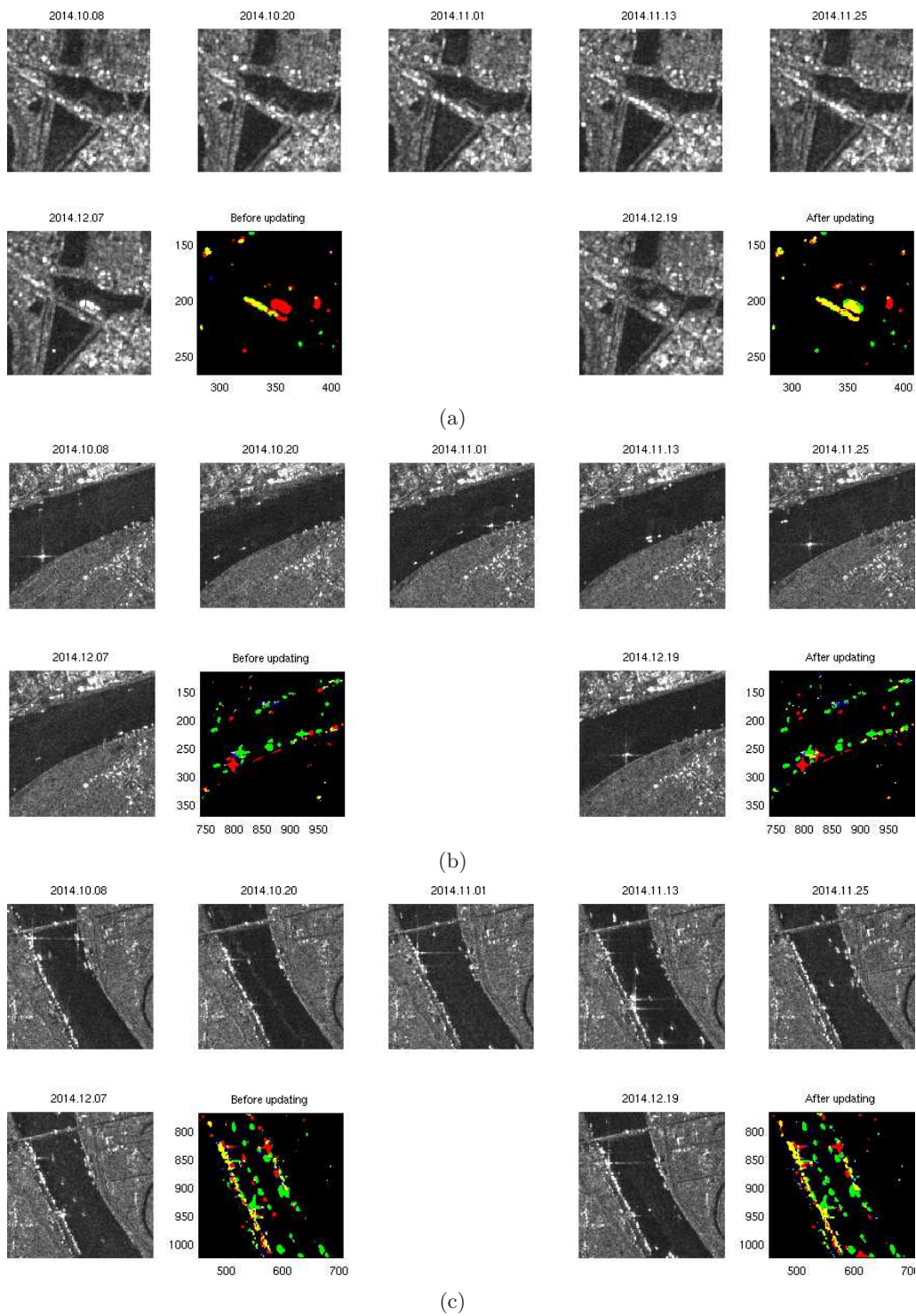


Figure 8.18: Updating of change classification results.

8.5 Conclusion

Based on the clustering of pixel series proposed in chapter 7, this chapter introduces a patch or pixel level compression for multi-temporal SAR images and applies it to update stable information (reflectivity estimation) and unstable information (change detection/classification map) when a new SAR image is acquired. Contrary to ordinary data compression mainly concerned by the compression ratio, this compression considers both time consumption of dealing with new image and space consumption (corresponding to the compression ratio) of saving the old SAR time series. The experimental results show that the denoising and change detection performance using the compressed data are comparable to those obtained using the original SAR time series. We also tested our proposed methods (2S-PPB filter, NORCAMA change detection and classification, updating method) on C-band SAR data from the newly launched Sentinel-1A sensor.

Chapter 9

Conclusion

This chapter concludes this thesis by summarizing and discussing the results obtained in the development of the different research topics. Finally, it gives an outlook for future work.

9.1 Summary

This thesis focuses on the information exploitation of multi-temporal synthetic aperture radar (SAR) images. More specifically, the exploited information is 1) redundancy information in both spatial and temporal domains for reflectivity estimation of SAR since the *speckle* noise corrupts SAR images and makes their interpretation very difficult, 2) change information for analyzing the difference between two dates and monitoring the urban development and 3) similar information for compressing the multi-temporal SAR images to reduce the space and time consumption.

Two-steps multi-temporal non local means. Non local means (NLM) search redundant pixels in a non-local or global area and average them to estimate the noise-free values. Under the NLM framework, we investigated NLM's successful extension to SAR images (patch-based probability (PPB) filter) and developed it to deal with multi-temporal SAR images. The proposed multi-temporal filter is based on a two steps multi-temporal NLM, dividing the denoising process into two main steps: temporal step averaging temporal pixels with binary weights and spatial step averaging spatial pixels based on the PPB filter. The patch comparison criterion used in PPB filter has been developed to handle patches with different levels of noise. We also extended the proposed denoising framework to the case of miss-registered SAR images by adding an offset estimation step. This 2S-PPB approach is one of the major contribution of the PhD and has been published in [Su et al., 2012, 2014b].

Likelihood ratio test based change criteria. The change detection problem between two SAR images has been considered through a likelihood ratio test. To calculate the likelihood ratio, various estimation or approximation of noise-free parameters have been proposed in the literature. In this work, we proposed to use our multi-temporal denoising results to estimate the parameters of the likelihood ratio. Two change criteria have been proposed: 1) the approximate likelihood ratio, in which the noise-free value is directly replaced by the denoised value; 2) the generalized likelihood ratio, in which we estimated

the noise-free parameters using both the denoised value and the noisy value by a maximum likelihood estimation.

Change classification by normalized cut on change criterion matrix. In this part, we focused on the temporal behaviors of changes and classified them into step, impulse, circle and complex changes. To classify the changes, we first represented the full change information of a pixel time series by a matrix of change criterion based on the proposed change criteria. A normalized-cut was then applied on the change criterion matrix to cluster the pixels in each pixel series and the changes were recognized according to their clustering labels. This part is the second major contribution of this PhD and has been published in [Su et al., 2013, 2014a, 2015].

SAR time series compression and information updating. We focused on the big data problem of multi-temporal SAR images in this work and proposed patch level and pixel level compressions to reduce the space and time consumption when dealing with SAR time series. When a new SAR image is acquired, the compressed data can be easily and quickly used to estimate the reflectivity of a new SAR image and update the change classification maps, without processing the whole stored SAR time series.

9.2 Perspectives

Reflectivity estimation of SAR data. Different denoising approaches have different advantages when filtering noisy images. For instance NLM highly reduces the local variance, regularity based methods enhance image details, dictionary based methods handles well the rare features of noisy images and so on. A *best* filter may consist of a combination of these methods. The challenges are thus what to be combined and how to combine. A research axis inspired from [Sutour et al., 2013] could provide improved results for multi-temporal denoising.

SAR change information analysis. Our preliminary results are promising but should be validated on more data sets, for instance more Sentinel-1 images etc. A short term perspective of this work is to improve the pixel level change classification by introducing shape information. Our results rely on pixel based classification but shape analysis could help the change classification and could be a way to introduce semantic information. Markov Random Fields, Conditional Random Fields and so on are efficient frameworks for this aim. Another short term perspective is the validation and extension of the work on long multi-temporal series. In particular 'smooth' changes, useful for vegetation and agricultural areas could be introduced.

Extensions to other remote sensing data. The multi-temporal SAR images concerned in this thesis are from the same sensor with the same spatial resolution, the same incidence angle, the same ascending/descending mode and the same polarimetric mode, and have been finely registered (except in section 4.4). However the multi-temporal SAR images in reality are much more than that. Applying the proposed methods to *complex* multi-temporal SAR data, specially with different incidence angles and different track directions will be a challenging task. The full interest of the 'World-SAR' concept, combining different SAR acquisitions rely on these new approaches to be developed. And some new

developments should be proposed to deal with these complex input data. In addition, optical images and other modes of remote sensing images can also be efficiently. Among the possible methods to achieve this aim, learning approaches could help our understanding and the definition of new methods.

Publication List

Journals

[1] NORCAMA: Change analysis in SAR time series by likelihood ratio change matrix clustering. Su X., Deledalle C.-A., Tupin F., Sun H.. *ISPRS Journal of Photogrammetry and Remote Sensing*, Volume 101, Pages: 247-261, 2015.

[2] Two-Step Multitemporal Nonlocal Means for Synthetic Aperture Radar Images. Su X., Deledalle C.-A., Tupin F., Sun H.. *Geoscience and Remote Sensing, IEEE Transactions on*, Volume:52 , Issue: 10, Pages: 6181-6196, 2014.

[3] A supervised classification method based on conditional random fields with multiscale region connection calculus model for SAR image. Xin Su, Chu He, Qian Feng, Xinpeng Deng, Hong Sun. *Geoscience and Remote Sensing Letters, IEEE*, Volume:8 , Issue: 3, Pages: 497-501, 2011.

[4] Weakly supervised object extraction with iterative contour prior for remote sensing images. Chu He, Yu Zhang, Bo Shi, Xin Su, Xin Xu and Mingsheng Liao *EURASIP Journal on Advances in Signal Processing*, doi:10.1186/1687-6180-2013-19, 2013.

[5] Local Topographic Shape Patterns for Texture Description. He, C., Zhuo, T., Su, X., Tu, F., Chen, D. *Signal Processing Letters, IEEE*, Volume:22 , Issue: 7, Pages: 871-875, 2014.

Conferences

[6] Change detection and classification of multi-temporal SAR series based on generalized likelihood ratio comparing-and-recognizing. Su X., Deledalle C.-A., Tupin F., Sun H.. *Geoscience and Remote Sensing Symposium (IGARSS), 2014 IEEE International*, Pages: 1433-1436

[7] SAR image change detection by likelihood ratio test in multi-temporal time series. Su X., Deledalle C.-A., Tupin F., Sun H.. *Geoscience and Remote Sensing Symposium (IGARSS), 2013 IEEE International*, Pages: 3439-3442

[8] Two steps multi-temporal Non-Local Means for SAR images. Su X., Deledalle C.-A., Tupin F., Sun H.. *Geoscience and Remote Sensing Symposium (IGARSS), 2012 IEEE International*, Pages: 2008-2011

[9] The algorithm of building area extraction based on boundary prior and conditional random field for SAR image. Chu He, Bo Shi, Yu Zhang, Xin Su, Wen Yang, Xin Xu. *Geoscience and Remote Sensing Symposium (IGARSS), 2013 IEEE International*, Pages: 1321-1324

[10] Target detection on high-resolution SAR image using Part-based CFAR Model. Chu He, Yu Zhang, Xin Su, Xin Xu, Ming-sheng Liao. *Geoscience and Remote Sensing Symposium (IGARSS), 2013 IEEE International*, Pages: 3570-3573

Acknowledgments

I would like to thank the CNES and ONERA for the 100-look SAR images, the German Aerospace Agency (DLR) for the Terra-SAR-X images *Paris* and *Saint-Gervais-les-Bains* (project MTH0232 and LAN1746), the ESA for the Sentinel-1 SAR images and the IGARSS Data Fusion Contest for the *San-Francisco* SAR images.

Bibliography

- A. Achim, P. Tsakalides, and A. Bezerianos. SAR image denoising via Bayesian wavelet shrinkage based on heavy-tailed modeling. *Geoscience and Remote Sensing, IEEE Transactions on*, 41(8):1773–1784, 2003.
- A. Alonso-González, C. López-Martínez, and P. Salembier. Filtering and segmentation of polarimetric SAR data based on binary partition trees. *Geoscience and Remote Sensing, IEEE Transactions on*, 50(2):593–605, 2012.
- A. Alonso-González, C. López-Martínez, and P. Salembier. PolSAR Time Series Processing With Binary Partition Trees. *Geoscience and Remote Sensing, IEEE Transactions on*, 52:3553 – 3567, 2014.
- D. Amitrano, G. Di Martino, A. Iodice, D. Riccio, and G. Ruello. A new perspective for multitemporal SAR data analysis. In *Geoscience and Remote Sensing Symposium (IGARSS), 2014 IEEE International*, pages 4695–4698. IEEE, 2014.
- E. P. Attema. The active microwave instrument on-board the ERS-1 satellite. *Proceedings of the IEEE*, 79(6):791–799, 1991.
- A. M. Atto, E. Trouvé, Y. Berthoumieu, and G. Mercier. Multidate Divergence Matrices for the Analysis of SAR Image Time Series. *Geoscience and Remote Sensing, IEEE Transactions on*, 51(4):1922–1938, 2013.
- Y. Bazi, L. Bruzzone, and F. Melgani. An unsupervised approach based on the generalized Gaussian model to automatic change detection in multitemporal SAR images. *Geoscience and Remote Sensing, IEEE Transactions on*, 43(4):874–887, 2005.
- Y. Bazi, L. Bruzzone, and F. Melgani. Image thresholding based on the EM algorithm and the generalized Gaussian distribution. *Pattern Recognition*, 40(2):619–634, 2007.
- J. W. Berger, T. R. Patel, D. S. Shin, J. R. Piltz, and R. A. Stone. Computerized stereochronoscopy and alternation flicker to detect optic nerve head contour change. *Ophthalmology*, 107(7):1316–1320, 2000.
- H. Berkovich, D. Malah, and M. Barzohar. Non-local means denoising using a content-based search region and dissimilarity kernel. In *Image and Signal Processing and Analysis (ISPA), 2013 8th International Symposium on*, pages 10–15. IEEE, 2013.
- F. Bovolo. A multilevel parcel-based approach to change detection in very high resolution multitemporal images. *Geoscience and Remote Sensing Letters, IEEE*, 6(1):33–37, 2009.
-

-
- F. Bovolo and L. Bruzzone. A detail-preserving scale-driven approach to change detection in multitemporal SAR images. *Geoscience and Remote Sensing, IEEE Transactions on*, 43(12):2963–2972, 2005.
- F. Bovolo and L. Bruzzone. A theoretical framework for unsupervised change detection based on change vector analysis in the polar domain. *Geoscience and Remote Sensing, IEEE Transactions on*, 45(1):218–236, 2007.
- F. Bovolo and L. Bruzzone. An adaptive multiscale random field technique for unsupervised change detection in VHR multitemporal images. In *Geoscience and Remote Sensing Symposium, 2009 IEEE International, IGARSS 2009*, volume 4, pages IV–777. IEEE, 2009.
- F. Bovolo, L. Bruzzone, and M. Marconcini. A novel approach to unsupervised change detection based on a semisupervised SVM and a similarity measure. *Geoscience and Remote Sensing, IEEE Transactions on*, 46(7):2070–2082, 2008.
- F. Bovolo, G. Camps-Valls, and L. Bruzzone. A support vector domain method for change detection in multitemporal images. *Pattern Recognition Letters*, 31(10):1148–1154, 2010.
- T. Brox, O. Kleinschmidt, and D. Cremers. Efficient nonlocal means for denoising of textural patterns. *Image Processing, IEEE Transactions on*, 17(7):1083–1092, 2008.
- D. Brunner, G. Lemoine, and L. Bruzzone. Earthquake damage assessment of buildings using VHR optical and SAR imagery. *Geoscience and Remote Sensing, IEEE Transactions on*, 48(5):2403–2420, 2010.
- L. Bruzzone and D. Prieto. An adaptive parcel-based technique for unsupervised change detection. *International Journal of Remote Sensing*, 21(4):817–822, 2000a.
- L. Bruzzone and D. Prieto. Automatic analysis of the difference image for unsupervised change detection. *Geoscience and Remote Sensing, IEEE Transactions on*, 38(3):1171–1182, 2000b.
- L. Bruzzone and D. Prieto. An adaptive semiparametric and context-based approach to unsupervised change detection in multitemporal remote-sensing images. *Image Processing, IEEE Transactions on*, 11(4):452–466, 2002.
- L. Bruzzone and D. F. Prieto. A Bayesian approach to automatic change detection. In *Geoscience and Remote Sensing Symposium, 1999. IGARSS'99 Proceedings. IEEE 1999 International*, volume 3, pages 1816–1818. IEEE, 1999.
- L. Bruzzone and S. Serpico. An iterative technique for the detection of land-cover transitions in multitemporal remote-sensing images. *Geoscience and Remote Sensing, IEEE Transactions on*, 35(4):858–867, 1997.
- L. Bruzzone, R. Cossu, and G. Vernazza. Detection of land-cover transitions by combining multirate classifiers. *Pattern Recognition Letters*, 25(13):1491–1500, 2004a.
- L. Bruzzone, M. Marconcini, U. Wegmuller, and A. Wiesmann. An advanced system for the automatic classification of multitemporal SAR images. *Geoscience and Remote Sensing, IEEE Transactions on*, 42(6):1321–1334, 2004b.
-

-
- A. Buades. *Image and film denoising by non-local means*. PhD thesis, Citeseer, 2006.
- A. Buades, B. Coll, and J. Morel. A non-local algorithm for image denoising. In *Computer Vision and Pattern Recognition, 2005. CVPR 2005. IEEE Computer Society Conference on*, volume 2, pages 60–65. IEEE, 2005a.
- A. Buades, B. Coll, and J.-M. Morel. A review of image denoising algorithms, with a new one. *Multiscale Modeling & Simulation*, 4(2):490–530, 2005b.
- A. Buades, B. Coll, and J. Morel. Nonlocal image and movie denoising. *International journal of computer vision*, 76(2):123–139, 2008.
- A. Buades, B. Coll, and J.-M. Morel. Non-Local Means Denoising. *Image Processing On Line*, 1, 2011. doi: 10.5201/ipol.2011.bcm_nlm.
- F. Bujor, E. Trouvé, L. Valet, J. Nicolas, and J. Rudant. Application of log-cumulants to the detection of spatiotemporal discontinuities in multitemporal SAR images. *Geoscience and Remote Sensing, IEEE Transactions on*, 42(10):2073–2084, 2004.
- M. Burrows and D. J. Wheeler. A block-sorting lossless data compression algorithm. 1994.
- G. Byrne, P. Crapper, and K. Mayo. Monitoring land-cover change by principal component analysis of multitemporal Landsat data. *Remote Sensing of Environment*, 10(3):175–184, 1980.
- G. Camps-Valls, L. Gómez-Chova, J. Muñoz-Marí, J. Rojo-Alvarez, and M. Martínez-Ramón. Kernel-based framework for multitemporal and multisource remote sensing data classification and change detection. *Geoscience and Remote Sensing, IEEE Transactions on*, 46(6):1822–1835, 2008.
- M. Carlotto. A cluster-based approach for detecting man-made objects and changes in imagery. *Geoscience and Remote Sensing, IEEE Transactions on*, 43(2):374–387, 2005.
- T. Celik and K.-K. Ma. Unsupervised change detection for satellite images using dual-tree complex wavelet transform. *Geoscience and Remote Sensing, IEEE Transactions on*, 48(3):1199–1210, 2010.
- T. Celik and K.-K. Ma. Multitemporal image change detection using undecimated discrete wavelet transform and active contours. *Geoscience and Remote Sensing, IEEE Transactions on*, 49(2):706–716, 2011.
- M. Cha, R. D. Phillips, and P. J. Wolfe. Combined intensity and coherent change detection for synthetic aperture radar. In *Acoustics, Speech and Signal Processing (ICASSP), 2014 IEEE International Conference on*, pages 8120–8123. IEEE, 2014.
- A. Chambolle. An algorithm for total variation minimization and applications. *Journal of Mathematical imaging and vision*, 20(1-2):89–97, 2004.
- A. Chambolle and T. Pock. A first-order primal-dual algorithm for convex problems with applications to imaging. *Journal of Mathematical Imaging and Vision*, 40(1):120–145, 2011.
- S. H. Chan, T. Zickler, and Y. M. Lu. Monte Carlo non local means: Random sampling for large-scale image filtering. *arXiv preprint arXiv:1312.7366*, 2013.
-

-
- P. Chatterjee and P. Milanfar. Clustering-based denoising with locally learned dictionaries. *Image Processing, IEEE Transactions on*, 18(7):1438–1451, 2009.
- J. Chen, P. Gong, C. He, R. Pu, and P. Shi. Land-use/land-cover change detection using improved change-vector analysis. *Photogrammetric Engineering & Remote Sensing*, 69(4):369–379, 2003.
- V. Cheung, B. J. Frey, and N. Jojic. Video epitomes. *International Journal of Computer Vision*, 76(2):141–152, 2008.
- F. R. Chung. *Spectral graph theory*, volume 92. American Mathematical Soc., 1997.
- J. Cimino, C. Elachi, and M. Settle. SIR-B-The second shuttle imaging radar experiment. *Geoscience and Remote Sensing, IEEE Transactions on*, (4):445–452, 1986.
- M. Ciuc, P. Bolon, E. Trouve, V. Buzuloiu, and J. Rudant. Adaptive-neighborhood speckle removal in multitemporal synthetic aperture radar images. *Applied Optics*, 40(32):5954–5966, 2001.
- S. R. Cloude and E. Pottier. A review of target decomposition theorems in radar polarimetry. *Geoscience and Remote Sensing, IEEE Transactions on*, 34(2):498–518, 1996.
- S. R. Cloude and E. Pottier. An entropy based classification scheme for land applications of polarimetric SAR. *Geoscience and Remote Sensing, IEEE Transactions on*, 35(1):68–78, 1997.
- D. Coltuc, E. Trouvé, F. Bujor, N. Classeau, and J.-P. Rudant. Time-space filtering of multitemporal SAR images. In *Geoscience and Remote Sensing Symposium, 2000. Proceedings. IGARSS 2000. IEEE 2000 International*, volume 7, pages 2909–2911. IEEE, 2000.
- K. Conradsen, A. A. Nielsen, J. Schou, and H. Skriver. A test statistic in the complex Wishart distribution and its application to change detection in polarimetric SAR data. *Geoscience and Remote Sensing, IEEE Transactions on*, 41(1):4–19, 2003.
- P. R. Coppin and M. E. Bauer. Processing of multitemporal Landsat TM imagery to optimize extraction of forest cover change features. *Geoscience and Remote Sensing, IEEE Transactions on*, 32(4):918–927, 1994.
- P. Coupé, P. Yger, S. Prima, P. Hellier, C. Kervrann, and C. Barillot. An optimized blockwise nonlocal means denoising filter for 3-D magnetic resonance images. *Medical Imaging, IEEE Transactions on*, 27(4):425–441, 2008.
- D. Cozzolino, S. Parrilli, G. Scarpa, G. Poggi, and L. Verdoliva. Fast adaptive nonlocal SAR despeckling. 2014.
- E. P. Crist. A TM tasseled cap equivalent transformation for reflectance factor data. *Remote Sensing of Environment*, 17(3):301–306, 1985.
- S. Cui. Spatial and temporal SAR image information mining. 2014.
- K. Dabov, A. Foi, and K. Egiazarian. Video denoising by sparse 3D transform-domain collaborative filtering. In *Proc. 15th European Signal Processing Conference*, volume 1, page 7, 2007a.
-

-
- K. Dabov, A. Foi, V. Katkovnik, and K. Egiazarian. Image denoising by sparse 3-D transform-domain collaborative filtering. *Image Processing, IEEE Transactions on*, 16(8):2080–2095, 2007b.
- K. Dabov, A. Foi, V. Katkovnik, K. Egiazarian, et al. BM3D image denoising with shape-adaptive principal component analysis. In *SPARS'09-Signal Processing with Adaptive Sparse Structured Representations*, 2009.
- X. Dai and S. Khorram. Development of a new automated land cover change detection system from remotely sensed imagery based on artificial neural networks. In *Geoscience and Remote Sensing, 1997. IGARSS'97. Remote Sensing-A Scientific Vision for Sustainable Development., 1997 IEEE International*, volume 2, pages 1029–1031. IEEE, 1997.
- M. Dalla Mura, J. Benediktsson, F. Bovolo, and L. Bruzzone. An unsupervised technique based on morphological filters for change detection in very high resolution images. *Geoscience and Remote Sensing Letters, IEEE*, 5(3):433–437, 2008.
- M. Dalla Mura, J. Atli Benediktsson, B. Waske, and L. Bruzzone. Morphological attribute profiles for the analysis of very high resolution images. *Geoscience and Remote Sensing, IEEE Transactions on*, 48(10):3747–3762, 2010.
- R. De Jong, S. de Bruin, A. de Wit, M. Schaepman, and D. Dent. Analysis of monotonic greening and browning trends from global NDVI time-series. *Remote Sensing of Environment*, 115(2):692–702, 2011.
- C. Deledalle, L. Denis, and F. Tupin. Iterative weighted maximum likelihood denoising with probabilistic patch-based weights. *Image Processing, IEEE Transactions on*, 18(12):2661–2672, 2009.
- C.-A. Deledalle. *Image denoising beyond additive Gaussian noise Patch-based estimators and their application to SAR imagery*. PhD thesis, Telecom ParisTech, 2011.
- C.-A. Deledalle, F. Tupin, and L. Denis. Poisson NL means: Unsupervised non local means for Poisson noise. In *Image processing (ICIP), 2010 17th IEEE international conference on*, pages 801–804. IEEE, 2010a.
- C.-A. Deledalle, F. Tupin, and L. Denis. Polarimetric SAR estimation based on non-local means. In *Geoscience and Remote Sensing Symposium (IGARSS), 2010 IEEE International*, pages 2515–2518. IEEE, 2010b.
- C.-A. Deledalle, L. Denis, and F. Tupin. NL-InSAR: Nonlocal interferogram estimation. *Geoscience and Remote Sensing, IEEE Transactions on*, 49(4):1441–1452, 2011.
- C.-A. Deledalle, L. Denis, and F. Tupin. How to Compare Noisy Patches? Patch Similarity Beyond Gaussian Noise. *International Journal of Computer Vision*, 99:86–102, 2012a. ISSN 0920-5691. 10.1007/s11263-012-0519-6.
- C.-A. Deledalle, V. Duval, and J. Salmon. Non-local methods with shape-adaptive patches (NLM-SAP). *Journal of Mathematical Imaging and Vision*, 43(2):103–120, 2012b.
- C.-A. Deledalle, L. Denis, F. Tupin, A. Reigber, M. Jäger, et al. NL-SAR: a unified Non-Local framework for resolution-preserving (Pol)(In) SAR denoising. *Geoscience and Remote Sensing, IEEE Transactions on*, 2014.
-

- F. Dellinger, J. Delon, Y. Gousseau, J. Michel, and F. Tupin. SAR-SIFT: A SIFT-like algorithm for applications on SAR images. In *Geoscience and Remote Sensing Symposium (IGARSS), 2012 IEEE International*, pages 3478–3481. IEEE, 2012.
- F. Dellinger, J. Delon, Y. Gousseau, J. Michel, and F. Tupin. Change detection for high resolution satellite images, based on SIFT descriptors and an a contrario approach. In *Geoscience and Remote Sensing Symposium (IGARSS), 2014 IEEE International*, pages 1281–1284. IEEE, 2014.
- B. Demir, F. Bovolo, and L. Bruzzone. Updating land-cover maps by classification of image time series: A novel change-detection-driven transfer learning approach. *Geoscience and Remote Sensing, IEEE Transactions on*, 51(1):300–312, 2013.
- W. Dong, X. Li, D. Zhang, and G. Shi. Sparsity-based image denoising via dictionary learning and structural clustering. In *Computer Vision and Pattern Recognition (CVPR), 2011 IEEE Conference on*, pages 457–464. IEEE, 2011.
- D. L. Donoho. Compressed sensing. *Information Theory, IEEE Transactions on*, 52(4):1289–1306, 2006.
- P. Dubois-Fernandez, J. Boutry, J. Canny, H. Cantalloube, M. Chanteclerc, E. Colin, C. Coulombeix, P. Dreuillet, X. Dupuis, P. Fromage, et al. The ONERA RAMSES SAR system: Status in 2004. *Proc. Radar 2004*.
- V. Duval, J. Aujol, Y. Gousseau, et al. On the parameter choice for the non-local means. *HAL*, 2010.
- V. Duval, J. Aujol, and Y. Gousseau. A bias-variance approach for the nonlocal means. *SIAM Journal on Imaging Sciences*, 4(2):760–788, 2011.
- M. Elad and M. Aharon. Image denoising via sparse and redundant representations over learned dictionaries. *Image Processing, IEEE Transactions on*, 15(12):3736–3745, 2006.
- A. Freeman and S. L. Durden. A three-component scattering model for polarimetric SAR data. *Geoscience and Remote Sensing, IEEE Transactions on*, 36(3):963–973, 1998.
- V. Frost, J. Stiles, K. Shanmugan, and J. Holtzman. A model for radar images and its application to adaptive digital filtering of multiplicative noise. *Pattern Analysis and Machine Intelligence, IEEE Transactions on*, (2):157–166, 1982.
- T. Fung and E. LeDrew. The determination of optimal threshold levels for change detection using various accuracy indices. *Photogramm. Eng. Remote Sensing*, 54:1449–1454, 1988.
- L. Gagnon and A. Jouan. Speckle filtering of SAR images: a comparative study between complex-wavelet-based and standard filters. pages 80–91, 1997.
- R. Gens and J. Van Genderen. Review article SAR interferometry—Issues, techniques, applications. *International Journal of Remote Sensing*, 17(10):1803–1835, 1996.
- M. Gianinetto and P. Villa. Mapping Hurricane Katrina’s widespread destruction in New Orleans using multisensor data and the normalized difference change detection (NDCD) technique. *International Journal of Remote Sensing*, 32(7):1961–1982, 2011.
-

-
- D. Gleich, M. Kseneman, and M. Datcu. Despeckling of TerraSAR-X data using second-generation wavelets. *Geoscience and Remote Sensing Letters, IEEE*, 7(1):68–72, 2010.
- R. M. Goldstein, H. A. Zebker, and C. L. Werner. Satellite radar interferometry: Two-dimensional phase unwrapping. *Radio Science*, 23(4):713–720, 1988.
- M. Gong, L. Su, M. Jia, and W. Chen. Fuzzy clustering with a modified mrf energy function for change detection in synthetic aperture radar images. *Fuzzy Systems, IEEE Transactions on*, 22(1):98–109, 2014.
- J. Goodman. Some fundamental properties of speckle. *JOSA*, 66(11):1145–1150, 1976.
- B. Goossens, Q. Luong, A. Pizurica, and W. Philips. An improved non-local denoising algorithm. In *2008 International Workshop on Local and Non-Local Approximation in Image Processing (LNLA 2008)*, pages 143–156, 2008.
- L. C. Graham. Synthetic interferometer radar for topographic mapping. *Proceedings of the IEEE*, 62(6):763–768, 1974.
- J. Granger. Shuttle Imaging Radar: A/B sensors. In *Spaceborne Imaging Radar Symposium*, volume 1, pages 26–31, 1983.
- A. Gray, N. Short, K. Mattar, and K. Jezek. Velocities and flux of the Filchner Ice Shelf and its tributaries determined from speckle tracking interferometry. *Canadian Journal of Remote Sensing*, 27(3):193–206, 2001.
- H. Guo, J. Odegard, M. Lang, R. Gopinath, I. Selesnick, and C. Burrus. Wavelet based speckle reduction with application to SAR based ATD/R. 1:75–79, 1994.
- G. Hazel. Object-level change detection in spectral imagery. *Geoscience and Remote Sensing, IEEE Transactions on*, 39(3):553–561, 2001.
- W. A. Holm and R. M. Barnes. On radar polarization mixed target state decomposition techniques. In *Radar Conference, 1988., Proceedings of the 1988 IEEE National*, pages 249–254. IEEE, 1988.
- J. Homer, I. Longstaff, and G. Callaghan. High resolution 3-D SAR via multi-baseline interferometry. In *Geoscience and Remote Sensing Symposium, 1996. IGARSS'96. 'Remote Sensing for a Sustainable Future.', International*, volume 1, pages 796–798. IEEE, 1996.
- O. Hondt, S. Guillaso, and O. Hellwich. Risk based parameter selection for polarimetric SAR speckle reduction. In *IGARSS 2014*, 2014.
- A. Hooper, H. Zebker, P. Segall, and B. Kampes. A new method for measuring deformation on volcanoes and other natural terrains using InSAR persistent scatterers. *Geophysical research letters*, 31(23), 2004.
- R. Horn. The DLR airborne SAR project E-SAR. In *Geoscience and Remote Sensing Symposium, 1996. IGARSS'96. 'Remote Sensing for a Sustainable Future.', International*, volume 3, pages 1624–1628. IEEE, 1996.
- R. Horn, A. Nottensteiner, and R. Scheiber. F-SAR - DLR's advanced airborne SAR system onboard DO228. In *Synthetic Aperture Radar (EUSAR), 2008 7th European Conference on*, pages 1–4. VDE, 2008.
-

-
- C. Huo, B. Fan, C. Pan, and Z. Zhou. Combining local features and progressive support vector machine for urban change detection of vhr images. *ISPRS Annals*, 1:221–226, 2012.
- J. R. Huynen. *Phenomenological theory of radar targets*. PhD thesis, Drukkerij Bronder-Offset NV, 1970.
- S. Ingebritsen and R. Lyon. Principal components analysis of multitemporal image pairs. *International Journal of Remote Sensing*, 6(5):687–696, 1985.
- J. Inglada and G. Mercier. A new statistical similarity measure for change detection in multitemporal SAR images and its extension to multiscale change analysis. *Geoscience and Remote Sensing, IEEE Transactions on*, 45(5):1432–1445, 2007.
- C. S. Jha and N. V. M. Unni. Digital change detection of forest conversion of a dry tropical Indian forest region. *International Journal of Remote Sensing*, 15(13):2543–2552, 1994.
- R. L. Jordan. The SEASAT-A synthetic aperture radar system. *Oceanic Engineering, IEEE Journal of*, 5(2):154–164, 1980.
- R. L. Jordan, B. L. Huneycutt, and M. Werner. The SIR-C/X-SAR synthetic aperture radar system. *Geoscience and Remote Sensing, IEEE Transactions on*, 33(4):829–839, 1995.
- A. Julea, N. Méger, P. Bolon, C. Rigotti, M. Doin, C. Lasserre, E. Trouvé, and V. Lazarescu. Unsupervised spatiotemporal mining of satellite image time series using grouped frequent sequential patterns. *Geoscience and Remote Sensing, IEEE Transactions on*, 49(4):1417–1430, 2011.
- V. Katkovnik, K. Egiazarian, and J. Astola. Adaptive window size image de-noising based on intersection of confidence intervals (ICI) rule. *Journal of Mathematical Imaging and Vision*, 16(3):223–235, 2002.
- R. J. Kauth and G. Thomas. The tasselled cap—a graphic description of the spectral-temporal development of agricultural crops as seen by Landsat. In *LARS Symposia*, page 159, 1976.
- C. Kervrann and J. Boulanger. Optimal spatial adaptation for patch-based image denoising. *Image Processing, IEEE Transactions on*, 15(10):2866–2878, 2006.
- G. Krieger, I. Hajnsek, K. P. Papathanassiou, M. Younis, and A. Moreira. Interferometric synthetic aperture radar (SAR) missions employing formation flying. *Proceedings of the IEEE*, 98(5):816–843, 2010.
- E. Krogager. New decomposition of the radar target scattering matrix. *Electronics Letters*, 26(18):1525–1527, 1990.
- V. Krylov, G. Moser, A. Voisin, S. Serpico, and J. Zerubia. Change detection with synthetic aperture radar images by Wilcoxon statistic likelihood ratio test. In *Proc. IEEE International Conference on Image Processing (ICIP)*, Orlando, United States, October 2012. URL <http://hal.inria.fr/hal-00724284>.
-

-
- D. Kuan, A. Sawchuk, T. Strand, and P. Chavel. Adaptive noise smoothing filter for images with signal-dependent noise. *Pattern Analysis and Machine Intelligence, IEEE Transactions on*, (2):165–177, 1985.
- D. Kuan, A. Sawchuk, T. Strand, and P. Chavel. Adaptive restoration of images with speckle. *Acoustics, Speech and Signal Processing, IEEE Transactions on*, 35(3):373–383, 1987.
- T. T. Le, A. M. Atto, E. Trouvé, and J.-M. Nicolas. Adaptive Multitemporal SAR Image Filtering Based on the Change Detection Matrix. *Geoscience and Remote Sensing Letters, IEEE*, 11:1826 – 1830, 2014.
- J.-S. Lee. Digital image enhancement and noise filtering by use of local statistics. *Pattern Analysis and Machine Intelligence, IEEE Transactions on*, (2):165–168, 1980.
- J.-S. Lee. Speckle analysis and smoothing of synthetic aperture radar images. *Computer graphics and image processing*, 17(1):24–32, 1981.
- J.-S. Lee. Digital image smoothing and the sigma filter. *Computer Vision, Graphics, and Image Processing*, 24(2):255–269, 1983.
- E. L. Lehmann and J. P. Romano. *Testing statistical hypotheses*. springer, 2006.
- P. Li, B. Song, and H. Xu. Urban building damage detection from very high resolution imagery by One-Class SVM and shadow information. In *Geoscience and Remote Sensing Symposium (IGARSS), 2011 IEEE International*, pages 1409–1412. IEEE, 2011.
- C. Liu and W. T. Freeman. A high-quality video denoising algorithm based on reliable motion estimation. In *Computer Vision–ECCV 2010*, pages 706–719. Springer, 2010.
- G. Liu and H. Zhong. Nonlocal Means Filter for Polarimetric SAR Data Despeckling Based on Discriminative Similarity Measure. *Geoscience and Remote Sensing Letters, IEEE*, 11:514 – 518, 2014.
- G. Liu, L. Jiao, F. Liu, H. Zhong, and S. Wang. A new patch based change detector for polarimetric SAR data. *Pattern Recognition*, 48:685–695, 2014.
- P. Lombardo and C. Oliver. Maximum likelihood approach to the detection of changes between multitemporal SAR images. In *Radar, Sonar and Navigation, IEE Proceedings-*, volume 148, pages 200–210. IET, 2001.
- P. Lombardo and T. M. Pellizzeri. Maximum likelihood signal processing techniques to detect a step pattern of change in multitemporal SAR images. *Geoscience and Remote Sensing, IEEE Transactions on*, 40(4):853–870, 2002.
- A. Lopes, E. Nezry, R. Touzi, and H. Laur. Maximum a posteriori speckle filtering and first order texture models in SAR images. In *Geoscience and Remote Sensing Symposium, 1990. IGARSS'90. Remote Sensing Science for the Nineties'. 10th Annual International*, pages 2409–2412. IEEE, 1990.
- C. Louchet and L. Moisan. Total variation as a local filter. *SIAM Journal on Imaging Sciences*, 4(2):651–694, 2011.
-

- D. G. Lowe. Distinctive image features from scale-invariant keypoints. *International journal of computer vision*, 60(2):91–110, 2004.
- X. Lu. *Reasear on objects-oriented change detection using high resolution synthetic aperture radar images*. PhD thesis, Wuhan University, 2014.
- R. S. Lunetta, C. D. Elvidge, et al. *Remote sensing change detection: environmental monitoring methods and applications*. Taylor & Francis Ltd, 1999.
- S. Lyu and E. P. Simoncelli. Modeling multiscale subbands of photographic images with fields of gaussian scale mixtures. *Pattern Analysis and Machine Intelligence, IEEE Transactions on*, 31(4):693–706, 2009.
- M. Maggioni, G. Boracchi, A. Foi, and K. Egiazarian. Video denoising using separable 4D nonlocal spatiotemporal transforms. In *IS&T/SPIE Electronic Imaging*, pages 787003–787003. International Society for Optics and Photonics, 2011.
- M. Maggioni, G. Boracchi, A. Foi, and K. Egiazarian. Video denoising, deblocking, and enhancement through separable 4-d nonlocal spatiotemporal transforms. *Image Processing, IEEE Transactions on*, 21(9):3952–3966, 2012.
- M. Mahmoudi and G. Sapiro. Fast image and video denoising via nonlocal means of similar neighborhoods. *Signal Processing Letters, IEEE*, 12(12):839–842, 2005.
- J. Mairal, F. Bach, J. Ponce, G. Sapiro, and A. Zisserman. Non-local sparse models for image restoration. In *Computer Vision, 2009 IEEE 12th International Conference on*, pages 2272–2279. IEEE, 2009.
- W. A. Malila. Change vector analysis: an approach for detecting forest changes with Landsat. In *LARS Symposia*, page 385, 1980.
- F. Marin, C. Bovolo and L. Bruzzone. Detection of changed buildings in multitemporal Very High Resolution SAR images. In *Geoscience and Remote Sensing Symposium (IGARSS), 2013 IEEE International*, 2013.
- B. Martínez and M. Gilabert. Vegetation dynamics from NDVI time series analysis using the wavelet transform. *Remote Sensing of Environment*, 113(9):1823–1842, 2009.
- J. L. Michalek, T. W. Wagner, J. J. Luczkovich, and R. W. Stoffle. Multispectral change vector analysis for monitoring coastal marine environments. 1993.
- M. Molinier, J. Laaksonen, and T. Hame. Detecting man-made structures and changes in satellite imagery with a content-based information retrieval system built on self-organizing maps. *Geoscience and Remote Sensing, IEEE Transactions on*, 45(4):861–874, 2007.
- W. M. Moon, G. Staples, D.-j. Kim, S.-E. Park, and K.-A. Park. RADARSAT-2 and coastal applications: Surface wind, waterline, and intertidal flat roughness. *Proceedings of the IEEE*, 98(5):800–815, 2010.
- V. Neagoe, A. Ciurea, L. Bruzzone, and F. Bovolo. A novel neural approach for unsupervised change detection using SOM clustering for pseudo-training set selection followed by CSOM classifier. In *Geoscience and Remote Sensing Symposium (IGARSS), 2014 IEEE International*, pages 1437–1440. IEEE, 2014.
-

-
- H. Nemmour and Y. Chibani. Fuzzy neural network architecture for change detection in remotely sensed imagery. *International journal of remote sensing*, 27(4):705–717, 2006a.
- H. Nemmour and Y. Chibani. Multiple support vector machines for land cover change detection: An application for mapping urban extensions. *ISPRS journal of photogrammetry and remote sensing*, 61(2):125–133, 2006b.
- J.-M. Park, W.-J. Song, and W. Pearlman. Speckle filtering of SAR images based on adaptive windowing. *IEE Proceedings-Vision, Image and Signal Processing*, 146(4):191–197, 1999.
- S. Parrilli, M. Poderico, C. Angelino, and L. Verdoliva. A nonlocal SAR image denoising algorithm based on LLMMSE wavelet shrinkage. *Geoscience and Remote Sensing, IEEE Transactions on*, 50(2):606–616, 2012.
- W. B. Pennebaker and J. L. Mitchell. *JPEG: Still image data compression standard*. Springer, 1993.
- F. Petitjean, A. Ketterlin, and P. Gançarski. A global averaging method for dynamic time warping, with applications to clustering. *Pattern Recognition*, 44(3):678–693, 2011.
- F. Petitjean, J. Inglada, and P. Gançarski. Satellite image time series analysis under time warping. *Geoscience and Remote Sensing, IEEE Transactions on*, 50(8):3081–3095, 2012.
- J. Polzehl and V. Spokoiny. Propagation-separation approach for local likelihood estimation. *Probability Theory and Related Fields*, 135(3):335–362, 2006.
- J. Portilla, V. Strela, M. J. Wainwright, and E. P. Simoncelli. Image denoising using scale mixtures of Gaussians in the wavelet domain. *Image Processing, IEEE Transactions on*, 12(11):1338–1351, 2003.
- M. Preiss and N. Stacy. Coherent change detection: theoretical description and experimental results. Technical report, DTIC Document, 2006.
- S. Quegan and T. Le Toan. Analysing multitemporal SAR images. *EUROPEAN SPACE AGENCY-PUBLICATIONS-ESA SP*, 434:17–28, 1998.
- S. Quegan and J. J. Yu. Filtering of multichannel SAR images. *Geoscience and Remote Sensing, IEEE Transactions on*, 39(11):2373–2379, 2001.
- S. Quegan, T. Le Toan, J. J. Yu, F. Ribbes, and N. Floury. Multitemporal ERS SAR analysis applied to forest mapping. *Geoscience and Remote Sensing, IEEE Transactions on*, 38(2):741–753, 2000.
- G. Quin, B. Pinel-Puysegur, J.-M. Nicolas, and P. Loreaux. MIMOSA: An Automatic Change Detection Method for SAR Time Series. *Geoscience and Remote Sensing, IEEE Transactions on*, (99):1–15, 2013.
- R. J. Radke, S. Andra, O. Al-Kofahi, and B. Roysam. Image change detection algorithms: a systematic survey. *Image Processing, IEEE Transactions on*, 14(3):294–307, 2005.
-

- J. Ranjani and S. Thiruvengadam. Dual-tree complex wavelet transform based SAR despeckling using interscale dependence. *Geoscience and Remote Sensing, IEEE Transactions on*, 48(6):2723–2731, 2010.
- B. Riedel and A. Walther. InSAR processing for the recognition of landslides. *Advances in Geosciences*, 14(14):189–194, 2008.
- E. Rignot and J. van Zyl. Change detection techniques for ERS-1 SAR data. *Geoscience and Remote Sensing, IEEE Transactions on*, 31(4):896–906, 1993.
- P. A. Rosen, S. Hensley, I. R. Joughin, F. K. Li, S. N. Madsen, E. Rodriguez, and R. M. Goldstein. Synthetic aperture radar interferometry. *Proceedings of the IEEE*, 88(3):333–382, 2000.
- C. Rosito Jung and J. Scharcanski. Adaptive image denoising and edge enhancement in scale-space using the wavelet transform. *Pattern Recognition Letters*, 24(7):965–971, 2003.
- L. I. Rudin, S. Osher, and E. Fatemi. Nonlinear total variation based noise removal algorithms. *Physica D: Nonlinear Phenomena*, 60(1):259–268, 1992.
- M. E. Salih, X. Zhang, and M. Ding. Two Modifications of Weight Calculation of the Non-Local Means Denoising Method. *Engineering*, 5:522, 2013.
- J. Salmon. On two parameters for denoising with non-local means. *Signal Processing Letters, IEEE*, 17(3):269–272, 2010.
- J. Salmon and Y. Strozeci. From patches to pixels in non-local methods: Weighted-average reprojection. In *Image Processing (ICIP), 2010 17th IEEE International Conference on*, pages 1929–1932. IEEE, 2010.
- J. Salmon, Z. Harmany, C.-A. Deledalle, and R. Willett. Poisson noise reduction with non-local PCA. *Journal of mathematical imaging and vision*, 48(2):279–294, 2014.
- A. Schmitt, B. Wessel, and A. Roth. Curvelet approach for SAR image denoising, structure enhancement, and change detection. *International Archives of Photogrammetry, Remote Sensing and Spatial Information Sciences*, 38(3/W4):151–156, 2009.
- K. Schulz, E. Cadario, M. Boldt, and A. Thiele. Improving high-resolution repeat pass SAR image interpretation by the CoVAmCoh method. In *Synthetic Aperture Radar (EUSAR), 2010 8th European Conference on*, pages 1–4. VDE, 2010.
- Sensor Data Management System (SDMS) Public web site. VHF Change Detection Problem Set. https://www.sdms.afrl.af.mil/index.php?collection=vhf_change_detection, 2008. [Online].
- M. Sester, H. Hild, and D. Fritsch. Definition of ground-control features for image registration using GIS data. *International Archives of Photogrammetry and Remote Sensing*, 32:538–543, 1998.
- J. Shi and J. Malik. Normalized cuts and image segmentation. *IEEE Transactions on Pattern Analysis and Machine Intelligence*, 22(8):888–905, 2000.
-

-
- M. Shimada. SAR programmes in JAXA: from JERS-1 to the future. *IEE Proceedings-Radar, Sonar and Navigation*, 153(2):122–128, 2006.
- M. Simons, Y. Fialko, and L. Rivera. Coseismic deformation from the 1999 Mw 7.1 Hector Mine, California, earthquake as inferred from InSAR and GPS observations. *Bulletin of the Seismological Society of America*, 92(4):1390–1402, 2002.
- A. Singh. Digital change detection techniques using remotely-sensed data. *International journal of remote sensing*, 10(6):989–1003, 1989.
- R. Sluiter and S. de Jong. Spatial patterns of Mediterranean land abandonment and related land cover transitions. *Landscape Ecology*, 22(4):559–576, 2007.
- S. M. Smith and J. M. Brady. SUSAN-a new approach to low level image processing. *International journal of computer vision*, 23(1):45–78, 1997.
- T. Strozzi, A. Luckman, T. Murray, U. Wegmuller, and C. L. Werner. Glacier motion estimation using SAR offset-tracking procedures. *Geoscience and Remote Sensing, IEEE Transactions on*, 40(11):2384–2391, 2002.
- X. Su, C. Deledalle, F. Tupin, and H. Sun. Two steps multi-temporal Non-Local Means for SAR images. In *Geoscience and Remote Sensing Symposium (IGARSS), 2012 IEEE International*, pages 2008–2011. IEEE, 2012.
- X. Su, C. Deledalle, F. Tupin, and H. Sun. SAR Image Change Detection by Likelihood Ratio test in Multi-Temporal Time Series. In *Geoscience and Remote Sensing Symposium (IGARSS), 2013 IEEE International*, pages 2008–2011. IEEE, 2013.
- X. Su, C.-A. Deledalle, F. Tupin, and H. Sun. Change detection and classification of multi-temporal SAR series based on generalized likelihood ratio comparing-and-recognizing. In *Geoscience and Remote Sensing Symposium (IGARSS), 2014 IEEE International*, pages 1433–1436. IEEE, 2014a.
- X. Su, C.-A. Deledalle, F. Tupin, and H. Sun. Two-Step Multitemporal Nonlocal Means for Synthetic Aperture Radar Images. *Geoscience and Remote Sensing, IEEE Transactions on*, 52:6181 – 6196, 2014b.
- X. Su, C.-A. Deledalle, F. Tupin, and H. Sun. NORCAMA: Change Analysis in SAR Time Series by Likelihood Ratio Change Matrix Clustering. *ISPRS Journal of Photogrammetry and Remote Sensing*, 101:247–261, 2015.
- G. J. Sullivan, J. Ohm, W.-J. Han, and T. Wiegand. Overview of the high efficiency video coding (HEVC) standard. *Circuits and Systems for Video Technology, IEEE Transactions on*, 22(12):1649–1668, 2012.
- C. Sutour, J.-F. Aujol, C.-A. Deledalle, et al. Adaptive regularization of the NL-means: Application to image and video denoising. *IEEE Trans. on Image Processing*, 23:3506–3521, 2013.
- C. Sutour, J.-F. Aujol, and C.-A. Deledalle. Adaptive Regularization of the NL-Means: Application to Image and Video Denoising. *IEEE TRANSACTIONS ON IMAGE PROCESSING*, 23:3506–3521, 2014.
-

- S. Tabti, C.-A. Deledalle, L. Denis, F. Tupin, et al. Modeling the distribution of patches with shift-invariance: application to SAR image restoration. 2014.
- J. Tao, S. Auer, P. Reinartz, and R. Bamler. Object-based change detection for individual buildings in SAR images captured with different incidence angles. In *Geoscience and Remote Sensing Symposium (IGARSS), 2013 IEEE International*, 2013.
- T. Tasdizen. Principal neighborhood dictionaries for nonlocal means image denoising. *Image Processing, IEEE Transactions on*, 18(12):2649–2660, 2009.
- J. Tian, S. Cui, and P. Reinartz. Building change detection based on satellite stereo imagery and digital surface models. *Geoscience and Remote Sensing, IEEE Transactions on*, 52(1):406–417, 2014.
- C. Tomasi and R. Manduchi. Bilateral filtering for gray and color images. In *Computer Vision, 1998. Sixth International Conference on*, pages 839–846. IEEE, 1998.
- B. Tracey, E. Miller, Y. Wu, P. Natarajan, and J. Noonan. A constrained optimization approach to combining multiple non-local means denoising estimates. *Signal Processing*, 103:60–68, 2014.
- D. Tschumperlé and L. Brun. Non-Local Regularization and Registration of Multi-Valued Images By PDEs and Variational Methods on Higher Dimensional Spaces. In *Mathematical Image Processing*, pages 181–197. Springer, 2011.
- C. Unsalan. Detecting Changes in Multispectral Satellite Images using Time Dependent Angle Vegetation Indices. In *Recent Advances in Space Technologies, 2007. RAST'07. 3rd International Conference on*, pages 345–348. IEEE, 2007.
- D. Van De Ville and M. Kocher. SURE-based non-local means. *Signal Processing Letters, IEEE*, 16(11):973–976, 2009.
- D. Van De Ville and M. Kocher. Nonlocal means with dimensionality reduction and SURE-based parameter selection. *Image Processing, IEEE Transactions on*, 20(9):2683–2690, 2011.
- G. Vasile, E. Trouvé, J.-S. Lee, and V. Buzuloiu. Intensity-driven adaptive-neighborhood technique for polarimetric and interferometric SAR parameters estimation. *Geoscience and Remote Sensing, IEEE Transactions on*, 44(6):1609–1621, 2006.
- J. Verbesselt, R. Hyndman, G. Newnham, and D. Culvenor. Detecting trend and seasonal changes in satellite image time series. *Remote sensing of Environment*, 114(1):106–115, 2010a.
- J. Verbesselt, R. Hyndman, A. Zeileis, and D. Culvenor. Phenological change detection while accounting for abrupt and gradual trends in satellite image time series. *Remote Sensing of Environment*, 114(12):2970–2980, 2010b.
- M. Volpi, D. Tuia, F. Bovolo, M. Kanevski, and L. Bruzzone. Supervised change detection in VHR images using contextual information and support vector machines. *International Journal of Applied Earth Observation and Geoinformation*, 20:77–85, 2013.
-

- U. Von Luxburg. A tutorial on spectral clustering. *Statistics and computing*, 17(4):395–416, 2007.
- T. Wiegand, G. J. Sullivan, G. Bjontegaard, and A. Luthra. Overview of the H. 264/AVC video coding standard. *Circuits and Systems for Video Technology, IEEE Transactions on*, 13(7):560–576, 2003.
- R. Wiemker. An iterative spectral-spatial Bayesian labeling approach for unsupervised robust change detection on remotely sensed multispectral imagery. In *Computer Analysis of Images and Patterns*, pages 263–270. Springer, 1997.
- G. Xian and C. Homer. Updating the 2001 National Land Cover Database impervious surface products to 2006 using Landsat imagery change detection methods. *Remote Sensing of Environment*, 114(8):1676–1686, 2010.
- G. Xian, C. Homer, and J. Fry. Updating the 2001 National Land Cover Database land cover classification to 2006 by using Landsat imagery change detection methods. *Remote Sensing of Environment*, 113(6):1133–1147, 2009.
- L. Xu, J. Li, Y. Shu, and J. Peng. SAR Image Denoising via Clustering-Based Principal Component Analysis. *Geoscience and Remote Sensing, IEEE Transactions on*, 52(11):6858–6869, 2014.
- T. Yamamoto, H. Hanaizumi, and S. Chino. A change detection method for remotely sensed multispectral and multitemporal images using 3-D segmentation. *Geoscience and Remote Sensing, IEEE Transactions on*, 39(5):976–985, 2001.
- H. A. Zebker. Studying the Earth with interferometric radar. *Computing in Science & Engineering*, 2(3):52–60, 2000.
- H. A. Zebker, P. A. Rosen, and S. Hensley. Atmospheric effects in interferometric synthetic aperture radar surface deformation and topographic maps. *Journal of Geophysical Research: Solid Earth (1978–2012)*, 102(B4):7547–7563, 1997.
- L. Zhang, W. Dong, D. Zhang, and G. Shi. Two-stage image denoising by principal component analysis with local pixel grouping. *Pattern Recognition*, 43(4):1531–1549, 2010.
- X. Zhang, G. Hou, J. Ma, W. Yang, B. Lin, Y. Xu, W. Chen, and Y. Feng. Denoising MR Images Using Non-Local Means Filter with Combined Patch and Pixel Similarity. *PLoS one*, 9(6):e100240, 2014.
- Z. Zhu and C. E. Woodcock. Continuous change detection and classification of land cover using all available Landsat data. *Remote Sensing of Environment*, 144:152–171, 2014.
-